# OPTIMIZING AND DESIGNING POSITIVE ELECTRODE MATERIALS FOR SODIUM ION BATTERIES

by

Lituo Zheng

Submitted in partial fulfilment of the requirements
for the degree of Doctor of Philosophy

at

Dalhousie University
Halifax, Nova Scotia
March 2019

## TABLE OF CONTENTS

## LIST OF TABLES

## LIST OF FIGURES

## ABSTRACT

Sodium ion batteries have the potential to be a more sustainable alternative to the widely-used lithium ion batteries. Layered sodium transition metal oxides as positive electrode materials have been a focus of research. However, most sodium transition metal oxide materials suffer from low operating voltage, unstable crystal structure, poor cycling performance, and air-sensitivity. In order for sodium ion batteries to have practical application, more studies on positive electrodes are required.

This work focuses on the investigation of strategies to improve the behavior of positive electrode materials in sodium ion batteries. Some examples were given using transition metal layer substitution to develop novel positive electrode materials. Doping with certain elements significantly enhances the performance and alleviates some of the aforementioned problems. The possible role of dopant elements, specifically titanium or copper, was investigated. The structural and electrochemical performance of some nickel rich materials, which are possibly high-capacity materials, namely $Na_3Ni_2BiO_6$ and $NaNi_{0.8}Co_{0.15}Al_{0.05}O_2$ were also studied.

Besides transition metal layer doping, other methods were employed to modify the positive electrode materials. Washing $NaNi_{0.5}Mn_{0.5}O_2$ with ethanol removes most of the sodium residues on the surface, resulting in improved air stability, smaller hysteresis and higher capacity. Doping in the sodium layer with calcium leads to improved cycling performance, higher coulombic efficiency, and better air-stability. Finally, a preliminary study of using mechanofusion method to coat electrode materials with nanoparticles was demonstrated. Future directions of research are discussed.

## LIST OF ABBREVIATIONS USED

| | |
|---|---|
| *a, b, c* | Lattice constants of a unit cell |
| BET | Brunauer–Emmett–Teller |
| BMF | Blown microfiber polyethylene membrane |
| CE | Coulombic efficiency |
| *d* | Distance between lattice planes |
| DEC | Diethylene carbonate |
| DMC | Dimethyl carbonate |
| DW | Thermal factor |
| EC | Ethylene carbonate |
| EDS | Energy dispersive spectrometer |
| EMC | Ethyl methyl carbonate |
| F | Faraday constant |
| F(*hkl*) | Structure factor |
| FE | Field emission |
| FEC | Monofluoroethylene carbonate |
| $f_n$ | Atomic form factor |
| FTIR | Fourier transform infrared spectroscopy |
| *h, k, l* | Miller indices |
| I | Intensity |
| ICP-OES | Inductively coupled plasma optical emission spectrometry |
| L | Lorentz polarization factor |
| LCO | $LiCoO_2$ |
| LFP | $LiFePO_4$ |
| M | Molar mass |
| m | Multiplicity |
| N | Avogadro's number |
| n | Number of moles of charge carriers |
| NCA | $LiNi_{0.8}Co_{0.15}Al_{0.05}O_2$ |

| | |
|---|---|
| NMC | $LiNi_xMn_yCo_{1-x-y}O_2$ |
| NMC111 | $LiNi_{1/3}Mn_{1/3}Co_{1/3}O_2$ |
| NMC442 | $LiNi_{0.4}Mn_{0.4}Co_{0.2}O_2$ |
| NMC532 | $LiNi_{0.5}Mn_{0.3}Co_{0.2}O_2$ |
| NMC622 | $LiNi_{0.6}Mn_{0.2}Co_{0.2}O_2$ |
| NMC811 | $LiNi_{0.8}Mn_{0.1}Co_{0.1}O_2$ |
| NMP | N-methyl-2-pyrrolidone |
| O | Octahedral |
| P | Prismatic |
| $P_f$ | Pressure in a pycnometer after gas exchange |
| $P_i$ | Pressure inside the loaded sample chamber of a pycnometer |
| PO | Preferred orientation factor |
| PVDF | Polyvinylidene fluoride |
| $Q_c$ | Charge capacity |
| $Q_d$ | Discharge capacity and |
| $Q_t$ | Theoretical specific capacity |
| s | Cross-sectional area of one adsorbate molecule |
| S | Surface area |
| SEI | Solid electrolyte interphase |
| SEM | Scanning electron microscopy |
| v | Gas volume measured by BET method |
| V | Molar volume of gas |
| $V_1$ | Empty volume of sample chamber in a pycnometer |
| $V_2$ | Volume of internal chamber in a pycnometer |
| $V_s$ | Volume of the sample measured in a pycnometer |
| x, y, z | Positional coordinates |
| XRD | X-ray diffraction |
| $\theta$ | Angle between incident X-rays and diffraction planes |
| $\lambda$ | Wavelength |

## ACKNOWLEDGEMENTS

I would first like to thank my supervisor Dr. Mark Obrovac for the opportunity to work here. Mark has given me a lot of freedom and flexibility to let me explore my research. I am grateful for all the guidance, patience, and encouragement he provided. I would also like to thank my supervisory committee, Dr. Mita Dasog, Dr. Harm Rotermund, and Dr. Peng Zhang for their help and support along the way.

I would like to thank Dr. Jeff Dahn for use of his equipments, and Dr. Tim Hatchard for countless help with instruments. All the members of the Obrovac lab, past and present, are acknowledged. Most notably, I would like to thank summer students Peter Nguyen, Jerry Li, Rebecca Boyd and visiting professor, Dr. Lingjun Li, for their contribution to this work, and for the good time we spent together.

Finally I would like to thank all my families and friends, who have always been the source of inspiration and happiness.

# CHAPTER 1 INTRODUCTION

## 1.1 Background

In the past century humanity has started to influence the Earth's environment at unprecedented rates. The widescale use of fossil fuels enabled Industrial Revolution, but also produced large amounts of carbon dioxide, leading to an unusually rapid increase in global average temperature, known as global warming. Concerns have been raised regarding the decreasing availability of fossil fuels and the degradation of environment, which ultimately threatens the inhabitability of the planet [2]. As a result, there is a trend towards transition to sustainable energies that do not rely on fossil fuels. For example, Canada intends to phase out coal-fired electricity by 2030 and replace it with more renewable energy, which would have significant environmental and health impacts [3].

On the other hand, green and renewable energy resources, such as wind or solar energy, are usually intermittent and unstable. Efficient energy storage systems are therefore needed for load-leveling. As of the end of 2018, the most widely used energy storage system for grid energy storage is pumped hydroelectric storage, which stores excess energy as gravitational potential energy of water [4]. The disadvantage of such a system is that it requires special topography and is difficult to miniaturize. Portable energy storage systems that can be made into various sizes are desirable, especially for electric vehicle and home use. Rechargeable battery technology is a promising technology for applications in grid energy storage and electric vehicles [5]. There are already a variety of commercially available home batteries and electric vehicles powered by lithium ion batteries. It is

anticipated that lithium ion batteries will continue to gain more market share in these areas [6].

The widespread use of lithium ion batteries is due to their many amazing characteristics. Lithium ion batteries have the merits of high energy density, long cycle life, high charge/discharge efficiency and low maintenance. However, problems regarding their cost, availability, and safety still remain [7]. In recent years rechargeable lithium batteries have been used increasingly in portable electronic devices, electric vehicles, and grid energy storage. In 2017, the manufacture of lithium batteries accounted for 46% of the worldwide lithium production, a sharp increase compared to 39% from the previous year [8,9]. In response to increased demand for lithium ion batteries, global lithium production increased by an estimated 13% in 2017 [9]. Nevertheless, lithium is not regarded as an abundant element. The abundance of lithium is only about 20 parts-per-million in earth's crust. Lithium is also a geographically limited resource with more than half of the lithium reserves located in South America [9]. As electric vehicles and electric grid energy storage become popular, the increasing demand for lithium ion batteries could lead to a price rise and lithium scarcity. According to the USGS, in 2017 the price of battery-grade lithium carbonate has doubled since 2013 [9].

Sodium ion battery technology might be a more sustainable alternative to the currently used lithium ion batteries. From a chemical perspective, sodium shares the same group with lithium and has many similarities to lithium. Both lithium and sodium have one valence electron. The standard electrode potential is -3.04 V for $Li^+/Li$ and -2.76 V for $Na^+/Na$ [10]. Compared with lithium, sodium is cheaper, more abundant, and more uniformly distributed on the planet. Sodium is the sixth most abundant element on earth

and sodium salt is one of the most easily accessible reserves everywhere. There is a virtually unlimited sodium source in the ocean as well. In addition, lithium ion battery positive electrode materials typically comprise cobalt, which is toxic, expensive, and scarce. However, cobalt may not be necessary as a component of cathode materials in sodium ion batteries. Positive electrode materials based on earth abundant elements, such as iron and manganese, have been reported with decent energy density and cyclability [11]. Moreover, current collectors are a major cost in battery production. Copper is used as the negative electrode current collector in lithium ion batteries. Unlike lithium, sodium does not alloy with aluminum, therefore aluminum could be used as the current collector for sodium ion battery negative electrodes instead of more expensive copper [10]. All these features show that sodium ion batteries have the potential to be a low-cost alternative to lithium ion batteries.

Both lithium and sodium can store one charge per ion. Nevertheless it should be noted that as lithium has a smaller ionic radius, a smaller atomic mass, and a lower reduction potential than sodium, lithium ion batteries have inevitably a higher energy density than sodium ion batteries. The lower energy density predicted for sodium ion batteries would make them more appropriate for grid storage where size and weight are not as pressing concerns, compared to cell phone or other portable electronic devices. Therefore, much research in the sodium ion battery field is focused on stationary power applications. There has been accelerating research activity in sodium ion batteries in the past few years. Developing suitable positive electrode materials for sodium ion batteries is crucial for the realization of commercial sodium ion batteries. Transition metal oxides have been the focus of positive electrode materials research, as they are easy to synthesize and

have relatively high energy density [12]. However, most layered sodium transition metal oxide materials suffer from low operating voltage, unstable crystal structure, poor cycling performance, and air-sensitivity, compared to their lithium counterparts [13]. In order for sodium ion batteries to have practical application, more studies on positive electrode materials are required.

This thesis is devoted to optimizing and designing positive electrode materials that can hopefully contribute to the commercialization of sodium ion batteries. Various strategies were shown to alleviate some of the aforementioned problems and they will be the subject of this thesis.

## 1.2 Lithium Ion Batteries

The operating mechanism of sodium ion batteries can be seen as being analogous to lithium ion batteries. For that reason, an introduction to lithium ion batteries, which is already a relatively mature technology, is given here as a basis for understanding sodium ion battery chemistry. Each component of lithium ion batteries is discussed, with a focus on layered type positive electrode materials because of their relevance to the subject of this thesis.

### 1.2.1 Operating Mechanism

Lithium ion batteries comprise a negative electrode, a positive electrode, a separator and an electrolyte. In commercial batteries both negative and positive electrodes are composite materials, prepared from active material powders, binders and conductive additives. The active materials, such as $LiCoO_2$ for positive electrodes and graphite for

negative electrodes, are capable of reversibly intercalating lithium ions in their crystal structures. A porous membrane separator containing electrolyte is used to separate the negative electrode from the positive electrode. The separator is made from electrically insulating polymers (typically polyethylene and/or polypropylene), so as to keep the positive and negative electrodes electrically isolated and prevent internal shorting. The electrolyte is ionically conductive to allow lithium ion transport between positive and negative electrodes. Both negative and positive electrodes are attached to current collectors, which are copper foil for the negative electrode and aluminum foil for the positive electrode. When the cell is being charged or discharged, an external circuit connects the positive electrode and the negative electrode, allowing current to flow. A schematic diagram of a lithium ion battery is shown in Figure 1.1.

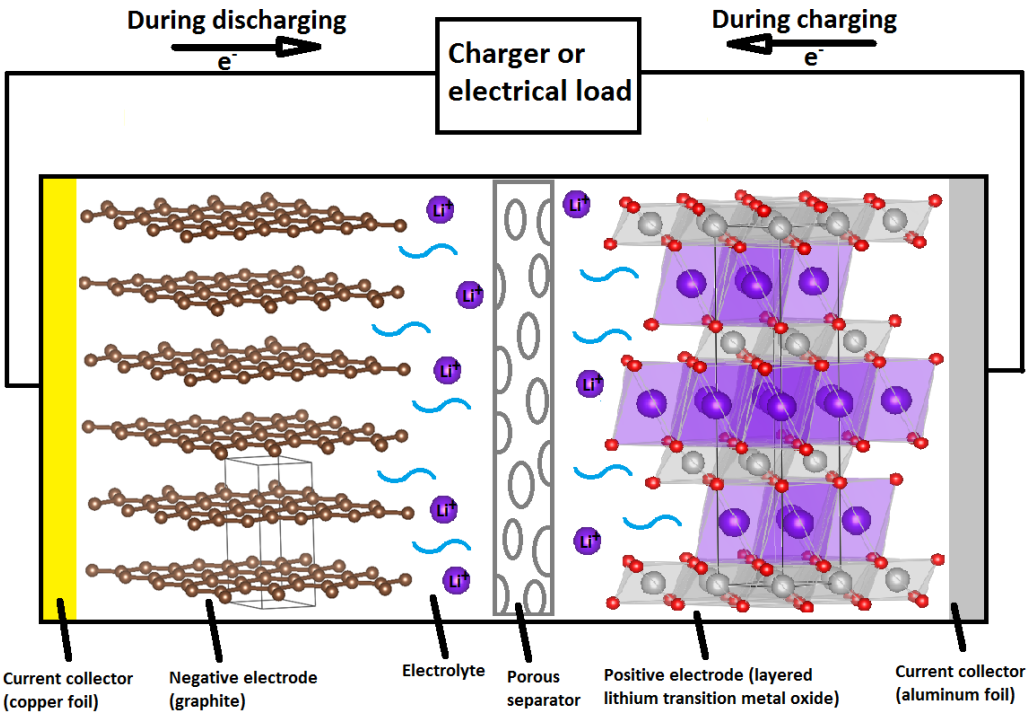


Figure 1.1 Schematic of a lithium ion battery. Oxygen ions are shown in red, lithium ions are shown in purple, transition metal ions are shown in grey, and carbon atoms are shown in brown.

In most cases a lithium ion battery is manufactured in its discharged state, with all the lithium in the positive electrode and no lithium in the negative electrode. In electrochemistry, the term “cathode” refers to the electrode that is accepting electrons, while the term “anode” refers to the electrode that is losing electrons. The flow of electrons is always from anode to cathode outside of the cell. During the charge of a lithium ion battery, the negative electrode acts as a cathode and positive electrode acts as an anode. An external voltage is applied during charge, which causes the positive electrode to have a higher chemical potential with respect to lithium than the negative electrode. Lithium ions are removed from the positive electrode, to the negative electrode through electrolyte. At the same time, electrons are removed from the positive electrode to the negative electrode through the external circuit. After fully charging, lithium vacancies exist in the positive electrode, while the negative electrode is lithium-rich.

The discharge process is driven by the difference between the chemical potential of positive electrode and negative electrode with respect to lithium. As the positive electrode has a lower chemical potential with respect to lithium than the negative electrode, lithium ions spontaneously travel from negative electrode to the positive electrode through electrolyte when an external circuit is connected to the battery. The electrons simultaneously travel from the negative electrode to the positive electrode via the external circuit. After fully discharging, there should be little or no lithium in the negative electrode. In this case, the negative electrode acts as anode and the positive electrode acts as cathode. It should be noted that in most literature, “cathode” and “positive electrode” have been used interchangeably, while “anode” and “negative electrode” have been used interchangeably. This convention will be followed in this thesis.

The reactions on each electrode and the total reaction can be represented by the following equations:

$$LiCoO_2 \leftrightarrow x\ Li^+ + x\ e^- + Li_{1-x}CoO_2 \quad (1.1)$$

$$x\ Li^+ + x\ e^- + y\ C \leftrightarrow\ Li_xC_y \quad (1.2)$$

$$LiCoO_2 + y\ C \leftrightarrow\ Li_xC_y + Li_{1-x}CoO_2 \quad (1.3)$$

The working voltage of such a cell can be expressed as

$$E = -\frac{(\mu_{cathode} - \mu_{anode})}{e} \quad (1.4)$$

where $\mu_{cathode}$ and $\mu_{anode}$ are the chemical potentials in electron volts (eV) of the cathode and the anode, respectively, with respect to lithium and e is the charge of an electron.

### 1.2.2 Lithium Ion Battery Positive Electrode (cathode) Materials

Positive electrode materials are synthesized in lithium-rich form and act as a lithium source in a lithium ion battery. An ideal cathode should have high capacity and voltage, stable structure, good cyclability, good safety characteristics and low cost [14]. Common cathode materials include lithium transition metal oxides, such as layered-type $LiCoO_2$ or spinel-type $LiMn_2O_4$, and polyanion compounds, such as $LiFePO_4$.

The first commercial lithium ion batteries developed by Sony in 1991 employed $LiCoO_2$ (LCO) as the positive electrode material. LCO has since been the most commonly used positive electrode material. The typical crystal structure of LCO is shown in Figure 1.2 (a). LCO is composed of alternating lithium layers and cobalt layers, separated by

oxygen layers. Each lithium or cobalt atom is octahedrally coordinated by six oxygen atoms and there are three layers of lithium (or cobalt) in each unit cell. This structure is called an O3-type structure. This notation was first proposed by Delmas et al. and has been used extensively to describe alkali metal-containing materials with layered structures [15]. The letter O or P describes the chemical environment of the alkali ion in the structure ($Na^+$ or $Li^+$), either in an octahedral (O) or prismatic (P) site formed by oxygen. The number 2 or 3 describes the number of repeating transition metal layers (or alkali metal layers) in a unit cell. Therefore, for an O3-type structure, "O" indicates that lithium ions are located in octahedral sites formed by neighboring oxygens, and "3" indicates there are three repeating lithium layers in a unit cell. Besides the O3 structure, LCO with O2 and O4 structures have also been reported [16]. They all have comparable electrochemical performance. However, O2 and O4 type LCO are not likely to have industrial application since it is more difficult to prepare O2 and O4 than O3-LCO.

LCO has the merits of having a stable structure, high energy density, and easy synthesis. During charge, lithium ions are removed from the interlayers of LCO and pass through the electrolyte into the anode. Concurrently, $Co^{3+}$ is partially oxidized to $Co^{4+}$. The layered structure of LCO allows facile lithium diffusion. When all the lithium is removed, LCO transforms into O1-type $CoO_2$ with a very high theoretical capacity of 274 mAh/g. Nevertheless, this capacity cannot be used practically because the O3-O1 phase transition is not fully reversible, leading to material degradation and rapid capacity fade during repeated cycling [17]. In addition, in order to remove all the lithium, the cell has to be charged to a high voltage (~5 V), which causes severe electrolyte decomposition and poor cyclability [18]. Therefore in a commercial lithium ion cell, LCO is usually cycled

reversibly to remove ~0.5 lithium per LCO, resulting in a practical capacity of ~140 mAh/g and an average voltage of ~3.9 V. Because of the toxicity and the high cost of cobalt, researchers have been attempting to develop other cathode materials.

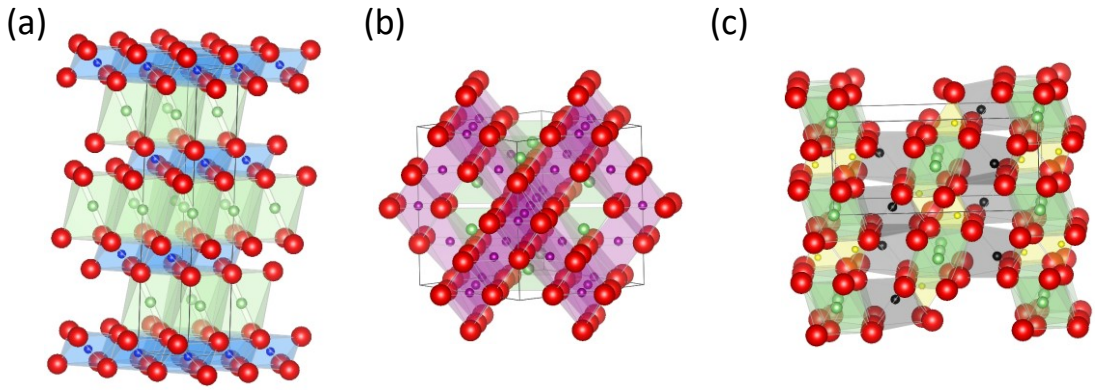


Figure 1.2 Crystal structure of O3-$LiCoO_2$, spinel $LiMn_2O_4$, and olivine $LiFePO_4$. Oxygen ions are shown in red, lithium ions are shown in green, cobalt ions are shown in blue, manganese ions are shown in purple, iron ions are shown in black, and phosphorus ions are shown in yellow. The coordination sites formed by oxygen are shown by polyhedra. Solid black lines show the unit cell in each structure.

One alternative cathode material that has been extensively studied is $LiNiO_2$, which is isostructural to LCO [19]. Compared with LCO, $LiNiO_2$ has higher capacity and lower cost. Unfortunately, $LiNiO_2$ has some intrinsic drawbacks. The synthesis of phase pure $LiNiO_2$ is very difficult (perfectly stoichiometric $LiNiO_2$ probably does not exist) and the material tends to form $Li_{1-x}Ni_{1+x}O_2$ [20]. This off-stoichiometry would make some $Ni^{3+}$ become reduced to $Ni^{2+}$. Because of the similar size of $Ni^{2+}$ and $Li^+$, $Ni^{2+}$ can easily migrate to the lithium layer and mix with $Li^+$. Such phenomenon is called cation disorder/mixing, which usually causes increased voltage hysteresis and low capacity, and is to be avoided [19,21]. $LiNiO_2$ also shows a distinct deterioration after it is stored in air. The air-sensitivity makes the material hard to handle [22]. Most importantly, it has been reported that delithiated $LiNiO_2$ readily releases oxygen upon heating, leading to thermal runaway in

charged cells, which could possibly lead to an explosion [23]. As a result, $LiNiO_2$ is not a promising cathode for commercial lithium ion batteries.

The substitution of nickel with other metals, such as cobalt and aluminum, can overcome some of the problems associated with $LiNiO_2$. Doping $LiNiO_2$ with cobalt is effective at reducing cation disorder and improving cyclability, while doping $LiNiO_2$ with aluminum can shorten the M-O bond, leading to improved safety [24,25]. One material that has shown to be particularly successful in regard to performance and economics is $LiNi_{0.8}Co_{0.15}Al_{0.05}O_2$ (NCA) with an O3 structure [26]. NCA is now being widely used in commercial lithium ion batteries. Similarly, in LCO, the substitution of cobalt with other metals could reduce cost and improve performance. The most common substitution elements used are nickel and manganese, to form a composition of $LiNi_xMn_yCo_{1-x-y}O_2$ (NMC), also with an O3 structure [27,28]. The performance of NMC strongly depends on its exact composition. Increasing the nickel content provides high capacity but poor thermal stability and cyclability, while increasing the manganese content leads to good safety and cyclability, at the expense of a lower capacity and rate performance [29]. This fact indicates a trade-off relationship between different aspects of cathode materials. Some of the typical commercial NMC materials are $LiNi_{1/3}Mn_{1/3}Co_{1/3}O_2$ (NMC111), $LiNi_{0.4}Mn_{0.4}Co_{0.2}O_2$ (NMC442) and $LiNi_{0.5}Mn_{0.3}Co_{0.2}O_2$ (NMC532), as each offer a different balance between price, lifetime, safety, rate performance, and energy density. Recently, nickel-rich NMC materials, such as $LiNi_{0.6}Mn_{0.2}Co_{0.2}O_2$ (NMC6222) and $LiNi_{0.8}Mn_{0.1}Co_{0.1}O_2$ (NMC811), have drawn lots of attention because of their high capacity and relatively low cost [30]. However, challenges still exist for nickel-rich NMC materials in terms of synthesis,

cyclability, and safety. Other doping elements, such as Mg, Ti, Zr, etc., have also been reported to improve the performance of layered cathode materials [31–33].

Another type of promising layered cathode material is the Li and Mn-rich type of cathode materials. A classic example is $Li(Li_{1/3}Mn_{2/3})O_2$, which can also be written as $Li_2MnO_3$. Materials within the solid solution formed by $Li_2MnO_3$ and regular NMC, such as x $Li_2MnO_3$·(1-x) $LiNi_{1/3}Mn_{1/3}Co_{1/3}O_2$ have been the focus of much study [34,35]. In these materials, excess lithium ions replace some of the transiton metal ions in the transition metal layers. Since the theoretical capacity of a material is limited by the amount of lithium that can be extracted from the crystal structure, lithium rich materials can potentially deliver higher cpacities (up to 300 mAh/g) and higher energy densities [36]. It is typically belived that Ni, Mn and Co cannot be oxidized to an oxidation state beyond 4+ in an octahedral environment. Interestingly, when lithium is removed from lithium rich materials, part of the charge compensation is achieved by the oxidation of oxygen ions [37]. This process is not fully reversible, therefore lithium rich materials usually have a large first cycle irreversible capacity and a continous voltage decay over extended cycling. The cycling performance of lithium rich materials is also not satifactory [38]. More studies are required in order for lithium-rich materials to have practical applications.

As lithium ion batteries are to be used increasingly in applications that require long life time, such as electric vehicles, cycle life is of paramount importance. In order to improve cycle life, researchers have used different strategies, such as surface coating modification, the use of advanced binders, and designing concentration-gradient structures [39–41]. These approaches have been shown to effectively improve the cycle life without compromising the energy density and cost. For example, a core-shell NMC material that

contains a nickel-rich core and manganese-rich shell can offer better cyclability than tranditional nickel-rich materials, due to the more stable manganese-rich surface [41].

Other cathode materials that are not layered are spinel $LiMn_2O_4$ and olivine $LiFePO_4$. Materials with these structures are not studied in this thesis. However, they important commercial battery materials that account for more than one third of the market share, and so will be mentioned here briefly. $LiMn_2O_4$ has a spinel structure with lithium in tetrahedral sites and manganese in octahedral sites, as shown in Figure 1.2(b). $LiMn_2O_4$ has excellent rate performance due to its 3D network that facilitates fast lithium diffusion. It also has low cost and high operating voltage. Problems with this material lie in its low capacity, poor high temperature performance, and the dissolution of manganese into electrolyte [42]. The stability of $LiMn_2O_4$ can be improved by substituting $Mn^{3+}$ with other transition metals having a 2+ oxidation state, such as $Ni^{2+}$, thus increasing the $Mn^{4+}$ concentration and thereby reducing the concentration of $Mn^{3+}$ that induces Jahn-Teller distortion [42].

$LiFePO_4$ (LFP) is the most studied polyanion-based positive electrode. Iron is naturally abundant and less toxic than nickel, manganese and cobalt. Therefore LFP is believed to have greater envrionemtal benefit over LCO or NMC. LFP has a olivine structure, as shown in Figure 1.2(c). The main obstacle with LFP in the early days of its development was its poor ionic and electronic conductivity. The 1-D tunnels in which lithium ions diffuse in LFP can be easily blocked by defects and impurities, which results in slow diffusion kinetics and extremely poor rate capability [43]. By nanosizing the particle and coating with carbon, LFP can achieve high-rate capability and can be used for practical applications [43]. LFP is also known for its very good safety performance. When

LFP is heated with electrolyte, minimum self heating is observed compared to other cathode materials [44]. The drawback of LFP is its low average voltage and volumetric capacity, which makes it a poor choice for applications where high energy density is required.

### 1.2.2 Lithium Ion Battery Negative Electrode (anode) Materials

Although anode materials are not a part of this thesis, information regarding anode materials is given here as general background knowledge. Lithium metal has extremely high volumetric/gravimetric capacity. Because of the low redox potential of lithium (E = -3.04 V versus the standard hydrogen electrode), it also results in a high battery operating voltage and thus a high energy density. Therefore lithium metal was first used as the negative electrode for commercial lithium batteries. Nevertheless, it was later discovered that batteries employing lithium metal anodes have severe safety issues. As a lithium battery is charged and discharged, lithium dendrites, which have a branched structure, forms on the surface of lithium metal [45]. The continuous formation of dendrites leads to increased surface area, causing more side reactions between electrolyte and the reactive lithium metal, resulting in poor cycling performance and thermal instability. Dendrites can also penetrate the separator between anode and cathode, inducing internal shorting, thermal runaway, fire or even explosion [45]. Moli Energy, the first company to mass-produce lithium metal batteries, recalled all its rechargeable lithium metal batteries after several safety incidents in 1989. As a result, research moved to develop batteries without metallic lithium [46].

As of 2018, graphite is the most commonly used negative electrode material for lithium ion batteries. Other forms of carbon, such as hard carbon, soft carbon have also been studied and used as negative electrode materials [47]. Lithium ions can electrochemically intercalate/deintercalate into the layered structure of graphite with low hysteresis. Under normal temperature and pressure, up to one lithium ion can be inserted per 6 carbon atoms, forming $LiC_6$ with a theoretical capacity of 372 mAh/g [48]. This is a very high specific capacity for an intercalation compound. Graphite is light-weight, inexpensive and has stable structure during cycling. The high conductivity also ensures good rate capability. A low average operating voltage of ~0.1 V vs. Li+/Li provides high energy density, but also poses risk of lithium plating, especially at the end of lithium insertion where the voltage approaches 0 V [49]. As mentioned above, lithium plating leads to poor cycling and safety concerns. Moreover, the operating voltage of graphite is outside of the electrochemical stability window of most common electrolytes, therefore a continuous reaction of electrolyte occurs on graphite during cycling, leading to cell fade [50].

Spinel-type $Li_4Ti_5O_{12}$, which can also be written as $Li(Li_{1/3}Ti_{5/3})O_4$, has a structure similar to that of $LiMn_2O_4$. With an average operating voltage of ~1.5 V, each $Li_4Ti_5O_{12}$ can accommodate 3 lithium ions and transforms into rocksalt $Li_7Ti_5O_{12}$, resulting in a theoretical capacity of 175 mAh/g. Compared to graphite, $Li_4Ti_5O_{12}$ has a much lower energy density and is not suitable for applications that require high energy density [51]. Nevertheless, its merits lie in its better cycling stability and safety because the high operating voltage prevents dendrite formation. $Li_4Ti_5O_{12}$ is also known to be a “zero-strain” insertion material with almost no volume change during cycling, therefore the cycle life of

$Li_4Ti_5O_{12}$ is superior to graphite [52]. Moreover, as the electrolyte reduction voltage is well below the operating voltage of $Li_4Ti_5O_{12}$, there is minimum electrolyte consumption on the $Li_4Ti_5O_{12}$ surface, which further improves the cyclability [53].

Extensive research has also been conducted using alloy as anodes for lithium ion batteries. Alloys are attractive as they can store more lithium per unit volume than graphite, leading to a higher capacity and energy density [54]. For example, silicon and tin can react with lithium to form $Li_{15}Si_4$ and $Li_{17}Sn_4$ with theoretical volumetric capacities of 2190 $mAh/cm^3$ and 2111 $mAh/cm^3$, respectively [54,55]. For comparison, graphite has a theoretical volumetric capacity of 719 $mAh/cm^3$. The enormous capacity of Si is accompanied with an enormous volume change during cycling, leading to particle fracture, progressive consumption of electrolyte, and disconnection of the electrode from the current collector [54]. As a result, alloy type anodes usually have poor cyclability compared to intercalation type materials. More studies are required to improve the cyclability and reduce the cost of alloy materials [54].

### 1.2.3 Lithium Ion Battery Electrolyte

The electrolyte acts as a medium to transport lithium ions back and forth between the positive electrode and the negative electrode in a cell. Electrolytes used in commercial lithium ion batteries commonly consist of organic solvents and a lithium salt. Ideal solvents should possess a wide operating temperature, low viscosity, good electrochemical stability and good salt solubility. However, often a solvent may satisfy some of these requirements, while lacking in others. Therefore, a mixture of two or more solvents are typically used to achieve the best performance [56]. Some of the common solvents used include ethylene

carbonate (EC), diethylene carbonate (DEC), dimethyl carbonate (DMC), and ethyl methyl carbonate (EMC) [57]. $LiPF_6$ is the most common salt used in commercial lithium ion batteries because of its good solubility and chemical stability [56]. Disadvantages of using $LiPF_6$ stem from its thermal instability and its moisture sensitivity. $LiPF_6$ readily reacts with traces of water in the cell to form HF, which can corrode active materials and other cell parts [58]. Alternative electrolyte systems including ionic liquids, aqueous electrolytes and solid/polymer electrolytes have also been studied [57].

Electrolyte deterioration is probably one of the most important causes of cell fade in commercial lithium ion batteries. On the electrode surfaces, electrolyte decomposes and forms a surface layer known as the solid electrolyte interphase (SEI). The composition of the SEI is complex and usually comprises LiF, $Li_2CO_3$, $Li_2O$, etc. The SEI is characterized by low electronic conductivity and high ionic conductivity, allowing the passage of lithium ions during cycling [59]. EC is widely deemed to be an essential electrolyte solvent. One of the reasons is that it forms a stable SEI on graphite and inhibits solvent co-intercalation [60]. The formation of SEI is a continuous process that spans the entire life of a cell, but it is most prominent in the first few cycles. After first few cycles, the formed SEI acts as a passivation layer that slows down further SEI formation [61]. During cycling, the SEI thickens, causing continuous consumption of lithium and increased impedance. Therefore, much research effort has been focused on understanding and optimizing the SEI. Typical approaches to modify the SEI include the use of advanced lithium salts and electrolyte additives [40,62].

## 1.3 Sodium Ion Batteries

Sodium ion battery technology is a promising alternative to lithium ion batteries. The operating mechanism of sodium ion batteries is similar to that of lithium ion batteries. They can both be described as “rocking-chair batteries”, where the charge carriers (lithium or sodium ions) are shuttled between the two electrodes during charge/discharge. A sodium ion battery consists of a positive electrode, a negative electrode, a separator and an electrolyte. During cycling, sodium ions act as charge carriers and are shuttled back and forth between two electrodes that can reversibly intercalate sodium ions. Similar to lithium ion batteries, no metallic sodium is present in a sodium ion battery. This can prevent the formation of metallic dendrites, resulting in better cyclability and safety. Layered sodium transition metal oxides were first studied for use in sodium ion batteries in the 1980s, but research slowed due to outstanding success of lithium ion batteries [63,64]. In recent years, because of concerns of human impact on the environment, sodium ion batteries have regained interest as a possible alternative to lithium ion batteries for grid energy storage systems [10]. The amount of papers published every year in this field is steadily increasing. Figure 1.3 shows the number of academic results regarding sodium ion batteries published every year, as obtained when “sodium ion batteries” is searched using Google Scholar.

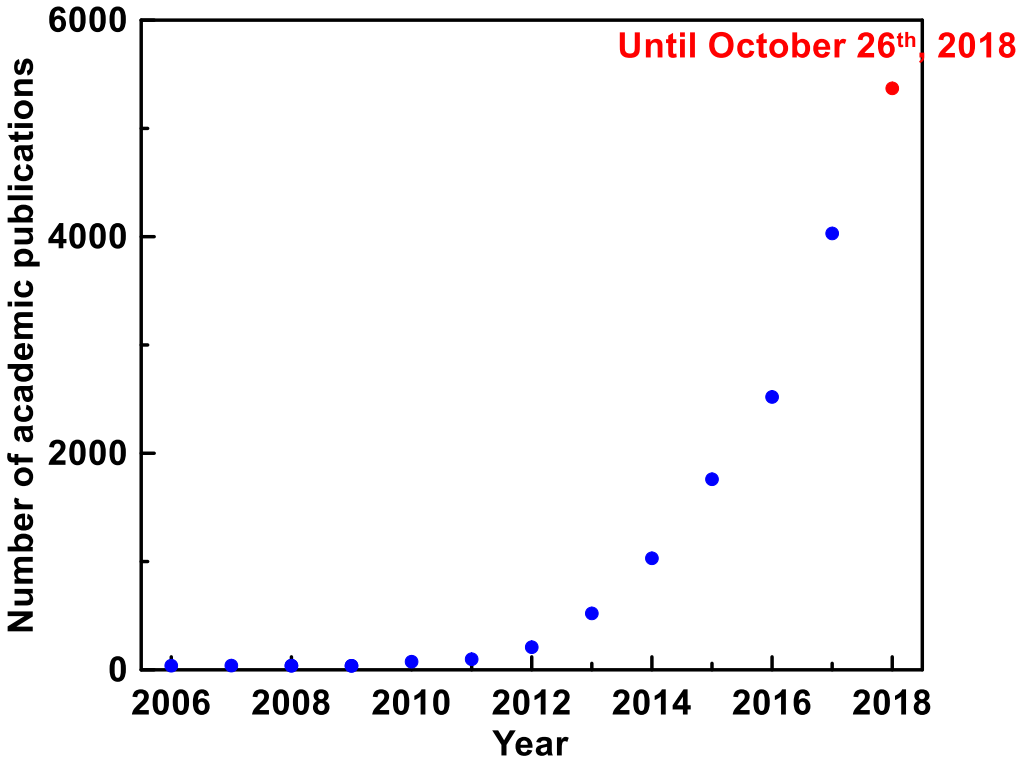


Figure 1.3 Number of academic publications regarding sodium ion batteries as obtained using Google Scholar (retrieved October 26th, 2018).

### 1.3.1 Layered Type Positive Electrode (cathode) Materials for Sodium Ion Batteries

Like lithium ion batteries, there are many choices of positive electrode materials for sodium ion batteries, including oxides and polyanionic compounds [65]. Layered structure sodium transition metal oxides have been the most studied materials because of their easy synthesis and high energy densities [12]. Layered structure materials will be the focus of this thesis. These layered oxides generally can be described with a formula of $Na_xMO_2$, where x is usually between 0.5 and 1, and M stands for one or more transition metals. In a full sodium ion battery, $Na_xMO_2$ is the sodium source and the battery is assembled in the discharged state. During charge, sodium is removed from $Na_xMO_2$ and

M is oxidized to a higher oxidation state. During the discharge, sodium is intercalated back into the structure and M is reduced.

The layered structures are closely related to the dense packing of spheres. As a starting point, consider oxygen ions as perfect spheres with identical size. They can be densely packed to form a structure with each sphere in contact with six other spheres in a plane, as shown in Figure 1.4 (a). This is labelled layer A. The next layer of spheres, labelled layer B, is placed on top of the hollow between three spheres of layer A, as shown in Figure 1.4 (b). All the spheres in layer A and B have the same arrangement. A third layer of oxygens can be superimposed on the first layer, as shown in Figure 1.4 (c), which would make the third layer and first layer equivalent, thus forming an ABA oxygen sequence. Alternatively, the third layer can be constructed by placing oxygens in the interstitial site of the first two layers, as shown in Figure 1.4 (d), forming an ABC stacking sequence. These two packings are also referred to as hexagonal close packing (ABAB) and cubic close packing (ABCABC). Figure 1.4 (e) shows the two structures with first layer shown in black, second layer shown in red and third layer shown in blue. The projections of first and third layer on the second layer are shown to demonstrate the relative position of atoms. Both these two packing methods result in the maximum possible density for sphere arrangements and they are commonly observed in crystallography. Different layered structures can be described using a specific sequence of letters A, B and C, such as ABAB, ABCABC, and others.

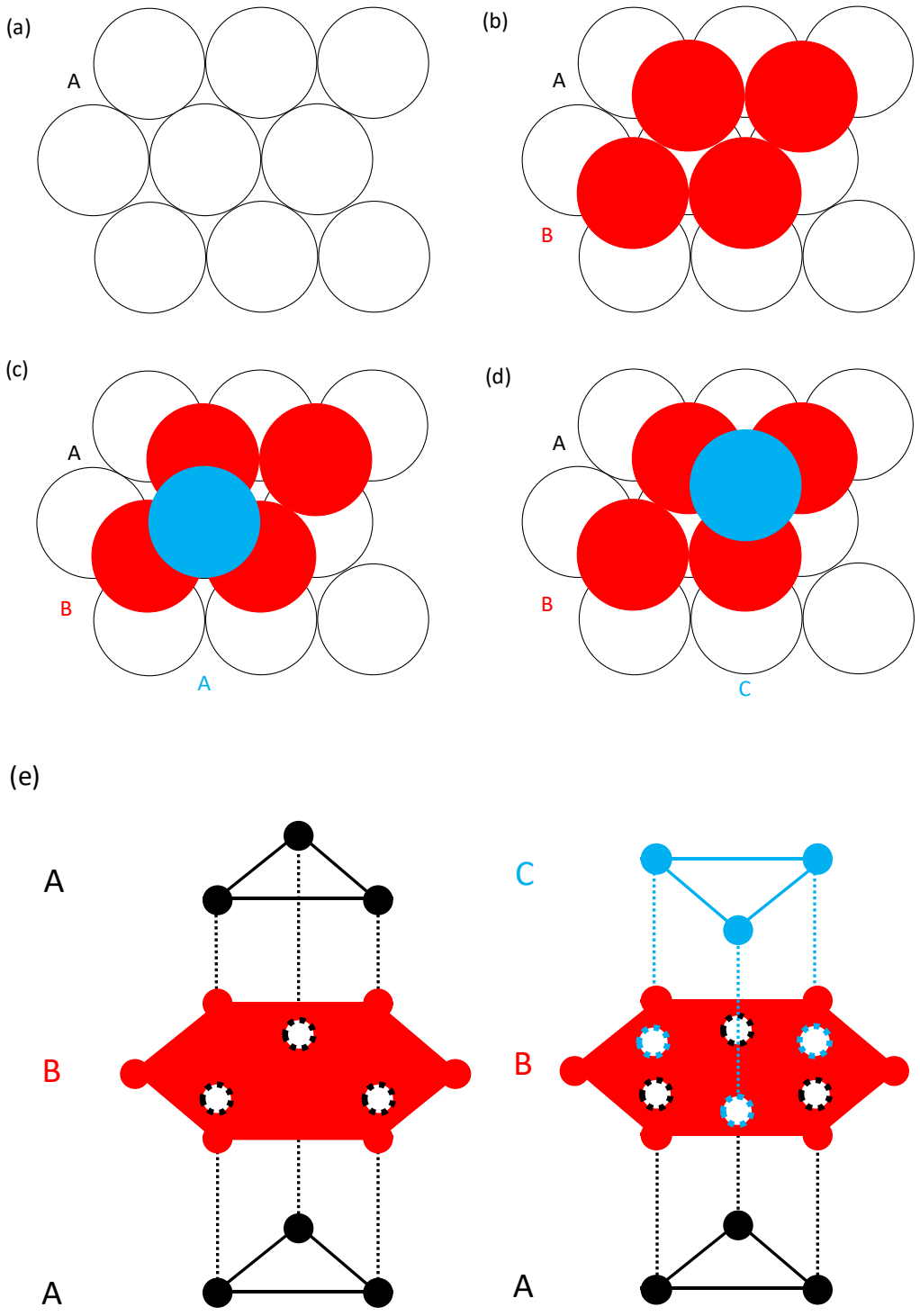


Figure 1.4 Different oxygen layer stacking arrangements. (a) Densely packed oxygen in layer A. (b) Densely packed oxygen in layer A and B. (c) Hexagonal close packing of oxygen. (d) Cubic close packing of oxygen. (e) Hexagonal and cubic close packing of oxygen.

In these layered structures, there are interstitial sites between oxygen ions. Figure 1.5(a) shows a tetrahedral site and an octahedral site between two different layers of oxygen ions. Figure 1.5(b) shows a prismatic site between two equivalent layers of oxygen ions (AA oxygen stacking). The shape of each site is shown in Figure 1.5(c). Both octahedral and prismatic sites are coordinated to six oxygen ions and tetrahedral sites coordinated to four oxygen ions. These interstitial sites can accommodate transition metal ions and alkali metal ions, forming layered structure cathode materials.

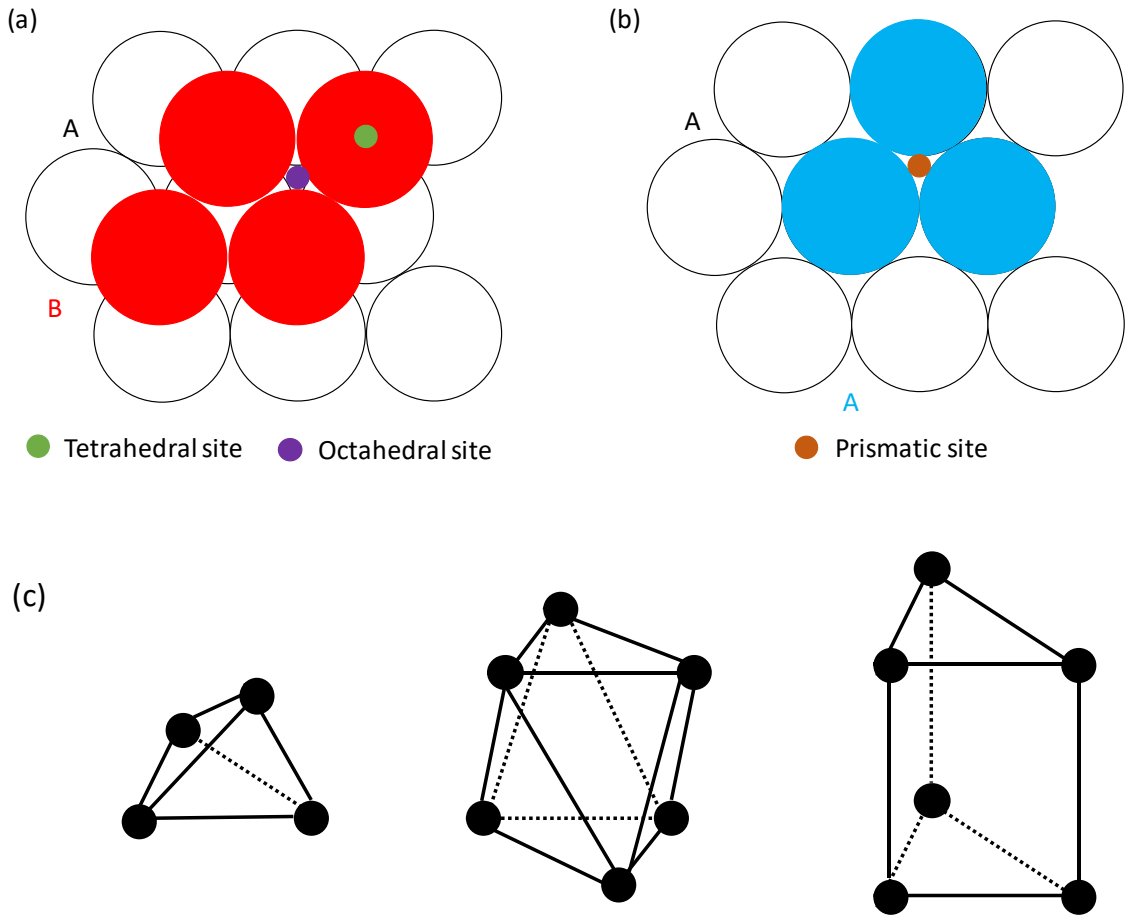


Figure 1.5 Interstitial sites formed in different oxygen layer stackings. (a) Positions of tetrahedral and octahedral sites. (b) Position of prismatic site. (c) Shape of tetrahedral, octahedral, and prismatic sites.

$Na_xMO_2$ commonly takes the form of O3 or P2 type structures (shown in Figure 1.6). The oxygen stacking sequence is ABBA for P2 type materials and ABCABC for O3 type materials. It is common for sodium rich materials ($Na_xMO_2$ where x is close to 1) to form an O3 structure, and sodium deficient materials ($Na_xMO_2$ where x is close to 2/3) to form a P2 structure [12].

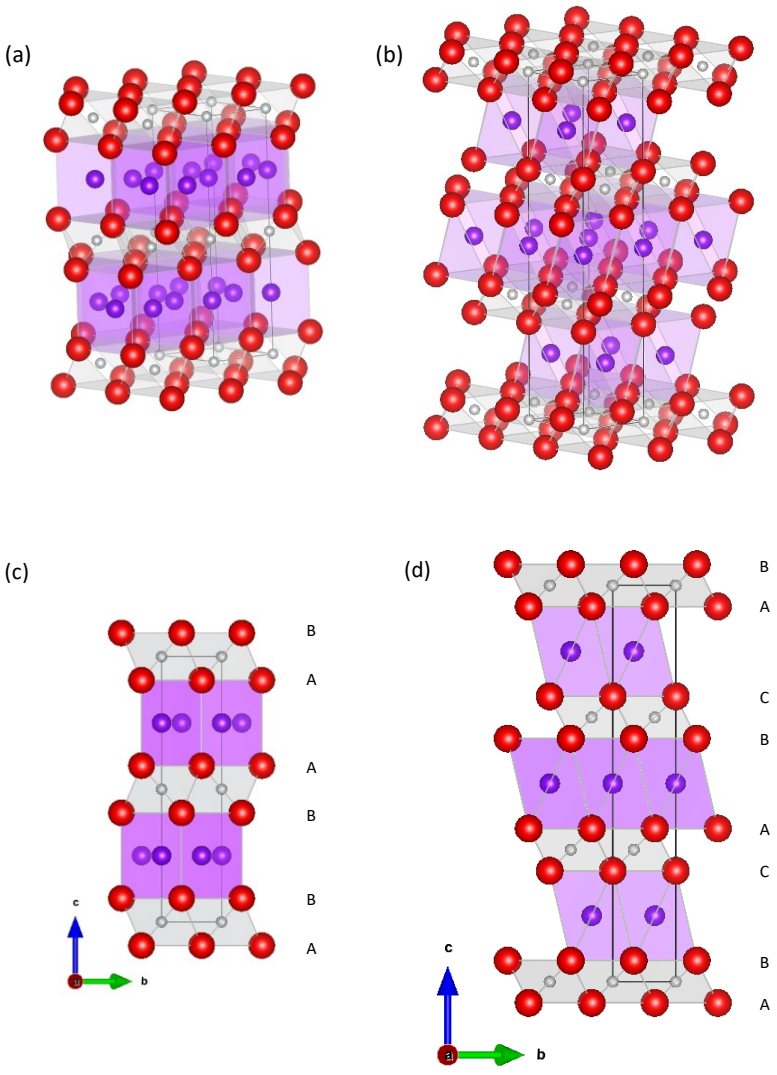


Figure 1.6 Crystal structures of layered (a) P2 and (b) O3 materials. Grey spheres are transition metal ions, red spheres are oxygen ions, and purple spheres correspond to sodium ions. $MO_6$ octahedra are highlighted in grey and $NaO_6$ octahedra (or prisms) in purple.

While O3 and P2 structures are the most common, other structures can be formed by alkali metal-containing transition metal oxides, including O2, P3, O6, T2 (T stands for tetrahedral), etc [66–68]. For example, Figure 1.7 shows the crystal structure and the oxygen stacking of O2 and P3 phases. The oxygen stacking sequence is ABACABAC for O2 type materials and ABBCCA for P3 type materials. Some of these structures are metastable phases at room temperature and can only be synthesized using ion exchange or other topotactic methods. For instance, Paulsen et al. synthesized T2 type $Li_{2/3}Ni_{1/3}Mn_{2/3}O_2$ by ion exchange from P2 type $Na_{2/3}Ni_{1/3}Mn_{2/3}O_2$ [66]. There are also some very interesting structures that contain both octahedral and prismatic alkali metal sites in one phase, such as the OP4 and OPP9 structures [69,70]. In the OP4 structure, each unit cell has four alkali metal layers, two of which form P-type ordering and the other two have O-type ordering [69]. Similarly, the OPP9 structure is characteristic with nine alkali metal layers in a unit cell, six of them being P-type and three of them O-type [70]. These metastable phases have garnered academic interest but their chances of being used in industry are small due to the complex ion exchange processes used in their synthesis.

Sodium transition metal oxides have the advantage of forming P-type structures. While lithium ions can only be accommodated in octahedral sites (and sometimes tetrahedral sites), sodium ions can also be placed in prismatic sites, allowing the formation of P-type structures [66]. This phenomenon is thought to be due to the ionic size difference between sodium and lithium ions. Prismatic sites are larger than octahedral sites, therefore a larger alkali metal ion is required to stabilize the structure [71]. When a substantial amount of sodium is removed from a P-type structure chemically or electrochemically, the

P-type structure can no longer be maintained, resulting in the gliding of the oxygen planes to form O-type or T-type structures [66].

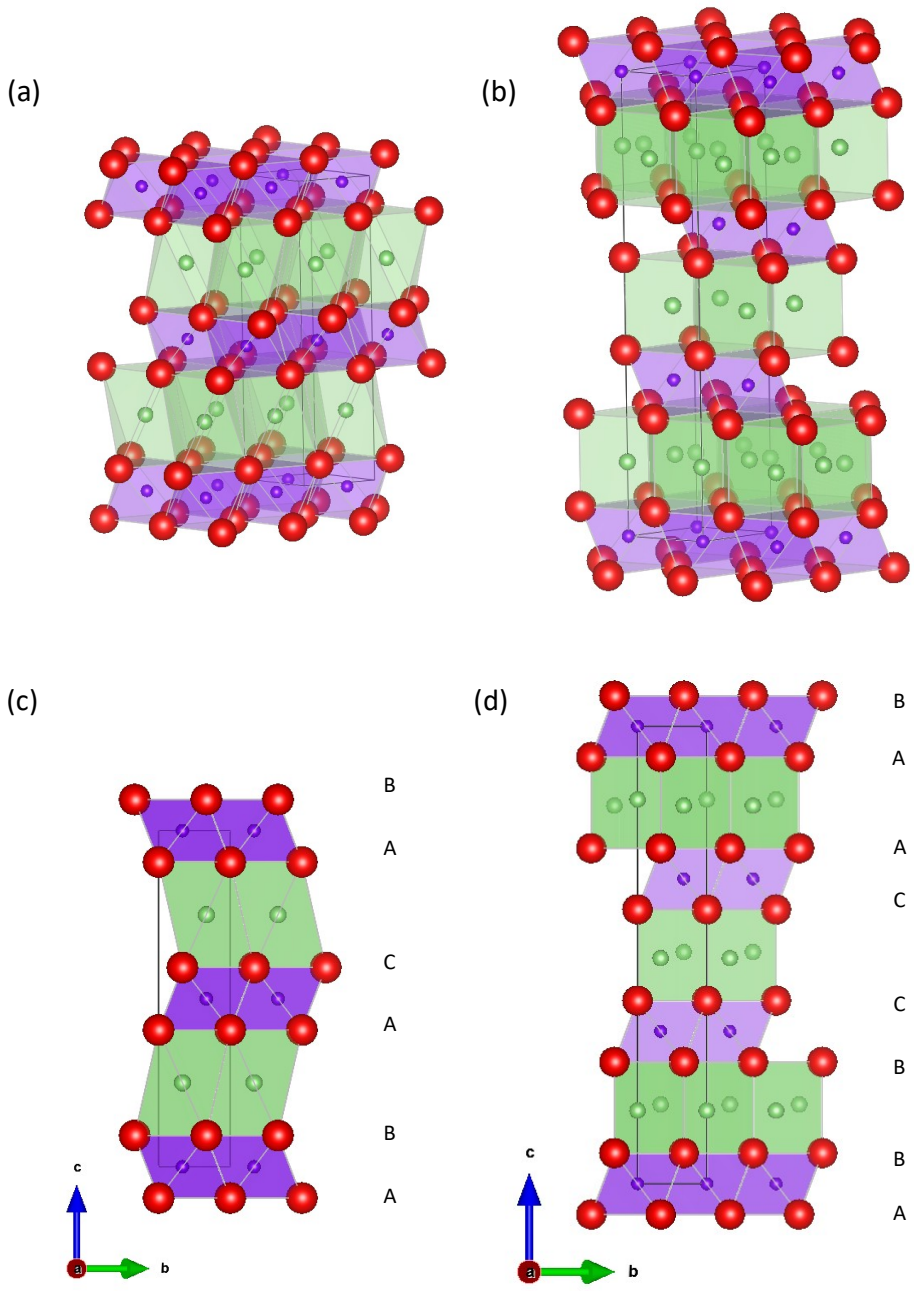


Figure 1.7 Crystal structures of layered (a) O2 and (b) P3 materials. Purple spheres are transition metal ions, red spheres are oxygen ions, and green spheres correspond to alkali metal ions. $MO_6$ octahedra are highlighted in purple and $NaO_6$ octahedra (or prisms) in green.

Though both P2 and O3 phases are electrochemically active towards reversible sodiation/desodiation, the P2 phase usually delivers better overall electrochemical performance than a respective O-type structure [12]. An example of this would be the comparison of the P2-$Na_{2/3}Mn_{1/2}Fe_{1/2}O_2$ and O3-$NaMn_{1/2}Fe_{1/2}O_2$ materials reported by Komaba et al. [11]. The O3-type structure has 100 - 110 mAh/g reversible capacity, whereas the P2-type has a reversible capacity of up to 190 mAh/g, both in the voltage range of 1.5 - 4.2 V vs. $Na/Na^+$ and at a current density of 12 mA/g. Because the particle size and morphology of both materials are similar, the difference in electrochemical performance was not due to diffusion length. Instead, it was concluded that P2-type structures allow for faster diffusion kinetics [11]. In an O-type structure, octahedral sites only share edges and do not share faces between two neighboring octahedral sites. Sodium cannot diffuse directly from one octahedral site into another octahedral site due to the high activation energy barrier. The sodium migration in an O-type structure requires sodium to pass through a narrow tetrahedral site between two octahedral sites, as shown in Figure 1.8(a). In contrast to the tortuous path for the O-type structure, sodium diffusion in the P-type structure is more straightforward. All the prismatic sites directly share faces with each other [72]. The open path allows for easy sodium hopping within the structure, as shown in Figure 1.8(b). This results in a higher ionic conductivity of P-type materials than O-type materials for samples with similar chemical compositions.

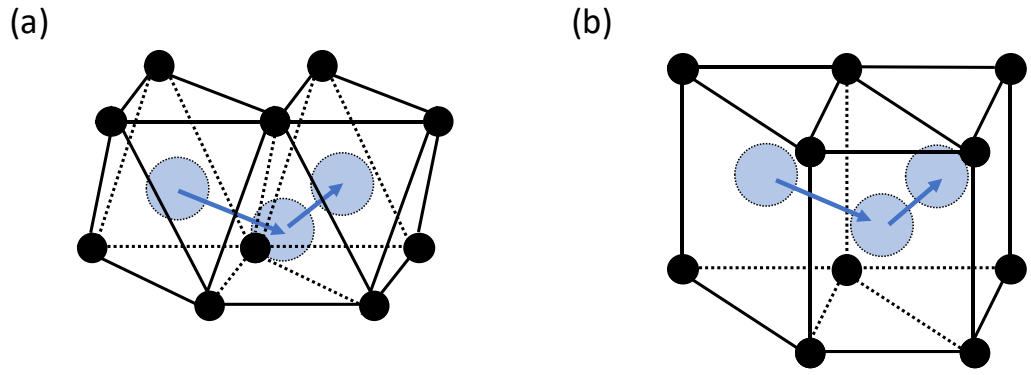


Figure 1.8 Sodium ion diffusion path in cathode materials with (a) O-type and (b) P-type structures.

Another advantage of sodium containing layered oxides is the possibility of new chemistry. For example, $LiFeO_2$ and $LiCrO_2$ are almost electrochemically inactive, whereas $NaFeO_2$ and $NaCrO_2$ are highly active, each in spite of having the same structure and transition metal [73–75]. One of the reasons is that lithium and iron (or chromium) cations tend to mix in layered oxides because of their similar ionic radii, while the larger difference of ionic size between sodium and transition ions results in them having less tendency to mix [10]. Utilizing environmentally friendly elements like iron, which is among the most abundant and inexpensive on earth, is attractive for large scale applications. Iron-based and chromium-based materials have been studied extensively and some materials have high energy densities and good cyclability [11,76]. Hatchard et al. demonstrated a high coulombic efficiency of 99.97% for $NaCrO_2/NaCrO_2$ symmetric cells, the highest coulombic efficiency reported so far for sodium ion battery materials [77]. Xia et al. reported that $NaCrO_2$ is an extremely safe material. Desodiated $Na_{0.5}CrO_2$ shows minimal oxygen release and reactivity with electrolyte when heated [78]. These properties are desirable for large scale applications.

Compared to second and third row transition metals, first row transition metals are more studied because they are cheaper, lighter, and confer higher voltage to cathode materials. There is an interesting trend in the average voltage of $NaMO_2$ for different transition metals. Generally, the average voltage of $NaMO_2$ increases as the transition metal element M is changed from left to right in the periodic table, as shown in Figure 1.9. This can be explained by the increasing electronegativity and ionization energy for later transition metals. A higher ionization energy means that it takes more energy to remove an electron from its outer shell, and therefore a higher voltage is required to further oxidize the ion. Consequently it can be expected that later transition metals and higher valence transition metals exhibit higher average voltage. However this voltage trend is only prominent for the first few transition metals (Ti, V, Cr), because the operating voltage is complex and also influenced by other factors.

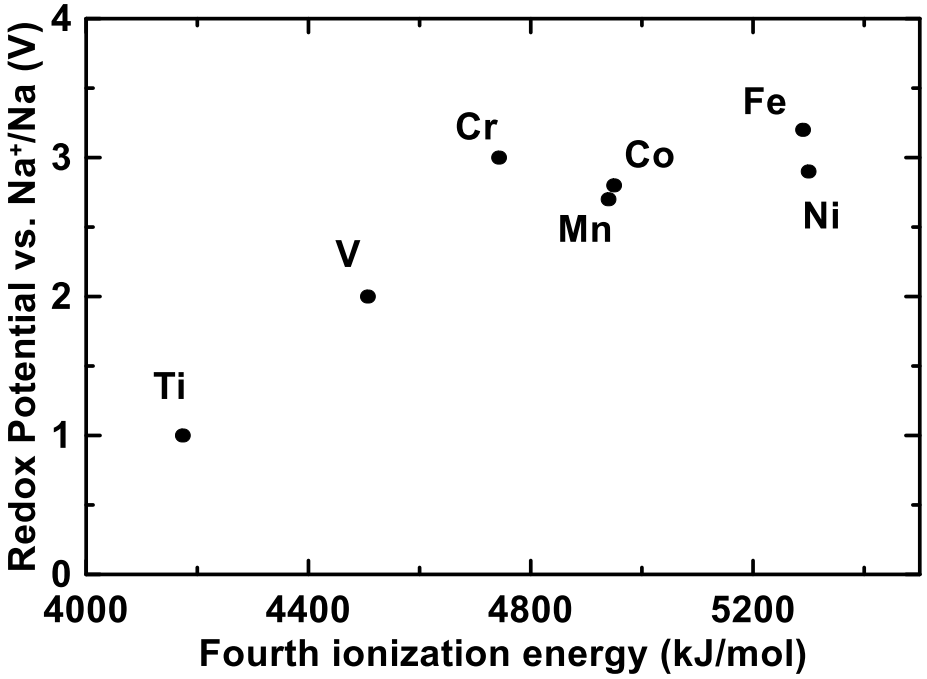


Figure 1.9 Redox potential of O3-$NaMO_2$ vs. fourth ionization energy [1].

The structure and electrochemistry of layered sodium transition metal oxides $Na_xMO_2$ (M= V, Ti, Cr, Mn, Fe, Co, Ni, Cu) have been studied since the 1980s [12]. Of these, $Na_xMO_2$ with a single transition metal M, $Na_xVO_2$ and $Na_xTiO_2$ are usually considered negative electrode materials because their operating voltages are relatively low, which will be discussed later. For the rest of the transition metal elements, an average voltage of ~3 V is typically observed, which is ~0.8 V lower than most lithium ion battery layered cathodes (LCO, NMC, NCA) [1]. By adjusting the sodium content and transition metal composition, a high voltage material can be developed. For example, P2-$Na_{2/3}Ni_{1/3}Mn_{2/3}O_2$ and P2-$Na_{2/3}Cu_{1/3}Mn_{2/3}O_2$ both have a high average voltage of ~3.6 V, which is comparable to positive electrode materials for lithium ion batteries [72,79].

Due to the larger radius of sodium ions, stronger structural reordering or phase transitions during sodiation/desodiation are often observed, compared to what occurs in Li-containing transition metal oxides during lithiation/delithiation. This results in a stepwise voltage curve for sodium ion cathode materials and, often, poor cyclability [1]. Phase transitions during cycling appear to be a source of capacity fade [72]. Binary, ternary and beyond $NaMO_2$ systems have been studied in order to alleviate the problems of poor capacity retention and structural instability. Some of the most studied materials include P2-$Na_{2/3}Mn_{1/2}Fe_{1/2}O_2$, P2-$Na_{2/3}Ni_{1/3}Mn_{2/3}O_2$, O3-$NaFe_{1/2}Ni_{1/2}O_2$, O3-$NaNi_{1/2}Mn_{1/2}O_2$, etc [11,72,80,81]. This combining of transition metals provides possibilities of tuning material properties, leading to an increase in energy densities, the suppression of phase transitions, and better cyclability. In order to develop commercially applicable sodium layered positive electrodes, the role and effect of each transition metal in these materials must be systematically studied and understood.

Another common source of capacity fade is the migration of transition metals into the sodium layer, which is typically observed in O3-type materials [74,82]. As sodium is removed electrochemically during cycling, the vacancies created in the sodium layer can accommodate transition metals, especially at higher voltages where there are a lot of vacant sites in the sodium layer [74,82]. A schematic diagram of transition metal migration is shown in Figure 1.10. When there are enough vacancies in the sodium layer, transition metal ions can first migrate to either tetrahedral sites in the transition metal layer, or to tetrahedral sites in the sodium layer. Afterwards, transition metal ions can migrate from tetrahedral sites into octahedral sites that originally hosted sodium ions [82]. Both these two paths are possible. Such migration is mostly irreversible and leads to the transition metals blocking sodium diffusion pathways in the sodium layer in subsequent cycles [74,82]. As a result, a large hysteresis and irreversible capacity can be observed during cycling. Transition metal migration has been reported for materials containing Ti, Cr, and Fe [74,82,83]. For instance, $NaFeO_2$ has relatively good capacity retention in the voltage range of 2.5 V – 3.4 V. Its capacity retention is much worse when the upper cut-off voltage increases, which has been ascribed to irreversible iron migration [74]. Suppressing such migration can be achieved by modifying the material's structure or composition. Yoshida et al. demonstrated that iron migration in $NaFeO_2$ can be suppressed by cobalt substitution, leading to higher capacity and cyclability [84].

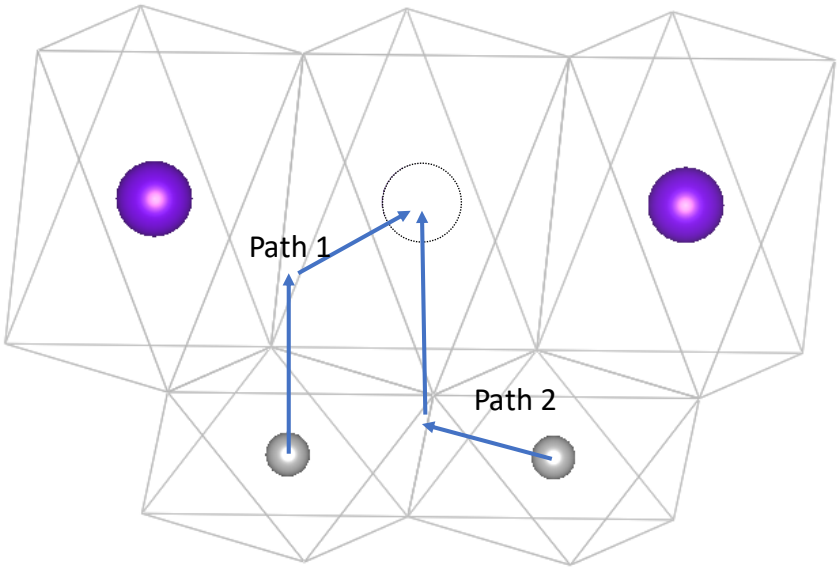


Figure 1.10 Schematic diagram of transition metal migration into the sodium layer in an O-type structure.

It should be noted that most sodium cathode materials, including both P2 and O3 type structures, are air-sensitive [85,86]. The reaction between cathode materials and air is complex and different for various materials. Lu et al. reported that water can be intercalated into the sodium layer of P2-type $Na_{2/3}Co_{1/3}Mn_{2/3}O_2$, forming $Na_{2/3}(H_2O)_{2/3}Co_{1/3}Mn_{2/3}O_2$ [87]. Such intercalation is reversible and the water can be completely removed by heating the hydrated phase [87]. Kubota et al. reported that most O3-type materials readily react with water by an irreversible ion exchange process, in which $Na^+$ in the O3 structure is ion-exchanged with $H^+$ in the water and forms NaOH [13]. Duffort et al. reported an unprecedented insertion of $CO_3^{2-}$ ions into P2-$Na_{2/3}Fe_{1/2}Mn_{1/2}O_2$ within transition metal layers when exposed to air [85]. Air-sensitive materials exhibit deteriorated performance when exposed to air and require special handling conditions, which would increase manufacturing cost [85]. Therefore, understanding and improving the air-stability is an important research subject in the sodium ion battery research community. Recently, some

air-stable materials have been reported, such as O3-$Na_{0.9}Cu_{0.22}Fe_{0.3}Mn_{0.48}O_2$ and P2-$Na_{7/9}Cu_{2/9}Fe_{1/9}Mn_{2/3}O_2$ [88,89].

### 1.3.2 Sodium Ion Battery Negative Electrode (anode) Materials

Due to safety concerns, sodium metal is not considered as a viable anode candidate. Carbonaceous anode materials are appealing for their low cost and availability. Unfortunately, sodium ions cannot insert into graphite to any appreciable extent at ambient pressure, in contrast to the easy intercalation of lithium into graphite [1]. There are some reports of solvated sodium ion insertion into graphite. Such co-intercalation is usually accompanied with low capacity (~100 mAh/g) and is therefore not attractive for commercial applications [90,91]. More practically relevant, the intercalation of sodium ions into carbon materials has been reported using hard carbon, which is composed of disordered graphene sheets [92,93]. Sodium can be intercalated between the graphene sheets or be absorbed into the pores formed by the random stacking of graphene sheets, resulting in a reversible capacity of about 300 mAh/g. This gravimetric capacity is comparable to the capacity of graphite in lithium ion batteries (372 mAh/g). It should be noted that more than half of the capacity is at voltage below 50 mV. At this voltage sodium plating can happen especially during fast charging or overcharging, which leads to poor cycling and safety concerns. Therefore the usefulness of capacity at such low voltage is doubtful. In addition, the density of hard carbon is lower (1.5 $g/cm^3$) than graphite (2.1 $g/cm^3$), resulting in a lower volumetric capacity of 450 Ah/L, compared with 750 Ah/L for graphite in lithium ion batteries [94]. Recent studies on hard carbon anode materials focus on improving capacity and cycle life by modifying the carbon precursors, heating conditions, and electrolyte additives [95–97].

Alloys have long been considered and studied as negative electrode material candidates of both lithium and sodium ion batteries [98]. Compared to intercalation materials, such as hard carbon, alloy materials can store more sodium ions per formula and deliver a higher capacity [98]. Many Group 14 and 15 elements are known to form alloys with sodium [99]. Both theoretical and experimental studies show the viability of using alloy negative electrodes for sodium ion batteries [100,101]. Reversible sodiation of tin, antimony, lead, and bismuth have been reported [101,102]. However, like the case of alloy materials in lithium ion batteries, a poor long-term cycling performance is usually observed due to significant volume change during cycling. There is an ongoing effort regarding the optimization of binders, electrode structures, electrolyte additives, etc. for use with alloy materials [1,100]. More studies are required to improve the cycle life for the practical use of alloy materials to be realized.

Transition metal oxides that can reversibly intercalate sodium have also been studied intensively as anodes. A lot of these materials contain titanium because the low voltage of $Ti^{3+}/Ti^{4+}$ compared to other transition metals, as shown in Figure 1.9. Some examples include $TiO_2$, $NaTiO_2$, $Na_2Ti_3O_7$ and $Na_2Ti_6O_{13}$ [83,103–105]. One advantage of titanium-based oxide anode materials is that they usually have a smaller volume change and better cyclability than alloys. Similar to what is observed in layered cathodes, using a combination of titanium and another metal element can further improve the stability of the crystal structure and cycling performance. For example, $Na_{2/3}Co_{1/3}Ti_{2/3}O_2$ exhibits a capacity retention of 84% after 3000 cycles [106]. Interestingly, when the other metal coupled with titanium is electrochemically active at a suitable redox voltage, the material can be used as both positive and negative electrodes, and are referred to as bi-functional

electrodes. Bi-functional electrodes can potentially lower the cost of manufacturing as only one electrode needs to be processed. Examples of bi-functional materials include $Na_{0.6}Cr_{0.6}Ti_{0.4}O_2$ and $Na_{2/3}Ni_{1/3}Ti_{2/3}O_2$, in which $Cr^{3+}/Cr^{4+}$ or $Ni^{2+}/Ni^{4+}$ act as cathode redox couples and $Ti^{3+}/Ti^{4+}$ acts as an anode redox couple [107,108].

# CHAPTER 2 EXPERIMENTAL METHODS

## 2.1 Materials Synthesis

In this thesis, sodium transition metal oxides were synthesized using high temperature solid state reactions. Stoichiometric amounts of powder precursors were first mixed by high energy ball milling using a SPEX 8000 mill. Typically, a 3:1 ball:sample mass ratio with a sample size of ~6 g and four 7/16 inch diameter stainless steel balls were sealed into one hardened steel milling vessel in air and milled for 2 hours. Precursors were usually in the form of metal oxides, hydroxides, or carbonates, such as sodium carbonate, nickel hydroxide, manganese oxide, etc., as specified below. After ball milling, the XRD patterns show that the resulting powders are usually semi-amorphous. This is evidence of mixing at the atomic scale, which results in short atomic diffusion lengths for crystallization and a faster reaction rate during annealing. Due to the evaporation of sodium at high temperature, an excess amount of sodium precursor (typically 5% - 10%) is used to compensate for sodium loss.

Ball milled precursor powders were compressed into pellets using a hydraulic press. Pelletization not only reduces the sodium loss during sintering, but also increases the reaction rate by reducing porosity and increasing the contact area between powders. Pellets were transferred into an alumina boat and placed in a quartz tube. The tube was heated at specified temperatures, typically between 600 °C to 1000 °C in a tube furnace for different times. A controlled gas flow, such as argon, oxygen, or dry air, was used during heating. During heating, gas-phase decomposition products, such as carbon dioxide, oxygen, and water vapor, were carried away by the flowing gas. Desired layered structure compounds

were obtained from the interdiffusion of the remaining atoms in the solid, including sodium, transition metal, and oxygen.

After heating, samples were either slow-cooled in the furnace, quenched in air, or quenched in liquid nitrogen. Because of the potential air-sensitivity of sodium cathode materials, samples were transferred directly from the tube furnace to an Ar-filled glovebox still sealed within the quartz furnace tube without air exposure. The pellets were retrieved, ground using a mortar and pestle to fine powders and stored in an Ar-filled glovebox for further studies.

## 2.2 X-ray Diffraction

### 2.2.1 Basic Concept of X-ray Diffraction

X-rays are electromagnetic waves with a wavelength range between 0.01 to 10 nanometers, which is on the same scale of the distance between lattice planes in a crystal. X-ray diffraction (XRD) has been one of the most fundamental techniques used to determine the crystal structure and atomic distribution within a material. In XRD, the studied sample is struck with incident X-ray beams. By measuring the angles and intensities of coherent diffracted X-rays, researchers are able to reconstruct the atomic arrangements of the sample. XRD measurement is fast, non-destructive, and requires minimum sample preparation. In this thesis, XRD is the most important tool for determining the atomic structure of materials.

A common source of X-rays used for XRD is a copper X-ray tube (other materials such as molybdenum or tungsten tubes are typical as well). For a copper X-ray tube, the

evacuated tube contains a tungsten filament cathode and a copper anode. A voltage difference is applied between the cathode and anode. The cathode filament is heated via an electric current to produce electrons and the electrons are accelerated toward the anode by an applied voltage difference (45 kV is used in this thesis). Some electrons are slowed due to the collisions between incident electrons and matter, and the lost energy is released as a continuous background spectrum of X-rays, referred to as white radiation. At the same time, when the energy of accelerated electrons is sufficiently high, the inner shell electrons of copper can be knocked out by incident electrons. Electrons in the outer shell drop to vacant level immediately to fill the vacancy, emitting characteristic X-rays with energies equal to the energy difference between orbitals. This leads to a series of characteristic X-rays, as shown in Figure 2.1(a). The X-radiation used for XRD is mainly Kα radiation, which is emitted when electrons from an 2p orbital drop to fill an empty 1s orbital. It should be noted that Kα radiation is in fact a doublet, because of the slightly different energy possessed by 2p electrons in different spin states. When 2p electrons with quantum number $j = 1/2$ and $j = 3/2$ fill the 1s orbital, the X-rays emitted correspond to Kα1 and Kα2 radiation, respectively. The preference for Kα is due to its appropriate wavelength and strong intensity. However, white radiation and other X-rays are also produced, resulting in a continuous spectra of X-rays with different wavelength, as shown in Figure 2.1(b).

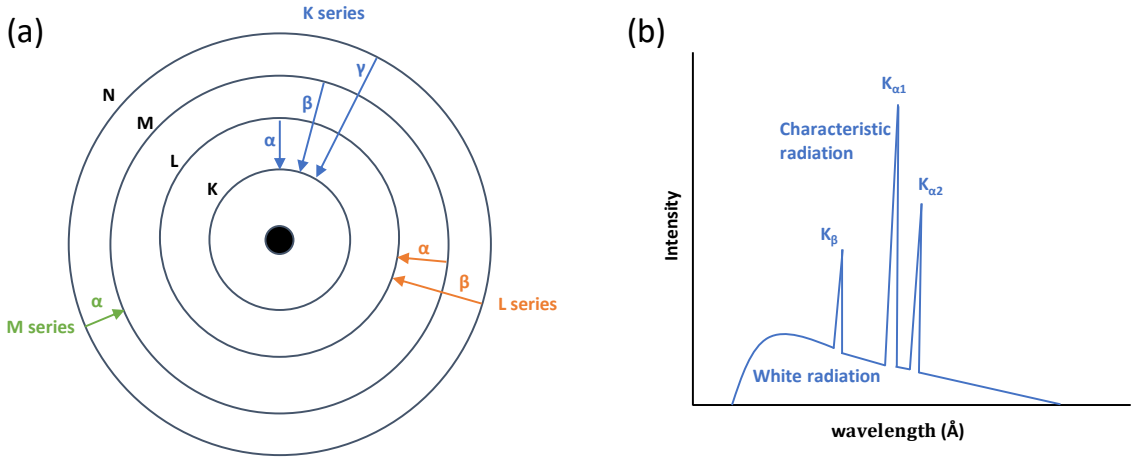


Figure 2.1 (a). Generation of X-rays when electrons at high-energy orbitals fall to empty low-energy orbitals. (2) Radiation spectrum of the X-rays emitted by an X-ray tube.

Once X-rays leave the X-ray tube, slits, filters, and monochromators can be used to control the wavelength and width of the beam. The choice of filter material depends on the choice of X-ray tube. For example, nickel is used for copper X-ray tubes because the absorption edge of the nickel 1s electron lies between the energies of the Kα and Kβ radiations of copper. Therefore, a nickel foil filter can greatly reduce the intensity of copper Kβ radiation as well as high-energy white radiation. Monochromators use Bragg's Law, which will be introduced later, to produce monochromatic X-ray beams. A monochromator employs a single crystal (typically silicon or graphite) with known d-spacing arranged to diffract the X-rays. At particular angle only X-rays with desired wavelength will be diffracted.

When a material is hit by X-rays, electrons in the material oscillate and emit X-rays with the same wavelength as the incident X-rays in all directions. This is also known as Thomson scattering or elastic scattering. All oscillating electrons generate coherent X-rays and interference takes place because the wavelength of X-rays and the interatomic distances are on the same order of magnitude. X-rays also interact with matter via inelastic

scattering events, known as Compton scattering. Compton scattering is characterized by a decreased energy of the photon and contributes to the background in diffraction patterns.

In diffractometers with Bragg-Brentano geometry and scintillation detectors, only the diffracted X-rays with the same angle as incident beam of interest is recorded, as shown in Figure 2.2. The intensity of diffracted X-rays is continuously recorded as the X-ray source and the detector rotate through the same angle. The obtained XRD data is plotted as intensity versus the scattering angle, $2\theta$. For a fixed X-ray wavelength, constructive interference and a peak in intensity occur when the distance between two lattice planes and the angle $\theta$ satisfy Braggs' Law:

$$2\,d\sin\theta = n\,\lambda \qquad (2.1)$$

where d is the distance between lattice planes, θ is the angle of the incident X-rays to the sample, n is an integer, λ is the wavelength of the X-rays used (~1.54 Å). $2\,d\sin\theta$ is the path length difference between X-rays scattered from adjacent lattice planes. When the diffracted beam is retarded by an integral number of wavelengths, constructive interference occurs and a peak is recorded by the diffracted beam detector. When the diffracted beam is scattered from an odd multiple of half the wavelength, destructive interference occurs and there is no XRD peak.

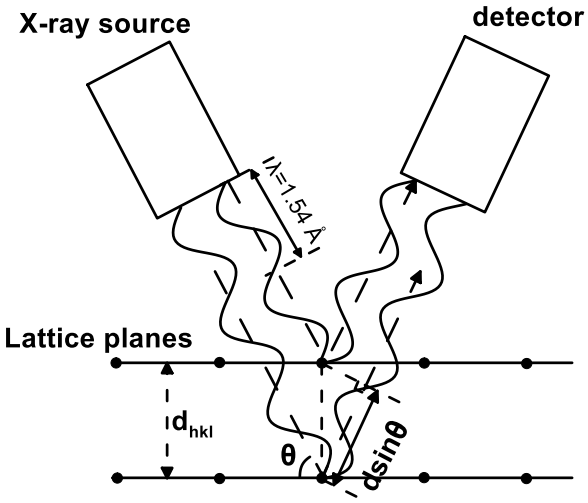


Figure 2.2 Bragg scattering from lattice planes in a crystal structure.

The peak position in an XRD pattern is determined by the distance between lattice planes. Miller indices are used to define the crystal lattice planes. For a given set of lattice planes, three lattice vectors, $a_1$, $a_2$, and $a_3$, define a unit cell in three-dimensional space. The reciprocal of the intercepts of the lattice planes along the lattice vectors, $h$, $k$ and $l$, are defined as Miller indices. $h$, $k$ and $l$ are written in integers with their greatest common divisor as 1. For a simple crystal, such as a cubic crystal, the spacing, $d$, between adjacent (hkl) lattice planes is

$$d = \frac{a}{\sqrt{h^2+k^2+l^2}} \qquad (2.2)$$

where $a$ is the lattice constant of the unit cell, and $h$, $k$ and $l$ are the Miller indices of the specific lattice plane. Other crystal families have different formulas that relate $h$, $k$ and $l$

with the spacing *d*. The spacing *d* is related to the diffraction angle by Bragg's Law. For a measured XRD pattern, the distance between adjacent lattice planes can be calculated using the known peak position, and the peaks can be associated with their specific lattice planes.

Relative peak intensities are mainly determined by the structure factor. For a set of lattice planes with Miller indices of *h*, *k*, *l*, the structure factor *F* is defined as

$$F(hkl) = \sum_n f_n \, e^{2\pi i(hx+ky+lz)} \qquad (2.3)$$

where the sum is over all the atoms in the unit cell (n atoms in total). For each atom, *x*, *y*, and *z* are its positional coordinates, and $f_n$ is the atomic form factor of the atom. The atomic form factor is the scattering amplitude of X-rays by the atom. Heavy atoms have larger atomic form factors because they possess more X-ray scatterers (electrons).

Sometimes the calculated structure factor for a set of planes can be zero and therefore the intensity of diffractions and peaks are zero. This is called a systematic absence. Physically speaking, a systematic absence is due to destructive interference between X-ray beams diffracted by different planes. For example, for a rock-salt type crystal with a *fcc* unit cell, diffraction by (110) planes is absent due to the destructive interference of (220) planes. When the diffraction angle satisfies the Bragg's Law for (110) planes, the phase difference between X-rays scattered by two adjacent (110) planes is $\lambda$. At the same time, the phase difference between X-rays scattered by two adjacent (220) planes is $\frac{\lambda}{2}$, which completely cancels out the (110) diffraction. Therefore (110) diffraction is absent in the diffraction pattern. In this case, the calculated (110) structure factor is also zero.

Other factors that affect the peak intensity include the Lorentz polarization factor, the multiplicity, preferred orientation, and the thermal factor. The Lorentz polarization factor describes the dependence of scattering intensity on scattering angles. Multiplicity relates the scattering of different set of planes with the same d-spacings. For example, in a rock-salt structure the (220) plane is equivalent to the (202) planes, resulting in a single XRD peak with increased intensity. Therefore, in general, crystals with higher symmetry have fewer peaks, while complicated crystals with lower symmetry have more peaks. Preferred orientation is due to the anisotropic property of some materials. For example, plate crystals with layered-type structures tend to align with each other, leading to a strong (00l) diffraction. The thermal factor takes into account the electron density distribution during the vibration of atoms at non-zero temperature. The overall intensity can be represented as follows,

$$I \propto m_{hkl} \cdot F_{hkl}^2 \cdot L_\theta \cdot PO_{hkl} \cdot DW_{hkl} \qquad (2.4)$$

where m is the multiplicity, F is the structure factor, L is the Lorentz polarization factor, PO is the preferred orientation factor and DW is the thermal factor. In order to identify the phases present in the sample, the experimental data can be compared with a reference database. In this thesis the computer program Match! (Crystal Impact) was used to identify phases with known standard XRD patterns in the International Centre for Diffraction Data (ICDD) Powder Diffraction File (PDF-2) database. This method can only be used for simple phase identification.

Further detailed characterization can be done using Rietveld refinement by fitting calculated XRD intensities to the experimental data. In Rietveld refinement, an XRD

pattern is calculated using the crystal structure data of the material of interest. Mathematical functions are used to simulate the background, peak shape, and sample displacement. The least squares method is used to minimize the difference between calculated data and the experimental profile. Rietveld refinement results in the quantitative determination of lattice parameters, atom positions, atom occupancies, and the relative quantity of different phases present. In this thesis, the program Rietica is used for XRD refinement.

During refinement using Rietica, the space group of the material was first identified and selected. Tentative phase scale, element type, atomic position, and lattice constant were entered into the software to generate a preliminary simulation pattern. This should result in a pattern with peak positions similar to the experimental result. Next, certain variables were allowed to change, including background, peak shape, preferred orientation, lattice parameters, atomic coordinates, phase scale, and sample displacement. Typically, only one or two parameters were refined each time until the refined pattern matched with experimental pattern well. The number of simultaneously refinable parameters can then be increased gradually. Finally, the thermal parameters and atom mixing can be refined, if necessary. The agreement between simulated and measured XRD pattern can be represented by Bragg-R factor, which is calculated as:

$$R_{Bragg} = \frac{\Sigma|I_o - I_c|}{\Sigma|I_o|} \qquad (2.5)$$

where $I_o$ is the observed intensity of a certain peak, and $I_c$ is the calculated intensity. A low Bragg-R factor indicates a good fit. Normally in this thesis a refinement with a Bragg-R factor less than 5 is considered to be optimum. However in some cases certain factors, such

as the presence of an unrefined superlattice, stacking fault or impurity, can lead to a larger Bragg-R factor.

### 2.2.2 Characterization by XRD

In this thesis, XRD measurements were made with a Rigaku Ultima IV powder diffractometer equipped with a Cu Kα X-radiation source. A scintillation detector with a diffracted beam monochromator was used to measure the diffraction patterns of powder samples and *ex situ* samples. A D/TeX Ultra linear detector with a Ni filter was used to measure XRD patterns of *in situ* coin cells. A filament current of 40 mA and an accelerating voltage of 45 kV were used to generate X-rays. For non-air sensitive samples, sample powders were placed into a stainless steel sample well with a dimension of 25 mm × 20 mm × 3 mm on a stainless steel plate. The sample was then pressed down and packed with a glass slide to create a flat upper surface that was even with the top of the sample holder before measurement.

Figure 2.3 Air sensitive XRD holer before (left) and after (after) assembly.

For air-sensitive samples, as shown in Figure 2.3, a specially designed air-sensitive sample holder was used. The sample holder has an arc-shaped aluminized Mylar window

so that it is perpendicular to the incident and scattered X-ray beam and does not contribute to the detected X-ray diffraction pattern. Sample preparation of air-sensitive samples was conducted in an Ar-filled glovebox. The sample holder was sealed and transferred to the X-ray diffractometer for measurements. XRD measurements for both air-stable and air-sensitive samples were collected at a typical scattering angle range of 10 to 80 degrees 2-theta with a step of 0.05 degrees between each measurement.

For *ex situ* XRD measurement, cells cycled to different voltages were stopped and opened carefully in an Ar-filled glove box. The electrodes were recovered from the cell and washed several times with dimethyl carbonate (DMC, from BASF). The electrode coating was then scraped off the current collector and transferred to a zero-background silicon wafer, which is mounted in the air-sensitive sample holder as mentioned above.

### 2.3 Scanning Electron Microscopy

Scanning electron microscopes (SEM) produce images of sample morphology by scanning the surface of a sample with an electron beam. In contrast to an optical microscope, an SEM has a substantially higher resolution. This is because image resolution in optical microscopy is inversely related to the wavelength, while the resolution in SEM depends on the spots size of the electron beam. This allows examining sample morphology at nanoscales.

In a conventional SEM, the electron beam is produced by a tungsten filament heated to very high temperature. Electrons can be freed from the filament when the thermal energy of electrons overcomes the work function of tungsten. This is also known as thermionic emission. Compared to conventional thermal electron emission, field emission (FE)

systems are more advanced electron sources. In a FE electron gun, a huge electrostatic gradient field is applied to the filament tip to free the electrons. FE systems can operate at lower temperature (such as room temperature) therefore the lifetime of FE filaments are much longer than thermal emission gun filaments. This is because operating at white-hot temperature, the filament of a thermionic emission gun gradually evaporates with time and needs to be replaced frequently. Compared to thermal electron emission, electron beams produced by FE are smaller in diameter, more coherent, and brighter, resulting in clearer images with higher resolution.

After electrons are produced, the electrons are accelerated using high voltage (up to 60 kV). Accelerated electrons pass through a series of lenses to produce a focused electron beam. The electron beam is deflected to scan the sample in a raster fashion over a rectangular area. Elastic and inelastic scattered electrons are captured by specialized detectors, forming black-and-white images with the intensity of each pixel corresponding to the number of electrons received by detectors.

Secondary electrons and backscattered electrons are both used in SEM imaging. Secondary electrons are inelastic scattered electrons with much lower energy (typically less than 50 eV) than the beam electron. These electrons originate within a few nanometers of the sample surface and can produce images with great resolution. Backscattered electrons are electrons that undergo elastic scattering with sample atoms. They come from a deeper and larger region of the sample. Heavy atoms scatter electrons more strongly than light atoms and therefore look brighter in images generated using backscattered electrons. As a result, backscattered electrons can be used to observe changes in element composition within the material, where heavy elements are brighter and light elements are darker.

Samples for SEM should be flat and immobilized. No loose powders should present in order to prevent any powder entering the SEM, which can damage the instrument. Samples are also supposed to be sufficiently conductive to conduct electrons away during the measurements. Non-conductive samples result in electronic charge building up within the sample, leading to distorted images.

In this thesis, several SEMs were used to characterize the morphology of samples, including a Phenom G2-pro scanning electron microscope, a Hitachi S-4700 FEG scanning electron microscope, and a TESCAN MIRA 3 field emission scanning electron microscope. A small piece of double-sided carbon tape was first mounted onto an aluminum SEM stub. Powdered samples (less than 50 mg) were sprinkled onto the carbon tape. Excessive powders were blown off using compressed air. The sample/stub was sometimes sputtered with a thin layer of gold/palladium to improve conductivity, which results in better image quality. Afterwards, the stub was placed into the vacuum chamber of the SEM for imaging. Typically, an electron beam voltage between 15 kV to 20 kV was used.

If the inner structure of samples is of interest, cross-sections of samples were prepared using a JEOL IB-19530CP cross section polisher. Samples were first taped onto a specimen holder and then placed in the vacuum chamber of the instrument. An argon ion beam was used to mill the sample and polish the cross section. Each sample was processed with an initial step (6 kV) for 80 minutes then a fine mode (4 kV) for 5 minutes with an argon flow rate setting of 5.5.

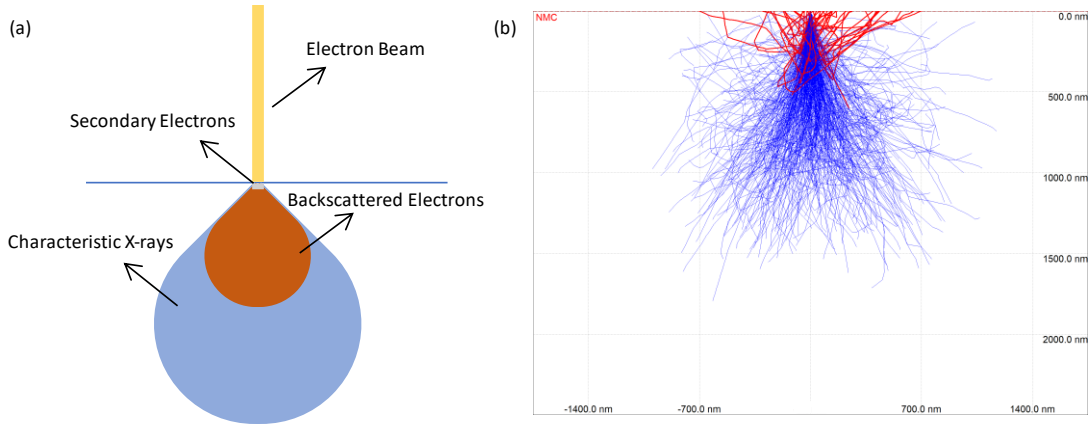


Figure 2.4 (a) Schematic of a volume excitation when the material is hit by electron beams. (b) Simulation of electron trajectory within NMC 111.

## 2.4 Energy Dispersive X-ray Spectroscopy

Modern SEM instruments are commonly equipped with an energy dispersive spectrometer (EDS). In EDS, characteristic X-rays generated by the sample are used to detect the element present in the studied material. The electron source in an EDS is the same as the electron source used for SEM imaging. When the studied sample is bombarded with electrons, electron beams with energy higher than the binding energy of the target material interact with the inner shell electrons of the target material. The inner shell electrons can be ejected, leaving a vacancy site in the inner shell orbital. The formed vacancy is filled immediately by one of the outer shell electrons with higher energy, accompanied by the release of a photon with an energy equal to the energy difference of the two electron orbitals. This energy is in the X-ray range and unique for each element. This process is actually the same as the process used to generate X-rays for XRD, as described in the previous section.

By comparing the detected X-ray energy with a reference database, one can determine the elements present in the sample. The intensity of the characteristic X-ray is

also an indication of the element content in the sample. Spot analysis, line analysis, and elemental area maps can be generated. Multiple elements can be measured at once within a single scan. It should be noted that while SEM imaging can have a resolution on the scale of a few nanometers, the resolution of EDS is typically lower. This is because when electron beams hit the sample, some electrons penetrate the material surface and enter the bulk. As a result, a larger volume of material is excited to produce characteristic X-rays. This leads to the detector collecting X-rays not just from the beam spot, but also from the whole volume excited by the incoming electrons, resulting in a lower resolution. Figure 2.4(a) shows a schematic of a volume excitation. Figure 2.4(b) shows a simulation of electron trajectory within NMC 111 performed using the Monte Carlo simulation program CASINO. Red lines show the region where backscattered electrons occur and blue lines show the region where X-rays are generated. A beam radius of 2 nm and an electron energy of 15 keV were used for the simulation. These conditions result in a volume excitation of about 500 nm in size and a resulting resolution of about 100 nm.

## 2.5 Transmission Electron Microscopy

Transmission electron microscopes (TEM) produce images by transmitting a high energy electron beam through a sample material. TEM has higher resolution than SEM because the image resolution in TEM depends on the wavelength of the electron beam, while the resolution in SEM is limited by the spot size, which is significantly larger than the electron wavelength.

The electron generation process in a TEM is similar to that of an SEM. The electrons are then accelerated using a high voltage (typically 100 – 400 kV) and

concentrated on the sample. As the electron beam is transmitted through the sample, the interaction between electrons and the sample produces the sample image, which can be captured by an imaging device. By adjusting the geometry of lenses, TEM can also produce selected area electron diffraction (SAED) patterns. In diffraction mode, atoms in the sample scatter the incoming electron beams to form a series of spots, each corresponding to a satisfied diffraction condition.

In this thesis, TEM measurements were conducted using a Philips CM30 electron microscope. TEM sample powders were sonicated for 5 minutes in hexane and then dropped onto a carbon coated grid for measurements.

### 2.6 Inductively Coupled Plasma Optical Emission Spectroscopy

Inductively coupled plasma optical emission spectrometry (ICP-OES) is an analytical method used to determine the elemental composition of samples. A plasma is an ionized gas full of positively charged ions and negatively charged electrons at extremely high temperature. In an ICP-OES, a plasma is created by heating argon gas with an induction coil. The coil is supplied with a high frequency current, while the argon gas is ignited with an electric arc. The solution to analyze is pumped through a nebulizer, transforming the sample solution into fine mist of spray. The mist is lead by the argon gas flow into the plasma. The high-energy plasma breaks down the sample into individual atoms. Atoms further lose electrons to form ions and recombine with the electrons repeatedly. The continuous atomization and ionization of the sample releases energy as light (photons), each element having its own characteristic radiation. The light is measured

with a spectrometer. By comparing the intensity of measured spectra with standard calibration curves, the concentration of a specific element can be obtained.

In this thesis, ICP-OES measurements were performed using a PerkinElmer Optima 8000. An appropriate amount of powder sample was first dissolved in 2 mL aqua regia made from HCl (VWR 36.5 - 38.0% ) : $HNO_3$ (Caledon, 68.0% to 70.0%) with a molar ratio of 2:1, which was then diluted using 2% $HNO_3$ (Caledon, 68.0% to 70.0%) prior to measurements. Standard solutions (1000 ppm, Sigma-Aldrich) were diluted with distilled water to form a series of standard references for calibration.

**2.7 Gas Pycnometry**

A gas pycnometer is a common instrument used for measuring the density of solid samples. A pycnometer measures the volume of a sample with known mass. The sample's density can then be calculated as the mass/volume ratio. Typically there are two chambers in a gas pycnometer, a sample chamber with empty volume $V_1$ and an internal chamber with volume $V_2$. The two chambers are separated by a valve, which can be opened to allow gas exchange between the two chambers. A pressure measuring device is connected to the sample chamber. When the valve is closed and the two chambers are isolated, the pressure inside the loaded sample chamber is measured as $P_i$. The valve is then opened to admit gas from the sample chamber into the internal chamber. The pressure is measured as $P_f$ after gas exchange. The volume of the sample $V_s$ can be deduced as follows:

$$V_s = V_1 - \frac{V_2}{\frac{P_i}{P_f} - 1} \qquad (2.6)$$

The density is then calculated using the volume and the mass of the sample.

In this thesis, densities were measured using a Micromeritics AccuPyc II 1340 Pycnometer. A powder sample was first weighed using an analytical balance to obtain the mass. The sample was then transferred to sample chamber and placed in the pycnometer with minimum air exposure. Helium gas (PRAXAIR, ultra high purity, 99.999%) was used for purging the sample and measuring the volume because it is inert and has small atom size. Each sample was measured with five cycles and the average volume was obtained to calculate the density of the sample.

### 2.8 Brunauer–Emmett–Teller (BET) Surface Area

The specific surface area of samples were measured by the BET method, which employs the monolayer adsorption/ desorption of gas molecules on solid surfaces. Nitrogen is the most common gas adsorbate for BET measurement. At liquid nitrogen temperature, physical adsorption of nitrogen on the sample occurs. The surface area analyzer measures how many nitrogen molecules are adsorbed and the surface area can be calculated using

$$S = \frac{vNs}{V} \qquad (2.7)$$

where $v$ is the measured gas volume, $N$ is Avogadro's number, $s$ is the cross-sectional area of one adsorbate molecule (0.162 $nm^2$ for nitrogen), and $V$ is the molar gas volume (22400 milliliters).

In this thesis, a Flowsorb II 2300 (Micromeritics) analyzer was used to measure the surface area. Powdered samples were first degassed by heating in inert gas at 150 °C to remove traces of water. The instrument was calibrated using nitrogen gas before

measurements of each set of samples. A mixture gas of 30% $N_2$ and 70% He was used for measuring the surface area.

### 2.9 Fourier Transform Infrared Spectroscopy

Fourier transform infrared spectroscopy (FTIR) is a technique used to identify organic and sometimes inorganic compounds. FTIR measures the transmittance/absorption of light by the sample at different wavelengths. Light with varying frequencies is passed through a sample and the absorption rate is recorded. Materials absorb light with frequencies corresponding specifically to the bond vibrations present within their structure. Therefore, different materials produce different FTIR spectra. The obtained data can be compared with a reference database to identify the compounds present in the material. In this thesis, FTIR measurements were recorded using an Agilent Cary 630 FTIR spectrometer. The measurements were conducted in argon-filled glovebox.

### 2.10 Cell Construction

Cell construction was conducted in an argon-filled glovebox. Sample powders were made into composite electrodes before all electrochemical measurements. Active material, PVDF binder (polyvinylidene fluoride, HSV 900, KYNAR) and conductive additive (carbon black, Super P, Imerys Graphite and Carbon) in a typical weight ratio of 8:1:1 were mixed in an appropriate amount of N-methyl-2-pyrrolidone (Sigma Aldrich, anhydrous 99.5%) with two 0.5 inch tungsten carbide balls in a Retsch PM200 rotary mill (100 rpm, 1 hour) to create a uniform slurry. The slurry was then spread onto aluminum foil with a coating bar having a ~0.015 cm gap and dried under vacuum at 120 °C overnight. The resulting coatings were stored in an Ar-fileld glovebox and 1.3 $cm^2$ circular electrodes were

punched from the coatings. The mass of each electrode was measured before cell assembly for calculating the mass of active material. The loading was typically 1 - 2 mg/cm$^2$.

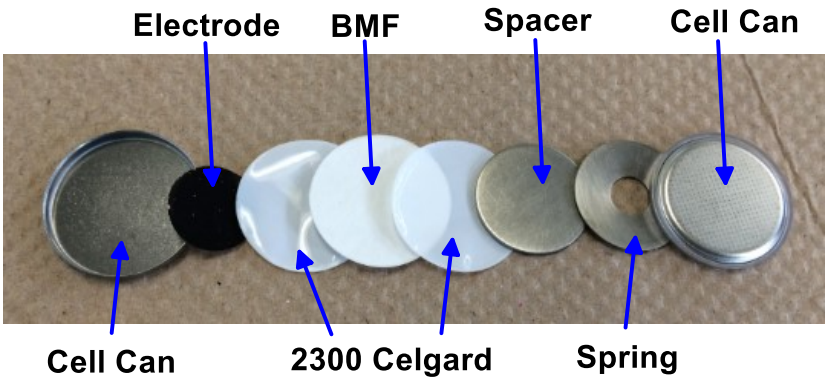


Figure 2.5 Exploded view of a 2325-type coin cell. Note that there should be a sodium foil (not shown here) between the Celgard separator and the spacer.

Half-cells were utilized for electrochemical studies in this thesis using 2325-type coin cell hardware. Assembly was performed in an Ar-filled glovebox. Sodium metal foils (~0.3 mm) were rolled from sodium ingot (Sigma Aldrich, ACS reagent grade) using a hand-turned rolling mill. Circular sodium disks were punched from the foil and used as counter/reference electrodes. 1 M $NaPF_6$ (Alfa Aesar, 99%) in a solution of ethylene carbonate (EC), diethyl carbonate (DEC) and monofluoroethylene carbonate (FEC) (volume ratio 3:6:1, from BASF) was used as electrolyte. FEC has been shown to be effective for improving the cycling of sodium half-cells. For lithium cells, lithium foils (Sigma Aldrich, 99.9%) and $LiPF_6$ (BASF) were used. As shown in Figure 2.5, the working electrode was placed on top of the cell can bottom. One layer of Celgard 2300, one layer of a blown microfiber polyethylene membrane (BMF, 3M Company) and another layer of Celgard 2300 were added as separators. This combination of separators can help avoid sodium dendrite effects. In addition, multiple separators also help make the stack pressure more uniform, reducing uneven current distribution in cells and leading to longer cycle life.

An appropriate amount of electrolyte was added in each layer. The circular sodium foil was then placed on this stack (not shown in Figure 2.5). Finally a spacer and a conical spring were added to apply an appropriate pressure on the electrodes, followed by the cell can top. The cell was then placed in two sequential crimpers to be properly sealed. All the cells fabricated in this report were cycled under thermostatically controlled conditions (30 ± 0.1 °C) using a Maccor Series 4000 Automated Test System (Maccor Inc., Tulsa OK).

For *in situ* XRD measurements, electrodes were made using a circular beryllium disk as current collector. Beryllium was chosen because it is conductive, air-stable, and effectively transparent to X-rays. For such cells, a special cell bottom can with a hole smaller in diameter than the beryllium disk was used. Electrode slurries made using the same procedure as described above were coated directly onto the beryllium window using a 0.3 mm coating bar. After drying overnight at 80 °C under vacuum, the beryllium window was affixed in the cell bottom can using Roscobond adhesive. *In situ* coin cells were then constructed and tested using the same procedure as described above.

## 2.11 Electrochemical Studies

Electrochemical techniques were used to characterize the electrochemical performance of the positive electrode materials in this report. Cells fabricated were charged and discharged galvanostatically at specified currents while their voltage was monitored. The time, voltage, and current were recorded for analysis. Different currents and cutoff voltages can be chosen, depending on the material tested and the test purpose. The theoretical specific capacity $Q_t$ of a material can be calculated using

$$Q_t = \frac{nF}{M} \qquad (2.8)$$

where $n$ is the number of moles of charge carriers (such as $Li^+$ or $Na^+$) that can be stored in one mole of the active material, $F$ is the Faraday constant (26802 mAh/mol), and $M$ is the molar mass of the active material. For example, graphite can accommodate 1/6 lithium atom per carbon atom. Therefore the theoretical specific capacity of graphite versus lithium can be expressed as

$$Q = \frac{nF}{M} = \frac{\frac{1}{6} * 26802 \text{ mAh/mol}}{12.0107 \text{ g/mol}} = 371.7 \text{ mAh/g} \quad (2.9)$$

Current magnitude is expressed as "C-rate". The theoretical capacity of a cell (in Ah or mAh) divided by desired charge/discharge time (in h) is the cycling current (in A or mA). For example, a C/20 rate means the rate at which a cell would be fully discharged/charged in 20 hours to reach its theoretical capacity. The higher the C-rate, the shorter time it takes to finish a full charge/discharge.

The electrochemical tests in this study resulted in a measurement of cell capacity, average voltage, coulombic efficiency, rate capability, and cycle life. Capacity, with a unit of either mAh or Ah, is determined by multiplying the current employed (in mA or A) by the charge/discharge time (in h). The gravimetric capacity of an electrode material is usually expressed as mAh/g, which is the measured capacity divided by the mass of the active material. Volumetric capacities are measured in $mAh/cm^3$ or Ah/L, which are calculated by using the measured capacity and active material volume. For positive electrode materials, gravimetric/volumetric energy density can be calculated by multiplying the gravimetric/volumetric capacity by the average voltage. Higher capacity and higher average voltage translate into higher energy density, which is desirable.

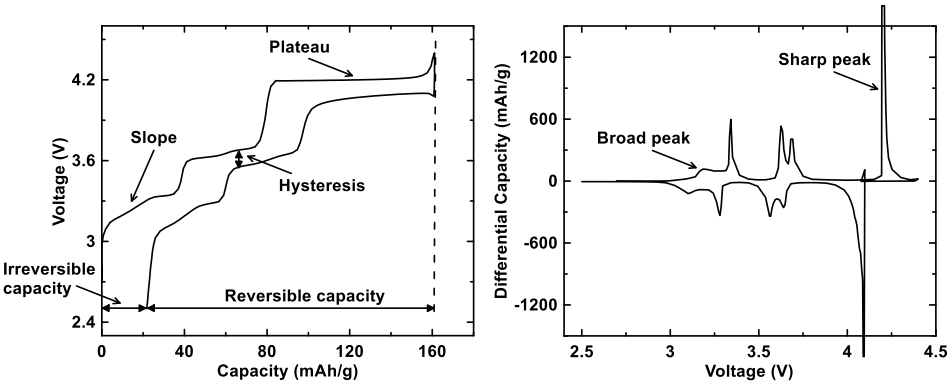


Figure 2.6 Voltage curve (left) and differential capacity curve (right) of $Na_{2/3}Ni_{1/3}Mn_{2/3}O_2$ in a sodium half-cell.

To illustrate some concepts of electrochemical testing, the first cycle voltage curve and differential capacity curve of a $Na_{2/3}Ni_{1/3}Mn_{2/3}O_2$ vs. sodium half-cell are shown as an example in Figure 2.6. In the voltage curve, the sloping region at ~3.2 V is due to the composition change of a $Na_xNi_{1/3}Mn_{2/3}O_2$ solid solution, and the plateau at ~4.2 V is due to a phase transition. A voltage curve slope and flat plateau correspond to a broad peak (slope) or a sharp peak (plateau) in the differential capacity curve. According to the Gibb's phase rule, plateaus are indicative of two phase regions, while slopes are indicative of single phase regions. Hysteresis is the difference between the average charge voltage and discharge voltage. Hysteresis is usually comprised of a combination of rate dependent polarization (ohmic polarization) and polarization inherent to the material (activation polarization). Large hysteresis leads to low energy efficiency and should be avoided. It is typical for cells to have increasing hysteresis during cycling, due to the growth of a solid electrolyte interphase (SEI) and depletion of electrolyte. For the same material, hysteresis can be reduced by increasing temperature, reducing particle size, increasing conducting additive content, adding additives to modify or inhibit SEI growth or reducing the current rate.

Coulombic efficiency (CE) is the ratio of the total charge extracted from the cell to the total charge put into the cell in a cycle. For a half cell with only a positive electrode vs. a sodium metal anode, the coulombic efficiency is defined as:

$$\mathrm{CE} = \frac{Q_d}{Q_c} \qquad (2.10)$$

where $Q_d$ is the discharge capacity and $Q_c$ is the charge capacity of the previous half-cycle. There are many factors that can affect the measured coulombic efficiency, such as the choice of active material, electrode composition (ratio of active material, binder, conductive carbon), cycling conditions (temperature, current rate, cutoff voltage), electrolyte composition, and the accuracy of the charger instrument. In this report, a Maccor Series 4000 Automated Test System was used to measure the coulombic efficiency, which has an accuracy of ~1470 ppm. Higher coulombic efficiency leads to better cycling performance, especially in a full cell, as the total number of active Na ions available in a full cell is fixed. Common strategies to improve coulombic efficiency include surface coating, adding electrolyte additives, and optimizing electrode composition. Tremendous efforts have been made to improve the coulombic efficiency of lithium ion batteries, while less have been reported for sodium ion batteries. However, it should be noted that if sodium ion batteries will ever be used for large scale practical applications, the coulombic efficiency of sodium ion batteries is as important as lithium ion batteries, if not more so. This is because applications like grid storage require a much longer service time (decades) than portable electronics (years). Given the inevitable lower energy density of sodium ion batteries than lithium ion batteries, a longer cycling life is imperative for

sodium ion batteries to compete with lithium ion batteries. In such cases, the price per kWh per cycle ($/(kWh*cycle)) should be considered.

Rate capability is an indication of how well a material can perform at high charge/discharge currents. It is tested by measuring the capacity of a material under different charge/discharge currents. A good rate performance is desired for applications that require short charging time, such as electric vehicles. Cycle life is the long-term cyclability of a battery. In industry, it is typically defined as the number of charge/discharge cycles until a battery fades to 80% of its initial capacity. Improving the cycle life is one of the important research subjects in the field.

Galvanostatic intermittent titration technique (GITT) is a method used for measuring the potential change of an electrode when an intermittent current is applied. In GITT, a current pulse is applied to an electrode for a specified time period, followed by a relaxation time in which the current is cut off, as shown in Figure 2.7. This process is conducted repeatedly until the cell reaches desired potential/capacity. The potential is constantly being monitored and the diffusion coefficient of Li or Na can be calculated from the potential change over time. The diffusion coefficient is calculated as:

$$\mathrm{D} = \frac{4}{\tau\pi}\left(\frac{mV_m}{MS}\right)^2\left(\frac{\Delta V_s}{\Delta V_t}\right)^2 \qquad (2.11)$$

where $\tau$ is the time period of the current flux, m is the mass of electrode material, M is formula weight of the material, $V_m$ is the molar volume of the material, S is electrode surface area, $\Delta V_s$ is the potential change in one flux-relation cycle, and $\Delta V_t$ is the potential change during the current pulse. It should be noted that in this thesis, the diffusion

coefficients were calculated throughout the whole potential range. However, the diffusion coefficient calculated using GITT is only valid in single-phase (solid solution) regions. Equation 2.11 does not apply to two-phase regions, since Fick's Law, on which it is based, is not followed in such regions. The sodium/lithium diffusion during two-phase regions is realized by the transport of phase front. Therefore the diffusion coefficients shown in two-phase regions is only meant for comparison, instead of strictly representing ion diffusion.

The diffusion length is defined as:

$$\mathrm{L} = (D \cdot \tau)^{\frac{1}{2}} \qquad (2.12)$$

where $D$ is the diffusion coefficient and $\tau$ is the time period when current is applied. The diffusion length should be similar or smaller than the particle size of the electrode material because equation 2.11 assumes that the diffusion length is not limited by the physical size of the particle. If the diffusion length is larger than the physical size, then the derived value of $D$ does not actually represent the diffusion coefficient and can only be used for comparison purposes within the same measurement.

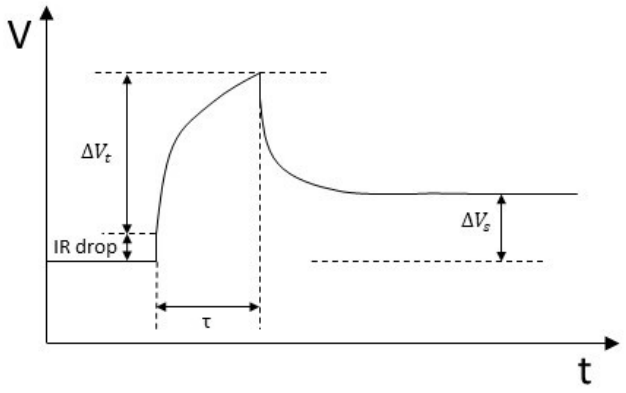


Figure 2.7 Changes in potential during a GITT measurement.

# CHAPTER 3 HONEYCOMB COMPOUND $Na_3Ni_2BiO_6$ [1]

## 3.1 Introduction

Layered sodium transition metal oxides generally have good electrochemical performance and structural stability. Nickel-based materials have been extensively studied as they offer high voltage and high capacity [109]. Partial substitution of Ni with other metals could modify the crystal structure and electrochemistry of these materials [94]. In the case of a binary $Na_xNi_yM_{1-y}^{z+}O_2$ (where x is usually between 2/3 and 1, M is a metal or metalloid) material, Ni usually exists as $Ni^{2+}$ and its charge is balanced by $M^{z+}$, which has a higher oxidation state (z = 4, 5, or 6). Sodium intercalation/deintercalation then operates on the $Ni^{2+}/Ni^{4+}$ redox couple [110]. Using this strategy, the formation of the $Ni^{3+}$ Jahn-Teller ion can be avoided. Maximization of the active $Ni^{2+}$ ion content of cathode materials is a strategy that may lead to higher energy density. For a typical O3 material which has a sodium content of x = 1 or a typical P2 material which has a sodium content of x = 2/3, the relationships between y and z in $Na_xNi^{2+}{}_yM^{z+}{}_{1-y}O_2$ are given by

$$y(O3) = \frac{z-3}{z-2}$$

$$y(P2) = \frac{3z-10}{3z-6}$$

[1] This chapter was adapted with permission from Zheng, L.; Obrovac, M. N. Honeycomb Compound $Na_3Ni_2BiO_6$ as Positive Electrode Material in Na Cells. *Journal of The Electrochemical Society*, **2016**, 163, A2362-A2367 [180]. Copyright 2016, The Electrochemical Society. The author's contribution includes performing the experimental work and writing the manuscript.

According to the above relations, having M with a high oxidation state will maximize the $Ni^{2+}$ content. By using this strategy, researchers have studied O3-type $Na_3Ni^{2+}{}_2Sb^{5+}O_6$ ($NaNi_{2/3}Sb_{1/3}O_2$) and P2-type $Na_2Ni^{2+}{}_2Te^{6+}O_6$ ($Na_{2/3}Ni_{2/3}Te_{1/3}O_2$) as positive electrode materials for sodium ion batteries [111,112]. In these materials, the $Ni^{2+}$ contents were successfully enriched to 2/3, compared to 1/2 for O3-$NaNi_{1/2}Mn_{1/2}O_2$, 1/3 for P2-$Na_{2/3}Ni_{1/3}Mn_{2/3}O_2$ and 1/4 for P2-$Na_{1/2}Ni_{1/4}Mn_{3/4}O_2$. [113–115]. Notably, O3-type $Na_3Ni_2SbO_6$ has high energy density and good rate capability [111]. $Na_3Ni_2SbO_6$ has a honeycomb structure that is generated by the 2:1 ordering of $Ni^{2+}$ and $Sb^{5+}$. Recently, Yamada et al. reported that honeycomb-ordered $Na_2RuO_3$ can deliver extra capacity through an oxygen redox reaction, compared to disordered $Na_2RuO_3$ [116]. They observed an improvement in ~1/3 of the capacity in honeycomb-ordered $Na_2RuO_3$ compared to disordered $Na_2RuO_3$ (180 mAh/g and 135 mAh/g, respectively). These results show that the honeycomb structure is of interest for sodium ion battery positive electrode materials.

$Na_3Ni_2BiO_6$ was first synthesized and studied by Cava et al. [117]. It has a honeycomb structure similar to that of $Na_3Ni_2SbO_6$. Cava et al. studied the structure and magnetic properties of this compound [117]. Here, a careful study of the electrochemistry of $Na_3Ni_2BiO_6$ honeycomb compound in Na cells is presented for the first time, including the structural changes that occur during sodium removal and insertion.

### 3.2 Experimental

Stoichiometric amounts of NiO (99%, -325 mesh, Sigma Aldrich), $NaBiO_3$ (ACS reagent, Sigma Aldrich) and $Na_2CO_3$ (99%, Sigma Aldrich) powders were mixed by high energy ball milling using a SPEX 8000 mill. Typically a 3:1 ball:sample mass ratio with a

sample size of ~6 g and four 7/16 inch diameter stainless steel balls were milled for 2 hours. The obtained powders were then pelletized. The pellets were heated at 700 ºC for 8 hours first then 750 ºC for 12 hours in a tube furnace in oxygen to obtain $Na_3Ni_2BiO_6$. After cooling, samples were then immediately transferred to an Ar-filled glovebox without air exposure.

Electrode preparation was carried out in an Ar-filled glovebox because $Na_3Ni_2BiO_6$ could be potentially air-sensitive. Electrodes consisted of active material, PVDF binder (HSV 900, KYNAR), carbon black (super P, Imerys Graphite and Carbon) in an 8:1:1 weight ratio. These components were mixed with an appropriate amount of N-methyl-2-pyrrolidone (Sigma Aldrich, anhydrous 99.5%) with two 0.5 inch tungsten carbide balls in a Retsch PM200 rotary mill (100 rpm, 1 hour) to create a uniform slurry. Typically, ~ 0.4 g of active material was loaded in the milling jar for making slurry. The slurry was then coated onto aluminum foil with a coating bar having a ~0.015 cm gap, and dried under vacuum at 80 °C overnight. Circular electrodes were punched from the coating and incorporated into coin cells. 2325-type coin cells were assembled in an Ar-filled glovebox. Na disks punched from thin foil (~0.3 mm) rolled from sodium ingot (Sigma Aldrich, ACS reagent grade) were used as counter/reference electrodes. Two Celgard 2300 and one blown microfiber separator (3M Company) were used as separators. 1 M $NaPF_6$ (Aldrich, 98%) in a solution of ethylene carbonate (EC), diethyl carbonate (DEC) and monofluoroethylene carbonate (FEC) (volume ratio 3:6:1, from BASF) was used as electrolyte. Cells were cycled with a Maccor Series 4000 Automated Test System (Maccor Inc., Tulsa OK). The ambient cycling temperature was 30.0 °C (± 0.1°C).

X-ray diffraction (XRD) patterns were measured with a Rigaku Ultima IV X-ray diffractometer equipped with a Cu anode X-ray tube and dual detectors. A D/TeX Ultra linear detector with a K-beta filter was used to measure XRD patterns of powder samples and *in situ* coin cells. Powder samples were loaded into a gastight X-ray sample holder (DPM Solutions, Hebbville NS) in an argon-filled glove box to avoid air contamination. A coin cell modified to have a thin beryllium window inset in the cell can was used for *in situ* XRD measurements. For such cells, electrode slurry made using the same procedure as described above was coated directly onto the beryllium window using a 0.3 mm coating bar. After drying overnight at 80 ºC under vacuum, the beryllium window was then affixed in the cell bottom can using Roscobond adhesive. *In situ* coin cells were then constructed using the same procedure as described above. *In situ* cells were cycled at a rate of C/10 for 2 cycles, first cycle between 1.5 V – 3.8 V and second cycle between 1.5 V – 4.5 V. Phase observed in *in situ* XRD data were compared to previously reported *in situ* XRD results of similar O3-type materials, such as $NaNi_{0.5}Mn_{0.5}O_2$, $Na_2RuO_3$, and $Na_3Ni_2SbO_6$ [111,113,116]. A scintillation detector with a diffracted beam monochromator was used to measure *ex situ* XRD patterns. For *ex situ* XRD studies, coin cells were prepared as described above, but were stopped at different cut-off voltages after trickle at constant voltage to achieve equilibrium. Electrodes for *ex situ* XRD measurements were recovered from these cells in an argon glove box, and the electrode materials were scraped off the aluminum foil and washed with dimethyl carbonate (DMC, BASF) several times. The recovered electrode materials were then transferred to a zero-background silicon wafer and sealed in the gastight sample holder for the *ex situ* XRD measurements. Rietveld refinements were conducted using Rietica software.

### 3.3 Results and Discussion

Figure 3.1 shows an XRD pattern of synthesized $Na_3Ni_2BiO_6$. The XRD pattern was found to be similar to that reported previously [117]. The structure resembles the α-$NaFeO_2$ structure, except for low angle peaks caused by the honeycomb superlattice ordering in the transition metal layer. The monoclinic space group C2/m has been used by researchers to describe this type of honeycomb structure [117]. Here, the honeycomb structure is generated by the 2:1 ordering of edge sharing $NiO_6$ and $BiO_6$ in the *a*-*b* plane, as shown in Figure 3.2. In the *a*-*b* plane, every $BiO_6$ octahedron is surrounded by six $NiO_6$ octahedra, thus forming a honeycomb ordering. A small amount of an NiO impurity phase was also present in the XRD pattern (indicated by solid circles). Atttempts to completely remove this phase by changing synthesis conditions were not successful. Rietveld refinement gives the lattice parameters $a$ = 5.3991±0.0009 **Å**, $b$ = 9.348±0.002 **Å**, $c$ = 5.6740±0.0009 **Å** and β = 108.40±0.01° , which are in close approximation to the values reported by Cava et al. [117].

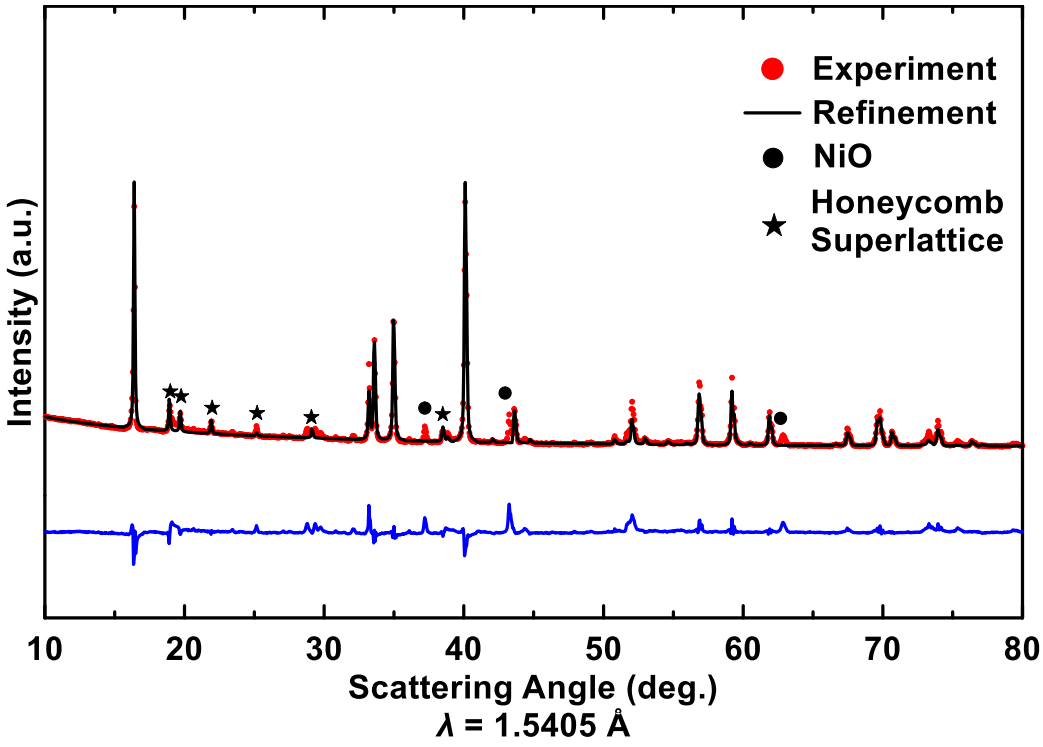


Figure 3.1 X-ray diffraction pattern for synthesized $Na_3Ni_2BiO_6$ and its Rietveld refinement. $R_{Bragg}$ = 12.71, $R_{wp}$ = 21.69, GOF = 2.15.

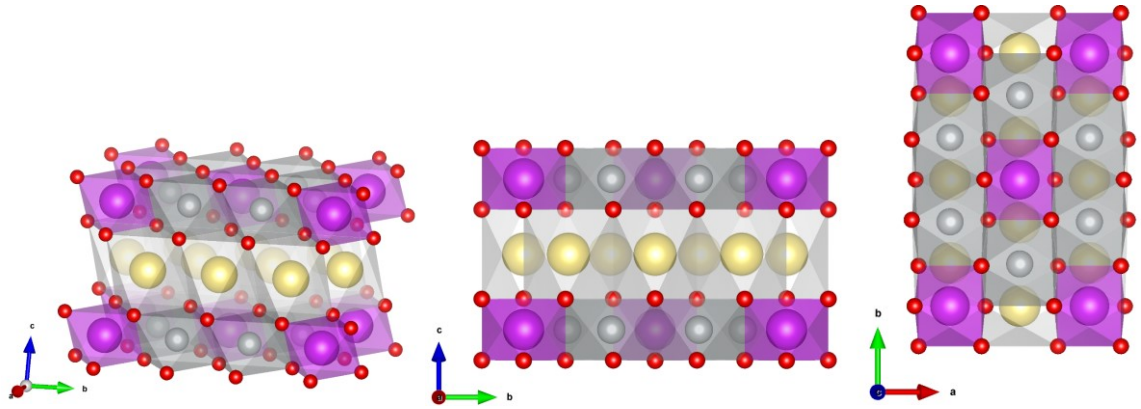

Figure 3.2 Structure of $Na_3Ni_2BiO_6$. Sodium is shown in yellow, oxygen in red, bismuth in purple, and nickel in grey.

Figure 3.3 shows the voltage curve of $Na_3Ni_2BiO_6$ for the first 2 cycles in the voltage range of 1.5 V – 3.8 V and 1.5 V – 4.5 V, respectively. Figure 3.4 shows the corresponding differential capacity curves of the same cells. $Na_3Ni_2BiO_6$ was found to have

a first charge capacity of ~82 mAh/g when cycled between 1.5 V and 3.8 V. This capacity of ~82 mAh/g corresponds to the removal of ~1.5 Na per $Na_3Ni_2BiO_6$. It should be noted that the heavy atomic weight of Bi inevitably lowers the gravimetric capacity, however its volumetric energy density is comparable to other Na-ion cathode materials. The volumetric capacity of $Na_3Ni_2BiO_6$ is calculated to be 1557 Wh/L, based on a bulk density of 6.0012 g/ml from XRD measurements. For comparison, the volumetric capacity of $NaCrO_2$ is estimated to be ~1570 Wh/L (120 mAh/g at ~3 V).

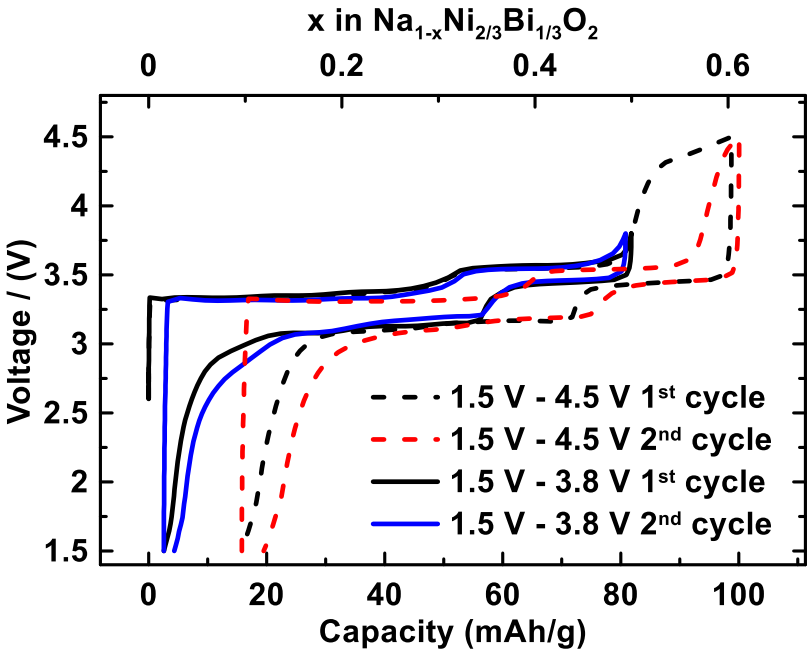


Figure 3.3 Voltage curves of $Na_3Ni_2BiO_6$ at C/20 current density for the first 2 cycles in the voltage range of 1.5 V – 3.8 V and 1.5 V – 4.5 V.

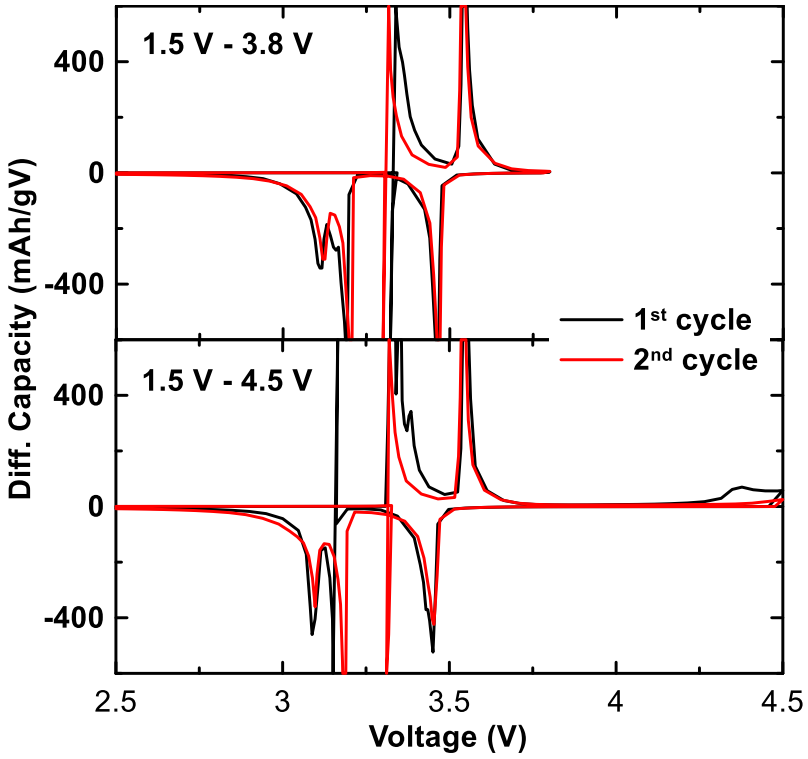


Figure 3.4 Differential capacity curve of $Na_3Ni_2BiO_6$ cells at a scan rate of C/20 between 1.5 V – 3.8 V and 1.5 V – 4.5 V (vs. Na+/Na).

The $Na_3Ni_2BiO_6$ voltage curve is characterized by two flat plateaus during charge. The two plateaus in the voltage curve correspond to two sharp peaks in the differential capacity centered at ~3.3 V and ~3.55 V. This redox potential is typical for layered sodium nickelates [72]. For example, P2-$Na_{2/3}Ni_{1/3}Mn_{2/3}O_2$ also has two plateaus at ~3.3 V and ~3.6 V [72]. These plateaus are due to $Na^+$/vacancy ordering and/or phase transitions, as suggested by previous reports [72]. In this study, assuming the starting material has a composition corresponding to x = 3 in $Na_xNi_2BiO_6$, the charge capacity associated with these two plateaus corresponds to the theoretical formation of $Na_{1.5}Ni_2BiO_6$ at 3.8 V. If the cell is subsequently discharged, both the two plateaus are completely reversible with a hysteresis of ~0.2 V. The first discharge capacity is ~79 mAh/g with a very small irreversible capacity ( ~3 mAh/g). The first cycle coulombic efficiency is ~96%. The lower

plateau during discharge is actually composed of two small plateaus, as can be seen from the two successive peaks at ~3.1 V and ~3.2 V in the differential capacity curve. When the cell was cycled between 1.5 V – 4.5 V, another plateau with a capacity of ~17 mAh/g appears at ~4.4 V upon charge. However this plateau is not reversible, as can be seen by the similar discharge curve to that of cell cycled between 1.5 V – 3.8 V. Below 3.8 V the differential capacity curve is nearly identical for the cells cycled in the two voltage ranges. The first discharge capacity is ~83 mAh/g, only slightly higher than that of cell cycled between 1.5 V – 3.8 V. This leads to an irreversible capacity of ~16 mAh/g and a low first cycle coulombic efficiency (~84%). After the first cycle, this high voltage plateau disappears and the charge capacity decreases to 84 mAh/g. The average discharge voltage is ~3.16 V vs. $Na^+/Na$.

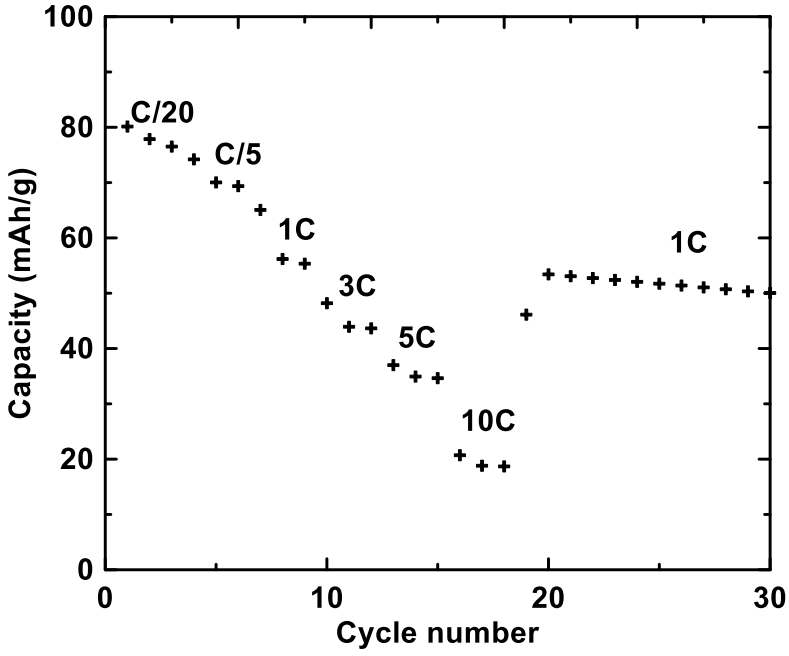


Figure 3.5 Rate capability at constant charge/discharge rates of C/20 - 10 C.

$Na_3Ni_2SbO_6$ has been shown to exhibit a superior rate capability by Yang et al. [111]. At 10C rate, the capacity reached 104 mAh/g, which exceeds 85% of its capacity at C/10 (117 mAh/g). Unfortunately, the rate capability of $Na_3Ni_2BiO_6$ is less attractive. Figure 3.5 shows the rate performance of $Na_3Ni_2BiO_6$. As can be seen in the figure, the reversible capacity drops significantly with increasing current rate. At 1C rate, a capacity of ~55 mAh/g was observed, corresponding to ~70% of the C/20 capacity. When the rate was increased to 5C, less than 50% of capacity is retained. The poor rate performance indicates slow kinetics and low sodium ion conductivity. When the current density increases, the capacity is limited by the kinetic barrier of sodium diffusion in the active material. Yang et al. attributed the superior rate capability of $Na_3Ni_2SbO_6$ to the weaker attraction force between sodium and the structure [111]. The average bond length of Na-O in $Na_3Ni_2SbO_6$ is 2.434 Å, larger than that in $Na_3Ni_2BiO_6$ (2.395 Å) [117]. This might also explain the inferior rate capability of $Na_3Ni_2BiO_6$. A longer bond length may indicate a weaker bonding strength, and therefore a more facile intercalation/deintercalation of sodium ions.

In order to understand the structural changes that occur during sodium extraction/insertion, *in situ* XRD experiments were performed. Figure 3.6 shows the XRD patterns of a $Na_3Ni_2BiO_6$ *in situ* XRD cell during the first 2 cycles, where the first cycle is between 1.5 – 3.8 V and the second cycle is between 1.5 – 4.5 V, respectively. The XRD patterns at the end of each charge or discharge are shown with red lines. Some of the peaks in the XRD patterns are caused by cell parts, such as beryllium and beryllium oxide from the beryllium window. These peaks could be easily identified as their positions and intensities do not shift during the charge and discharge process. The initial XRD pattern is

that of $Na_3Ni_2BiO_6$. Miller indices are indicated for each peak. During cycling the XRD peaks barely shift during the charge/discharge process. Instead peaks disappear and peaks from new phases appear during each plateau indicating multiphase processes. This will be discussed in detail below.

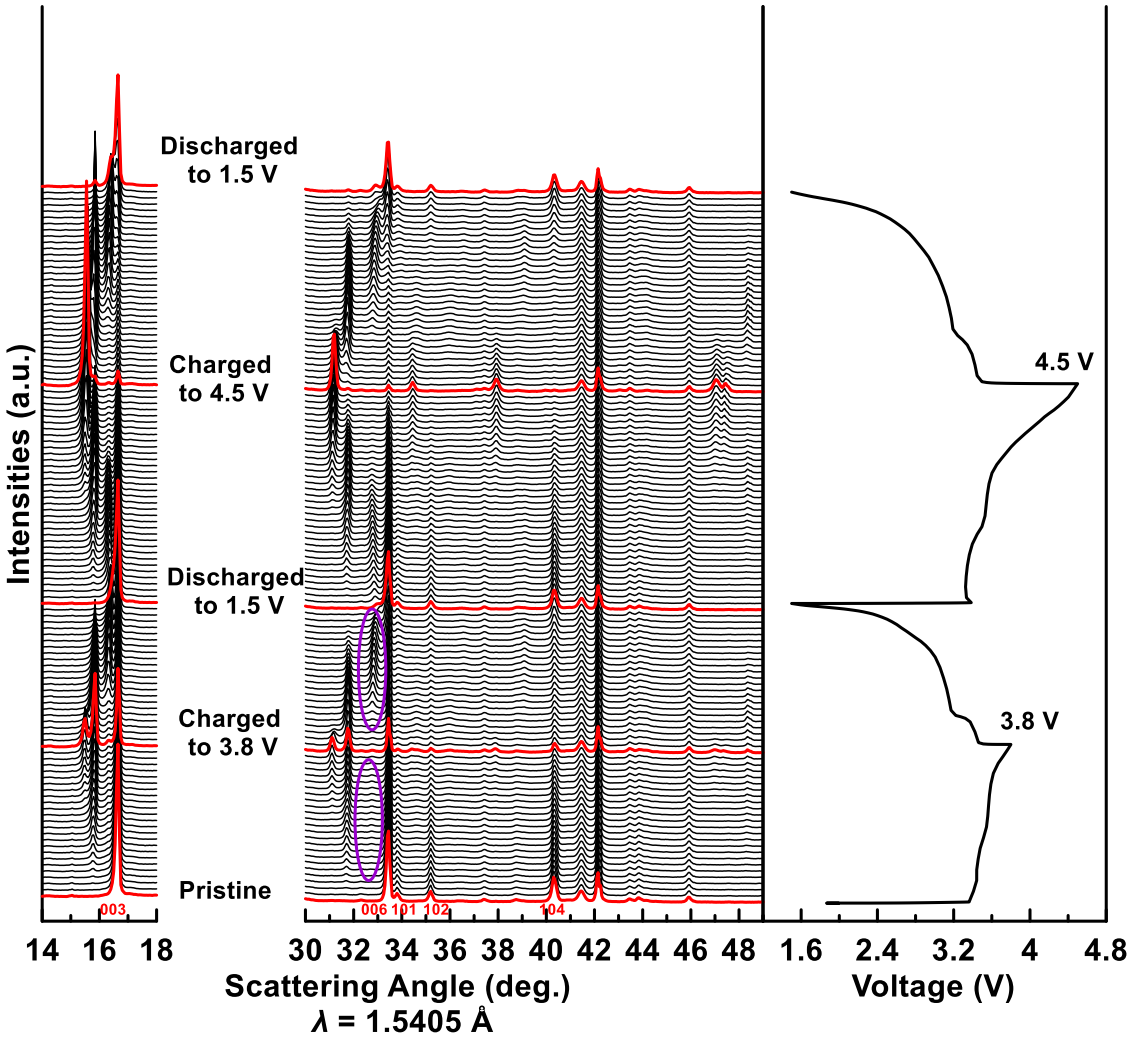


Figure 3.6 *In situ* XRD patterns of a $Na_3Ni_2BiO_6$ electrode at various charge/discharge states during the first two cycles (1.5 V – 3.8 V and 1.5 V – 4.5 V). Phase transitions are different for the first charge/discharge processes, as can be seen by the regions shown in purple ovals.

Overall, there are four major peak positions in the 2θ range of 14° – 18°, corresponding to four different phases (O3, O'3, P3, O1). Enlarged *in situ* XRD patterns at

selected states of charge/discharge are shown in Figure 3.7. It was found that the phase transitions that occur during charge and discharge are different during the first cycle. In the 2θ range of 32° – 33° (shown in two purple ovals for the first charge/discharge in Figure 3.6, respectively), only very small peaks could be observed during the first charge, yet large peaks appear and disappear during the first discharge process in this region. The low peak intensity during first charge could be due to kinetic hindrance in phase formation. In the first charge process, the O3 phase transforms into the P3 phase directly. According to Yang and co-workers' report on $Na_3Ni_2SbO_6$, the P3 phase corresponds to the formation of $Na_2Ni_2SbO_6$ with space group of C2/m [111]. Accordingly, in the case of $Na_3Ni_2BiO_6$, it is speculated here that the P3 phase should be $Na_2Ni_2BiO_6$. The desodiation capacity also supports the formation of $Na_2Ni_2BiO_6$. When the intensity of the P3 phase is at its highest, the desodiation capacity corresponds to the removal of ~0.35 Na per $NaNi_{2/3}Bi_{1/3}O_2$ (corresponding to a final stoichiometry of about $Na_{1.95}Ni_2BiO_6$). At the end of charging to 3.8 V, some diffraction peaks of the O1 phase also appears. This O3-P3-O1 transition agrees well with past observations of $Na_3Ni_2SbO_6$ during charge [111]. It should be noted that even at the end of charging to 3.8 V, there is still significant amount of the pristine O3 phase remaining in the structure. Such a phenomenon is indicative of the slow kinetics. During the first discharge process, the O1 phase starts to disappear, but instead of transforming to the O3 phase from the P3 phase, the P3 phase first transforms into a monoclinic O'3 phase, then the O'3 phase gradually disappears and a hexagonal O3 phase is formed. As discussed above, the formation of the O'3 phase during the first charge is hindered due to kinetic limitations. When the material was discharged to 1.5 V, it

transforms back to O3 phase and its XRD pattern looks almost identical to that of the pristine material.

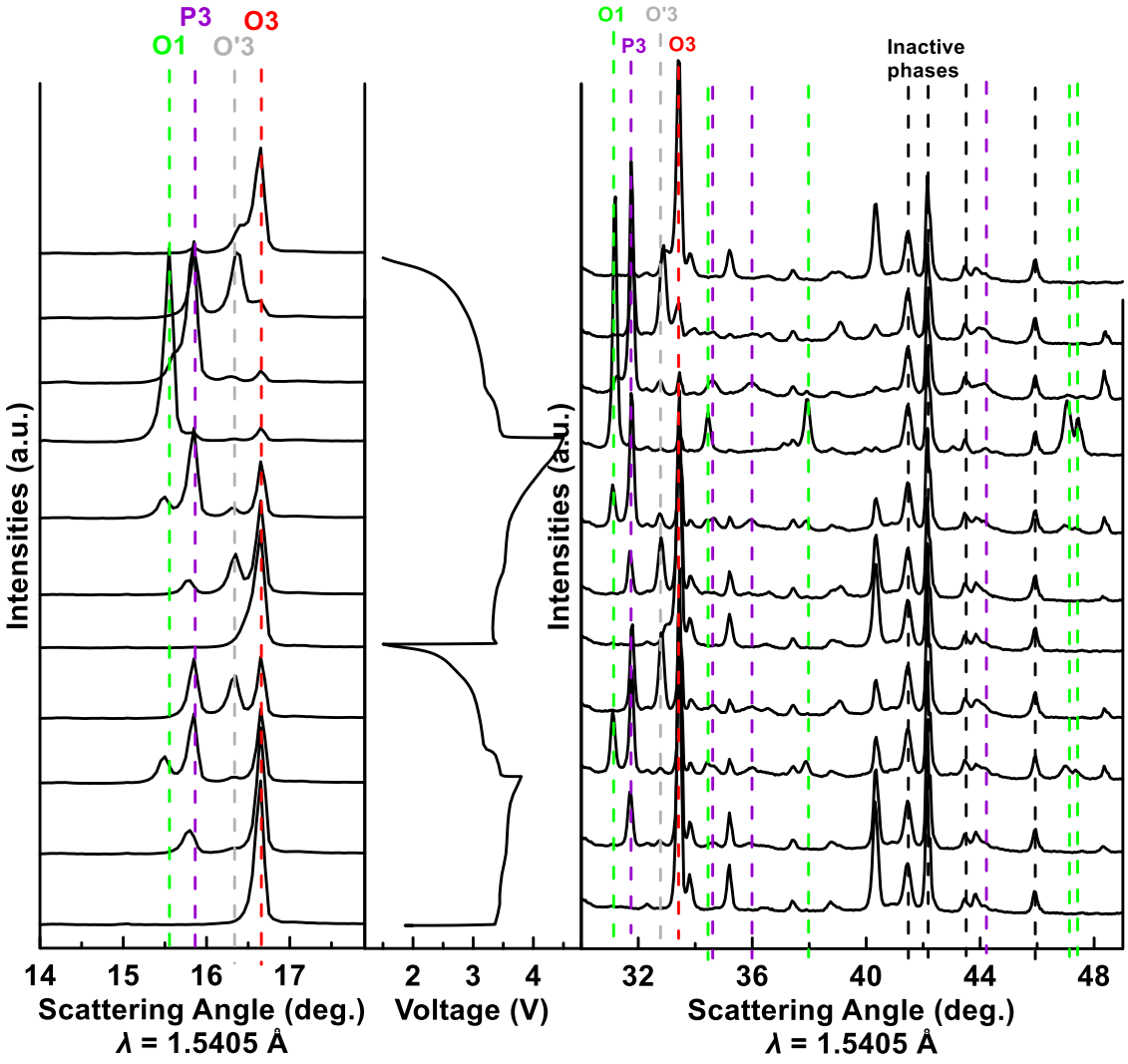


Figure 3.7 Enlarged *in situ* XRD patterns of the $Na_3Ni_2BiO_6$ electrode at various charge/discharge state during the first two cycles (1.5 V – 3.8 V and 1.5 V – 4.5 V).

After the first cycle, $Na_3Ni_2BiO_6$was then charged to 4.5 V. Unlike the first cycle, $Na_3Ni_2BiO_6$ undergoes an O3- O'3-P3-O1 process during the second cycle, indicating that the structure is stabilized after the first cycle. When $Na_3Ni_2BiO_6$ was charged to 4.5 V, all the diffraction lines can be indexed to an O1 phase. Yang et al. reported that the O1 phase

corresponds to a further removal of one Na from the P3-type $Na_2Ni_2SbO_6$ lattice and the formation of of $NaNi_2SbO_6$ with $P\bar{3}1m$ symmetry [111]. In the case of $Na_3Ni_2BiO_6$, the O1 phase should correspond to the formation of $NaNi_2BiO_6$, which agrees well with the desodiation capacity: at the end of second charge, the capacity is ~ 90 mAh/g, corresponding to the removal of ~1.7 Na per $Na_3Ni_2BiO_6$. The following discharge follows the course of O1-P3- O'3-O3. At the end of discharge $Na_3Ni_2BiO_6$ almost fully converts to O3 with a small amount of O'3 phase left, as can be seen by the small shoulder at ~16.4°.

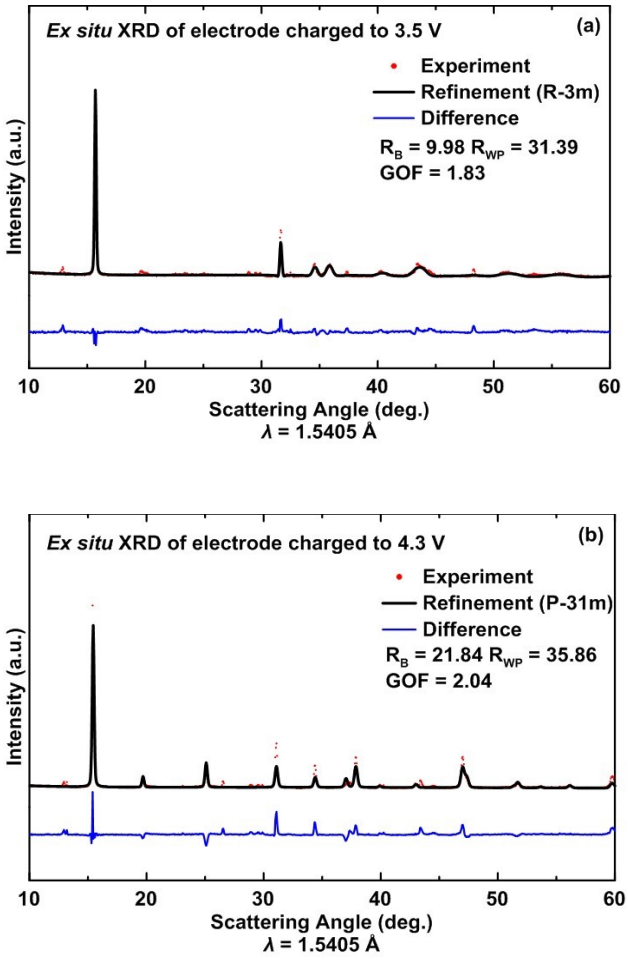


Figure 3.8 *Ex situ* XRD patterns and Rietveld refinements of electrodes charged to (a) 3.5 V and (b) 4.5 V.

Another pronounced feature with $Na_3Ni_2BiO_6$ is that there are several three-phase regions during cycling. Two-phase regions are dictated by thermodynamics for the number of degrees of freedom available to this system and are commonly observed for sodium ion battery positive electrode materials during sodium extraction/insertion [114]. The coexistence of three phases during cycling has not been reported to the best of our knowledge. This three-phase phenomenon indicates sluggish kinetics and poor sodium ion diffusion, as discussed above. The sluggish kinetics hinders the material's ability to undergo phase transitions. This can also explain the poor rate performance for this material. To confirm the hypothesis of the slow kinetics, *ex situ* XRD was performed. Coin cells were charged/discharged to indicated voltages and held at the voltage for 30 hours to achieve equilibrium. Figure 3.8 (a) shows an *ex situ* XRD pattern and Rietveld refinement of an electrode charged to 3.5 V. The XRD pattern was well-fitted with a P3 structure. Figure 3.8 (b) shows an *ex situ* XRD pattern and Rietveld refinement of an electrode charged to 4.5 V and the XRD was fitted with an O1 structure. Therefore, it can be concluded that the plateau before 3.5 V corresponds to the phase transition to P3 phase, and the plateau above 3.5 V corresponds to the phase transition to the O1 phase. Compared to the multiple phases observed in *in situ* XRD patterns, only single phases were present in the *ex situ* XRD patterns. This confirms the hypothesis that slow kinetics hinder phase transitions, and the phase transition process of O3-P3-O1. However, a single phase O'3 structure by *ex situ* XRD could not be obtained, as there is no distinct boundary between O3 and O'3 phases. This might be because the sodium diffusion gradients cause the plateaus to merge. Nevertheless, what is clear is that the formation of the O'3 phase occurs between the O3 and P3 phases, as can be seen from the *in situ* XRD data. It is also observed that the

peak positions of the O'3 phase change slightly during the charge/discharge process. The position shift of O'3 peaks indicates a single-phase region in the equilibrium phase diagram. However, the peak shift is accompanied by an increase in the peak intensity of new peaks and a decrease in the peak intensity of "old" peaks, implying a two-phase coexistence state. Such a contradiction exists because the system is in a non-equilibrium state due to kinetic hindrance. Phase transitions and $Na^+$/vacancy ordering have been associated with capacity fade and poor reversibility during cycling [72]. One strategy to address this issue is to introduce disorder in transition metal layers by partial substitution. Singh et al. studied the Mg substitutued Na-Ni-Mn-O system and they found that the addition of Mg effectively suppresses the P2-O2 phase transition and improves the capacity retention of P2-$Na_{2/3}Ni_{1/3}Mn_{2/3}O_2$ [118]. Meng et al. used Li substitution in the Na-Ni-Mn-O system and achieved good cyclability [119].

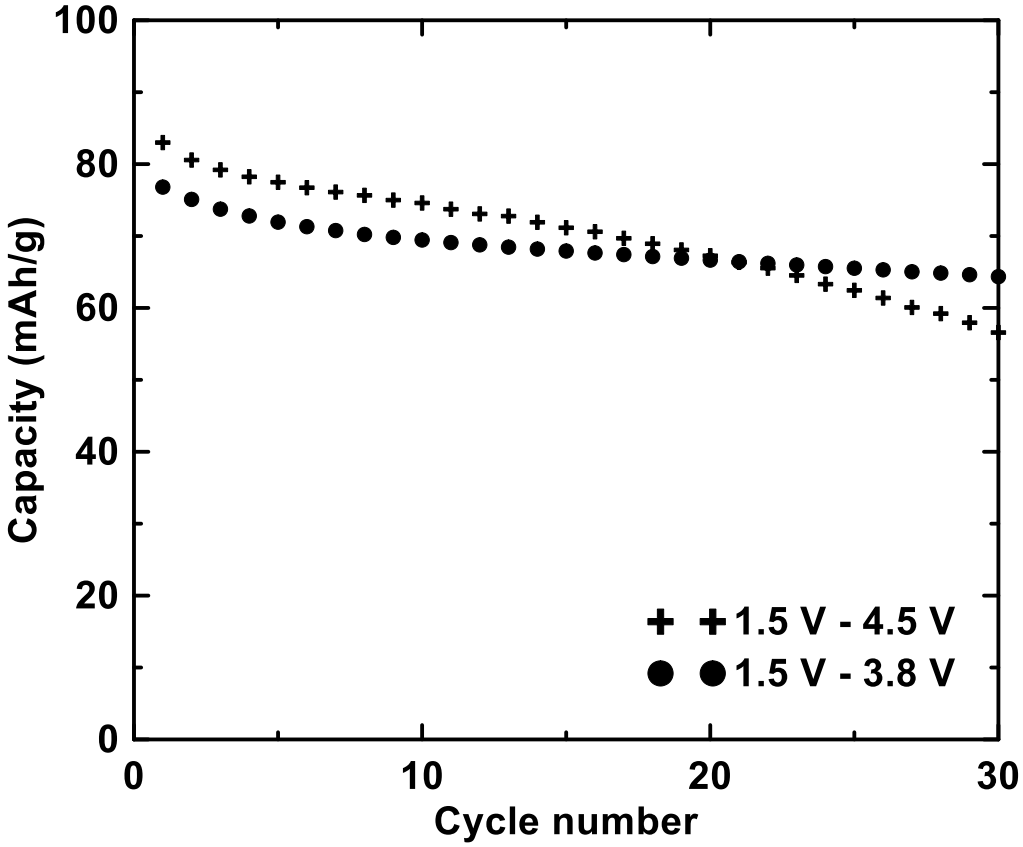


Figure 3.9 Cycling performance of $Na_3Ni_2BiO_6$ electrodes cycled at different voltage ranges at C/20 rate.

Figure 3.9 shows the cycling performance of $Na_3Ni_2BiO_6$. When cycled between 1.5 – 4.5 V, the capacity retention is ~75% after 25 cycles. By restricting the voltage range to 1.5 – 3.8 V at C/20 rate, $Na_3Ni_2BiO_6$ retained 85% of its initial discharge capacity after 25 cycles. Previously, $Li_3Ni_2BiO_6$ has been synthesized using a similar high temperature solid state reaction process by Subramanian et al. [120]. Subramanian et al. also studied the electrochemical performance of $Li_3Ni_2BiO_6$ in a lithium half-cell. They reported a first discharge capacity of 81.7 mAh/g, which is comparable to the capacity obtained here for $Na_3Ni_2BiO_6$. However, a rapid capacity fade was observed for $Li_3Ni_2BiO_6$ and after 10 cycles a capacity of only 22 mAh/g was retained [120]. Similarly, Meng et al. reported the synthesis and electrochemical properties of $Li_3Ni_2SbO_6$ in 2007 [121]. The first

charge/discharge capacities of $Li_3Ni_2SbO_6$ are 110/92 mAh/g, which are comparable to that of $Na_3Ni_2SbO_6$ (122/117 mAh/g) reported by Yang et al . Nevertheless, after 10 cycles, the reversible capacity of $Li_3Ni_2SbO_6$ drops rapidly to ~38 mAh/g, while $Na_3Ni_2SbO_6$ shows a good cycling performance (95% capacity retention after 50 cycles) [111,121]. Meng et al. studied Ni migration during $Li_3Ni_2SbO_6$ cycling by XRD and calculations. They attributed the drastic capacity fade to the structure degradation caused by the interlayer cation mixing of Li/Ni during cycling [121]. The migration of Ni into the Li layer not only reduces the available sites for Li but also blocks lithium diffusion pathways. It is well-known that Li/Ni mixing is common in cathode materials for lithium ion batteries due to the similar ionic size of Li and Ni, while the mixing of Ni and Na is usually negligible due to the large difference in ion sizes of $Na^+$(1.02 Å) and $Ni^{2+}$(0.69 Å) [27]. This may explain the better cycling performance of $Na_3Ni_2SbO_6$ and $Na_3Ni_2BiO_6$ compared to their lithium counterparts.

### 3.4 Conclusions

$Na_3Ni_2BiO_6$ was synthesized using a conventional high temperature solid-state reaction and its electrochemistry was studied for the first time. When cycled between 1.5 V – 3.8 V, this material has two voltage plateaus at ~3.1 V and ~3.4 V and a first discharge capacity of ~80 mAh/g with negligible irreversible capacity, corresponding to the reversible removal of ~1.5 Na per $Na_3Ni_2BiO_6$. It was found by *in situ* XRD that the first charge proceeds via an O3-P3-O1 phase transition, while the phase transitions during the first discharge proceed as O1-P3-O'3-O3. After the first cycle, the material was stabilized and reversible O3-O'3-P3-O1 phase transitions occur during cycling. The sluggish phase transitions and poor rate capability indicate slow kinetics of this material. It was also

observed that cycling is significantly better for $Na_3Ni_2SbO_6$ and $Na_3Ni_2BiO_6$ in Na cells compared to their Li counterparts in Li cells. This is attributed to the lack of cation mixing during cycling of the Na-containing oxides.

# CHAPTER 4 P2-type $Na_{2/3}Ni_{1/3-x}Cu_xMn_{2/3}O_2$ [2]

## 4.1 Introduction

P2-$Na_{2/3}Ni_{1/3}Mn_{1/3}O_2$ has one of the highest average discharge voltages reported (3.7 V) and a high reported capacity (150 mAh/g) [72,114]. Nevertheless, it has rapidly fading reversible capacity. The fade may be induced by structural transitions during charge/discharge, as indicated by multiple plateaus in its voltage curve [72,114]. Specifically, the rapid capacity loss could be caused by the P2-O2 phase transition and resulting volume change when the material is charged to above 4.2 V [72,114]. One strategy to address this issue is to replace $Mn^{4+}$ with other 4+ cations, such as $Ti^{4+}$. Komaba et al. showed that titanium substituted $Na_{2/3}Ni_{1/3}Mn_{1/2}Ti_{1/6}O_2$ delivers 127 mAh/g reversible capacity with an average voltage of 3.7 V [110]. The voltage curves are smooth and titanium-doped samples have superior cyclability compared to Ti-free $Na_{2/3}Ni_{1/3}Mn_{1/3}O_2$. Replacing $Ni^{2+}$ with other 2+ cations ($Zn^{2+}$ or $Mg^{2+}$) is another strategy [118,122]. Singh et al. demonstrated that substitution of $Ni^{2+}$ with $Mg^{2+}$ can suppress the P2-O2 phase transition and thus Mg-substituted $Na_{2/3}Ni_{1/3}Mn_{2/3}O_2$ has improved capacity retention [118]. Nevertheless, both of these strategies result in decreased reversible capacity. One of the reasons for this is that $Zn^{2+}$ or $Mg^{2+}$ ions are not redox active and therefore decreasing the $Ni^{2+}$ content can decrease capacity. The reason that $Ti^{4+}$ doping

[2]This chapter was adapted with permission from Zheng, L.; Li, J.; Obrovac, M.N., Crystal Structures and Electrochemical Performance of Air-Stable $Na_{2/3}Ni_{1/3-x}Cu_xMn_{2/3}O_2$ in Sodium Cells. *Chemistry of Materials.*, **2017**, *29*, 1623–1631[79]. Copyright 2017 American Chemical Society. The author's contribution includes performing the experimental work and writing the manuscript.

also decreases the capacity is unknown. It is possible that Ti increases the average desodiation voltage and therefore the capacity obtainable at a fixed voltage range becomes lowered as a result.

Recently it has been reported that $Cu^{2+}$ is electrochemically active in layered sodium transition metal oxides. For instance, it was found that $Cu^{2+}$ can be oxidized to $Cu^{3+}$ during cycling in $Na_{2/3}Cu_{1/3}Mn_{1/3}O_2$ and $Na_{2/3}Cu_xMn_{1-x}O_2$ [123,124]. Another copper-based material, P2-$Na_{7/9}Cu_{2/9}Fe_{1/9}Mn_{2/3}O_2$, also has high voltage (3.5 V) and is air stable [89]. Based on these results, and noting that $Cu^{2+}$ and $Ni^{2+}$ have similar ionic radii, copper could be a good substitution element in $Na_{2/3}Ni_{1/3}Mn_{2/3}O_2$. In this report, the structure, electrochemical performance, and air-stability of the series P2- $Na_{2/3}Ni_{1/3-x}Cu_xMn_{2/3}O_2$ (x = 0, 1/12, 1/6, 1/4, 1/3) are presented.

### 4.2 Experimental

$Na_{2/3}Ni_{1/3-x}Cu_xMn_{2/3}O_2$ compounds were prepared by solid-state reaction of $Na_2CO_3$ (99.0%, Sigma Aldrich), NiO (99%, -325 mesh, Sigma Aldrich), CuO (99%, Sigma Aldrich), and $MnO_2$ (99%, -325 mesh, Sigma Aldrich). A stoichiometric mixture of these materials was mixed by ball-milling in a SPEX-8000 mill for 1 hour in air. An excess of 10% $Na_2CO_3$ was added to compensate sodium loss at high temperature. The powder mixtures were then pressed into pellets. For $1/12 \leq x \leq 1/3$ compositions, pellets were heated at 900 °C in air for 15 hours. The $Na_{2/3}Ni_{1/3}Mn_{2/3}O_2$ sample was synthesized according to a previous report by Lu and Dahn [114]. For this sample, pellets comprising the ball milled precursors were heated for 24 hours, also at 900 °C, followed by quenching

in liquid nitrogen. All samples were transferred immediately to an argon filled glovebox after synthesis.

Electrode preparation was conducted in an Ar-filled glovebox. Slurries were made by mixing active materials, carbon black (Super P, Erachem Europe), and PVDF binder (polyvinylidene fluoride, Kynar HSV 900) with a mass ratio of 80/10/10 in an appropriate amount of N-methyl 2-pyrrolidone (Sigma-Aldrich, anhydrous 99.5%). These components were mixed with two 0.5 inch tungsten carbide balls in a Retsch PM200 planetary mill (100 rpm, 1 h). The slurry was then coated onto aluminum foil using a coating bar with a ~0.015 cm gap and dried under vacuum at 80 °C overnight. Electrode discs 1.27 cm in diameter were punched from the as-prepared coatings. Coin cells (2325-type) were assembled with sodium foils (~0.3 mm in thickness, cold rolled from sodium ingot, Sigma-Aldrich, ACS reagent grade) as counter/reference electrodes. Two Celgard 2300 and one polypropylene blown microfiber separator (3M Company) were used as separators. The electrolyte was 1 M NaPF6 (BASF) in a solution of ethylene carbonate, diethylcarbonate, and monofluoroethylene carbonate (volume ratio 3:6:1, all from BASF). Cells were cycled at 30.0 ± 0.1 °C with a Maccor Series 4000 Automated Test System at a constant current. Cycling rates were calculated by assuming a capacity of 170 mAh/g for all compositions in the $Na_{2/3}Ni_{1/3-x}Cu_xMn_{2/3}O_2$ series. For galvanostatic intermittent titration technique (GITT) measurements, cells were charged at a C/40 rate for 1 hour, followed by relaxing at open circuit for 5 hours between each charge.

X-ray diffraction (XRD) patterns were measured with a Rigaku Ultima IV X-ray diffractometer equipped with a Cu anode X-ray tube and dual detectors. Powder samples were loaded into a gastight X-ray sample holder (DPM Solutions, Hebbville NS) in an

argon-filled glove box to avoid air contamination. A D/TeX Ultra linear detector with a K-beta filter was used to measure XRD patterns of powder samples. For *ex situ* XRD studies, coin cells we-re prepared as described above, but were charged to 4.4 V once and then stopped. Electrodes for *ex situ* XRD measurements were recovered from these cells in an argon-filled glove box, and the electrode materials were scraped off the aluminum foil and washed with dimethyl carbonate (DMC, BASF). The recovered electrode coating was then transferred onto a zero-background silicon wafer and sealed in the gastight sample holder for the *ex situ* XRD measurements. A scintillation detector with a diffracted beam monochromator was used to measure *ex situ* XRD patterns. A Phenom G2-pro scanning electron microscope (SEM, Nanoscience, Arizona) was used to determine particle size and morphology of the powder samples. Inductively coupled plasma optical emission spectrometry (ICP-OES) was used to determine the elemental composition of the products. Measurements were performed using a PerkinElmer Optima 8000. Each sample was dissolved in 2 mL aqua regia solution which was then diluted using 2% $HNO_3$ prior to measurements.

## 4.3 Results and Discussion

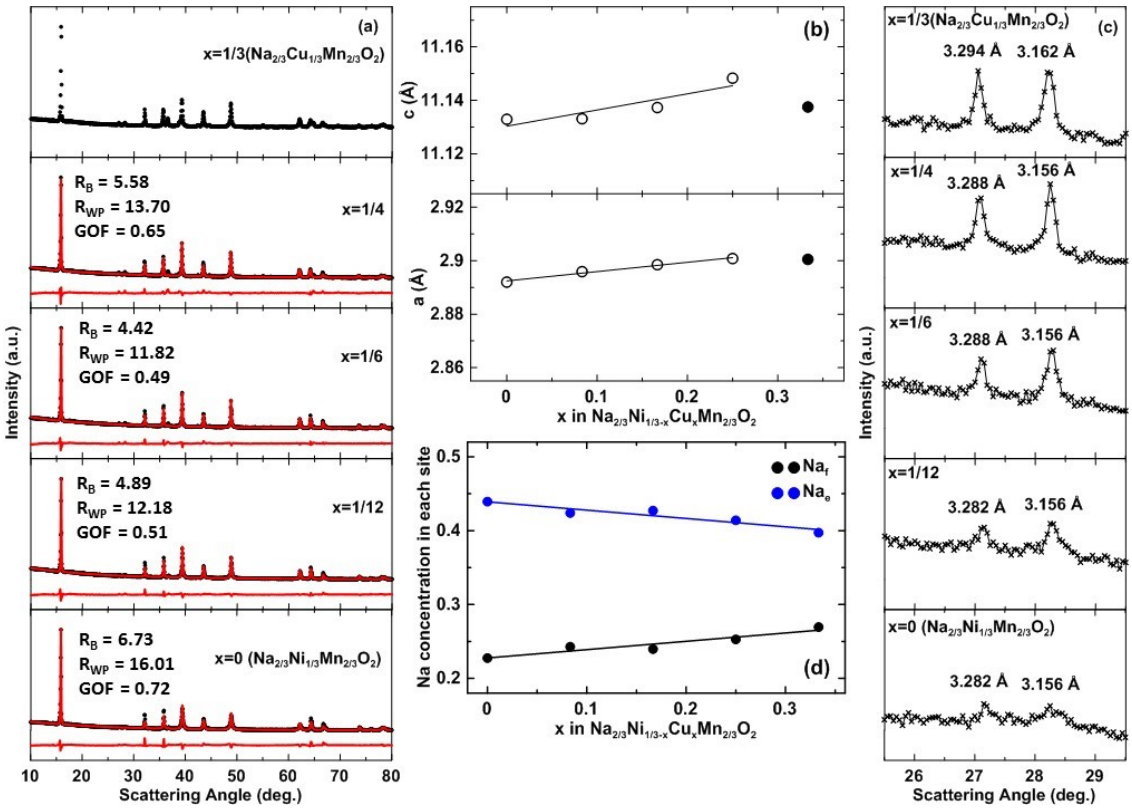


Figure 4.1 (a) X-ray diffraction patterns and Rietveld refinements of compounds in the $Na_{2/3}Ni_{1/3-x}Cu_xMn_{2/3}O_2$ series. (b) Changes in lattice parameters of the $Na_{2/3}Ni_{1/3-x}Cu_xMn_{2/3}O_2$ series. (c) Enlarged XRD patterns of the $Na_{2/3}Ni_{1/3-x}Cu_xMn_{2/3}O_2$ series between 25.5° to 29.5° including d-spacings. (d) Changes in $Na_f$ and $Na_e$ site occupancies of the $Na_{2/3}Ni_{1/3-x}Cu_xMn_{2/3}O_2$ series.

Figure 4.1(a) shows the XRD patterns of $Na_{2/3}Ni_{1/3-x}Cu_xMn_{2/3}O_2$. Samples with $0 \leq x \leq 1/4$ were phase pure with the P2 structure and no noticeable impurities were detected. A phase pure sample could not be obtained for x = 1/3 (nominal $Na_{2/3}Cu_{1/3}Mn_{2/3}O_2$) and an impurity phase, possibly CuO, was present in the final product. The formation of CuO impurity in $Na_{2/3}Cu_{1/3}Mn_{2/3}O_2$ is consistent with recent reports by Kang et al. and Xu et al. [124,125]. The presence of CuO impurity indicates that the ratio of Cu/Mn is smaller than 1/2 in the P2-structure. This suggests that stoichiometric $Na_{2/3}Cu_{1/3}Mn_{2/3}O_2$ is difficult to prepare, and that off-stoichiometric $Na_yCu_{1/3-z}Mn_{2/3+z}O_2$, where z is between 0 and 1/3, is

formed instead. The presence of this off-stoichiometric phase cannot be confirmed by ICP analysis, since any Cu impurity formed as a byproduct would still be present in the sample. However, the formation of this off-stoichiometric phase can affect the trends in structure and electrochemistry, as will be discussed later.

Table 4.1 Parameters used for Rietveld refinement of the $Na_{2/3}Ni_{1/6}Cu_{1/6}Mn_{2/3}O_2$ using space group *P6₃/mmc* (No. 194).

| Atom | Site | x | y | z | Occupancy | B (Å$^2$) |
|---|---|---|---|---|---|---|
| $Na_f$ | 2b | 0 | 0 | 0.25 | 0.245±0.007 | 4.2±0.4 |
| $Na_e$ | 2d | 1/3 | 2/3 | 0.25 | 0.422±0.007 | 4.2±0.4 |
| Ni | 2a | 0 | 0 | 0 | 1/6 | 0.7±0.1 |
| Mn | 2a | 0 | 0 | 0 | 2/3 | 0.7±0.1 |
| Cu | 2a | 0 | 0 | 0 | 1/6 | 0.7±0.1 |
| O | 4f | 2/3 | 1/3 | 0.0892±0.0006 | 1.02±0.02 | 0.01±0.3 |

The pattern calculated by Rietveld refinement of the P2 structure and a difference plot are also shown in Figure 4.1(a). An example of the refinement details is summarized in Table 4.1 for x = 1/6 ($Na_{2/3}Ni_{1/6}Cu_{1/6}Mn_{2/3}O_2$). For a typical P2 structure, transition metals and sodium occupy alternating layers of octahedral and prismatic sites, respectively, with vacancies occurring in the sodium layer. There are two different prismatic sites in the sodium layer that share either faces or edges with the transition metal octahedrons $MO_6$. These are denoted here as $Na_f$ and $Na_e$ sites, respectively. For the refinements, face-sharing

and edge-sharing sodium atoms were placed in 2b and 2d sites, respectively. Transition metals were placed in 2a sites, and oxygen atoms were placed in 4f sites. Na and Ni mixing was not considered in refinements due to the relatively large difference in the ionic radii of $Na^+$ (1.02 Å) and $Ni^{2+}$ (0.69 Å). The high displacement parameters refined for Na ions (~4 $Å^2$) agree with previous reports on P2-type materials and is associated with the fast diffusion of Na ions in the Na layer [126]. Komaba et al. studied the high displacement parameter using the maximum entropy method (MEM) and found that MEM analysis also suggests that the Na ions are widely distributed [126].

Figure 4.1(b) shows how the lattice constants *a* and *c* change with respect to *x*. Best fit lines according to Vegard's law are also shown for $0 \leq x \leq 1/4$. It should be noted that the evolution of cell parameter *c* has a curved shape, indicating Vegard's law is not precisely followed. It is speculated that transition metal ordering/sodium ordering also affects the lattice parameters, leading to this nonlinearity. Generally, as *x* is increased the lattice constants *a* and *c* both increase. However, the amplitude of variation is smaller than that in many other systems reported [94]. The minor change in *a* and *c* with *x* can be attributed to the slightly smaller ionic radius of $Ni^{2+}$ (0.69 Å) compared to $Cu^{2+}$ (0.73 Å). One exception in the series is $Na_{2/3}Cu_{1/3}Mn_{2/3}O_2$ (shown in solid circles), which shows a decrease in lattice constants *a* and *c*, compared to $Na_{2/3}Ni_{1/12}Cu_{1/4}Mn_{2/3}O_2$ ($x = 1/4$). As discussed above, $Na_{2/3}Cu_{1/3}Mn_{2/3}O_2$ is actually off-stoichiometric $Na_yCu_{1/3-z}Mn_{2/3+z}O_2$, which has more manganese in the P2-structure than the $Na_{2/3}Ni_{1/3-x}Cu_xMn_{2/3}O_2$ series with $0 \leq x \leq 1/4$, resulting in the formation of $Mn^{3+}$. Since the ionic radius of $Mn^{3+}$ (0.645 Å) is smaller than that of both $Ni^{2+}$ (0.69 Å) and $Cu^{2+}$ (0.73 Å), the lattice parameters *a* and *c* decrease from $Na_{2/3}Ni_{1/12}Cu_{1/4}Mn_{2/3}O_2$ ($x = 1/4$) to $Na_yCu_{1/3-z}Mn_{2/3+z}O_2$.

Figure 4.1(c) shows an expanded view of the $Na_{2/3}Ni_{1/3-x}Cu_xMn_{2/3}O_2$ XRD patterns between 25.5° and 29.5°. Two unrefined superstructure peaks at ~27.2° and ~28.3° can be observed at this region, which likely arise from the in-plane sodium/vacancy ordering. The *d*-spacings for these peaks are also shown for comparison. The *d*-spacings are close to those reported by Meng et al. [72]. for $Na_{2/3}Ni_{1/3}Mn_{2/3}O_2$. For the $Na_{2/3}Ni_{1/3-x}Cu_xMn_{2/3}O_2$ series, as *x* increases, the low angle peak gradually shifts to the left, corresponding to an increase in *d*-spacings, while the higher angle peak almost does not shift. The increase in *d*-spacings agrees with the expansion of lattice in the *a*–*b* plane as discussed above. Meng et al. studied the sodium/vacancy ordering and ascribed these peaks to the "large zigzag" ordering of $Na_f$ ions [72]. Typically for a P2 type material, there are more sodium atoms occupying $Na_e$ sites than $Na_f$ sites. This is because $Na_f$ sites have higher energy than $Na_e$ sites due to the stronger repulsion between sodium ions and adjacent transition metal ions. The relative difference leads to a higher occupancy ratio of sodium ions in $Na_e$ sites than $Na_f$ sites in order to minimize the repulsion. It can be seen from Figure 4.1(c) that, as the copper content increases, the intensity of these superstructure peaks also increases. This could be attributed to the increasing lattice constant *c*, which reduces the repulsion between sodium in $Na_f$ sites and neighboring transition metals. Therefore, as the copper content is increased, more sodium can be placed in the $Na_f$ sites and the "large zigzag" ordering between $Na_f$ ions becomes more distinct. This model was confirmed by Rietveld refinements. The sodium occupancy ratio in each site as obtained by the refinements are shown in Figure 4.1(d). As the copper content increases, the occupancy ratio of sodium increases in $Na_f$ sites and decreases in $Na_e$ sites.

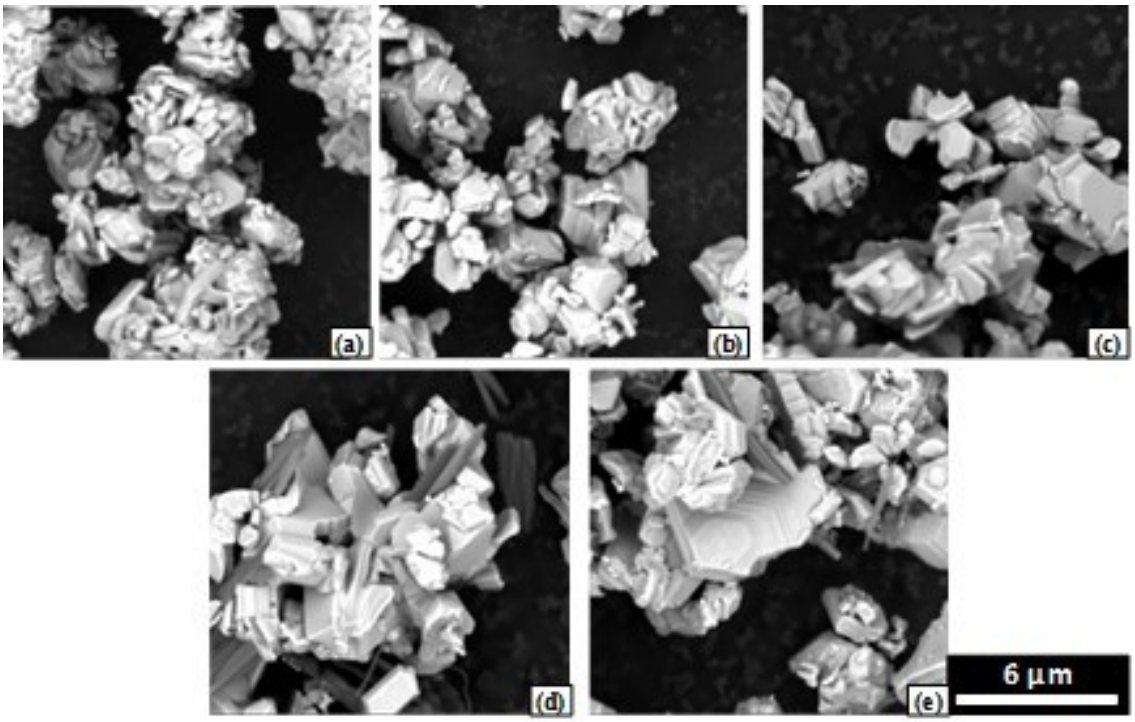


Figure 4.2 SEM images of compounds in the $Na_{2/3}Ni_{1/3-x}Cu_xMn_{2/3}O_2$ series for x = (a) 0, (b) 1/12, (c) 1/6, (d) 1/4 and (e) 1/3.

SEM images of compounds in the $Na_{2/3}Ni_{1/3-x}Cu_xMn_{2/3}O_2$ series are shown in Figure 4.2. Apparently all of the samples have a plate-like hexagonal morphology. The particle sizes range from 1 to 2 µm and increase in size as copper content increases. $Na_{2/3}Ni_{1/3}Mn_{2/3}O_2$ has a smaller particle size than the other compounds in the series, which might be due to the quenching process during its synthesis. ICP results are compared to target compositions in Table 4.2. All calibration curves were linear, with an $R^2$ value of 0.999985–1.00000. The standard deviations are less than 3% for all the measurements. The ICP results show good agreement with the anticipated atomic ratios for all the transition metals. However, extra sodium content was observed. These values are consistent with the 10% excess Na used during synthesis. This additional Na likely exists as $Na_2O$ or $Na_2CO_3$ at the particle surfaces.

Table 4.2 Target compositions compared with ICP measurement results (normalized to a total transition metal population of 1.000).

| Composition | | Na | Ni | Mn | Cu |
|---|---|---|---|---|---|
| x=0 | Target | 0.667 | 0.333 | 0.667 | 0.000 |
| | ICP | 0.731 | 0.367 | 0.630 | 0.003 |
| x=1/12 | Target | 0.667 | 0.250 | 0.667 | 0.083 |
| | ICP | 0.753 | 0.277 | 0.639 | 0.084 |
| x=1/6 | Target | 0.667 | 0.167 | 0.667 | 0.167 |
| | ICP | 0.775 | 0.190 | 0.636 | 0.174 |
| x=1/4 | Target | 0.667 | 0.083 | 0.667 | 0.250 |
| | ICP | 0.751 | 0.096 | 0.641 | 0.263 |
| x=1/3 | Target | 0.667 | 0.000 | 0.667 | 0.333 |
| | ICP | 0.768 | 0.001 | 0.644 | 0.355 |

The initial charge/discharge (corresponding to sodium deintercalation/intercalation) curves of $Na_{2/3}Ni_{1/3-x}Cu_xMn_{2/3}O_2$ vs Na cells cycled between 2.5 and 4.1 V or 2.5 and 4.4 V are compared in Figure 4.3. Figure 4.3 also shows the corresponding differential capacity curves for the cells. A hysteresis of ~0.2 V between charge and discharge half-cycles was observed for all the materials. The theoretical redox-limited capacities of $Na_{2/3}Ni_{1/3-x}Cu_xMn_{2/3}O_2$ compounds are also shown in the figure, as calculated based on the $Ni^{2+}/Ni^{4+}$ and/or $Cu^{2+}/Cu^{3+}$ redox couples. Because of the similar

atomic weight of Ni (58.69) and Cu (63.55), the formula weight varies only slightly in the composition series. Therefore, the change in redox-limited capacity originates almost exclusively from the substitution of $Ni^{2+}/Ni^{4+}$ with $Cu^{2+}/Cu^{3+}$ redox couples. With increasing copper content, the amount of $Ni^{2+}$ decreases and consequently the theoretical redox-limited capacity decreases from 85 mAh/g ($Na_{2/3}Cu_{1/3}Mn_{2/3}O_2$) to 172 mAh/g ($Na_{2/3}Ni_{1/3}Mn_{2/3}O_2$). On the other hand, the theoretical sodium-limited capacity, referring to the capacity if all the sodium can be extracted, almost does not change (169 mAh/g for $Na_{2/3}Cu_{1/3}Mn_{2/3}O_2$).

The voltage curve of the sample with $x = 0$ ($Na_{2/3}Ni_{1/3}\ Mn_{2/3}O_2$) agrees well with previous reports [72,114]. The step-like voltage curve indicates several sodium/vacancy ordering transitions and other phase transitions. The material exhibits a first charge/discharge capacity of ~80/75 mAh/g when cycled between 2.5 and 4.1 V. Accessing voltages above 4.1 V results in a flat voltage plateau at ~4.2 V. The full capacity of this plateau is accessed by charging the material to 4.4 V, which results in a plateau capacity of about 80 mAh/g. At this point almost all the sodium is removed from the structure. A first charge/discharge capacity of ~160/140 mAh/g is achieved, with ~20 mAh/g irreversible capacity. The first cycle coulombic efficiency is ~88%. Lu et al. showed that the irreversible capacity can be reduced by discharging the material to a lower cutoff voltage (2 V) [114]. According to Meng et al., the long plateau at ~4.2 V originates from the P2/O2 phase transition, which possibly causes the capacity fade [72]. The discharge capacity rapidly fades during cycling above 4.1 V (shown in Figure 4.3), and after 15 cycles less than half of the initial capacity is retained.

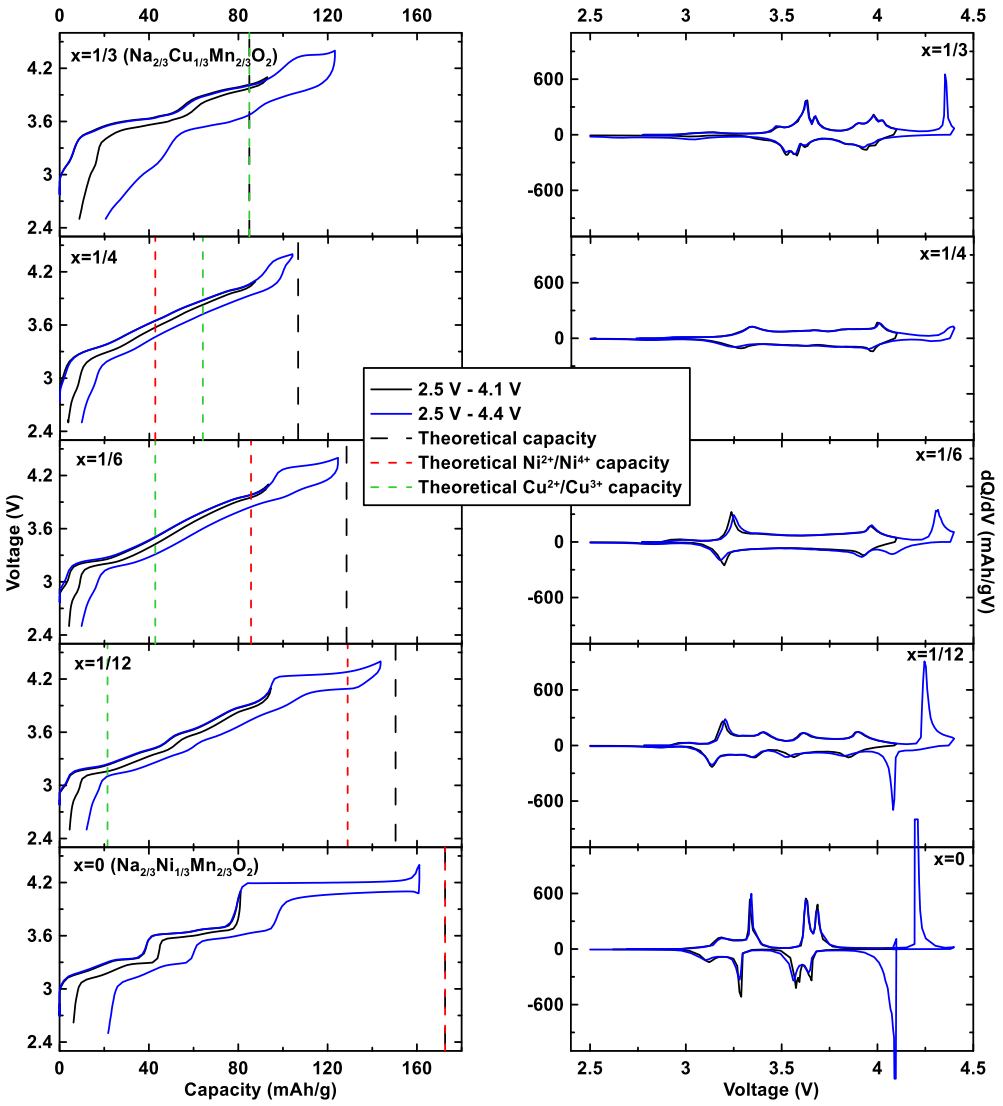


Figure 4.3 Voltage curves and corresponding differential capacity curves of $Na_{2/3}Ni_{1/3-x}Cu_xMn_{2/3}O_2$ vs. Na cells cycled between 2.5 V – 4.1 V (black lines) and 2.5 V – 4.4 V (blue lines).

The multiple plateaus present in the $Na_{2/3}Ni_{1/3}Mn_{2/3}O_2$ voltage curve correspond to the multiple sharp peaks in its differential capacity (Figure 4.3). In contrast, copper-substituted samples have smoother voltage curves, and broad peaks with low intensity were observed in the differential capacity. Even when $x = 1/12$ in $Na_{2/3}Ni_{1/3-x}Cu_xMn_{2/3}O_2$, the voltage curve was effectively smoothed and capacity retention improved. $Na_{2/3}Cu_{1/12}Ni_{1/4}Mn_{2/3}O_2$ has a reversible capacity of ~130 mAh/g when cycled between 2.5

and 4.4 V. Higher copper contents can smooth the voltage curve further, at the expense, however, of lower reversible capacities. On the other hand, when $x$ was increased to 1/3 ($Na_{2/3}Cu_{1/3}Mn_{2/3}O_2$), the step-like voltage curve reappears and sharp peaks were found in the differential capacity curve. The voltage curve agrees with previous reports of $Na_{2/3}Cu_{1/3}Mn_{2/3}O_2$ [123]. However, the observed capacity for $Na_{2/3}Cu_{1/3}Mn_{2/3}O_2$ is larger than its theoretical capacity based solely on transition metal oxidation when it is cycled between 2.5 and 4.4 V. As discussed earlier, this could be due to the formation of off stoichiometric $Na_yCu_{1/3-z}Mn_{2/3+z}O_2$. The presence of $Mn^{3+}$ in this structure would contribute to the total capacity. On the other hand, when $Na_{2/3}Cu_{1/3}Mn_{2/3}O_2$ is cycled between 2.5 and 4.4 V, an irreversible plateau appears at ~4.3 V, corresponding to an irreversible sharp peak at ~4.3 V in the differential capacity curve. Combined with the anomalously large voltage hysteresis and the extra capacity, this suggests an irreversible structural change, possibly due to an oxygen redox reaction. Further studies are needed to understand the source of extra capacity in $Na_{2/3}Cu_{1/3}Mn_{2/3}O_2$ when charged to 4.4 V.

The reversible capacities of all samples exceed their theoretical capacity based solely on either the $Ni^{2+}/Ni^{4+}$ (red dotted line) or the $Cu^{2+}/Cu^{3+}$ (green dotted line) redox couples. Therefore, both $Ni^{2+}$ and $Cu^{2+}$ participate in the redox reaction during cell cycling. Interestingly, when these materials were cycled between 2.5 and 4.1 V, the reversible capacity actually increases from ~75 mAh/g for $Na_{2/3}Ni_{1/3}Mn_{2/3}O_2$ ($x = 0$) to ~90 mAh/g for $Na_{2/3}Cu_{1/12}Ni_{1/4}Mn_{2/3}O_2$ and $Na_{2/3}Cu_{1/6}Ni_{1/6}Mn_{2/3}O_2$ ($x =$ 1/12 and 1/6), despite the decreased nickel content. This is caused by the lower redox potential of $Cu^{2+}/Cu^{3+}$ than $Ni^{2+}/Ni^{4+}$, resulting in a higher capacity utilization ratio in the low voltage range. As can be seen in Figure 4.3, while only half of the capacity is obtained for

$Na_{2/3}Ni_{1/3}Mn_{2/3}O_2$ when cycled between 2.5 and 4.1 V, ~80% of the capacity is obtained for $Na_{2/3}Cu_{1/3}Mn_{2/3}O_2$ at this voltage range. Compared with Mg or Zn, which are redox inactive, Cu substitution results in a higher capacity at a similar substitution level [118,122]. The high capacity originates from the inclusion of the active $Cu^{2+}/Cu^{3+}$ redox couple, rather than the inactive $Zn^{2+}$ and $Mg^{2+}$.

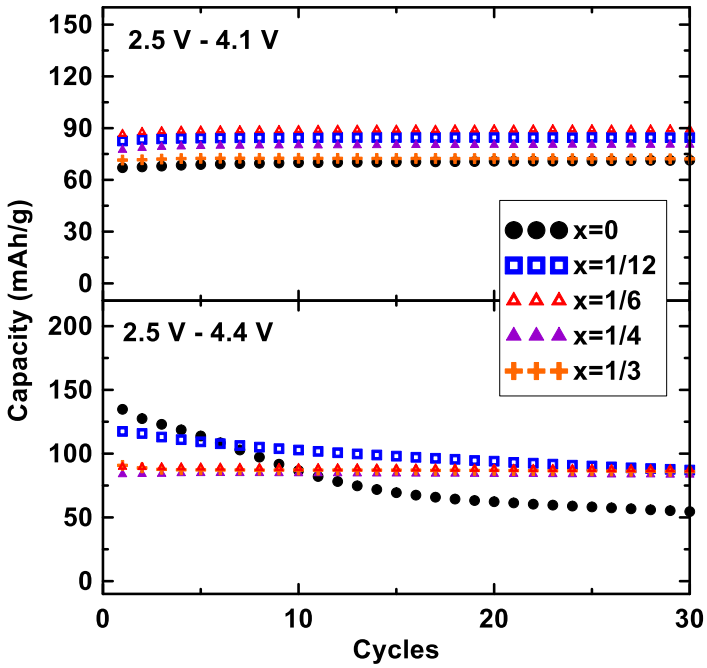


Figure 4.4 Discharge capacity versus cycle number of $Na_{2/3}Ni_{1/3-x}Cu_xMn_{2/3}O_2$ vs. Na cells cycled between 2.5 V – 4.1 V and 2.5 V – 4.4 V at 1C current rate.

The cycling performance of $Na_{2/3}Ni_{1/3-x}Cu_xMn_{2/3}O_2$ vs Na cells are shown in Figure 4.4. When cycled between 2.5 and 4.1 V at 1C, all the materials show good capacity retention after 30 cycles. When cycled between 2.5 and 4.4 V at 1C, severe capacity fade was observed for $Na_{2/3}Ni_{1/3}Mn_{2/3}O_2$ and less than half of its first cycle capacity was retained after 15 cycles. Copper substitution effectively improves the capacity retention of electrodes cycled at this voltage range. $Na_{2/3}Cu_{1/12}Ni_{1/4}Mn_{2/3}O_2$ retained 75% of its initial capacity after 30 cycles. Higher copper content is beneficial for better capacity

retention. For example, a capacity retention of 97% after 30 cycles was observed for $Na_{2/3}Cu_{1/6}Ni_{1/6}Mn_{2/3}O_2$.

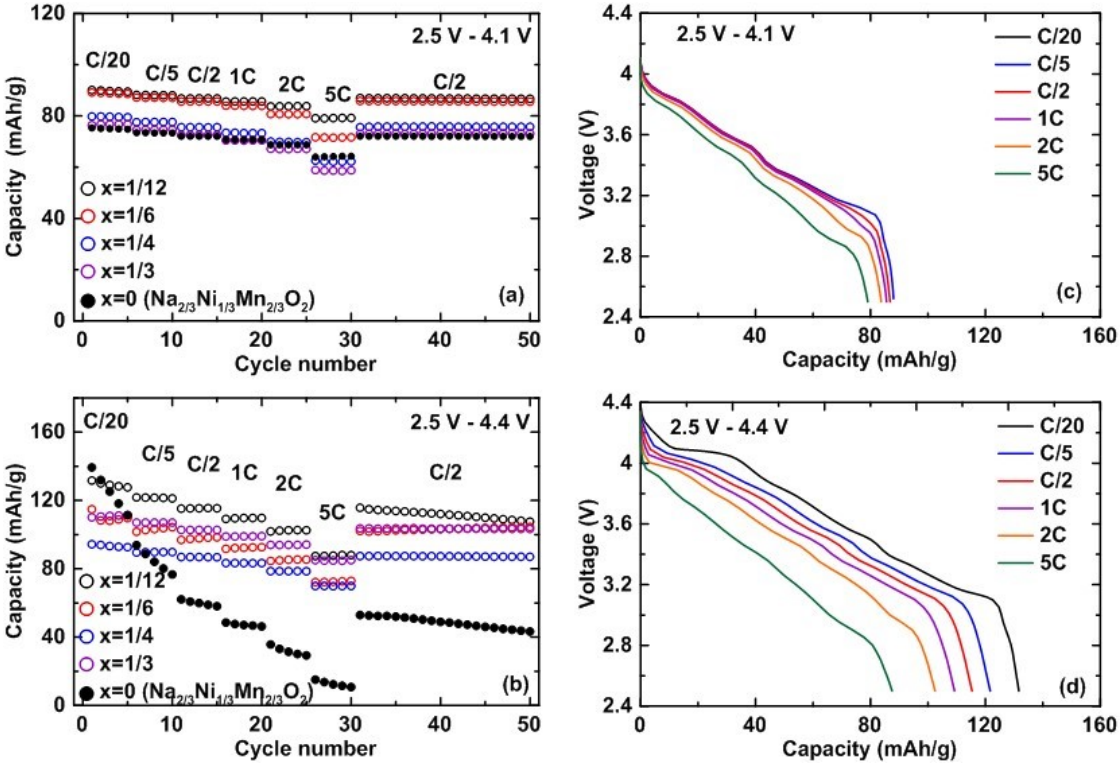


Figure 4.5 (a) Discharge capacity of $Na_{2/3}Ni_{1/3-x}Cu_xMn_{2/3}O_2$ compounds cycled at different C-rates between 2.5 V – 4.1 V and (b) between 2.5 V – 4.4 V. (c) Voltage curves of $Na_{2/3}Ni_{1/4}Cu_{1/12}Mn_{2/3}O_2$ cycled at different C-rates between 2.5 V – 4.1 V, and (d) between 2.5 V – 4.4 V.

Figure 4.5(a-b) shows the discharge capacity for $Na_{2/3}Ni_{1/3-x}Cu_xMn_{2/3}O_2$ vs Na cells cycled at different C-rates within 2.5 and 4.1 V and 2.5 and 4.4 V, respectively. Figure 4.5(c-d) shows the voltage curves of $Na_{2/3}Cu_{1/12}Ni_{1/4}Mn_{2/3}O_2$ cycled at different C-rates between 2.5 and 4.1 and 2.5 and 4.4 V, respectively. All of the materials with Cu substitution exhibit improved rate capability, especially in the voltage range of 2.5–4.4 V. When cycled between 2.5 and 4.1 V, $Na_{2/3}Cu_{1/12}Ni_{1/4}Mn_{2/3}O_2$ has discharge capacities of 90, 88, 87, 86, and 84 mAh/g at current rates of C/20, C/5, C/2, 1C, and 2C

with an average voltage of ~3.4 V. Even at a high rate of 5C (850 mA/g), a discharge capacity of 80 mAh/g was retained with an average voltage of ~3.3 V, corresponding to 89% of its capacity at C/20. When cycled between 2.5 and 4.4 V, $Na_{2/3}Cu_{1/12}Ni_{1/4}Mn_{2/3}O_2$ has discharge capacities of 130, 122, 116, 110, and 102 mAh/g at current rates of C/20, C/5, C/2, 1C, and 2C, all exceeding 75% of its capacity at C/20. Figure 4.6 shows the sodium diffusion coefficients ($D_{Na}$) in $Na_{2/3}Ni_{1/3-x}Cu_xMn_{2/3}O_2$ as calculated from GITT measurements. All samples have a similar $D_{Na}$ at voltages below 4.0 V. However, a rapid drop in $D_{Na}$ was observed for $Na_{2/3}Ni_{1/3}Mn_{2/3}O_2$ at voltages above 4.0 V. This phenomenon agrees with the results obtained by Meng et al., who observed that the minimum value of $D_{Na}$ occurred at low sodium content [72]. The P2–O2 phase transition is responsible for the low $D_{Na}$, as Meng et al. show that sodium has a much lower diffusion barrier in the P2 structure than in the O2 structure [72]. For comparison, the $D_{Na}$ for $Na_{2/3}Ni_{1/3-x}Cu_xMn_{2/3}O_2$ with $x = 1/12$ and $x = 1/6$ is much higher at voltages larger than 4.0 V, which indicates a faster sodium diffusivity, leading to a better rate capability at high voltage ranges. Materials with high copper content also show smoother $D_{Na}$ vs voltage curve, suggesting a more stable structure at different sodium contents. The result also implies that copper substitution could suppress the P2–O2 phase transition at high voltage. The diffusion length calculated from $D_{Na}$ is between 0.6 – 6 μm, which is on the same scale of the particle size.

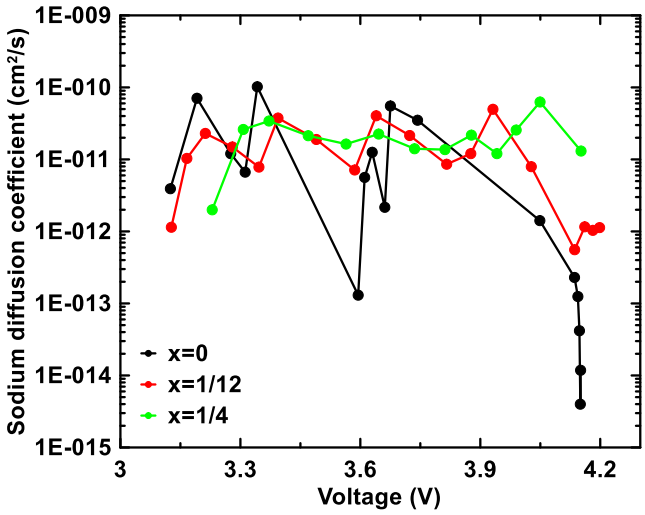


Figure 4.6 Sodium diffusion coefficient in $Na_{2/3}Ni_{1/3-x}Cu_xMn_{2/3}O_2$ calculated from GITT as a function of voltage.

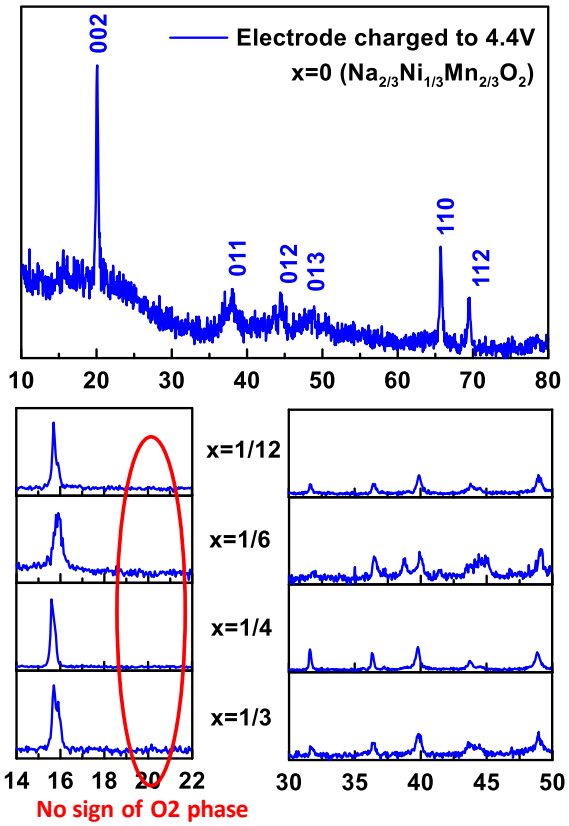


Figure 4.7 *Ex situ* X-ray diffraction patterns of compounds in the $Na_{2/3}Ni_{1/3-x}Cu_xMn_{2/3}O_2$ series after being fully charged to 4.4 V.

Figure 4.7 shows *ex situ* XRD patterns measured for each compound in the $Na_{2/3}Ni_{1/3-x}Cu_xMn_{2/3}O_2$series after charging to 4.4 V. After charging to 4.4 V, Cu-free $Na_{2/3}Ni_{1/3}Mn_{2/3}O_2$ ($x$ = 0) has an O2-type structure with random stacking faults. This is consistent with a P2–O2 phase transition during desodiation, as reported by Lu et al. [114]. This P2–O2 phase transformation has been associated with the rapid capacity fade [72]. In contrast, for copper substituted samples, *ex situ* XRD patterns taken after charging to 4.4 V (Figure 4.7) show no sign of a P2–O2 phase transition. At ~20°, where the (002) peak of the O2 phase usually occurs, no peak was observed for the copper substituted samples. The major reflections corresponding to the P2 phase are maintained after being charged to 4.4 V. The result indicates that the addition of Cu, similar to Mg, can also suppress the P2–O2 phase transition [118]. A closer examination shows that, excepting $x$ = 1/4, a splitting of the (002) peak for all other compositions can be observed. Such peak splitting has been assigned to the O2–OP4 phase transition [127]. The absence of such splitting for the material with $x$ = 1/4 is consistent with the results in Figure 4.3. In Figure 4.3, all the other materials have a plateau at ~4.2 V, except for the one with $x$ = 1/4. This result is similar to a previous report by Billaud et al., who studied the $Na_{2/3}Mg_xMn_{1-x}O_2$ series and observed in the *ex situ* XRD patterns that only the materials with a plateau at ~4.2 V have such OP4 peak splitting [127]. Therefore, instead of the P2–O2 transition, the material with $x$ = 1/4 retains its P2 phase, while a P2–OP4 transition occurs for other Cu-doped materials. The suppression of P2–O2 phase transitions in the Cu substituted materials might be responsible for their improved cycling performance.

Unlike many other Na–M–O materials that readily react with water, $Na_{2/3}Ni_{1/3}Mn_{2/3}O_2$ has been reported to be air-stable and does not uptake water into its

structure [87]. Lu et al. speculated that the superlattice ordering of transition metals induces a strong coupling between adjacent $MO_2$ sheets, which prevents the intercalation of water [87]. However, it has also been reported that as $Co^{3+}$ is added to form P2–$Na_{2/3}[Co_xNi_{1/3-x}Mn_{2/3}]O_2$, the superlattice ordering is suppressed and the materials become hygroscopic. P2–$Na_{2/3}[Co_xNi_{1/3-x}Mn_{2/3}]O_2$ readily reacts with water in the air and forms a hydrated phase, which can be easily spotted as the diffraction pattern changes significantly from the pristine phase even after only a few hours of air exposure [87]. The stability of materials against moisture is important as hygroscopic materials require a dry handling system, which would increase the cost of manufacturing [13]. For this reason the air-sensitivity of copper doped P2–$Na_{2/3}[Cu_xNi_{1/3-x}Mn_{2/3}]O_2$ were studied.

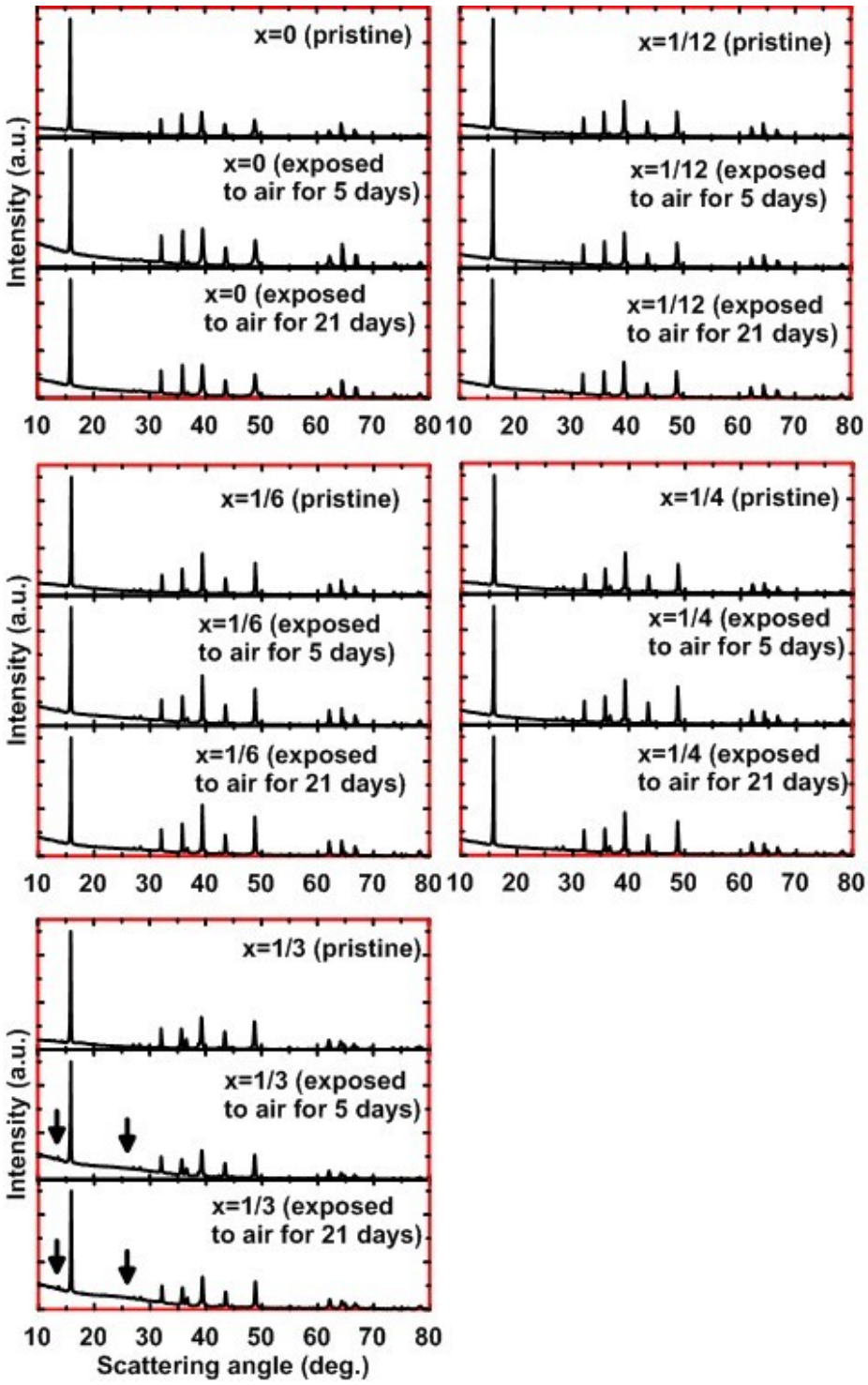


Figure 4.8 X-ray diffraction patterns of $Na_{2/3}Ni_{1/3-x}Cu_xMn_{2/3}O_2$ after air exposure, compared to pristine materials.

Figure 4.8 shows the XRD patterns of P2–$Na_{2/3}[Cu_xNi_{1/3-x}Mn_{2/3}]O_2$ powders after being exposed to air for 5 days and 21 days. Compared to XRD patterns of unexposed samples, no noticeable change was observed. The positions of the Bragg peaks do not change, and no new peaks are formed. Even after 3 weeks of air exposure, XRD patterns of $Na_{2/3}[Cu_xNi_{1/3-x}Mn_{2/3}]O_2$ materials show no significant change, except for $Na_{2/3}Cu_{1/3}Mn_{2/3}O_2$. It can be observed that after air exposure of $Na_{2/3}Cu_{1/3}Mn_{2/3}O_2$, there appears a weak peak formed at ~14° and a broad peak at ~28°, which are indicated by arrows in Figure 4.7. This is indicative of water intercalation as reported by Lu et al., who observed a similar XRD pattern for air-exposed $Na_{2/3}Co_{1/6}Ni_{1/6}Mn_{2/3}O_2$ [87]. Lu and Dahn proposed that these two peaks are due to a shift of the (002) and (004) peaks of the pristine phase upon the intercalation of water. It is speculated that copper does not disturb transition metal ordering due to the similar ionic radii of $Cu^{2+}$ (0.73 Å) and $Ni^{2+}$ (0.69 Å), while the relatively large ionic radii difference of $Co^{3+}$ (0.545 Å) and $Ni^{2+}$ (0.69 Å) would suppress transition metal superlattice ordering. Lu and Dahn also suggested that the presence of $Mn^{3+}$, which forms as $Co^{3+}$ is added, also possibly aids the intercalation of water [87]. However, when $Cu^{2+}$ is added to replace $Ni^{2+}$, the oxidation state of Mn does not change and presumably no $Mn^{3+}$ is formed. This may prevent water intercalation and be the reason why Cu imparts air stability to these materials. It can be concluded that water cannot be intercalated into $Na_{2/3}Cu_xNi_{1/3-x}Mn_{2/3}O_2$ ($0 \leq x \leq 1/4$) under the air exposure conditions employed here but can be intercalated into $Na_{2/3}Cu_{1/3}Mn_{2/3}O_2$.

The air stability of the materials was further studied in electrochemical tests. Electrode discs were intentionally taken from the glovebox and exposed to air on a lab bench. After 5 days, these electrodes were transferred back into the glovebox without any

further treatment and incorporated into coin cells as described above. Figure 4.9 shows the first two cycles of the voltage curves for electrodes exposed to air for 5 days, compared to the voltage curve of electrodes without air exposure. It was found that all the cells with air exposed electrodes have a higher open circuit voltage (~0.4 V) compared to cells made with air-protected electrodes. This suggests that the sodium content in the air exposed samples is slightly less than that in the as-synthesized samples. However, except for $Na_{2/3}Cu_{1/3}Mn_{2/3}O_2$ ($x$ = 1/3), the average voltage and reversible capacity did not change

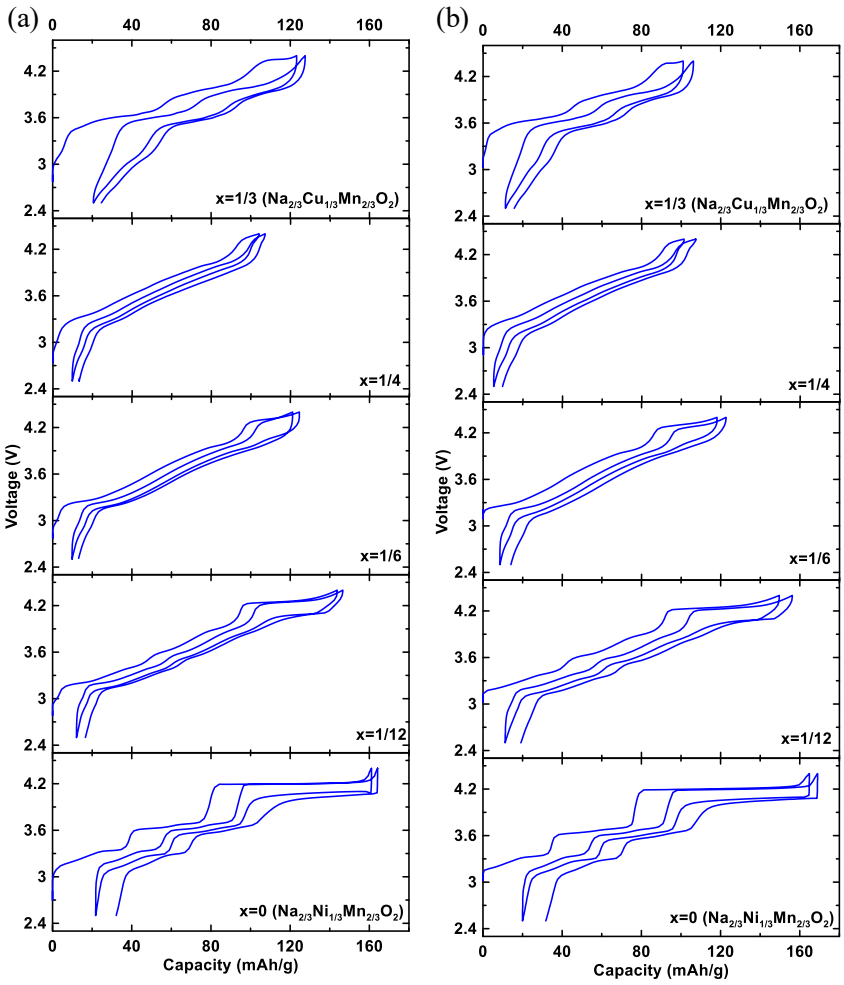


Figure 4.9 Voltage curves of $Na_{2/3}Ni_{1/3-x}Cu_xMn_{2/3}O_2$ (a) pristine materials and (b) after 5 days of air exposure.

and there is almost no decay in electrochemical performance, indicating the air stability of these materials. For $Na_{2/3}Cu_{1/3}Mn_{2/3}O_2$ ($x = 1/3$), a smaller reversible capacity was obtained after air exposure. The electrochemical test results agree with the XRD measurements that the $Na_{2/3}Cu_xNi_{1/3-x}Mn_{2/3}O_2$ series ($0 \leq x \leq 1/4$) are air-stable, while $Na_{2/3}Cu_{1/3}Mn_{2/3}O_2$ is air-sensitive. The air stability of these materials demonstrates the feasibility of using $Na_{2/3}Cu_xNi_{1/3-x}Mn_{2/3}O_2$ for practical sodium ion batteries.

### 4.4 Conclusion

P2-type $Na_{2/3}Ni_{1/3}Mn_{2/3}O_2$ could be a promising cathode candidate in sodium ion batteries for large scale applications such as grid storage due to its high capacity, high operating voltage, and air stability. However, this material suffers from its step-like voltage curve and rapid capacity fade during cycling. A doping strategy that substitutes part of the nickel with copper was proven to be an effective way to smooth the voltage curve and improve capacity retention and rate capability. Both $Ni^{2+}$/ $Ni^{4+}$ and $Cu^{2+}$/$Cu^{3+}$ participate in the redox reaction during cycling; therefore, less capacity reduction is observed compared to when Ni is substituted with Mg or Zn. *Ex situ* XRD studies reveal that these materials do not convert to the O2 phase when charged to a high voltage, which might be the reason for their improved cycling performance. This doping strategy is a promising approach for the future development of positive electrode materials for sodium ion batteries.

# CHAPTER 5 O3-Type $Na_{0.9}Ni_{0.45}Mn_xTi_{0.55-x}O_2$ [3]

## 5.1 Introduction

Compared to their lithium-counterparts, the cycle life of $Na_xMO_2$ usually do not meet the requirements for practical applications. Rapid capacity fade is common in $Na_xMO_2$ materials [1]. It is suspected that the presence of phase transitions during the cycling of Na-ion positive electrodes may contribute to capacity fade. For example, P2-$Na_{2/3}Ni_{1/3}Mn_{2/3}O_2$ has a high average discharge voltage of ~3.7 V and a first discharge capacity of ~150 mAh/g when cycled between 2.5 V – 4.5 V. However after 10 cycles only 67% of the initial capacity is retained [72]. This poor capacity retention could originate from the P2/O2 phase transition during cycling, as suggested by Komaba et al. and Meng et al. [72,110]. Meng et al. proposed that by limiting the cut-off voltage to 4.1 V, the P2/O2 phase transition could be prevented, thus better capacity retention was observed [72]. Komaba et al. reported that Ti substitution can suppress phase transitions and reduce volume change during cycling. They showed that the Ti-substituted $Na_{2/3}Ni_{1/3}Ti_xMn_{2/3-x}O_2$ series has improved cycling performance, at the expense of lowered reversible capacity in the voltage range of 2.5 V – 4.5 V [110]. In particular, $Na_{2/3}Ni_{1/3}Ti_{1/6}Mn_{1/2}O_2$ has 127 mAh/g of reversible capacity with an average discharge voltage of ~3.7 V. About 94% of the initial capacity is retained after10 cycles [110].

[3] This chapter was adapted with permission from Zheng, L.; Obrovac, M. N. Investigation of O3-type $Na_{0.9}Ni_{0.45}Mn_xTi_{0.55-x}O_2$ ($0 \leq x \leq 0.55$) as Positive Electrode Materials for Sodium-Ion Batteries. *Electrochimica Acta*, **2017**, *233*, 284-291 [181]. Copyright 2017, Elsevier. The author's contribution includes performing the experimental work and writing the manuscript.

O3-$NaNi_{0.5}Mn_{0.5}O_2$ has been extensively studied and has a high energy density of 2700 Wh/L in the voltage range of 2.2 V – 4.5 V [113]. Its stepwise voltage curve indicates several phase transitions and discharge capacity fades rapidly during charge/discharge cycling. Inspired by Komaba's report of $Na_{2/3}Ni_{1/3}Ti_xMn_{2/3-x}O_2$, it was suspected that the use of Ti substitution might be a good strategy to improve the cycling characteristics of O3-$NaNi_{0.5}Mn_{0.5}O_2$ [110]. However, all trials to prepare O3-type $NaNi_{0.5}Mn_xTi_{0.5-x}O_2$ were unsuccessful because of the presence of an NiO impurity, despite many efforts to alter the synthesis conditions (precursors, heating temperatures, heating atmosphere). The NiO impurity phase is common in Ni and Ti-containing O3-type materials. In fact, $NaNi_{0.5}Ti_{0.5}O_2$, one of the end members of $NaNi_{0.5}Mn_xTi_{0.5-x}O_2$, has been extensively studied yet its pure phase has never been reported. Instead, an NiO impurity was presented in all these previous reports [94,128,129]. This indicates that the stoichiometric ratio of Ni and Ti in the final O3-type material is actually less than the desired 1:1 ratio.

Delmas et al. reported that $NaNi_{0.5}Ti_{0.5}O_2$ without a NiO impurity could not be synthesized and, therefore, the composition $Na_{0.9}Ni_{0.45}Ti_{0.55}O_2$ was chosen to prevent the formation of the NiO phase [130]. Here, a similar strategy was employed to make phase pure materials with compositions close to $NaNi_{0.5}Mn_xTi_{0.5-x}O_2$. In this study, the stoichiometric ratios of Ni and (Ti + Mn) were optimized to be 0.45:0.55 in order to make a phase pure O3-type material. To balance charge and to maintain all the Ni as $Ni^{2+}$, and the Ti and Mn as $Ti^{4+}$ and $Mn^{4+}$, the Na content was reduced to 0.9. As a result the phase pure $Na_{0.9}Ni_{0.45}Mn_xTi_{0.55-x}O_2$ series could be synthesized. Here we present a study of the structure and electrochemistry of this phase pure series.

## 5.2 Experimental

Samples in the $Na_{0.9}Ni_{0.45}Mn_xTi_{0.55-x}O_2$ series were prepared by solid-state reactions. Stoichiometric amounts of $Na_2CO_3$ (BioXtra, ≥ 99.0% Sigma Aldrich), $MnO_2$ (ReagentPlus, 60 – 230 mesh, ≥99%, Sigma Aldrich), $TiO_2$ (puriss, 99 – 100.5%, Sigma-Aldrich) and NiO (325 mesh, 99% Alfa Aesar) were thoroughly mixed for 2 hours using a SPEX 8000 mill. An excess amount of 10% sodium carbonate was added to compensate sodium loss at high temperature. The ball to powder mass ratio is around 3:1 with ~6 grams of powder and four 7/16 inch diameter stainless steel balls. The mixed powders were then pressed into pellets and heated at 900 °C for 12 hours in dry air. The heated samples were immediately transferred into an Ar-filled glovebox to avoid moisture contamination. The pellets were then ground using a mortar and pestle and stored in the glovebox.

Electrodes were first prepared by mixing $Na_{0.9}Ni_{0.45}Mn_xTi_{0.55-x}O_2$, PVDF binder (HSV 900, KYNAR) and carbon black (super P, Imerys Graphite and Carbon) in a weight ratio of 8:1:1 with an appropriate amount of N-methyl-2-pyrrolidone (Sigma Aldrich, anhydrous 99.5%) with two 0.5 inch tungsten carbide balls in a Retsch PM200 rotary mill (100 rpm, 1 hour) to create a uniform slurry. The slurry was then coated onto aluminum foil with a coating bar having a ~0.010 cm gap and dried at 80 °C under vacuum overnight. Circular electrodes were punched from the resulting coatings. Half-cells were made in 2325-type coin cells in an Ar-filled glovebox. Na disks punched from thin foil (~0.3 mm) rolled from sodium ingot (Sigma Aldrich, ACS reagent grade) were used as counter/reference electrodes. Two Celgard 2300 and one blown microfiber separator (3M Company) were used as separators. 1 M $NaPF_6$ (Aldrich, 98%) in a solution of ethylene carbonate (EC), diethyl carbonate (DEC) and monofluoroethylene carbonate (FEC)

(volume ratio 3:6:1, all battery grade from BASF) was used as electrolyte. Cells were cycled with a Maccor Series 4000 Automated Test System (Maccor Inc., Tulsa OK). The ambient temperature during cell cycling was 30.0 °C (± 0.1 °C). For galvanostatic intermittent titration technique (GITT) measurements, cells were charged at a C/40 rate for 1 hour, followed by holding at open circuit for 5 hours between each charge.

XRD measurements were made with a Rigaku Ultima IV powder diffractometer equipped with a Cu Kα X-radiation source and a scintillation detector with a diffracted beam monochromator. XRD patterns were collected with samples under an argon atmosphere in a specially designed air-sensitive sample holder with an aluminized Mylar film window (DPM Solutions). For *ex situ* XRD studies, coin cells were prepared as described above, but were charged to 4.5 V once and then stopped. Electrodes for *ex situ* XRD measurements were scraped off the aluminum foil and rinsed with dimethyl carbonate (DMC, BASF). The recovered electrode was then transferred onto a zero-background silicon wafer and sealed in the gastight sample holder for the *ex situ* XRD measurements. Densities were measured using a Micromeritics AccuPyc II 1340 Pycnometer. Inductively coupled plasma optical emission spectrometry (ICP-OES) was used to determine the elemental composition of the products. Measurements were performed using a PerkinElmer Optima 8000. Each sample was dissolved in 2 mL aqua regia solution which was then diluted using 2% $HNO_3$ prior to measurements.

### 5.3 Results and Discussion

Figure 5.1 shows the X-ray diffraction (XRD) patterns of the synthesized $Na_{0.9}Ni_{0.45}Mn_xTi_{0.55-x}O_2$ ($0 \leq x \leq 0.55$) series of materials. No NiO impurity was present in

the product. All the materials were found to be phase pure with an O3 structure by XRD. It can be seen that as x increases from 0 to 0.55, the diffraction peaks shift to higher angles as a result of the contraction of the lattice. This is consistent with the smaller size of $Mn^{4+}$ compared to $Ti^{4+}$. Rietveld refinements were performed on all samples to obtain lattice parameters. Space group $R\bar{3}m$ ($\alpha$-$NaFeO_2$ structure) was used for all the refinements. Sodium atoms are accommodated at fixed 3b octahedral sites (0, 0, 0.5) and transition metal atoms (Ni, Mn, Ti) are placed at fixed 3a octahedral sites (0, 0, 0). Oxygen atoms were placed at 6c sites (0, 0, x) where x is ~0.26 and was allowed to vary during the fit. The lattice constants were also allowed to vary. Sodium content was fixed to be 0.9 during the refinement, and allowing sodium content to vary results in negligible improvement in Bragg-R factor. Cation mixing between $Na^+$ and transition metal ions was not considered in the refinement, due to the relatively large difference between the ionic radii of $Na^+$ and transition metal ions. An example of a refined pattern is shown in Figure 5.2 for the composition with x=1/6. Figure 5.3 shows the lattice parameters and the c/a ratio of the synthesized materials as determined by Rietveld refinement as a function of x. Best fit lines according to Vegard's law are also shown. Generally, as x is increased, both the *a* and *c* lattice constants decrease linearly. The decrease in *a* and *c* with x can be attributed to the smaller ionic radius of $Ti^{4+}$ compared to $Mn^{4+}$. The linearly changing cell parameters suggest that a solid solution is formed in the range of $0 \leq x \leq 0.55$ in $Na_{0.9}Ni_{0.45}Mn_xTi_{0.55-x}O_2$. The *c*/*a* ratios are all greater than 4.9, indicating a well-defined layered structure for the whole series. Data for $NaNi_{0.5}Mn_{0.5}O_2$ from Komaba et al. and $NaNi_{0.5}Ti_{0.5}O_2$ from Zhou et al. are also shown in Figure 5.3 for comparison [113,128]. It was found that lattice

parameters of the two end-members ($Na_{0.9}Ni_{0.45}Ti_{0.55}O_2$ and $Na_{0.9}Ni_{0.45}Mn_{0.55}O_2$) were very close to that of $NaNi_{0.5}Mn_{0.5}O_2$ and $NaNi_{0.5}Ti_{0.5}O_2$.

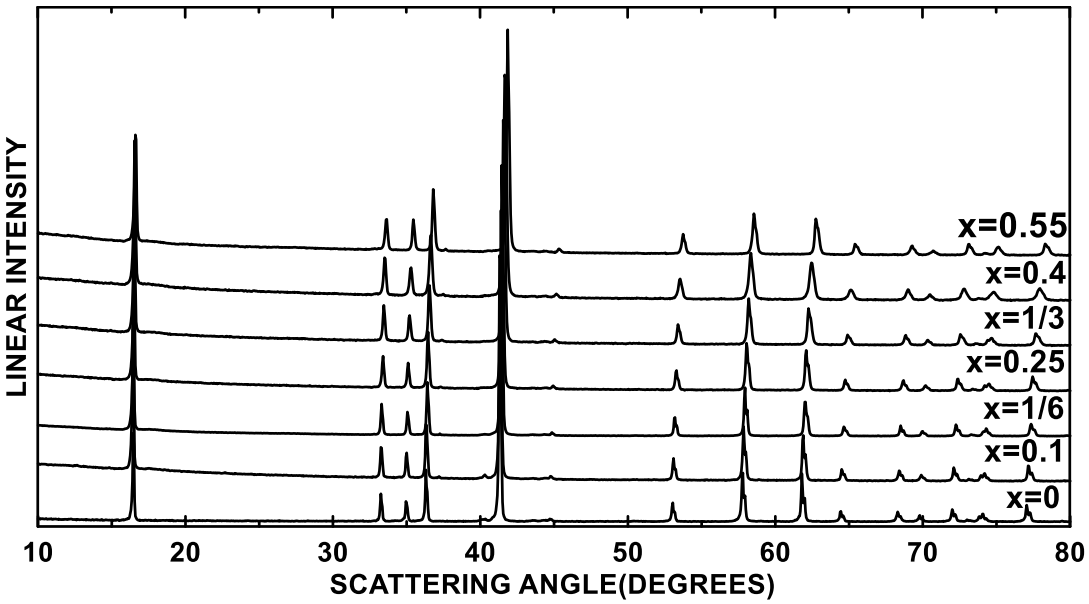


Figure 5.1 X-ray diffraction patterns for synthesized $Na_{0.9}Ni_{0.45}Mn_xTi_{0.55-x}O_2$ series.

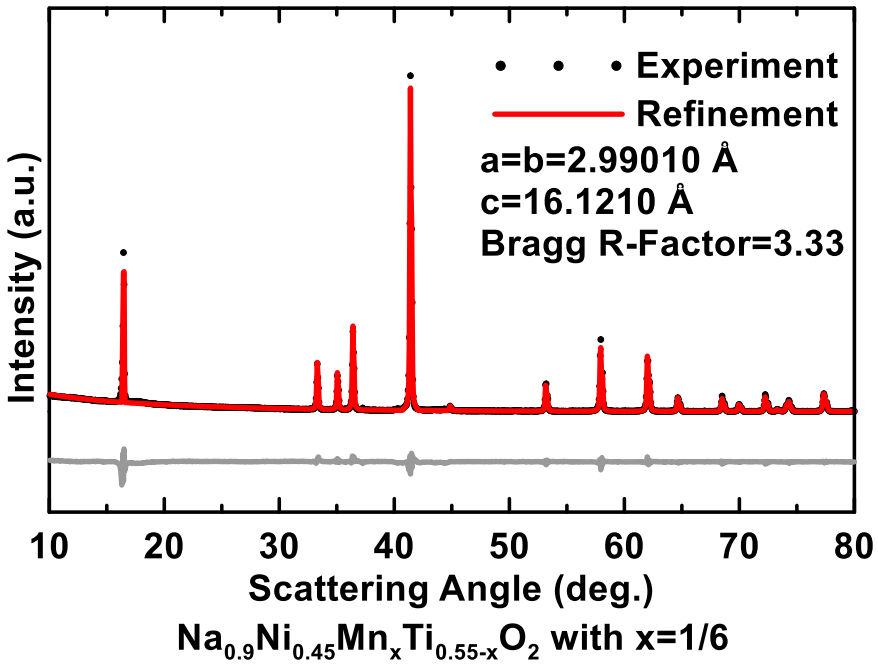


Figure 5.2 XRD pattern and Rietveld refinement of phase pure $Na_{0.9}Ni_{0.45}Mn_xTi_{0.55-x}O_2$ with x = 1/6. $R_{WP}$ = 14.04, GOF = 0.33.

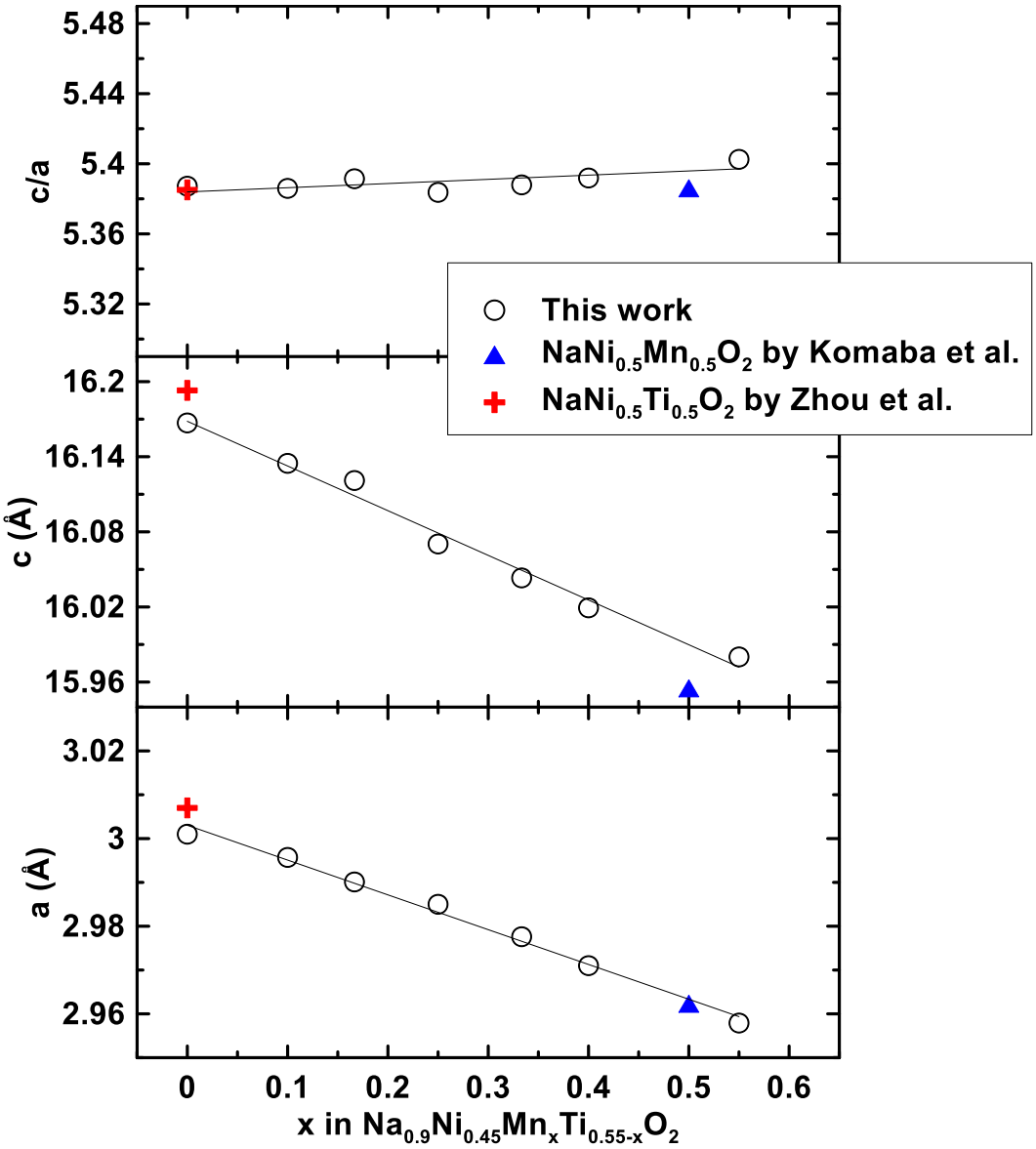


Figure 5.3 Changes in lattice parameters of $Na_{0.9}Ni_{0.45}Mn_xTi_{0.55-x}O_2$ samples.

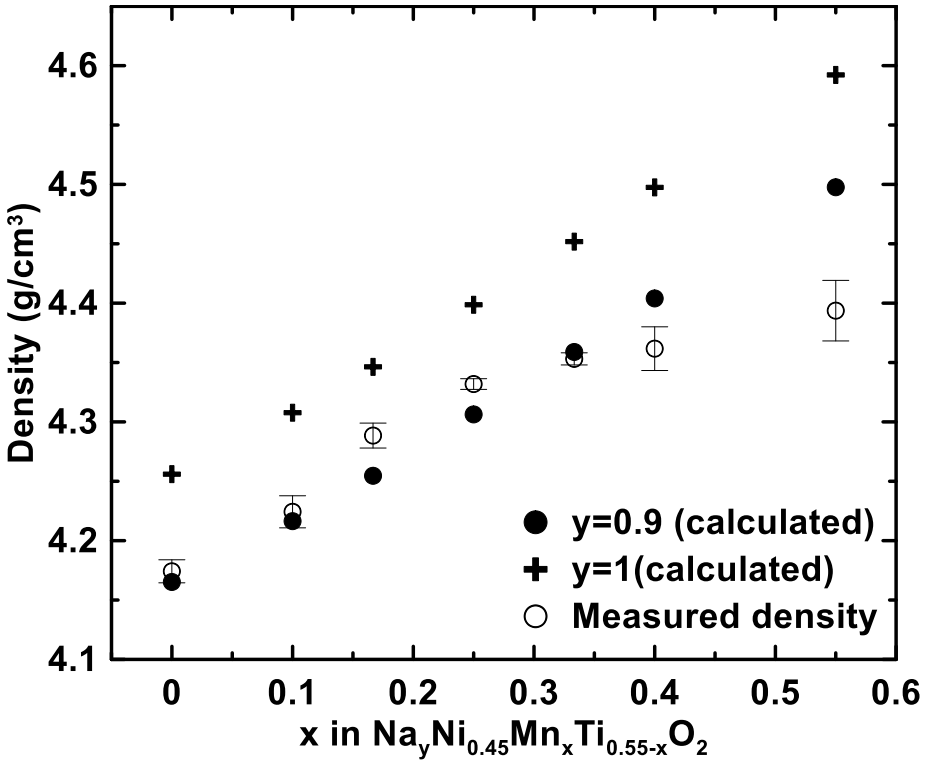


Figure 5.4 Calculated and measured densities of $Na_{0.9}Ni_{0.45}Mn_xTi_{0.55-x}O_2$ samples.

Figure 5.4 shows the calculated and measured densities of the synthesized $Na_yNi_{0.45}Mn_xTi_{0.55-x}O_2$ materials. The calculated densities, as determined from their lattice constants, vary linearly from 4.498 to 4.165 g/cm$^3$ as x decreases from 0.55 to 0 when y = 0.9. The calculated densities for y = 1 (no sodium vacancy) are also shown for comparison. Overall, a deliberate slight sodium vacancy was achieved, as can be seen by the lower measured densities than calculated densities for y = 1. The measured densities closely agree with the calculated densities for y = 0.9 at high Ti content ($x < 0.4$), while high Mn content results in measured densities lower than calculated densities. The lower measured densities indicate more sodium vacancies in the structure than anticipated, i.e. more sodium loss during synthesis. The reason for higher sodium loss at high Mn content is unknown.

Table 5.1 Target compositions compared with ICP measurement results (normalized to a total transition metal population of 1.000) of the $Na_{0.9}Ni_{0.45}Mn_xTi_{0.55-x}O_2$ series.

| x | | Na | Ni | Mn | Ti |
|---|---|---|---|---|---|
| 0 | Target | 0.90 | 0.45 | 0.00 | 0.55 |
| | ICP | 0.91 | 0.47 | 0.01 | 0.53 |
| 0.1 | Target | 0.90 | 0.45 | 0.10 | 0.45 |
| | ICP | 0.95 | 0.47 | 0.09 | 0.44 |
| 1/6 | Target | 0.90 | 0.45 | 0.17 | 0.38 |
| | ICP | 0.94 | 0.47 | 0.15 | 0.38 |
| 1/4 | Target | 0.90 | 0.45 | 0.25 | 0.30 |
| | ICP | 0.92 | 0.48 | 0.23 | 0.30 |
| 1/3 | Target | 0.90 | 0.45 | 0.33 | 0.22 |
| | ICP | 0.93 | 0.48 | 0.30 | 0.22 |
| 0.4 | Target | 0.90 | 0.45 | 0.40 | 0.15 |
| | ICP | 0.93 | 0.48 | 0.36 | 0.15 |
| 0.55 | Target | 0.90 | 0.45 | 0.55 | 0.00 |
| | ICP | 0.95 | 0.49 | 0.51 | 0.00 |

However, since the average desodiation voltage increases with increasing Ti content, as will be shown below, it may be inferred that the sodium binding energy increases with Ti content. This would tend to result in less Na loss in samples with high Ti contents during heating. Table 5.1 shows the elemental composition of the products determined by ICP-OES. The standard deviations are less than 3% for all the measurements. The ICP results are in good agreement with the anticipated atomic ratios for all the elements. An excess in Na content over stoichiometry as measured by ICP reflects the excess Na used during synthesis. It is believed that this Na exists as small amounts of $Na_2O$ or $Na_2CO_3$ in the sample, which are difficult to detect by XRD.

Figure 5.5 shows the voltage curves for $Na_{0.9}Ni_{0.45}Mn_xTi_{0.55-x}O_2$ vs. Na cells cycled between 1.5 V – 4.2 V for the first two cycles. For $Na_{0.9}Ni_{0.45}Mn_{0.55}O_2$, the voltage curve closely resembles that of $NaNi_{0.5}Mn_{0.5}O_2$, in accordance with their similar stoichiometry. A stepwise voltage profile with multiple voltage plateaus is observed for this composition due to the occurrence of phase transitions/vacancy ordering (O3→ O'3→P3→P'3→P"3) [113]. The first discharge capacity is ~190 mAh/g and a high coulombic efficiency of ~92.3% is obtained. The irreversible capacity is only ~15 mAh/g, smaller than reported previously for $NaNi_{0.5}Mn_{0.5}O_2$ (> 50 mAh/g) [113]. The improved reversibility may be a result of the addition of FEC to the electrolyte. Additionally, the slight sodium deficiency in this material may contribute to the high coulombic efficiency. It is well known that P2-type materials with ~1/3 sodium vacancies can have a first cycle coulombic efficiency higher than 100% because more sodium could be inserted back into the structure than was removed during the first desodation half-cycle [131]. Therefore, a small amount of sodium

vacancies, as confirmed by the density measurements discussed above, could increase the first cycle coulombic efficiency.

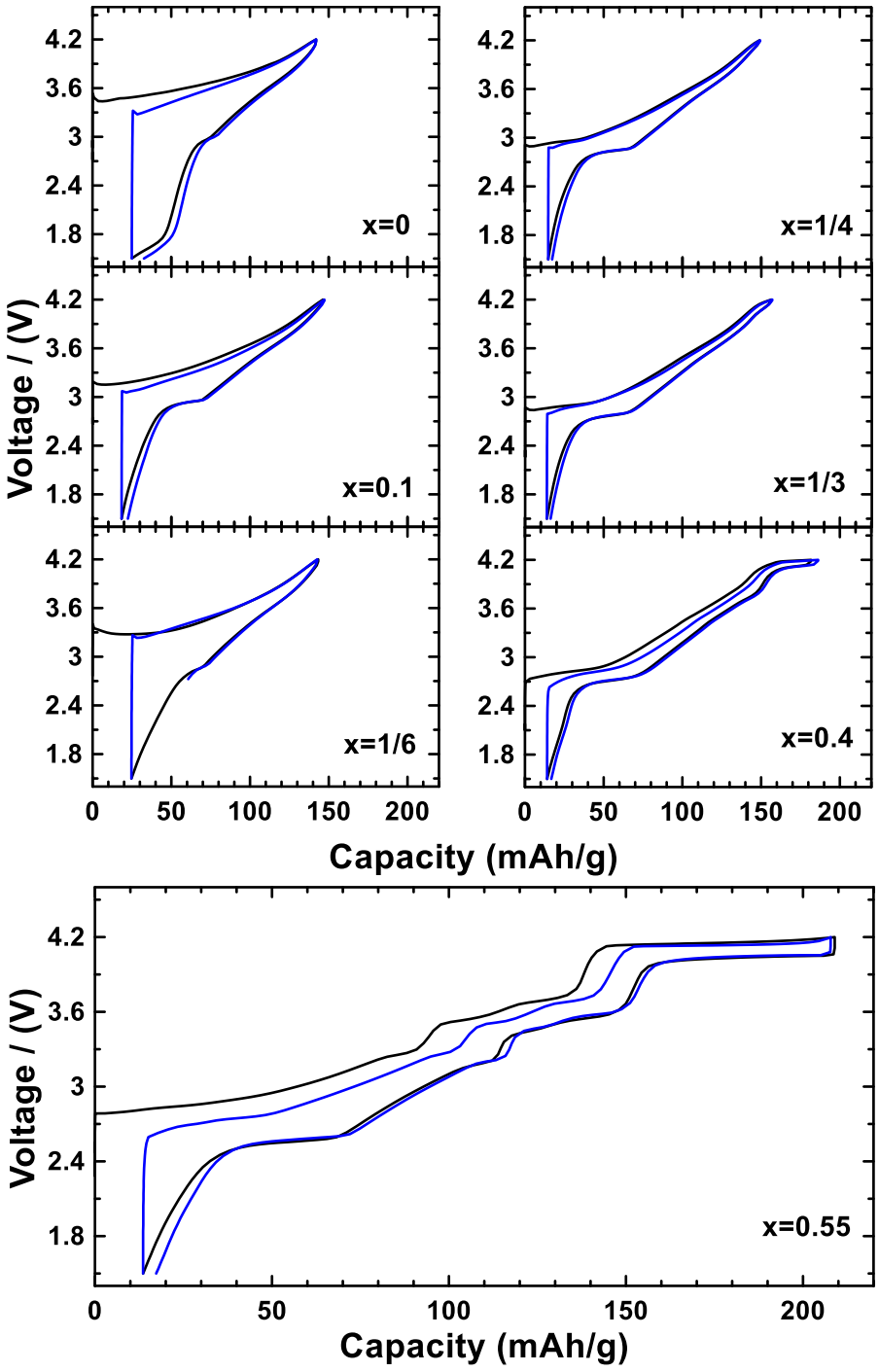


Figure 5.5 Voltage curves of $Na_{0.9}Ni_{0.45}Mn_xTi_{0.55-x}O_2$ at C/20 current density between 1.5 V and 4.2 V.

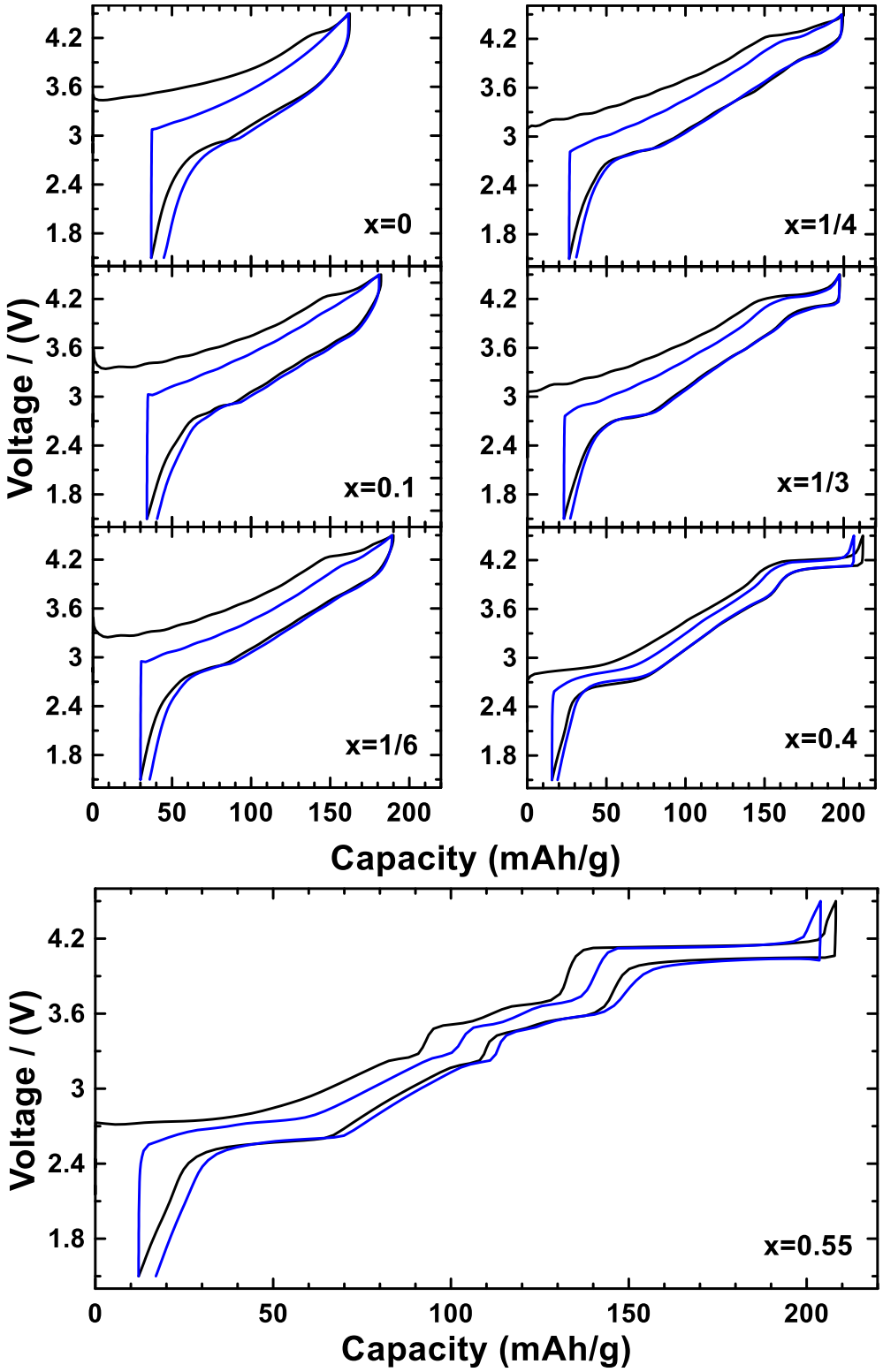


Figure 5.6 Voltage curves of $Na_{0.9}Ni_{0.45}Mn_xTi_{0.55-x}O_2$ at C/20 current density between 1.5 V and 4.5 V.

For the $Na_{0.9}Ni_{0.45}Mn_xTi_{0.55-x}O_2$ samples with $x < 0.55$, the appearance of plateaus in the voltage profile was increasingly suppressed by the presence of Ti. This behavior is similar to what has been observed for the $Na_{2/3}Ni_{1/3}Mn_{2/3-x}Ti_xO_2$ series [110]. Also similar to the $Na_{2/3}Ni_{1/3}Mn_{2/3-x}Ti_xO_2$ series, the addition of Ti causes a decrease in both charge/discharge capacity. As can be seen in Figure 5.5, the capacity continuously decreases with the increasing Ti content. This is because the desodiation voltage is increasing and the upper part of the voltage curve gradually becomes inaccessible at this voltage limit (1.5 – 4.2 V) as Ti is introduced. The charge voltage in the second cycle is slightly lower than the charge voltage in the first cycle, while the discharge voltage remains the same during successive cycles, indicating that the materials' cycling characteristics have become stabilized after first charge. This is illustrated in Figure 5.7(a), which shows the average charge and discharge voltage plotted as a function of x. Apparently, the addition of Ti causes increased voltage polarization in this system. It seems that higher Ti contents results in a decrease in discharge voltage and an increase in charge voltage. However, since the average charge/discharge voltage is strongly influenced by the plateau at ~4.2 V, the effect of Ti on average charge/discharge voltage is actually more complicated, as will be discussed later.

In order to increase cycling capacity, the $Na_{0.9}Ni_{0.45}Mn_xTi_{0.55-x}O_2$ series were also cycled between 1.5 V – 4.5 V. Figure 5.6 also shows the voltage curves of first two cycles for $Na_{0.9}Ni_{0.45}Mn_xTi_{0.55-x}O_2$ vs. Na cells cycled between 1.5 V – 4.5 V. When the cutoff voltages were increased to 4.5 V, it can be seen that even though an improved reversible capacity is observed, the voltage hysteresis and irreversible capacity are also increased significantly for samples with $x \leq 1/3$, compared to their counterparts cycled between 1.5

V and 4.2 V. The average charge/discharge voltages are plotted in Figure 5.7 (b). Again, a similar trend regarding average voltage vs. composition is observed. Materials with higher Mn content have higher average discharge voltages. We speculate that this behavior could arise as an artifact of the 4.2 V plateau. Figure 5.8 shows the charge and discharge curve of all samples when cycled between 1.5 V and 4.5 V. It is clear that the addition of Ti to $Na_{0.9}Ni_{0.45}Mn_xTi_{0.55-x}O_2$ series causes a shift in the desodiation voltage curve toward higher voltages, resulting in a drastic lowering of the capacity above 4.2 V. To exclude the effect of the 4.2 V plateau, the average voltage were calculated in the voltage range of 1.5 V – 4.0 V for charge and 1.5 V – 3.8 V for discharge. Figure 5.7 (c) shows the calculated average voltage vs. composition. Here, an opposite trend for the discharge voltage vs. composition was observed, i.e., both the average charge and discharge voltages were found to increases with the increase of Ti content at a given voltage range. Therefore, the observed decreasing average voltage with increasing Ti content does not reflect a shift in the discharge voltage curve towards negative voltages, instead it is an artifact of the disappearance of the 4.2 V plateau.

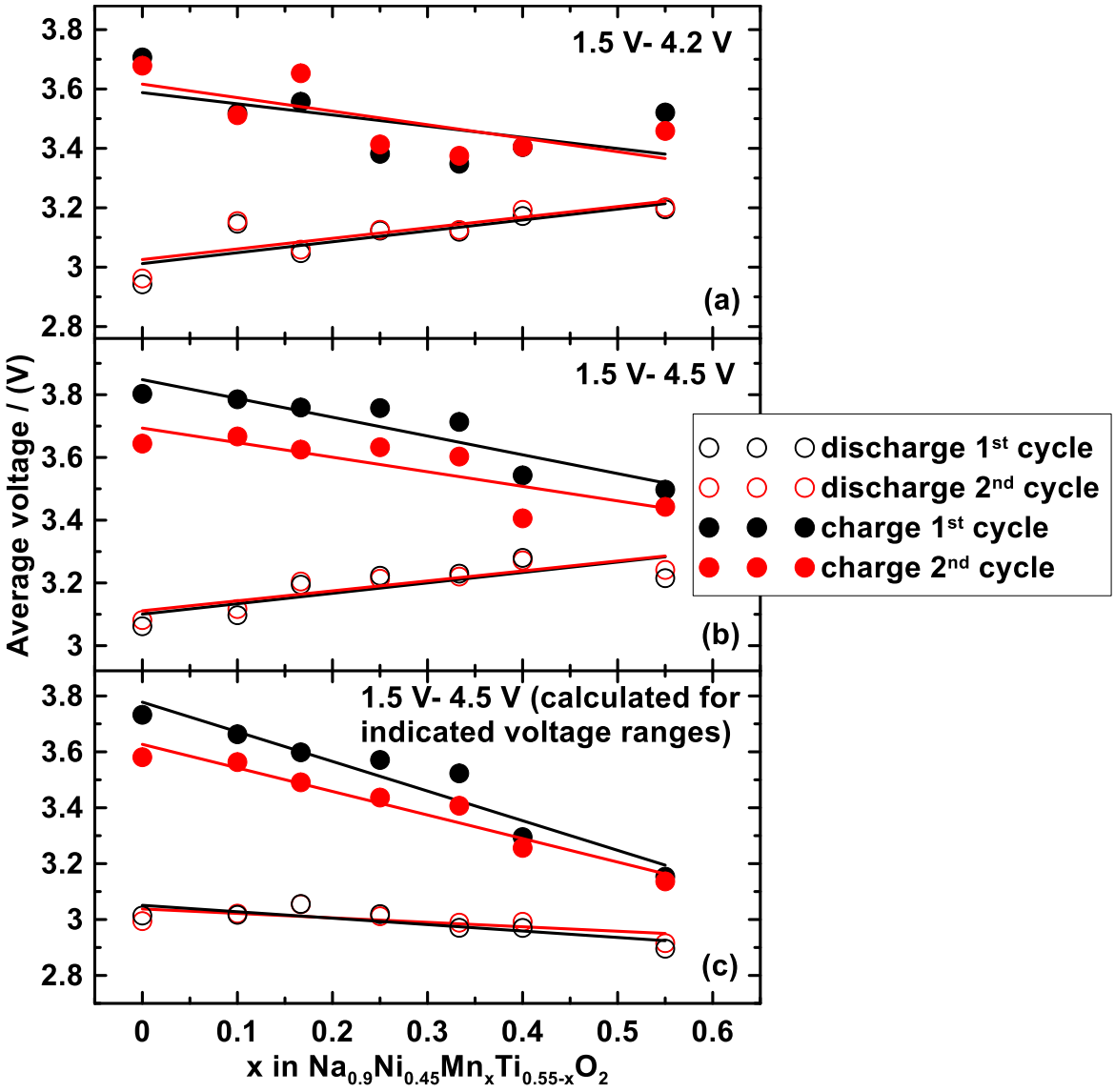


Figure 5.7 Average charging and discharging voltage versus x in $Na_{0.9}Ni_{0.45}Mn_xTi_{0.55-x}O_2$ (a) Cells cycled between 1.5 V – 4.2 V (b) Cells cycled between 1.5 V – 4.5 V (c) Cells cycled between 1.5 V – 4.5 V, average voltages were calculated in the voltage range of 1.5 V – 4.0 V for charge and 1.5 V – 3.8 V for discharge.

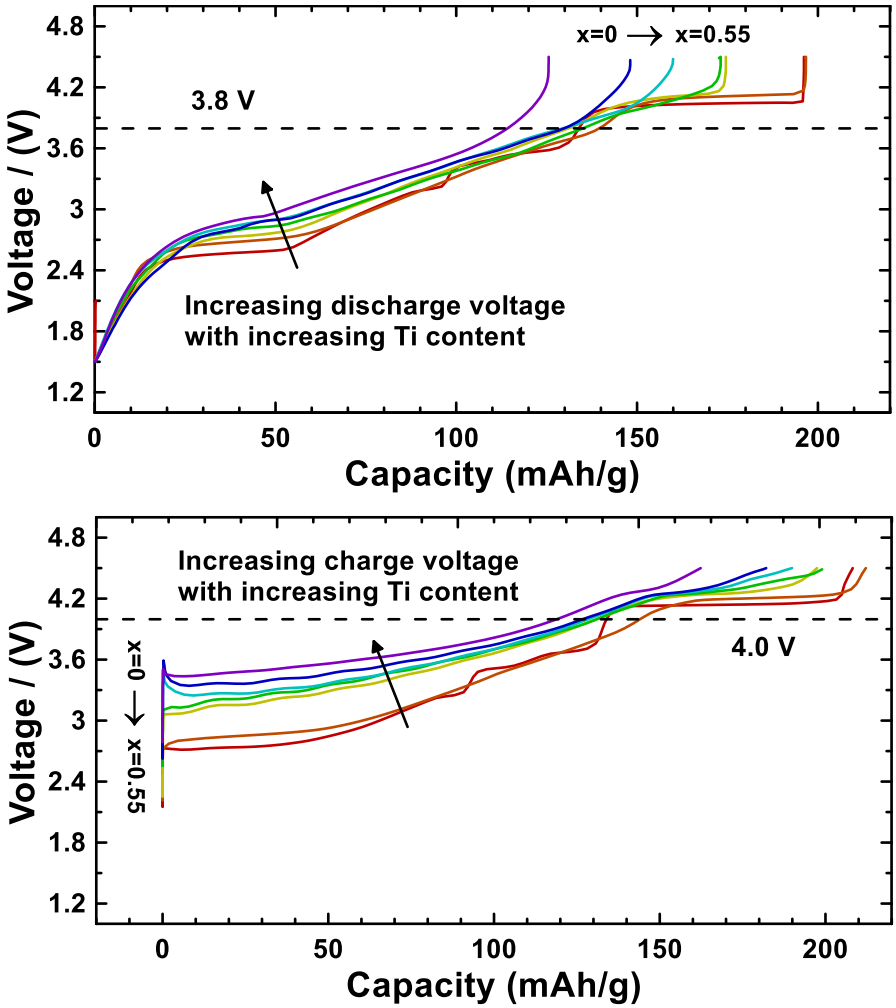


Figure 5.8 Charge (bottom) and discharge (top) curves for $Na_{0.9}Ni_{0.45}Mn_xTi_{0.55-x}O_2$.

Figure 5.9(a) shows the discharge capacities of $Na_{0.9}Ni_{0.45}Mn_xTi_{0.55-x}O_2$ in the voltage range of 1.5 V – 4.2 V at different rates. There is no general trend in the rate capability. The lowest rate capability is exhibited by the x = 0 and x = 0.55 samples. The poor rate performance of the $Na_{0.9}Ni_{0.45}Mn_{0.55}O_2$ sample is an artifact of the disappearance of the 4.2 V plateau at high rate. To better compare the rate performance of these materials, Figure 9(b) shows the measured capacity below 3.8 V for the same cells. In this voltage range, all samples have good rate performance, excepting the x = 0 composition, which has a rapid capacity drop with increasing rate. Apparently, titanium substitution in

$Na_{0.9}Ni_{0.45}Mn_{0.55}O_2$ has substantially improved its rate capability. However, when the titanium content becomes very high (x= 0), $Na^+$ diffusion is slow. The poor $Na^+$ diffusion in the x = 0 sample is also coincident with the very high hysteresis in its voltage curve, shown in in Figure 6. This is consistent with the results of, Lai et al., who found that P2-type Na-Ni-Mn-Ti layered oxides with low titanium content ($Na_{2/3}Ni_{1/3}Mn_{1/3}Ti_{1/3}O_2$) had a substantially higher diffusion coefficient than materials with a high titanium content ($Na_{2/3}Ni_{1/3}Ti_{2/3}O_2$) [132].

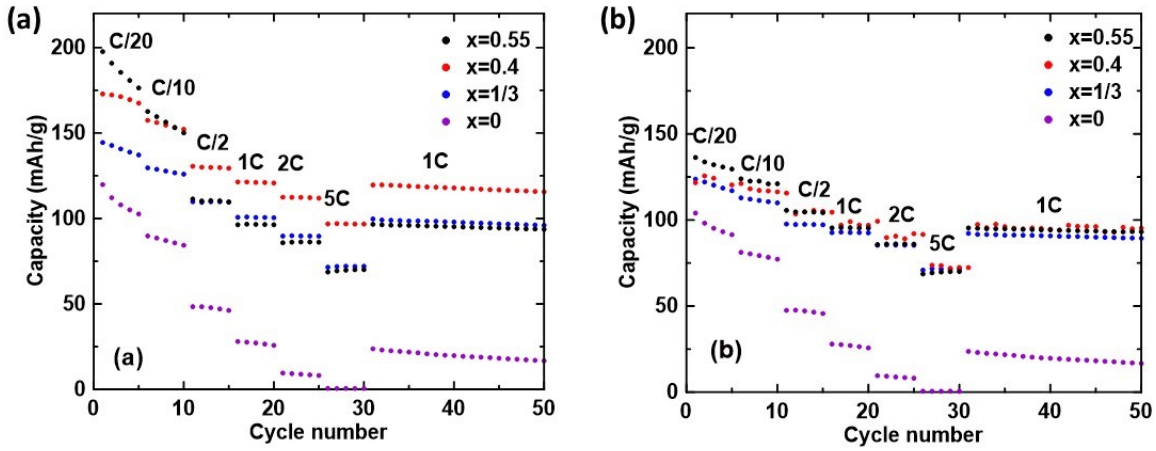


Figure 5.9 (a) Discharge capacity of $Na_{0.9}Ni_{0.45}Mn_xTi_{0.55-x}O_2$ cells cycled in the range of 1.5 V – 4.2 V.(b) $Na_{0.9}Ni_{0.45}Mn_xTi_{0.55-x}O_2$ cells cycled in the range of 1.5 V – 4.2 V, discharge capacities were calculated only in the voltage range of 1.5 V – 3.8 V.

To determine the effect of titanium substitution on $Na^+$ diffusion kinetics, GITT measurements were performed. Diffusion coefficients ($D_{Na}$) of $Na_{0.9}Ni_{0.45}Mn_{0.55}O_2$ and $Na_{0.9}Ni_{0.45}Mn_{0.4}Ti_{0.15}O_2$ calculated from the GITT measurements are shown in Figure 5.10. It should be noted that during two phase regions, the calculation of diffusion coefficients is realized by the transport of phase front. Below 3.2 V, the sodium diffusion constants of both materials are similar. In this region their voltage curves are similar also. Above 3.2 V, $D_{Na}$ for $Na_{0.9}Ni_{0.45}Mn_{0.55}O_2$ becomes erratic. Above this voltage, multiple plateaus are also

observed in the $Na_{0.9}Ni_{0.45}Mn_{0.55}O_2$ voltage curve (as shown in Figure 5.6). The poor rate capability of $Na_{0.9}Ni_{0.45}Mn_{0.55}O_2$ might be attributed to low diffusion coefficients encountered during some of the phase transitions that are associated with the plateaus in the voltage curve. In contrast, $D_{Na}$ for $Na_{0.9}Ni_{0.45}Mn_{0.4}Ti_{0.15}O_2$ remains stable above 3.2 V, and the voltage curve of this material has few features. Both these observations imply that phase transitions have been suppressed. At voltages above 4.0 V, $D_{Na}$ decreases significantly for both materials. In this region the voltage curves of both materials exhibit a plateau, indicating a structural change that is accompanied by slower $Na^+$ diffusion kinetics. Overall, these phenomena indicate more structural stability for $Na_{0.9}Ni_{0.45}Mn_{0.4}Ti_{0.15}O_2$ than $Na_{0.9}Ni_{0.45}Mn_{0.55}O_2$. The diffusion length calculated from $D_{Na}$ is between 0.6 – 6 μm, which is typical for materials synthesized using solid state reaction.

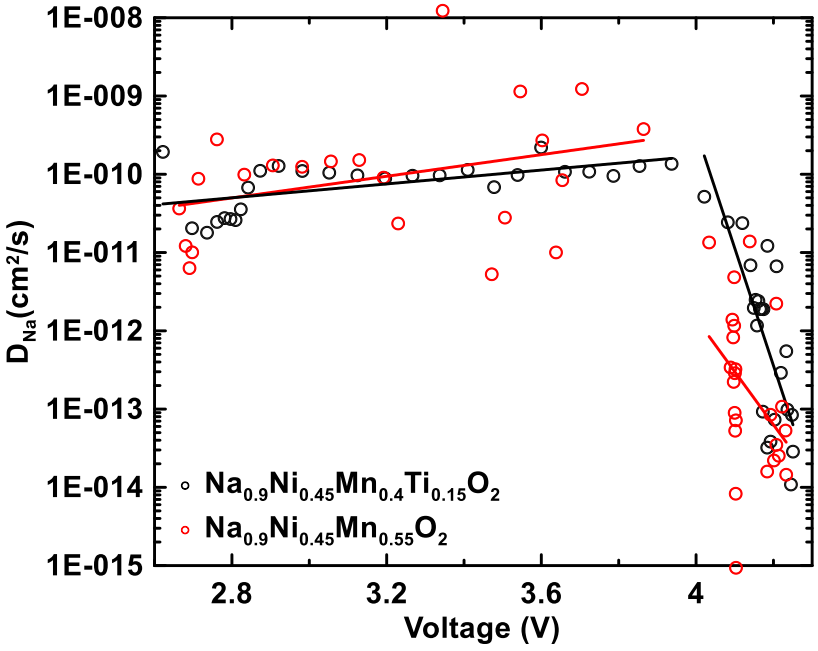


Figure 5.10 Sodium ion diffusion coefficients of $Na_{0.9}Ni_{0.45}Mn_xTi_{0.55-x}O_2$ (x = 0.55, x = 0.4) at different voltages calculated from GITT measurements.

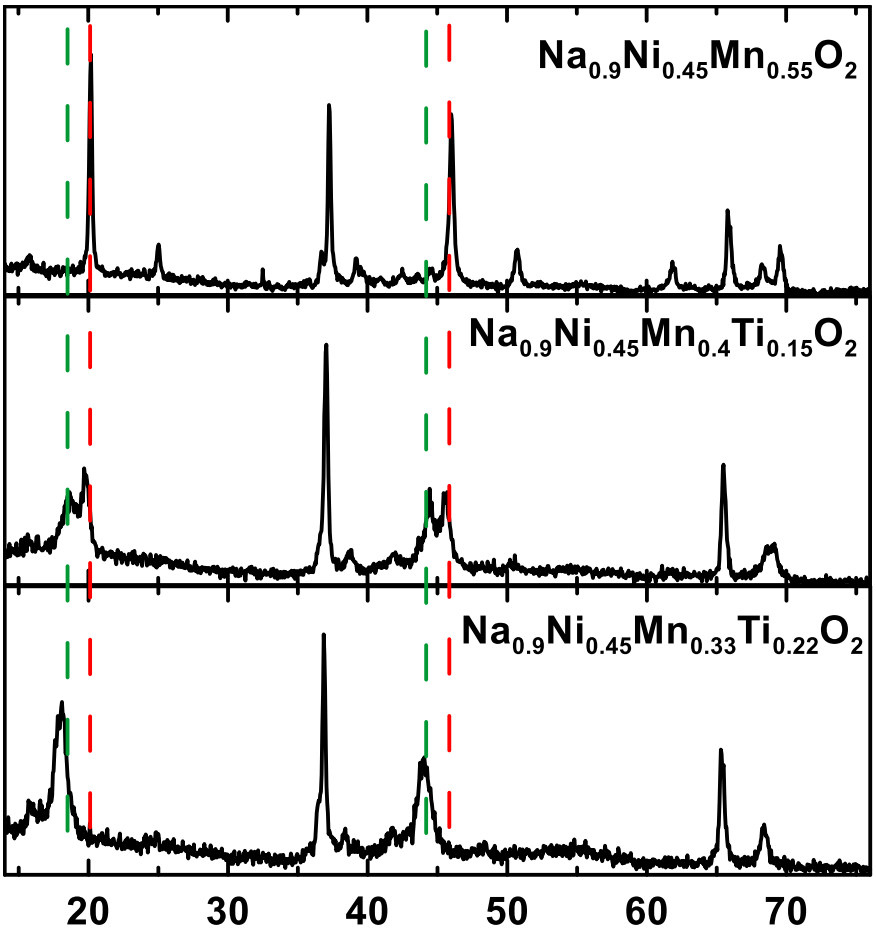


Figure 5.11 *Ex situ* XRD patterns of $Na_{0.9}Ni_{0.45}Mn_xTi_{0.55-x}O_2$ (x = 0.55, x = 0.4, x = 0.33) after being charged to 4.5 V.

Structural changes during cycling were investigated by *ex situ* XRD. Figure 5.11 shows the *ex situ* XRD patterns of $Na_{0.9}Ni_{0.45}Mn_{0.55}O_2$, $Na_{0.9}Ni_{0.45}Mn_{0.4}Ti_{0.15}O_2$, and $Na_{0.9}Ni_{0.45}Mn_{0.33}Ti_{0.22}O_2$ after being charged to 4.5 V. For $Na_{0.9}Ni_{0.45}Mn_{0.55}O_2$, both the 003 peak (~20°) and 104 peak (~45°) shift significantly to higher angles from their initial positions (~16° and ~41°), indicating a structural contraction after full desodiation. This structural contraction might be the reason for the low $D_{Na}$ at high voltages, as higher sodium diffusion barrier can be expected when diffusion path becomes less spacious. In contrast, increased titanium content results in samples with less structural contraction after being

charged to 4.5 V. Therefore, increasing the titanium content suppresses structural change during cycling. Among all the $Na_{0.9}Ni_{0.45}Mn_xTi_{0.55-x}O_2$ samples, $Na_{0.9}Ni_{0.45}Mn_{0.4}Ti_{0.15}O_2$ has the most attractive characteristics: a high capacity, low hysteresis, good rate capability, and low irreversible capacity. Therefore $Na_{0.9}Ni_{0.45}Mn_{0.4}Ti_{0.15}O_2$ is discussed in detail below.

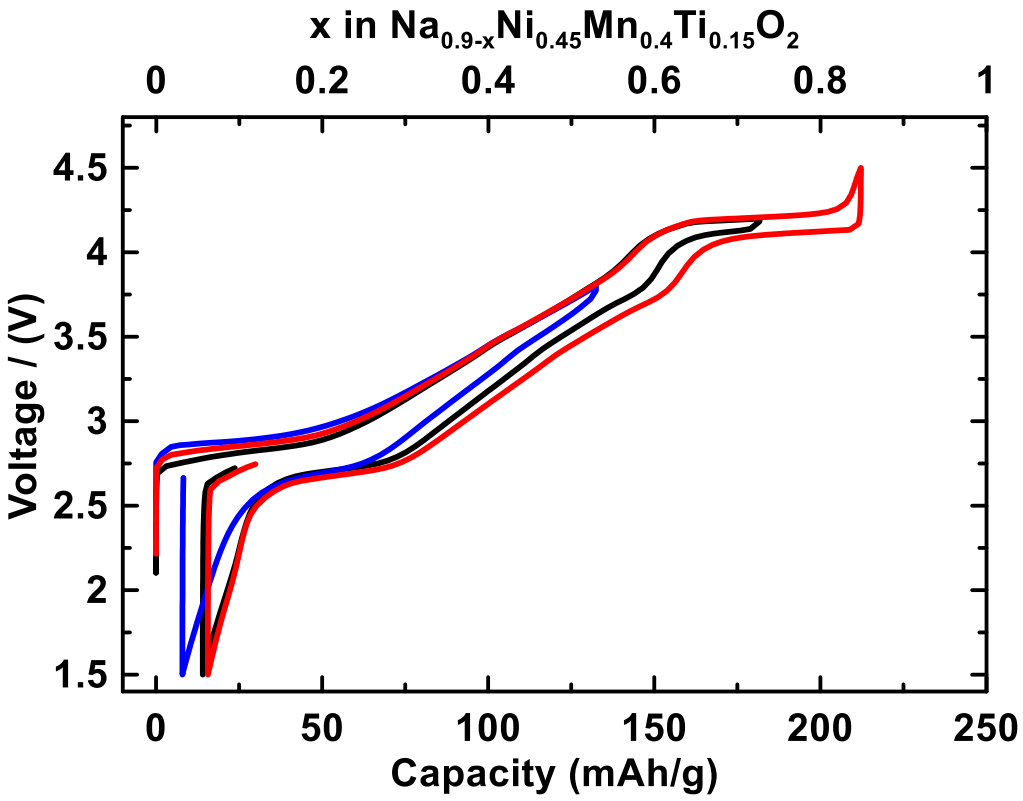


Figure 5.12 First cycle voltage profile of $Na_{0.9}Ni_{0.45}Mn_xTi_{0.55-x}O_2$ with x = 0.4 between 1.5 V and various cutoff voltages (3.8 V, 4.2 V, 4.5 V) using C/20 current density.

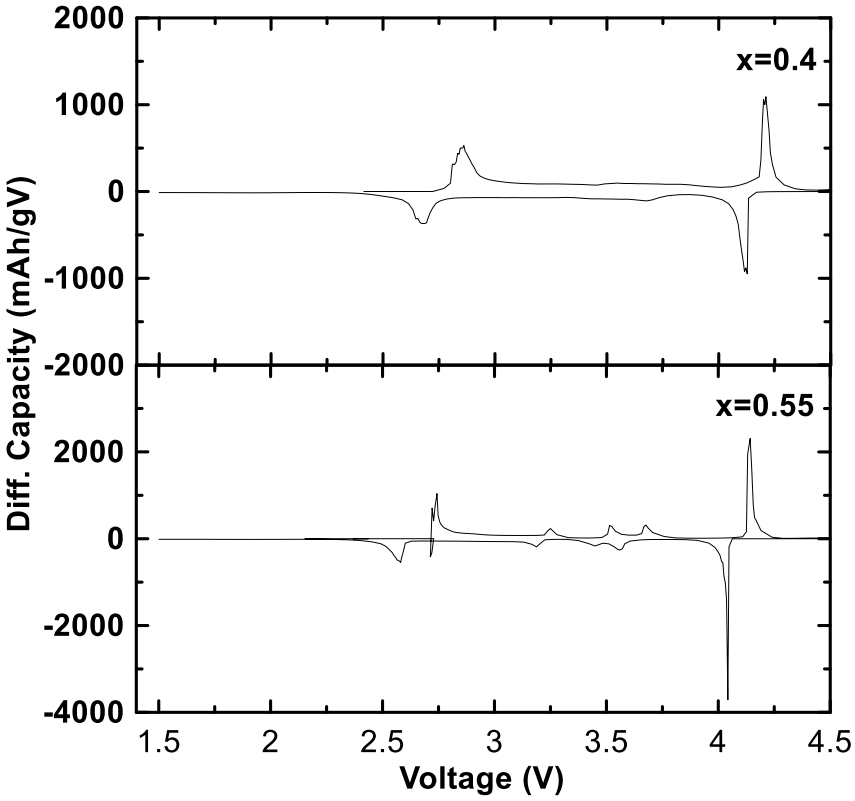


Figure 5.13 Differential capacity (dQ/dV) as a function of voltage for the first cycles for cells cycled between 1.5 V and 4.5 V.

For the sample with x = 0.4 ($Na_{0.9}Ni_{0.45}Mn_{0.4}Ti_{0.15}O_2$), first cycle voltage curves for cycling between 1.5 V and at different cutoff voltages of 3.8 V, 4.2 V and 4.5 V are shown in Figure 5.12. This resulted in first charge/discharge capacities of 132.4/124.5 mAh/g, 181.7/167.6 mAh/g, and 212.2/196.6 mAh/g, respectively. The first cycle coulombic efficiency is 94.0%, 92.2% and 92.6%, respectively. All the voltage curves are characterized with low voltage hysteresis and small irreversible capacities, even when the cell is cycled to 4.5 V. Upon charging to 4.5 V, the 4.2 V plateau is fully reversible and associated with small hysteresis. Compared to $Na_{0.9}Ni_{0.45}Mn_{0.55}O_2$, $Na_{0.9}Ni_{0.45}Mn_{0.4}Ti_{0.15}O_2$ is characterized with smoother sloping voltage curves. Assuming the starting material has an ideal composition corresponding to $Na_{0.9}Ni_{0.45}Mn_{0.4}Ti_{0.15}O_2$,

the charge capacity corresponds to the deintercalation of ~0.85 Na at 4.5 V, indicating the removal of almost all the sodium in the structure. For O3-type materials, removing such large amount of Na usually results in increased hysteresis and irreversible capacity [113]. However, such phenomenon is not observed in $Na_{0.9}Ni_{0.45}Mn_{0.4}Ti_{0.15}O_2$, indicating the good structure stability upon sodium extraction/insertion. Figure 5.13 shows the differential capacity (dQ/dV) as a function of voltage for $Na_{0.9}Ni_{0.45}Mn_{0.55}O_2$ and $Na_{0.9}Ni_{0.45}Mn_{0.4}Ti_{0.15}O_2$. The differential capacities are completely reversible for both materials. For $Na_{0.9}Ni_{0.45}Mn_{0.55}O_2$, several peaks in dQ/dV curve can be observed, corresponding to the plateaus in the capacity-voltage curve. The voltage curve and differential capacity curves are similar to previous report by Komaba et al. [113]. According to Komaba et al., the four peaks in the differential capacity are associated with the O3-O'3, O'3-P3, P3-P'3, and P'3-P"3 2-phase regions, in order of ascending voltage [113]. The three peaks at ~3.25 V, ~3.5 V and ~3.65 V of $Na_{0.9}Ni_{0.45}Mn_{0.55}O_2$ are not observable in the dQ/dV curve of $Na_{0.9}Ni_{0.45}Mn_{0.4}Ti_{0.15}O_2$. The two main peaks at ~2.75 V and ~4.2 V also became broader for $Na_{0.9}Ni_{0.45}Mn_{0.4}Ti_{0.15}O_2$, as can be seen from their intensities (~1000 mAh/gV, compared to ~2000 mAh/gV). These observations also imply the suppression of phase transitions.

The cycling performance of $Na_{0.9}Ni_{0.45}Mn_{0.4}Ti_{0.15}O_2$ at different cutoff voltages is shown in Figure 5.14. Figure 5.15 shows a comparison of discharge capacity versus cycle number for $Na_{0.9}Ni_{0.45}Mn_{0.4}Ti_{0.15}O_2$ and $Na_{0.9}Ni_{0.45}Mn_{0.55}O_2$ cycled between 1.5 V – 4.5 V. $Na_{0.9}Ni_{0.45}Mn_{0.4}Ti_{0.15}O_2$ retains 88% and 81% of its initial capacity after 15 cycles when it is cycled between 1.5 V – 4.2 V and 1.5 V – 4.5 V, respectively. When the cycling voltage range was narrowed to 1.5 V – 3.8 V, the capacity retention increased to 85% after 25

cycles. For comparison, the capacity of $Na_{0.9}Ni_{0.45}Mn_{0.55}O_2$ cycled between 1.5 V and 4.5 V fades to 71% after only 15 cycles. As expected, the sample with Ti delivers a better cyclability than Ti-free sample. Cycling performance of $Na_{0.9}Ni_{0.45}Mn_xTi_{0.55-x}O_2$ in the range of 1.5 V – 4.2 V are shown in Figure 5.16. For the $Na_{0.9}Ni_{0.45}Mn_xTi_{0.55-x}O_2$ series with $0 < x < 0.55$, all compositions had capacities greater than 100 mAh/g and capacity retentions greater than 80% for 20 cycles, except $x = 1/6$.

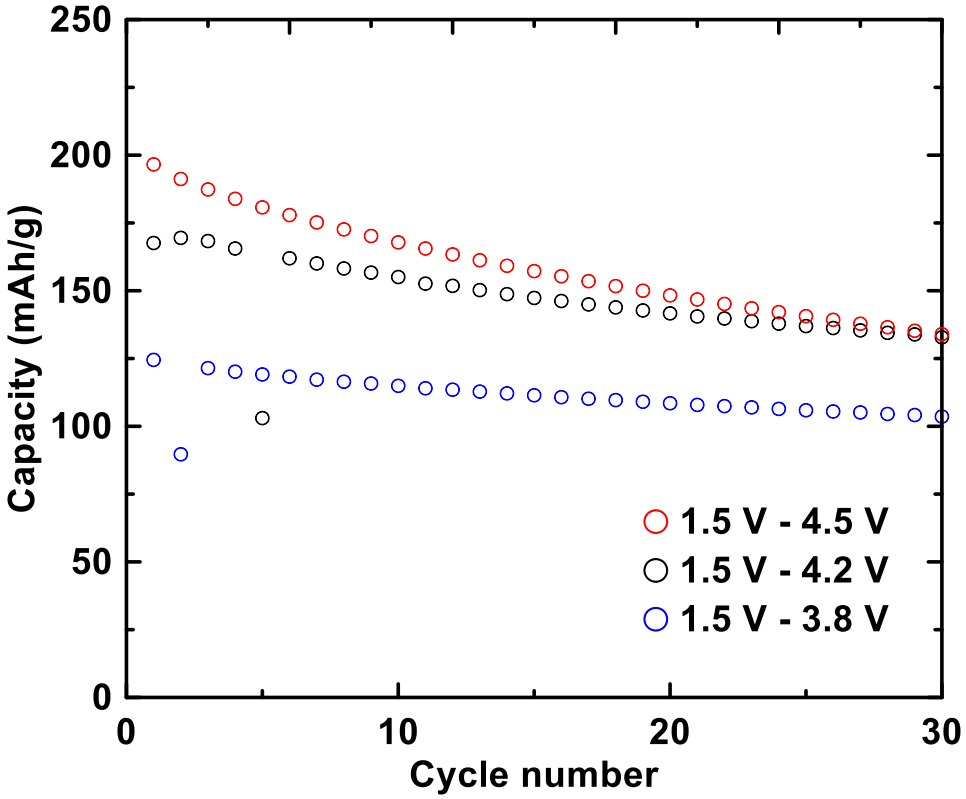


Figure 5.14 Discharge capacity versus cycle number for $Na_{0.9}Ni_{0.45}Mn_{0.4}Ti_{0.15}O_2$ with indicated voltage ranges.

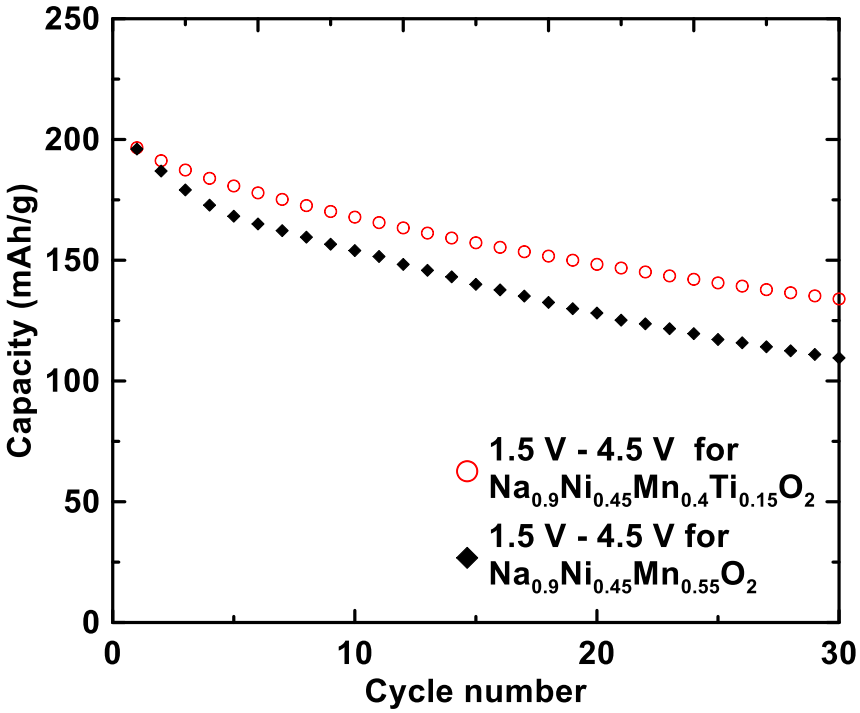


Figure 5.15 Comparison of discharge capacity versus cycle number for $Na_{0.9}Ni_{0.45}Mn_{0.4}Ti_{0.15}O_2$ and $Na_{0.9}Ni_{0.45}Mn_{0.55}O_2$.

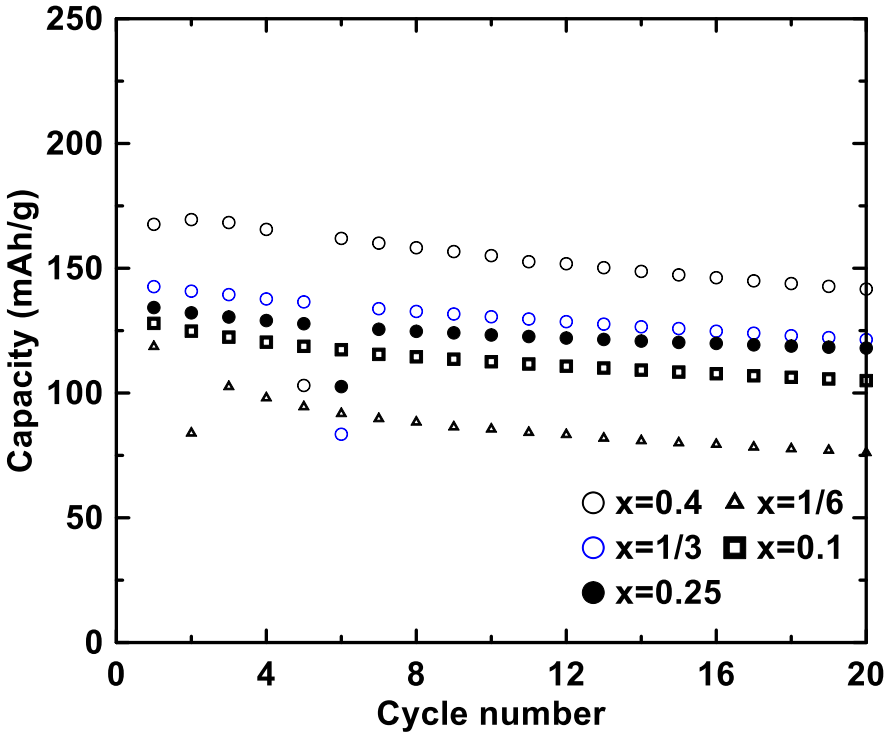


Figure 5.16 Discharge capacity versus cycle number in the range of 1.5 V – 4.2 V.

Table 5.2 Comparison of reversible capacity, average discharge voltage (vs. Na), calculated density and energy density for the $Na_{0.9}Ni_{0.45}Mn_xTi_{0.55-x}O_2$ series.

| x | First discharge capacity / (mAh/g) | Average discharge voltage / (V) | Density / ($g/cm^3$) | energy density / (Wh/kg) | energy density / (Wh/L) |
|---|---|---|---|---|---|
| 0 | 117.0 (4.2V) | 2.94 | 4.1742 | 344.3 | 1437.2 |
| | 125.4 (4.5V) | 3.08 | | 386.5 | 1613.5 |
| 0.1 | 127.9 (4.2V) | 3.15 | 4.2243 | 402.5 | 1700.1 |
| | 148.0 (4.5V) | 3.12 | | 461.3 | 1948.6 |
| 1/6 | 118.6 (4.2V) | 3.02 | 4.2885 | 361.5 | 1550.1 |
| | 159.8 (4.5V) | 3.20 | | 512.2 | 2196.7 |
| 0.25 | 134.2 (4.2V) | 3.12 | 4.3319 | 419.2 | 1816.1 |
| | 173.0 (4.5V) | 3.21 | | 555.9 | 2408.1 |
| 1/3 | 142.6 (4.2V) | 3.12 | 4.3531 | 444.9 | 1936.6 |
| | 174.4 (4.5V) | 3.22 | | 561.8 | 2445.4 |
| 0.4 | 167.6 (4.2V) | 3.17 | 4.3617 | 531.6 | 2318.9 |
| | 196.6 (4.5V) | 3.27 | | 643.2 | 2805.6 |
| 0.55 | 195.4 (4.2V) | 3.19 | 4.3937 | 624.2 | 2742.5 |
| | 196.0 (4.5V) | 3.24 | | 635.5 | 2792.0 |

The measured average voltage, discharge capacity, calculated density and energy density of the $Na_{0.9}Ni_{0.45}Mn_xTi_{0.55-x}O_2$ series are shown in Table 5.2. Generally, when Mn is decreased and Ti increased, the energy density decreases. $Na_{0.9}Ni_{0.45}Mn_{0.4}Ti_{0.15}O_2$ has a high density as well as high energy density. When cycled between 1.5 V – 4.5 V, it has an energy density of 643 Wh/kg or 2805 Wh/L, which is amongst the highest reported energy densities for Na-ion battery positive electrodes.

## 5.4 Conclusions

Phase pure layered oxides $Na_{0.9}Ni_{0.45}Mn_xTi_{0.55-x}O_2$ with O3 structure were synthesized via solid state reactions and tested in electrochemical cell. All compositions have high reversible capacities (>100 mAh/g) when cycled between 1.5 V to 4.2 V. Ti can effectively suppress the stepwise voltage profile and improve the capacity retention. At a given voltage range, the addition of Ti increases both charge and discharge average voltage. $Na/Na_{0.9}Ni_{0.45}Mn_{0.4}Ti_{0.15}O_2$ cell delivers 640 Wh/kg or 2832 Wh/L energy density in a voltage range of 1.5 – 4.5 V. It was found that even though higher Ti contents can smooth the voltage curve further, reversible capacities were also reduced and hysteresis were increased. Therefore, Ti could only be used in small amounts to achieve these benefits.

# CHAPTER 6 EFFECT OF CONTROLLED ATMOSPHERE-STORAGE AND ETHANOL RINSING ON $NaNi_{0.5}Mn_{0.5}O_2$ [4]

## 6.1 Introduction

One of the problems with many sodium-ion cathode materials, including $NaNi_{0.5}Mn_{0.5}O_2$, that hinders their commercial application is air-sensitivity [13]. Air-sensitive materials require special manufacturing conditions, which inevitably increases cost. As a targeted application of sodium ion batteries is large scale grid energy storage system, cost is a paramount factor. Kubota et al. showed that slurries made from $NaNi_{0.5}Mn_{0.5}O_2$ in air contain agglomerated particles, which also agrees with our experience with many other sodium cathode materials [13]. Kubota et al. proposed that such phenomenon is due to the NaOH contamination in the slurry. Nazar et al. carefully studied the air-sensitivity of $Na_{2/3}Fe_{0.5}Mn_{0.5}O_2$ and suggested that carbonate ions can insert into the layered structure. They also showed the improvement of air-stability by nickel doping [85].

Water or ethanol stability is also an important property of cathode materials. Sodium transition metal oxides with layered structures are commonly synthesized at high temperatures (typically 800 °C or above) [66]. Significant sodium evaporation occurs at such temperature. An excess amount of sodium precursors is usually used during the synthesis to compensate the sodium loss. The excess amount typically varies from 2% to

[4] This chapter was adapted with permission from Zheng, L.; Li, L.; Shunmugasundaram, R.; Obrovac, M. N. Effect of Controlled-Atmosphere Storage and Ethanol Rinsing on $NaNi_{0.5}Mn_{0.5}O_2$ for Sodium-Ion Batteries. *ACS Applied Materials&Interfaces*, **2018**, 10, 38246-38254 [86]. Copyright 2018, American Chemical Society. The author's contribution includes performing the experimental work and writing the manuscript.

20% [81,133,134]. As a result of this excess sodium, a small amount of sodium-containing residues may left in the final product. Due to the electrochemical inactivity of these residues, their removal by ethanol or water washing could improve electrochemical performance. Surface coating techniques have also been shown to improve the performance of cathode materials of both lithium and sodium ion batteries [135,136]. Surface coating processes usually involve mixing materials in solvents, such as water or ethanol. It is therefore important to study the influence of water/ethanol on the materials. Actually, ethanol/water washing of lithium cathode materials has been reported to improve their structural/electrochemical stability [137,138]. However, to the best of our knowledge, there are no reports on the ethanol/water washing of sodium ion battery cathode materials, which have different surface chemistries. In this chapter, we present a study of the air-sensitivity of $NaNi_{0.5}Mn_{0.5}O_2$ and the effect of ethanol/water washing on this material.

## 6.2 Experimental

$NaNi_{0.5}Mn_{0.5}O_2$ material was synthesized using the method reported in Reference [113]. A homogeneous mixture of co-precipitated $Ni_{0.5}Mn_{0.5}(OH)_2$ powder and $Na_2CO_3$ (BioXtra, 99.0%, Sigma Aldrich) powder (in 5% excess) was pelletized and heated at 800°C for 24h in air. Heated samples were transferred to an Ar-filled glovebox without air exposure and finely ground using a mortar and pestle. For ethanol/water washing, as-synthesized powder samples were added to a beaker filled with ethanol (99.8%) or distilled water with magnetic stirring for 20 minutes. The powders were then filtered, dried at 100 °C in vacuum overnight, and then transferred back to an Ar-filled glovebox.

A powder X-ray diffractometer (Rigaku Ultima IV with a Cu X-ray tube, scintillation detector and a diffracted beam monochromator) was used to measure the X-ray diffraction (XRD) patterns of all samples. Rietveld refinements were conducted using Rietica software. Sample morphology was examined by field emission scanning electron microscopy (SEM) using a FE-SEM, Hitachi S-4700 FEG equipped with energy dispersive X-ray spectroscopy (EDX) functionality for elemental analysis. Sample composition was determined by inductively coupled plasma atomic emission spectroscopy (ICP-AES) using a Perkin Elmer Optima 8300 ICP optical emission spectrophotometer. Fourier transform infrared (FT-IR) spectra were measured using an Agilent Cary 630 FTIR spectrometer.

For electrochemical tests, working electrodes were prepared in an Ar-filled glovebox. Slurries were made by mixing active material, polyvinylidene difluoride binder (HSV 900, Kynar), and carbon black (C-NERGY Super C 65, Imerys Graphite Carbon) in an 8:1:1 weight ratio with an appropriate amount of N-methyl-2-pyrrolidone (Sigma Aldrich, anhydrous 99.5%). The slurries were mixed with two 0.5 inch tungsten carbide balls in a Retsch PM200 rotary mill (100 rpm, 1 hour) in argon atmosphere. The mixed slurries were coated onto aluminum foil using a coating bar having a ~0.015 cm gap, followed by drying under vacuum at 80°C overnight. Circular electrodes were punched from the coatings and incorporated into 2325-type coin cells in an Ar-filled glove box. 1 M $NaPF_6$ (Alfa Aesar, 99%) in a solution of ethylene carbonate (EC), diethyl carbonate (DEC) and monofluoroethylene carbonate (FEC) (volume ratio 3:6:1, battery grade, all from BASF) was used as electrolyte. Two Celgard 2300 separators, one blown microfiber separator (3M Company), and one Na disk (rolled from sodium ingot, Sigma Aldrich, ACS reagent grade) counter/reference electrode were used in cell construction. Cells were

cycled galvanostatically with a Maccor Series 4000 Automated Test System (Maccor Inc., Tulsa OK) at 30.0°C (±0.1 °C).

### 6.3 Results and Discussion

Figure 6.1(a) shows XRD patterns of as-synthesized $NaNi_{0.5}Mn_{0.5}O_2$ powders and $NaNi_{0.5}Mn_{0.5}O_2$ powders that were exposed to ambient air. The pristine $NaNi_{0.5}Mn_{0.5}O_2$ has an ideal O3 structure as reported [113]. The XRD patterns of $NaNi_{0.5}Mn_{0.5}O_2$ after being exposed to air for 15 days and 30 days show a different structure, which can be indexed with a P3 phase. As reported by Komaba et al., $Na_{1-x}Ni_{0.5}Mn_{0.5}O_2$ transitions from the fully sodiated O3 structure to a P3 structure when x is ~0.25 [113]. The formation of the P3 structure therefore indicates some sodium loss from the layered structure during air exposure. It has been reported that desodiation readily occurs for most O3-type sodium metal oxides when they react with air [13]. In addition to the P3 phase, small peaks are observed at ~31° and ~34° (shown in black arrow) after air exposure. These peaks were identified as being from $NaHCO_3$, as will be shown below. Figure 6.1(b) shows FTIR spectra of as-synthesized and air-exposed $NaNi_{0.5}Mn_{0.5}O_2$ powders. The bands at ~900 $cm^{-1}$ and ~1400 $cm^{-1}$, which correspond to $CO_3^{2-}$ vibrations, become more intense after air exposure, suggesting the desodiation is accompanied by the formation of $Na_2CO_3$ or other $CO_3^{2-}$ containing substances during air exposure [139,140].

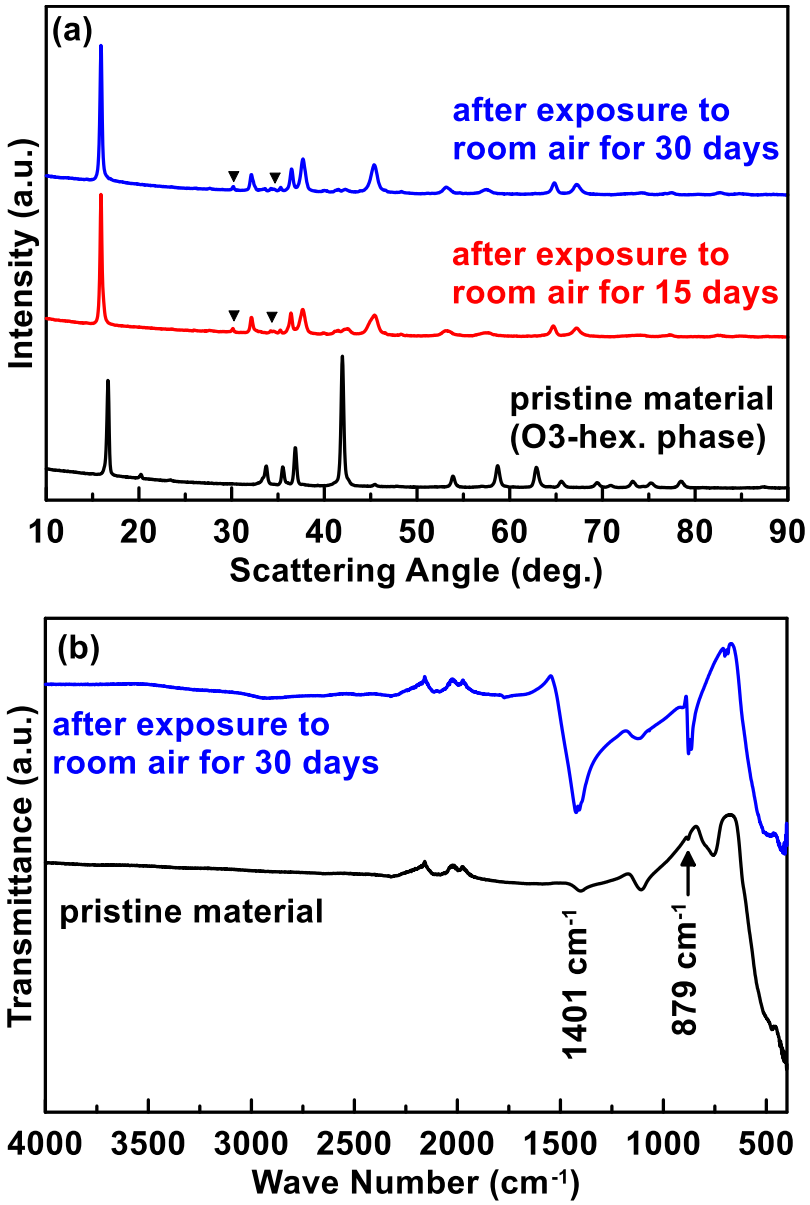


Figure 6.1 (a) XRD patterns and (b) FTIR results of the pristine and air-exposed $NaNi_{0.5}Mn_{0.5}O_2$.

Since air is a complex mixture containing oxygen, nitrogen, carbon dioxide, water, etc., to understand the air-sensitivity of $NaNi_{0.5}Mn_{0.5}O_2$ in more detail, $NaNi_{0.5}Mn_{0.5}O_2$ powders were stored in different atmospheres under flowing gas (oxygen, argon, carbon dioxide), either dry or wet, for 5 days. Figure 6.2 shows the XRD and FTIR spectra of the stored materials. There is no significant change in the XRD and FTIR results of

$NaNi_{0.5}Mn_{0.5}O_2$ stored in dry argon or oxygen. The appearance of a very small peak at ~13° is attributed to the intercalation of water into the layered structure, possibly due to a small amount of water exposure, despite the rigorous attempts at keeping these samples absolutely dry. When stored in dry carbon dioxide, similar to air exposure, the bands at ~900 $cm^{-1}$ and ~1400 $cm^{-1}$ in FTIR become more intense, suggesting the formation of carbonates. Nonetheless, the XRD peak positions in the XRD patterns of $NaNi_{0.5}Mn_{0.5}O_2$ do not change and no new peaks are formed after dry air, dry argon or dry carbon dioxide storage. Instead, XRD peak intensities are only weakened after storing in dry carbon dioxide, compared to the pristine material. This can be explained by the formation of small amounts of $Na_2CO_3$ on the surface, which are undetectable by XRD, but can reduce peak intensities. Based on XRD and FTIR results, it can be concluded that minimal reaction occurs between $NaNi_{0.5}Mn_{0.5}O_2$ and dry oxygen/argon. The sodium residues left from synthesis in the sample ($Na_2O$, $Na_2O_2$) can react with dry $CO_2$ and form $Na_2CO_3$. However, the bulk composition remains unchanged.

When stored in a wet atmosphere, apparent changes are observed in all the XRD results. $NaNi_{0.5}Mn_{0.5}O_2$ stored in wet argon still has the O3 structure, however all the peaks become broader. The peak broadening of layered cathode materials has been ascribed to the formation of stacking faults [120,126]. In this work, the slight loss of crystallinity is also believed to be an effect of stacking faults induced by water intercalation. It is also possible that the stacking faults are due to the oxidation by water, which leads to sodium extraction and the resulting O3/P3 phase transition. Another peak appearing at ~13° is attributed to a hydrated phase formed as water intercalated into the layered structure [87].$NaNi_{0.5}Mn_{0.5}O_2$ powders stored in wet oxygen also have low crystallinity. The

decreased intensity of the (104) peak and the increased intensity of the (015) peak indicates that the powders are a mixture of O3(O'3) and P3(P'3) phases. The appearance of the P3(P'3) phase is evidence that more sodium is lost during wet oxygen storage, compared to wet argon storage, suggesting oxygen participates in the reaction and facilitates the desodiation. Indeed, it has been reported that O3 type sodium cathode materials act as reducing agent against oxygen and/or water and, as a result, sodium is removed from the structure to form $Na_2O$/NaOH [13]. As shown in Figure 6.2(d), the FTIR spectra of $NaNi_{0.5}Mn_{0.5}O_2$ powders stored in wet argon/wet oxygen become featureless, confirming the amophization of $NaNi_{0.5}Mn_{0.5}O_2$.

Most dramatic changes are observed after $NaNi_{0.5}Mn_{0.5}O_2$ is exposed to wet carbon dioxide. The layered structure is barely retained after storage and most peaks can be well assigned to a $NaHCO_3$ phase (PDF# 00-015-0700), shown in the inset of Figure 6.2(b). The FTIR spectrum in Figure 6.2(d) also matches very well with that of pure $NaHCO_3$. This indicates that a significant amount of sodium is removed from the O3-structure after wet $CO_2$ exposure to form $NaHCO_3$. Moreover, the reference peak positions (~31° and ~34°) of $NaHCO_3$ phase also matches with the impurity peaks in the XRD of $NaNi_{0.5}Mn_{0.5}O_2$ after air exposure, as shown in Figure 6.1(a) with black arrow, suggesting that an $NaHCO_3$ phase is formed when $NaNi_{0.5}Mn_{0.5}O_2$ is exposed to air, due to its reaction with $CO_2/H_2O$. Besides the $NaHCO_3$ phase, there are a few unidentified peaks (indicated by blue arrows) in $NaNi_{0.5}Mn_{0.5}O_2$ stored in wet carbon dioxide. The origin of these peaks will be discussed below.

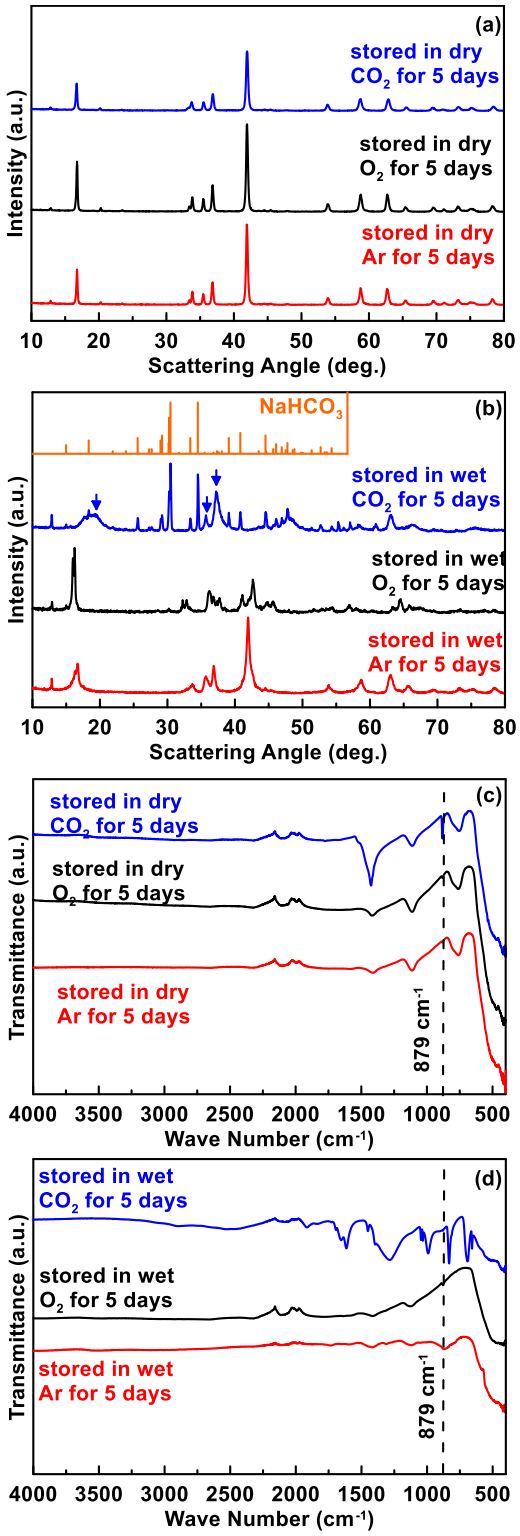


Figure 6.2 (a, b) XRD patterns and (c, d) FTIR spectra of $NaNi_{0.5}Mn_{0.5}O_2$ stored in under different flowing gases (oxygen, argon, carbon dioxide), either dry or wet, for 5 days.

Figure 6.3 shows the XRD patterns of water washed and also subsequently air-exposed $NaNi_{0.5}Mn_{0.5}O_2$. As reported previously and as demonstrated above, $NaNi_{0.5}Mn_{0.5}O_2$ is hygroscopic and readily reacts with water. Hence, it is no surprise that water washed $NaNi_{0.5}Mn_{0.5}O_2$ has completely different XRD pattern than the pristine material. Water likely has extracted most of the sodium in the structure by an ion-exchange process between $Na^+$and $H^+$ during the washing process. As such, this material is expected to be electrochemically inactive. After being stored in air, no change is observed in the XRD pattern of the water washed $NaNi_{0.5}Mn_{0.5}O_2$. The XRD pattern of the water washed sample has broad peaks, indicating poor crystallinity. A careful examination shows that these peaks coincide with the unidentified peaks in the XRD of $NaNi_{0.5}Mn_{0.5}O_2$ after storing in wet carbon dioxide, as shown in Figure 6.2(b) with blue arrows. Considering that almost all the sodium in $NaNi_{0.5}Mn_{0.5}O_2$ after storing in wet carbon dioxide could have reacted to form $NaHCO_3$, these peaks might be from a metal (Ni and Mn) (oxy)-hydroxide phase. Indeed, the XRD pattern of water washed $NaNi_{0.5}Mn_{0.5}O_2$ sample closely resembles the XRD pattern of $Ni_{1/3}Mn_{1/3}Co_{1/3}(OH)_2$ reported by Yabuuchi et al., with the peak positions matching exactly [141].

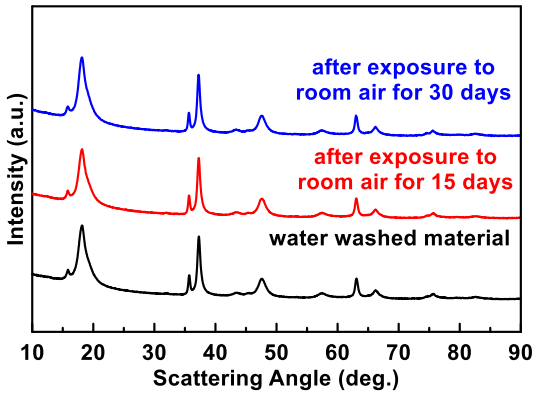


Figure 6.3 XRD patterns of water washed and air exposed $NaNi_{0.5}Mn_{0.5}O_2$.

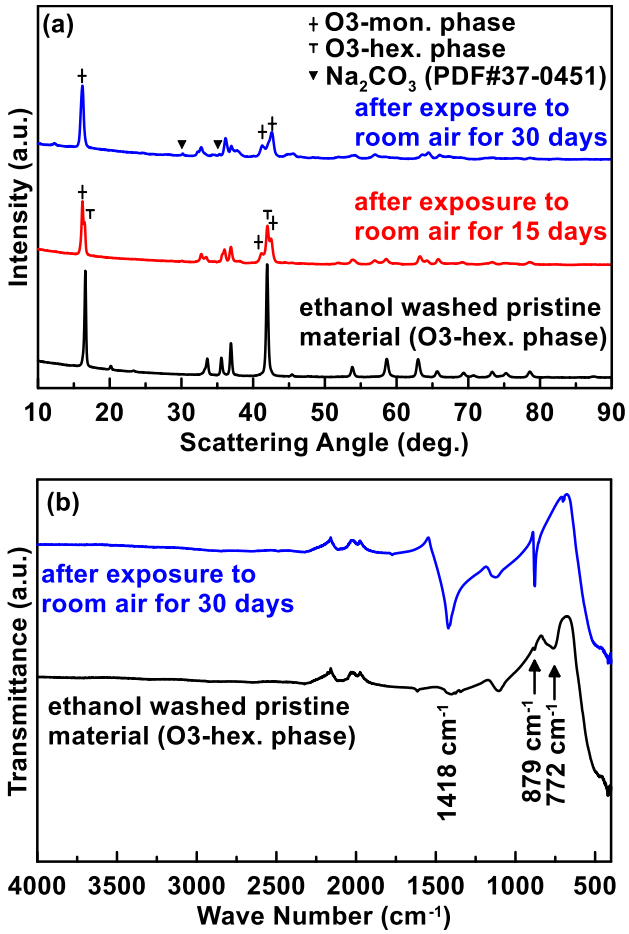


Figure 6.4 (a) XRD patterns and (b) FTIR results of the $NaNi_{0.5}Mn_{0.5}O_2$ stored in room air for different days.

Figure 6.4 shows the XRD and FTIR patterns of ethanol washed $NaNi_{0.5}Mn_{0.5}O_2$ powders before and after being exposed to room air. Before the air exposure, ethanol washed $NaNi_{0.5}Mn_{0.5}O_2$ has similar XRD and FTIR results with that of pristine $NaNi_{0.5}Mn_{0.5}O_2$, implying that the ethanol washing process does not cause significant damage to the O3 structure. After exposing $NaNi_{0.5}Mn_{0.5}O_2$ to air for 15 days, the XRD pattern shows that the original O3 phase coexists with the monoclinic O′3 phase. After 30 days of air exposure, $NaNi_{0.5}Mn_{0.5}O_2$ almost completely transforms to the monoclinic O'3 phase. The FTIR spectrum also shows more absorption from $CO_3^{2-}$after air exposure. The formation of O'3 phase instead of P3 phase indicates less sodium loss from the structure,

which further indicates a slower reaction of $NaNi_{0.5}Mn_{0.5}O_2$ with air, and a better air-stability of ethanol washed $NaNi_{0.5}Mn_{0.5}O_2$, compared to the pristine material.

In order to understand the mechanism of the ethanol/water wash process, Rietveld refinements and ICP measurements were conducted on pristine and washed $NaNi_{0.5}Mn_{0.5}O_2$. The Rietveld refinement results with lattice parameters of pristine and ethanol washed $NaNi_{0.5}Mn_{0.5}O_2$ are shown in Figure 6.5 (a) and (b). Reasonably good fits with low Bragg R-factors were obtained for both refinements. Ethanol washed $NaNi_{0.5}Mn_{0.5}O_2$ has a slightly smaller lattice constant *a* and a larger *c* lattice constant, implying less sodium in the layered structure and a slight sodium loss during the ethanol washing process. This is confirmed by the sodium occupancy obtained from the refinements. The sodium occupancies were allowed to vary during the fits and stabilized to a value of 0.913 and 0.886 respectively, for pristine and ethanol washed $NaNi_{0.5}Mn_{0.5}O_2$. Since ICP reflects the total content of sodium in the sample, while Rietveld refinement gives the amount of sodium in the refined O3 structure, the difference is an estimate of the sodium residues ($Na_2CO_3$, $NaHCO_3$, $Na_2O_2$, $Na_2O$, etc.) in the samples. Figure 6.5 (c) compares the sodium contents as obtained from ICP and XRD refinement results. Pristine $NaNi_{0.5}Mn_{0.5}O_2$ has a sodium residue of ~2.2%, while ethanol washed $NaNi_{0.5}Mn_{0.5}O_2$ only has ~0.1% sodium residue. This suggests that the ethanol wash process not only partially removes the sodium from the O3 structure, but also washes away most of the sodium residues in the synthesized samples. Finally, as expected, there is almost no sodium left in the water washed sample, as demonstrated by ICP measurement.

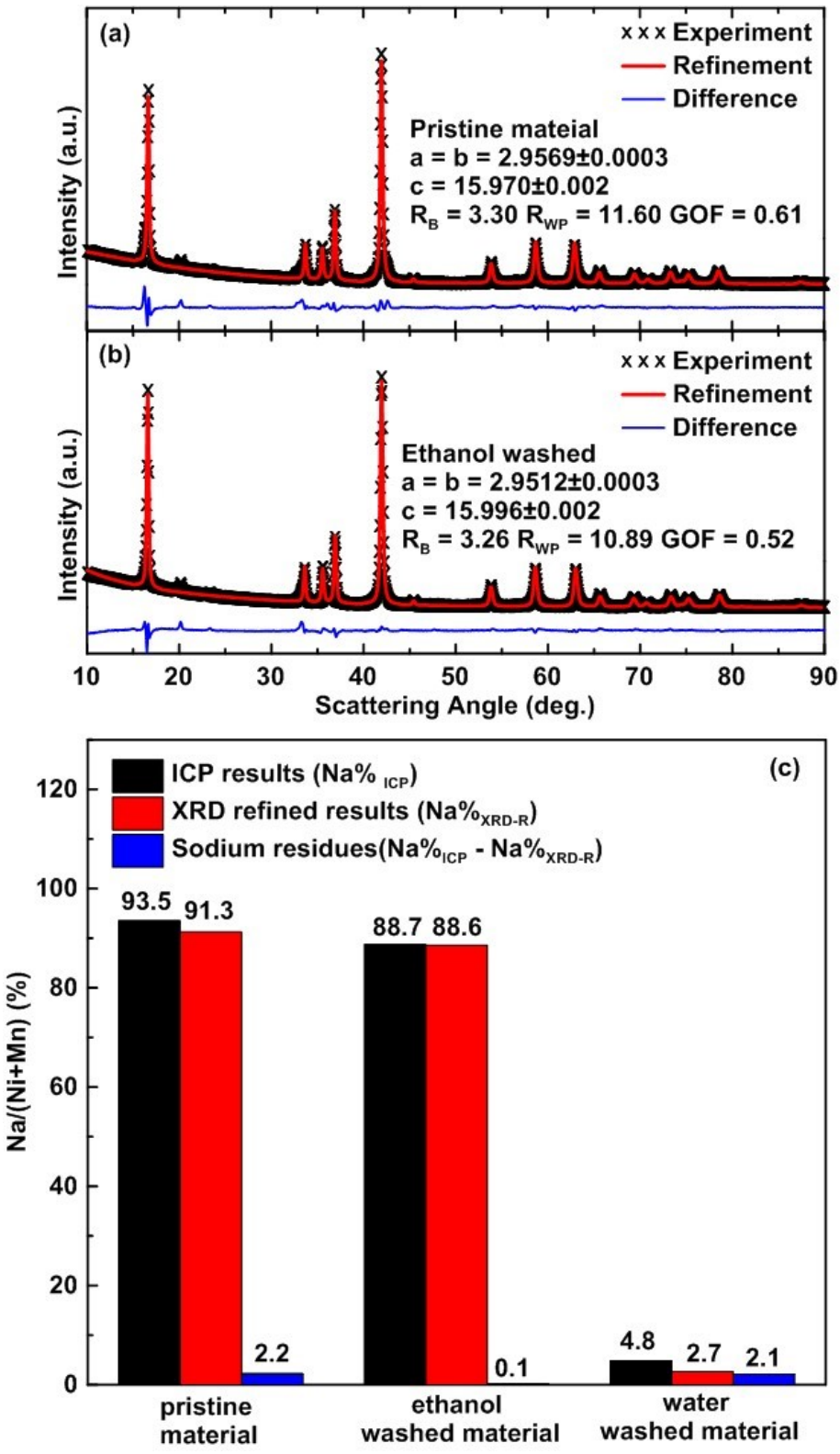


Figure 6.5 Rietveld refinement of (a) pristine and (b) ethanol washed $NaNi_{0.5}Mn_{0.5}O_2$, and (c) corresponding comparison of ICP and XRD refinement results.

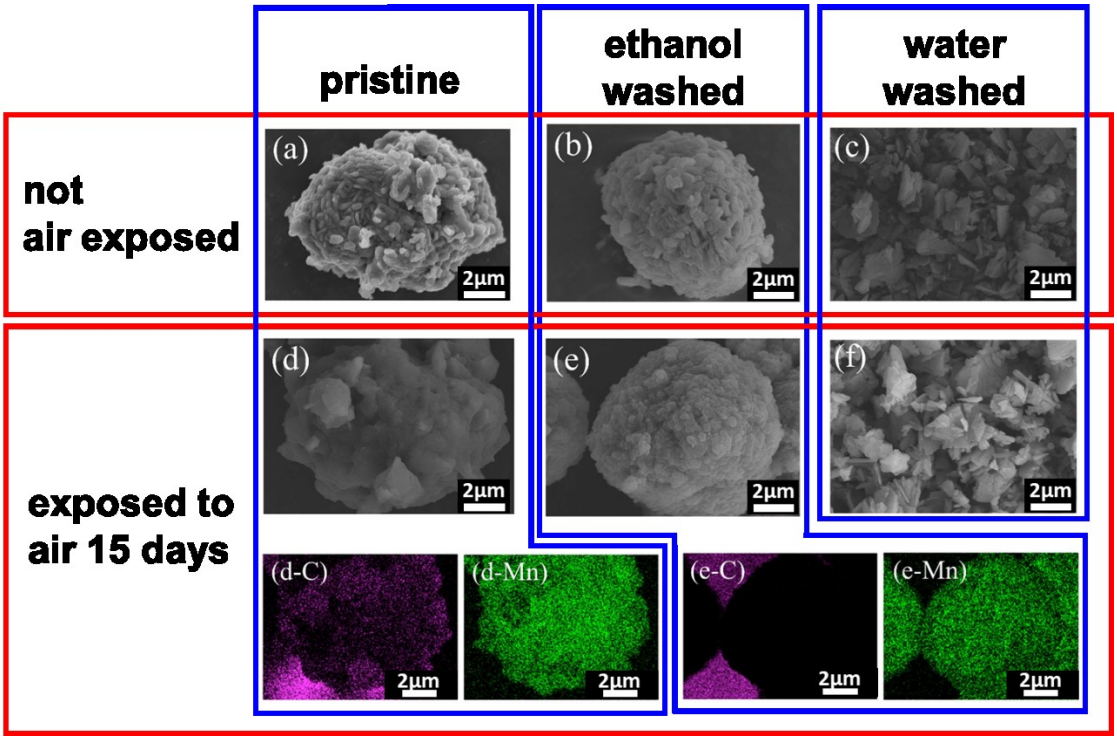


Figure 6.6 SEM images of fresh and air exposed (15 days) samples: (a, d) pristine, (b, e) ethanol washed and (c, f) water washed $NaNi_{0.5}Mn_{0.5}O_2$, and corresponding EDS mapping based on (d) and (e).

Figure 6.6(a-c) shows SEM images of pristine, ethanol washed, and water washed $NaNi_{0.5}Mn_{0.5}O_2$, respectively. Pristine and ethanol washed $NaNi_{0.5}Mn_{0.5}O_2$ have spherical secondary particles with a diameter of ~10 μm, which are comprised of needle-like primary particles. The ethanol washed sample is smoother, while the there are some unknown species on the surface of the pristine sample. Water washed $NaNi_{0.5}Mn_{0.5}O_2$ has an irregular flake morphology, suggesting irreversible structural change has occurred during the water washing process. The SEM images of these samples after 15 days air-exposure are shown in Figure 6.6(d-f). After air exposure, the particles of pristine $NaNi_{0.5}Mn_{0.5}O_2$ are entirely coated by a substance that also fills in the porosity between the primary particles, and the primary particles become indistinguishable. In contrast, for the ethanol washed sample, after air exposure the substance coated on the surface is much thinner and

the primary particles are still distinguishable. This also implies a better air stability of the ethanol washed sample, in accordance with the XRD results shown above. The unknown substance coated on the surface of air-exposed samples, which most likely consists of sodium residues such as $Na_2CO_3$, $NaHCO_3$, is due to the reaction between $NaNi_{0.5}Mn_{0.5}O_2$ sample and air. Water washed $NaNi_{0.5}Mn_{0.5}O_2$ shows no change in its morphology after air exposure, in accordance with the XRD results shown in Figure 6.3.

The air-exposed $NaNi_{0.5}Mn_{0.5}O_2$ samples were further characterized by EDX mapping and the results are shown at the bottom of Figure 6.6. A uniform distribution of manganese throughout the particle is observed for both pristine and ethanol washed $NaNi_{0.5}Mn_{0.5}O_2$. Nevertheless, the distributions of carbon are different for the two samples. On the surface of air-exposed pristine $NaNi_{0.5}Mn_{0.5}O_2$, a large amount of carbon is detected, while there are only very low levels of carbon observed on the surface of the air-exposed ethanol washed samples. This suggests the reaction to form carbon-containing substances is retarded on the surface of the ethanol washed sample upon exposure to air, in agreement with the XRD results of air-exposed samples. It is likely that pristine $NaNi_{0.5}Mn_{0.5}O_2$ powders are covered with Na-containing residues, such as $Na_2O$ and NaOH. These residues would readily react with $CO_2$ in the air to form carbonates, as is demonstrated by the FTIR results. These Na-containing residues are also hygroscopic, making the surface adsorb water when exposed to air. This in turn would induce the desodiation of $NaNi_{0.5}Mn_{0.5}O_2$ by ion exchange. Ethanol washing removes Na-containing residues from $NaNi_{0.5}Mn_{0.5}O_2$ surfaces. As a result, the formation of surface carbonates is retarded and the surface less hygroscopic. This would result in the ethanol-washed samples to be less air-sensitive, as observed here.

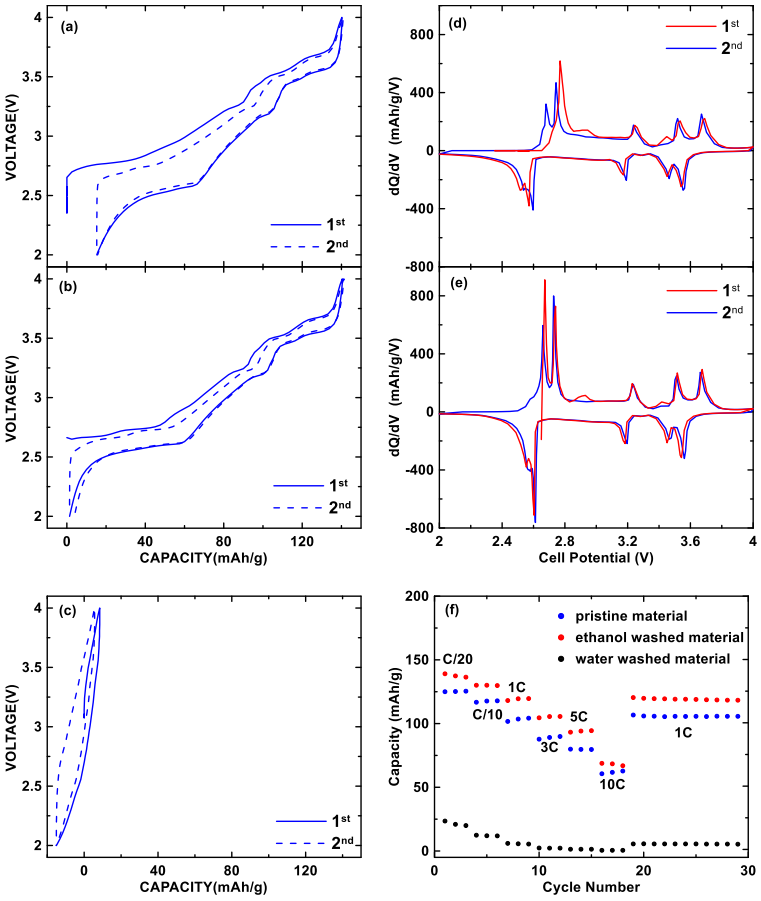


Figure 6.7 (a-c) Voltage curves, (d, e) corresponding differential capacity curves and (f) rate performance of pristine, ethanol washed and water washed $NaNi_{0.5}Mn_{0.5}O_2$.

Figure 6.7(a-b) shows the voltage curves of pristine and ethanol washed $NaNi_{0.5}Mn_{0.5}O_2$ cycled between 2 – 4 V at C/20 rate. Pristine $NaNi_{0.5}Mn_{0.5}O_2$ has a reversible capacity of ~120 mAh/g and an irreversible capacity of ~20 mAh/g, close to that reported earlier [113]. The stepwise voltage curve also resembles the literature result. Ethanol washed $NaNi_{0.5}Mn_{0.5}O_2$ has a comparable first charge capacity, but with a very small irreversible capacity, resulting a higher reversible capacity The higher initial coulombic efficiency of the ethanol washed sample is ascribed to its reduced reactivity with air, thus avoiding reactions that cause Na-loss via $H^+$ insertion into the cathode, and that results in irreversible structural changes during cycling [13].

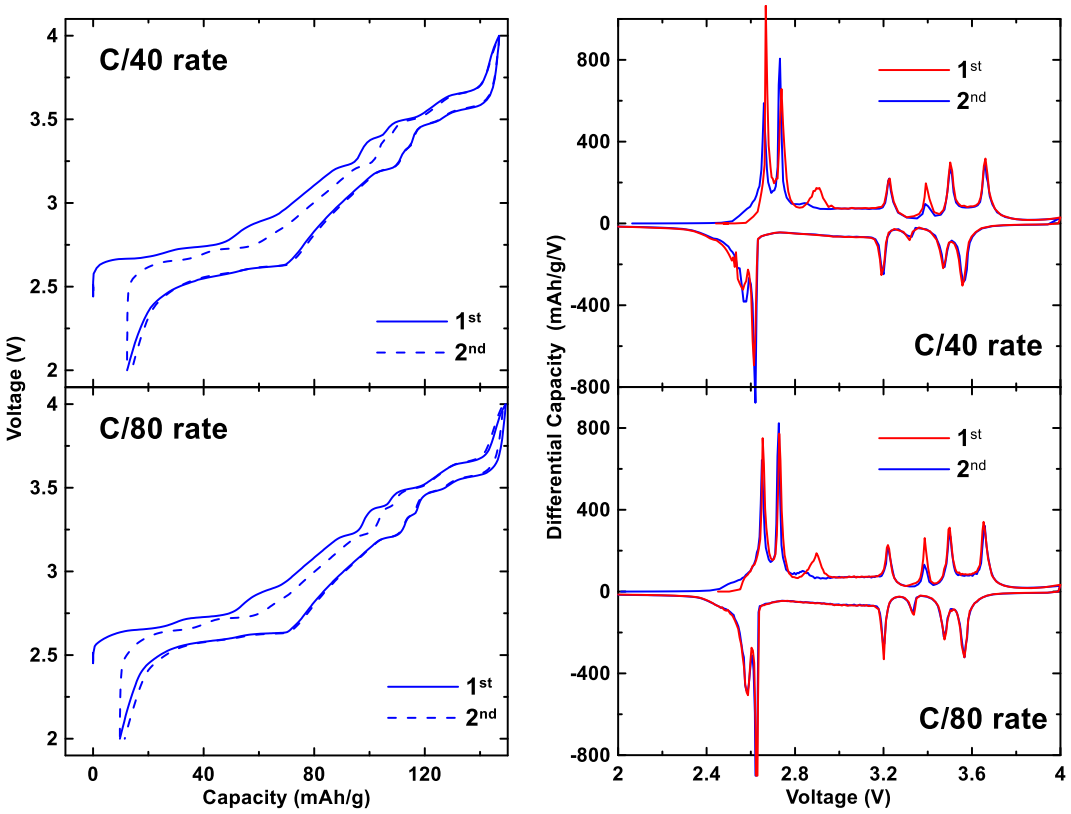


Figure 6.8 Voltage curves (left) and differential capacity curves (right) of pristine $NaNi_{0.5}Mn_{0.5}O_2$ cycled at C/40 and C/80 rates.

The voltage curve also has a lower hysteresis, compared to pristine $NaNi_{0.5}Mn_{0.5}O_2$. The large hysteresis of pristine $NaNi_{0.5}Mn_{0.5}O_2$ is in agreement with previous reports [113]. In the second cycle, although both materials have decreased hysteresis, the hysteresis of ethanol washed sample is still considerably smaller. This can also be clearly seen in the differential capacity curves of the two samples, as shown in Figure 7(d-e). The peaks are broader with lower intensity for pristine $NaNi_{0.5}Mn_{0.5}O_2$. During the first charge process, only one peak is observed at ~2.7 V in the differential capacity curve of pristine $NaNi_{0.5}Mn_{0.5}O_2$, while two peaks are observed in the differential capacity curve of ethanol washed sample. In the second cycle, both materials have two peaks at ~2.7 V upon charging, implying the structure is stabilized during the first cycle. The water washed

material is inactive, as shown in Figure 6.7(c), confirming the structure has been damaged after washing with water and supporting the conjecture that water washing removes all of the Na from the structure. Figure 6.7(f) compares the rate performance of the materials. The ethanol washed material shows the best rate capability, retaining about 70 mAh/g capacity at 10C.

In order to understand the difference between the electrochemical performance of pristine and ethanol washed samples, cells were made with pristine $NaNi_{0.5}Mn_{0.5}O_2$ and cycled at lower rates. Figure 6.8 shows the voltage curves and differential capacity curves of pristine $NaNi_{0.5}Mn_{0.5}O_2$ cycled at C/40 and C/80 rates. Cells cycled at lower current rates have smaller hysteresis, higher reversible capacity and lower irreversible capacity. In other words, at lower current rates they become more like ethanol washed $NaNi_{0.5}Mn_{0.5}O_2$. The differential capacity curves are also characterized with sharper peaks and two peaks at ~2.7 V during the first charge, similar to that of ethanol washed $NaNi_{0.5}Mn_{0.5}O_2$. This indicates the difference between the electrochemical performance of pristine and ethanol washed samples is due to the better kinetics of the ethanol washed sample. When cycled at higher current rate, sodium diffusion gradients might cause the plateaus at ~2.7 V to merge for the pristine material. Taking into account the SEM images and ICP/Rietveld refinement results, we suspect that the sodium residues on the surface of the pristine samples partially block $Na^+$ diffusion, resulting in large hysteresis. On the other hand, the clean surface of ethanol washed $NaNi_{0.5}Mn_{0.5}O_2$ with less sodium residues facilitates faster diffusion, resulting in better rate performance.

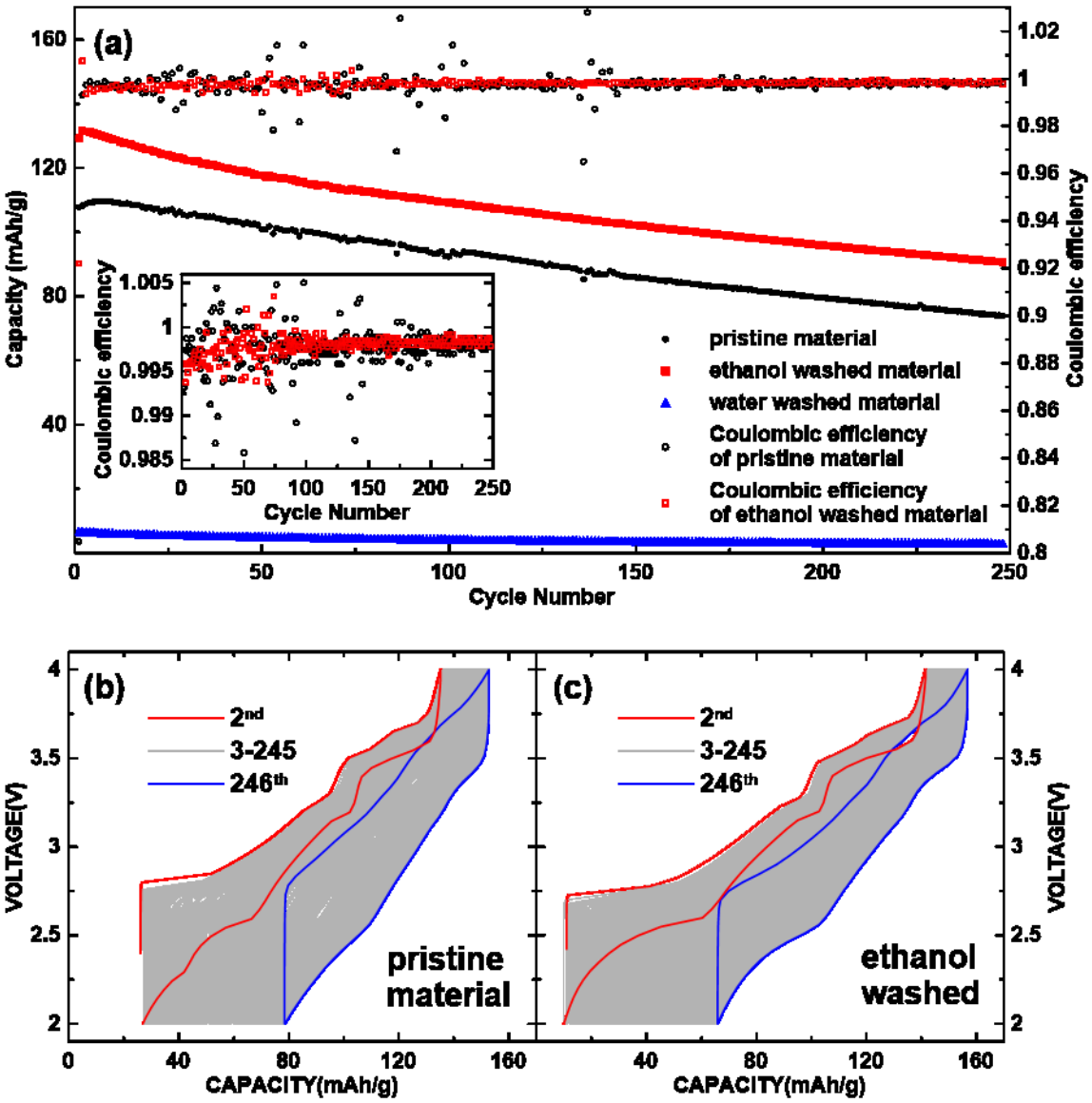


Figure 6.9 (a) Cycle performance, coulombic efficiency, and (b, c) voltage curves of pristine $NaNi_{0.5}Mn_{0.5}O_2$, ethanol washed and water washed samples, cycled between 2 – 4 V at 1C rate.

Figure 6.9(a) shows the cycle performance and coulombic efficiency (CE) vs. cycle number for cells tested at 1C rate. The inset shows an expanded CE plot comparison. The CEs of both materials are higher than 99%, however pristine $NaNi_{0.5}Mn_{0.5}O_2$ has an erratic CE. The unstable CE for the pristine $NaNi_{0.5}Mn_{0.5}O_2$ is attributed to surface residues, which could result in gas formation during cycling. In contrast, the CE for the ethanol washed

sample, in which the surface residues are removed, is much more stable. The capacity fade rate is similar for both pristine and ethanol washed materials, demonstrating a capacity retention of ~69% and ~72%, respectively, after 250 cycles. Figure 6.9(b-c) also shows the evolution of the voltage curves during cycling. No significant difference is observed between the two materials during long-term cycling, even though ethanol washed $NaNi_{0.5}Mn_{0.5}O_2$ consistently has a higher capacity than pristine $NaNi_{0.5}Mn_{0.5}O_2$, due to its lower hysteresis. However, the hysteresis of both materials gradually increases during cycling. This indicates ethanol washing cannot alleviate side reactions between the electrolyte and the active material. Possible reasons for the capacity fade/higher hysteresis include electrolyte deterioration, impedance growth on the electrode surface, and structure change of the material [96,142,143]. Other strategies, such as electrolyte optimization, transition metal doping or surface coating, are required to improve the cycling performance.

## 6.4 Conclusion

The sensitivity of $NaNi_{0.5}Mn_{0.5}O_2$ towards air exposure was studied in detail by XRD structural analysis, surface analysis by SEM imaging and FTIR spectroscopy, and by electrochemical measurements. The reactions that occur when $NaNi_{0.5}Mn_{0.5}O_2$ is exposed to air are complex. They involve synergistic interactions between $NaNi_{0.5}Mn_{0.5}O_2$, water, oxygen, and carbon dioxide. While water can react with $NaNi_{0.5}Mn_{0.5}O_2$ on its own, both oxygen and carbon dioxide require water to be present before they can also react with $NaNi_{0.5}Mn_{0.5}O_2$. These components of air react with $NaNi_{0.5}Mn_{0.5}O_2$ by extracting sodium from the structure and forming sodium containing residues on the $NaNi_{0.5}Mn_{0.5}O_2$ particle surfaces. Washing $NaNi_{0.5}Mn_{0.5}O_2$ with water completely destroys the $NaNi_{0.5}Mn_{0.5}O_2$

structure, while washing with ethanol does not cause significant structural damage. Instead, ethanol washing removes most of the sodium residues on $NaNi_{0.5}Mn_{0.5}O_2$ surfaces. This results in improved air-stability, as confirmed by XRD and EDX measurements. Ethanol washed $NaNi_{0.5}Mn_{0.5}O_2$ has a higher capacity, lower hysteresis, and better rate performance than pristine $NaNi_{0.5}Mn_{0.5}O_2$. This work gives insights into the air-sensitivity of potential sodium ion battery positive electrode materials, and provides an easy method to make such materials more air stable. This result is important for the utilization of Na-ion cathode materials in practical cells.

# CHAPTER 7 HEXAGONAL AND MONOCLINIC $NaNi_{0.8}Co_{0.15}Al_{0.05}O_2$ (Na-NCA)[5]

## 7.1 Introduction

The energy density of some sodium cathode materials reported rivals that of lithium ion cathode materials. For example, Li et al. reported a quaternary layered cathode $Na(Mn_{0.25}Fe_{0.25}Co_{0.25}Ni_{0.25})O_2$ has an energy density of 578 Wh/kg with good cyclability [144]. It is also shown in chapter 5 that $Na_{0.9}Ni_{0.45}Mn_{0.4}Ti_{0.15}O_2$ delivers an energy density of 643 Wh/kg. In order to further increase the capacity and energy density of sodium ion batteries, researchers have systematically studied the relationship between the transition metal composition and electrochemical performance [145]. Hwang et al. showed that higher Ni content in the composition contributes to a higher discharge capacity, similar to the case of lithium ion batteries [145].

One of the end members of Ni-rich sodium layered oxide, $NaNiO_2$, was first studied in 1953 by Dyer et al. [146]. In $NaNiO_2$, $Ni^{3+}$ is a Jahn-Teller ion with an electron configuration of $t_{2g}^6e_g^1$, which leads to a monoclinic distortion at room temperature. Later, Darie et al. studied the temperature dependence of the $NaNiO_2$ structure by measuring its diffraction pattern at temperatures between 300 and 600 K [147]. They reported a monoclinic O'3 to hexagonal O3 phase transition in $NaNiO_2$ during heating at 450 – 500 K. They proposed that symmetry reduction due to the Jahn-Teller effect was overcome at high temperature by thermal motion and a high symmetry space group $R\bar{3}m$ is formed as a

[5] This chapter was based on a manuscript from Zheng, L.; Fielden, R.; Obrovac, M. N. Hexagonal and Monoclinic $NaNi_{0.8}Co_{0.15}Al_{0.05}O_2$ (Na-NCA) for Sodium Ion Batteries. Submitted to *Journal of Power Sources* in **2019**. The author's contribution includes performing the experimental work and writing the manuscript.

result [147]. The first electrochemical investigation of $NaNiO_2$ was conducted by Braconnier et al., who showed that $NaNiO_2$ could be charged (desodiated) to a composition of $Na_{0.79}NiO_2$ [148]. Recently, Ceder et al. and Rojo et al. reinvestigated the electrochemical properties of monoclinic $NaNiO_2$ and showed that ~0.62 Na can be reversibly intercalated into the structure [109,149]. However, a large irreversible capacity and hysteresis were observed.

As is well-known, nickel-rich layered materials are promising candidates as cathode materials for next-generation lithium ion batteries as they offer high energy density [29]. However, $LiNiO_2$ suffers from difficult synthesis, poor cyclability, and safety issues [23,137]. Partial substitution of nickel with cobalt leads to improved electrochemical performance [150,151]. Doping with aluminum enhances the stability and safety, due to the strong Al-O bond [25,152]. Therefore, $LiNi_xCo_yAl_zO_2$ (NCA) materials, with a typical composition of $LiNi_{0.8}Co_{0.15}Al_{0.05}O_2$, have been extensively studied and used in commercial lithium ion batteries [153].

To our best knowledge, $NaNi_xCo_yAl_{1-x-y}O_2$ has not been reported before. In this chapter the synthesis and characterization of $NaNi_{0.8}Co_{0.15}Al_{0.05}O_2$ (Na-NCA) for sodium ion battery cathode material is reported for the first time. The effect of oxygen vacancies on its structure and electrochemistry is also discussed.

## 7.2 Experimental

$NaNi_{0.8}Co_{0.15}Al_{0.05}O_2$ (Na-NCA) materials were synthesized by solid state methods. Stoichiometric amounts of $Na_2O_2$ (Sigma-Aldrich, 97%), NiO (Sigma-Aldrich, 99%), $Co_3O_4$ (Alfa Aesar, 99.7%) and $Al_2O_3$ (Alfa Aesar, 99%) powders were mixed by

high energy ball milling using a SPEX 8000 mill. An excess of 10% $Na_2O_2$ was used to compensate sodium loss during heating. Typically a 3:1 ball:sample mass ratio with a sample size of ~6 g and four 7/16 inch diameter stainless steel balls were milled in argon atmosphere for 2 hours. The obtained powders were then pelletized and heated at 850 °C for 14 hours in a tube furnace in oxygen. Samples were either slow-cooled in the furnace in oxygen flow or quenched in liquid nitrogen. After the cooling process, samples were immediately transferred to an Ar-filled glove box to minimize air exposure.

To investigate the electrochemical properties, working electrodes were prepared by mixing an 80:10:10 weight ratio of active material, carbon black (Super C65, Imerys Graphite and Carbon) and polyvinylidene fluoride (HSV 900, Kynar) with an appropriate amount of N-methyl-2-pyrrolidinone (Sigma Aldrich, anhydrous 99.5%). These components were mixed using a Retsch PM200 planetary mill with two 0.5 inch tungsten carbide balls for 1 hour at 100 rpm to create uniform black slurries. The slurries were coated onto aluminum foil with a coating bar having a ~0.015 cm gap and then dried in vacuum at 80 °C overnight. A circular punch was then used to obtain circular electrode discs with a diameter of 1.3cm were and an average active loading of ~1.5 mg/cm$^2$. Coin cells (2325 type) were assembled using sodium foil (~0.3 mm, rolled from sodium ingot, Sigma Aldrich, ACS reagent grade) as reference/counter electrodes, 1 M $NaPF_6$ (Aldrich, 98%) in a solution of ethylene carbonate, diethyl carbonate and monofluoroethylene carbonate (volume ratio 3:6:1, all from BASF) as electrolyte. Two Celgard 2300 and one blown microfiber separator (3M Company) were used as separators. Cells were cycled with a Maccor Series 4000 Automated Test System (Maccor Inc., Tulsa OK). The ambient cycling temperature was 30.0 °C (±0.1 °C). For galvanostatic intermittent titration technique

(GITT) measurements, cells were cycled at C/25 rate for 1 hour, followed by relaxing at open-circuit of 5 hours between each charge.

X-ray diffraction (XRD) data were collected with a Rigaku Ultima IV X-ray diffractometer equipped with a Cu anode X-ray tube. A scintillation detector with a diffracted beam monochromator was used to measure the diffraction patterns of powder samples and *ex situ* samples. In order to avoid air contamination, powder samples were loaded into a gastight X-ray sample holder (DPM Solutions, Hebbville NS) in an argon-filled glove box. Structural models were refined using the Rietveld method within Rietica software. For *ex situ* measurements, coin cells were stopped at different cut-off voltages and then opened in an argon-filled glove box. Electrodes taken from the cells were rinsed with dimethyl carbonate (BASF) several times. The coatings were then scraped from the current collectors and incorporated into the airtight x-ray holder with a zero-background silicon wafer. A D/TeX Ultra linear detector with a K-beta filter was used to measure XRD patterns of *in situ* coin cells. *In situ* X-ray diffraction was performed on electrochemical cells equipped with a beryllium window coated with the same slurry as described above. *In situ* cells were cycled at a rate of C/10 between 1.5 V and 4.5 V. Inductively coupled plasma optical emission spectrometry (ICP-OES) was used to determine the elemental composition of the products. Measurements were performed using a PerkinElmer Optima 8000. Each sample was dissolved in 2 mL of aqua regia solution which was then diluted using 2% $HNO_3$ prior to measurements. The standard deviations are less than 1% for all the measurements.

## 7.3 Results and discussions

Figure 7.1(a) and (b) show XRD patterns and Rietveld refinement results of quenched and slow-cooled Na-NCA materials. Two different structures were obtained. Quenched Na-NCA is phase pure with a hexagonal O3 structure ($R\bar{3}m$), isostructural $LiNiO_2$ or Li-NCA at room temperature. Slow-cooled Na-NCA mainly has the monoclinic O'3 structure, which can be indexed to the C/2m space group, isostructural with $NaNiO_2$ at room temperature. A closer examination shows that slow-cooled Na-NCA actually consists two phases: a majority of O'3 phase and a minority of O3 phase, as can be seen from Figure 7.1 (c). The ratio of the two phases were determined to be 98.16% and 1.84%, respectively, from Rietveld refinement. Figure 7.1(d) shows crystal structure models of the O3 and monoclinic O'3 structures. Both structures consist of sodium-oxygen octahedra and transition metal-oxygen octahedra. The monoclinic O'3 structure has distorted MO6 octahedra, caused by two elongated M-O bonds and four shortened M-O bonds due to the cooperative Jahn-Teller effect of the $Ni^{3+}$ ions in the structure. ICP-OES results, shown in Table 7.1, are in good agreements with the anticipated atomic ratios.

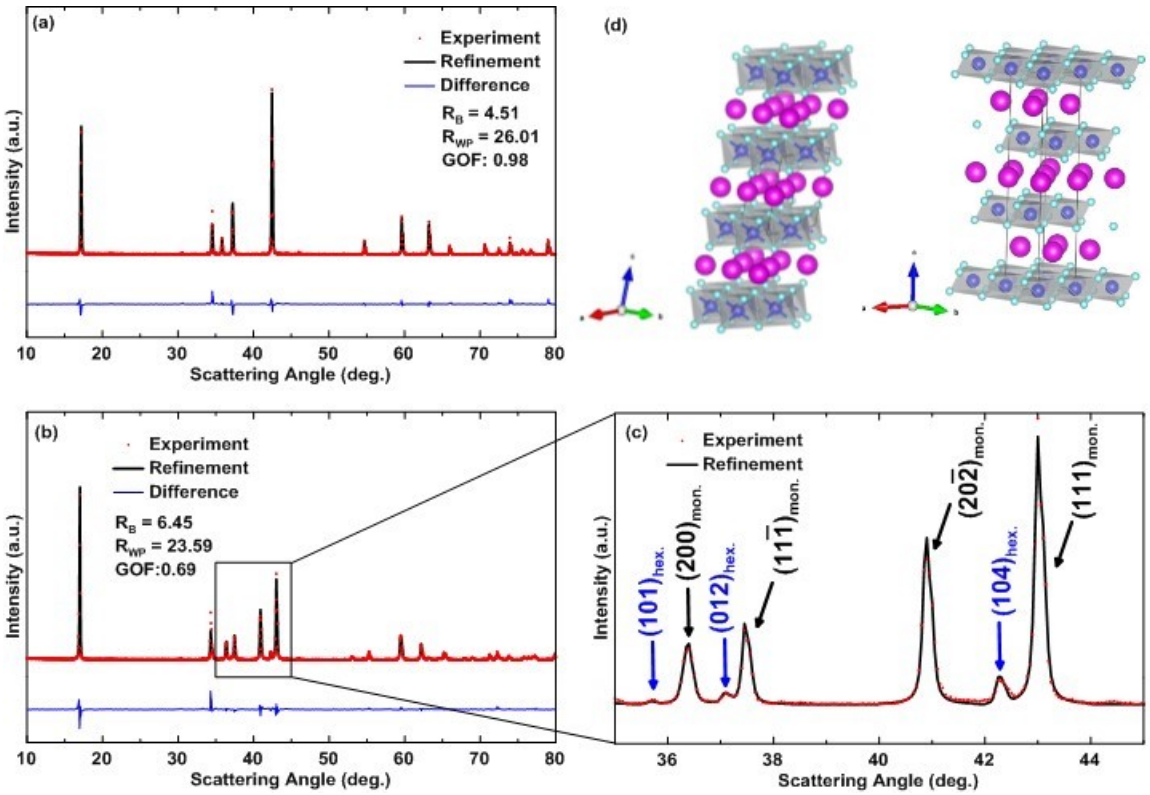


Figure 7.1 XRD patterns of (a) quenched O3 Na-NCA and (b) slow-cooled O'3 Na-NCA. (c) Enlarged XRD pattern of O'3 Na-NCA. (d) Schematic structure of hexagonal O3 and monoclinic O'3 layered-type oxides.

Table 7.1 ICP-OES measurement results of the Na-NCA samples.

| Sample | Ni | Co | Al | Na |
|---|---|---|---|---|
| Quenched O3 | 0.8 | 0.13 | 0.03 | 0.92 |
| Slow-cooled O'3 | 0.8 | 0.13 | 0.04 | 0.97 |

Table 7.2 Crystal data of the slow-cooled and quenched $NaNi_{0.8}Co_{0.15}Al_{0.05}O_{\delta}$ obtained by Rietveld refinements. Data with * are allowed to vary freely during refinements.

| Quenched $NaNi_{0.8}Co_{0.15}Al_{0.05}O_{\delta}$ space group $R\bar{3}m$ (No. 166) | | | | |
|---|---|---|---|---|
| Atom | x | y | z | Occupancy |
| Na | 0 | 0 | 0.5 | 1 |
| Ni | 0 | 0 | 0 | 0.8 |
| Co | 0 | 0 | 0 | 0.15 |
| Al | 0 | 0 | 0 | 0.05 |
| O | 0 | 0 | 0.2681±0.0004* | 0.92±0.01* |
| $a$ = 2.9492±0.0001* Å, $c$ = 15.6809±0.0007* Å | | | | |
| Slow-cooled $NaNi_{0.8}Co_{0.15}Al_{0.05}O_{\delta}$ space group $C/2m$ (No. 12) | | | | |
| Atom | x | y | z | Occupancy |
| Na | 0 | 0 | 0.5 | 1 |
| Ni | 0 | 0.5 | 0 | 0.8 |
| Co | 0 | 0.5 | 0 | 0.15 |
| Al | 0 | 0.5 | 0 | 0.05 |
| O | 0.219±0.001* | 0 | 0.198±0.001* | 0.96±0.01* |
| $a$ = 5.2485±0.0006* Å, $b$ = 2.8600±0.0003*Å, $c$ = 5.5552±0.0006* Å, $\beta$ = 109.825±0.004* ° | | | | |

| Slow-cooled $NaNi_{0.8}Co_{0.15}Al_{0.05}O_{\delta}$ space group $R\bar{3}m$ (No. 166) | | | | |
|---|---|---|---|---|
| Atom | x | y | z | Occupancy |
| Na | 0 | 0 | 0.5 | 1 |
| Ni | 0 | 0 | 0 | 0.8 |
| Co | 0 | 0 | 0 | 0.15 |
| Al | 0 | 0 | 0 | 0.05 |
| O | 0 | 0 | 0.277±0.002* | 1.02±0.06* |

$a$ = 2.9424±0.0005* Å, $c$ = 15.694±0.004* Å

During the refinements, allowing the sodium content to be variable resulted in sodium occupancies that were slightly larger than 1. This indicates full sodium occupancy and little or no sodium vacancies. Therefore the sodium content was fixed at 1 in the final refinements. Allowing the oxygen content to be variable results in ~9% oxygen vacancies for quenched $NaNi_{0.8}Co_{0.15}Al_{0.05}O_2$, while the oxygen vacancy content for slow-cooled $NaNi_{0.8}Co_{0.15}Al_{0.05}O_2$ is less (~4%). Table 7.1 shows the crystal data of the materials as obtained from Rietveld refinement. The average oxidation state of Ni is reduced due to the oxygen vacancies in the quenched $NaNi_{0.8}Co_{0.15}Al_{0.05}O_2$. By assuming a composition of $NaNi_{0.8}Co_{0.15}Al_{0.05}O_{1.82}$ (~9% oxygen vacancies), and the oxidation state of Na to be 1+, O to be 2-, Co and Al to be 3+, the average oxidation state of Ni would be 2.5+ instead of 3+. This significantly lowers the concentration of Jahn-Teller active $Ni^{3+}$, which leads to the formation of an O3 phase with higher symmetry. Indeed, it has been reported by many researchers that oxygen vacancies form at high temperature during the synthesis of metal

oxides [154–157]. Metastable oxygen-deficient materials at room temperature can be produced by quenching the heated samples in liquid nitrogen. Besides the oxygen vacancies, the quenching process itself might also assist the material to keep its high temperature O3 structure as a metastable structure at room temperature, while the slow-cooled material has enough time to undergo phase transition to a lower symmetry O'3 structure due to the Jahn-Teller distortion.

The electrochemical performance of O3 and O'3 Na-NCA as cathode materials in Na half cells was investigated. Figure 7.2 shows the voltage curves and corresponding differential capacity curves for O3 and O'3 Na-NCA cycled in the voltage range of 1.5 V – 4.5 V. O'3 Na-NCA has a step-like voltage curve, similar to that of O'3 $NaNiO_2$ reported in reference [109]. For O3 Na-NCA, even though voltage steps can be observed, the curve is smoother than the O'3 Na-NCA. This can also be seen from the differential capacity curves. There are multiple peaks in the differential capacity curve of O'3 Na-NCA. The peak position of O3 Na-NCA resembles that of O'3 Na-NCA, nevertheless, the peaks are broader and less intense for O3 Na-NCA than O'3 Na-NCA. O3 NCA also has higher reversible capacity than O'3 NCA. The higher capacity of O3 Na-NCA is attributed to the presence of $Ni^{2+}$ due to oxygen vacancies, as discussed earlier. Compared to $NaNiO_2$ previously reported, both Na-NCA materials show higher first cycle coulombic efficiency, lower irreversible capacity, and better capacity retention, which indicates the beneficial effect of cobalt and aluminum doping.

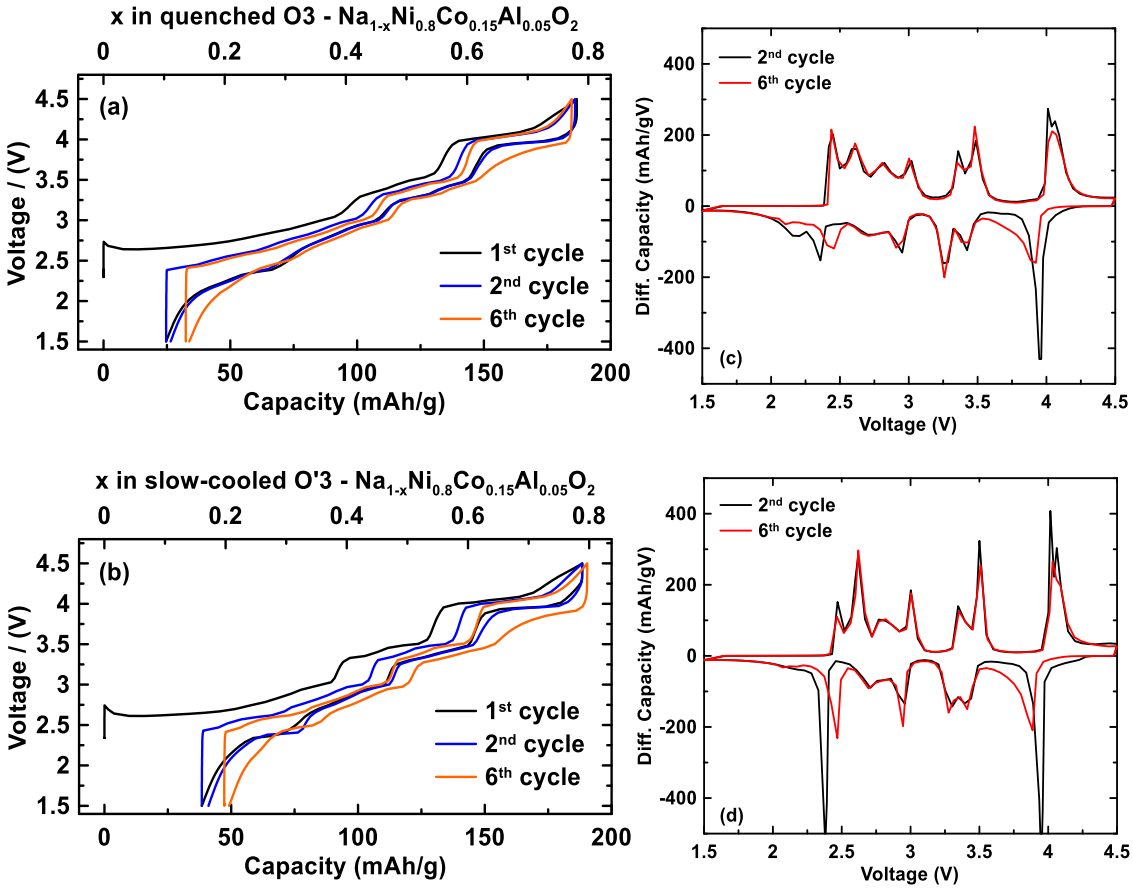


Figure 7.2 Voltage curves and corresponding differential capacity curves of O3 Na-NCA and O'3 Na-NCA.

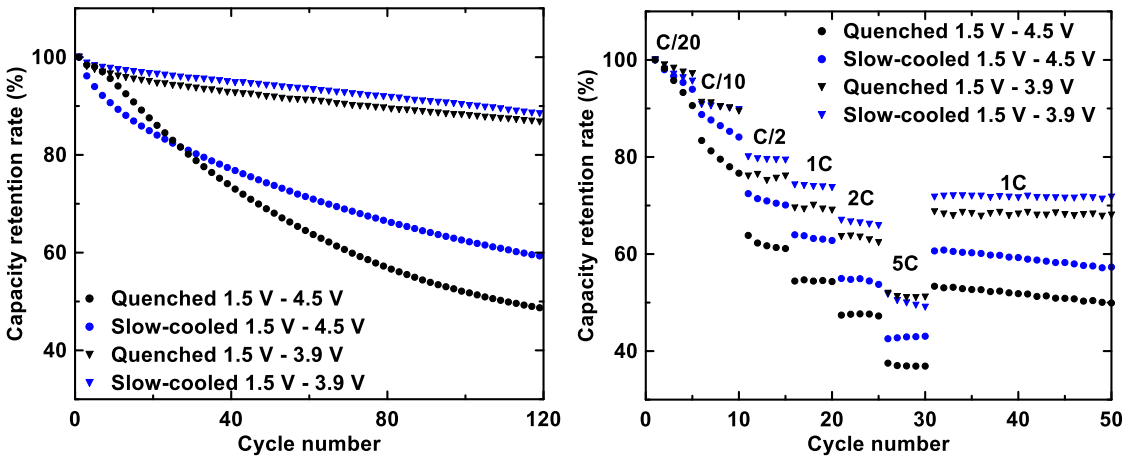


Figure 7.3 Comparison of the cycling performance and rate performance of O3 Na-NCA and O'3 Na-NCA.

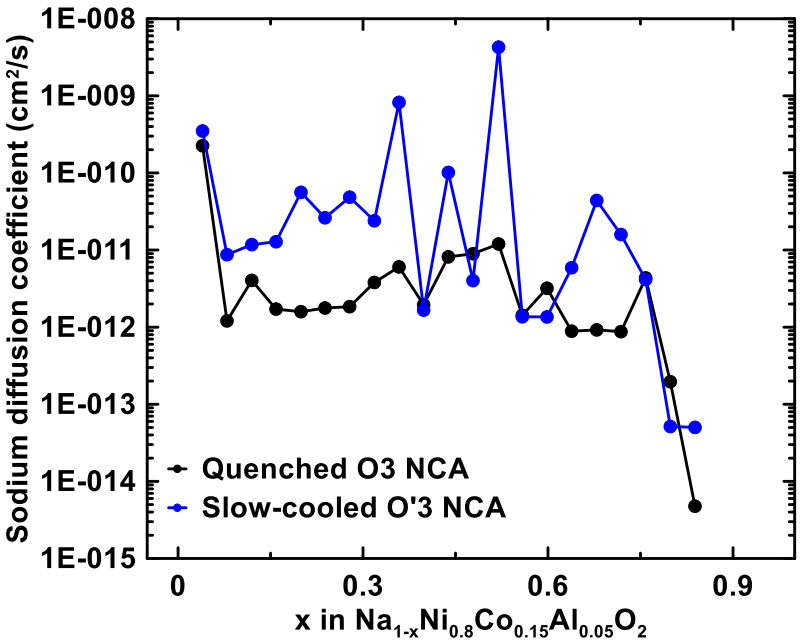


Figure 7.4 Comparison of the sodium diffusion coefficients of O3 Na-NCA and O'3 Na-NCA.

Figure 7.3 shows the cycling performance and the rate performance of O3 and O'3 Na-NCA. When cycled between 1.5 V – 3.9 V, both materials have good capacity retention: ~90% capacity retention after 120 cycles. When cycled between 1.5 V – 4.5 V, capacity fade can be observed for both materials. A slightly better performance was observed for O'3 Na-NCA than O3 Na-NCA. O'3 Na-NCA also has considerably better rate capability than O3 Na-NCA regardless of the cycling voltage range. When cycled between 1.5 V – 3.9 V, O'3 Na-NCA has a capacity retention of 80%, 75%, 65% at C/2, 1C and 2C current rates, while the capacity retention of O3 Na-NCA is 75%, 70%, 60%, respectively. To confirm the better rate performance of O'3 material, GITT measurements were performed. Figure 7.4 shows the sodium diffusion coefficient calculated from GITT measurements during the first charging process for both Na-NCA materials. It can be observed that $D_{Na}$ for O'3 Na-NCA is about an order of magnitude higher than that of O3

Na-NCA, which is consistent with the better rate performance of O'3 Na-NCA. However, $D_{Na}$ appears more erratic for slow-cooled O'3 Na-NCA, due to the step-wise voltage curve. In contrast, $D_{Na}$ for O3 Na-NCA, which has a smoother voltage curve, remains relatively stable until x approaches ~0.75. When x approaches ~0.75, both materials show a drastic decrease in $D_{Na}$, indicating poor sodium diffusion at high voltage. This corresponds to the shrinkage of crystal lattice when ~0.75 of the sodium is removed from the structure, as shown below. The diffusion length calculated from $D_{Na}$ is between 0.6 – 6 μm, similar to the particle size of the synthesized materials.

In order to understand the structural changes that occur during cycling, *in situ* XRD and *ex situ* XRD were performed when Na-NCA electrodes were cycled between 1.5 V - 4.5 V. Figure 7.5 shows simulated XRD patterns of O3($R\bar{3}m$), O'3(C/2m), P3($R\bar{3}m$) and P'3(C/2m) phases with the same cell parameters. These phases are commonly observed during the cycling of O3-type sodium cathode materials [113,158]. The peak positions are similar for all phases. For O3 and P3 phases, the most obvious difference lies in the relative intensity ratio of (104) peak and (015) peak. While the (104) peak is intense and the (015) peak is barely visible for the O3 phase, the opposite is true for the P3 phase. Monoclinic O'3 and P'3 phases can be identified from the splitting of peaks from O3 and P3 phase, respectively. These results are used to identify the *in situ* XRD results below.

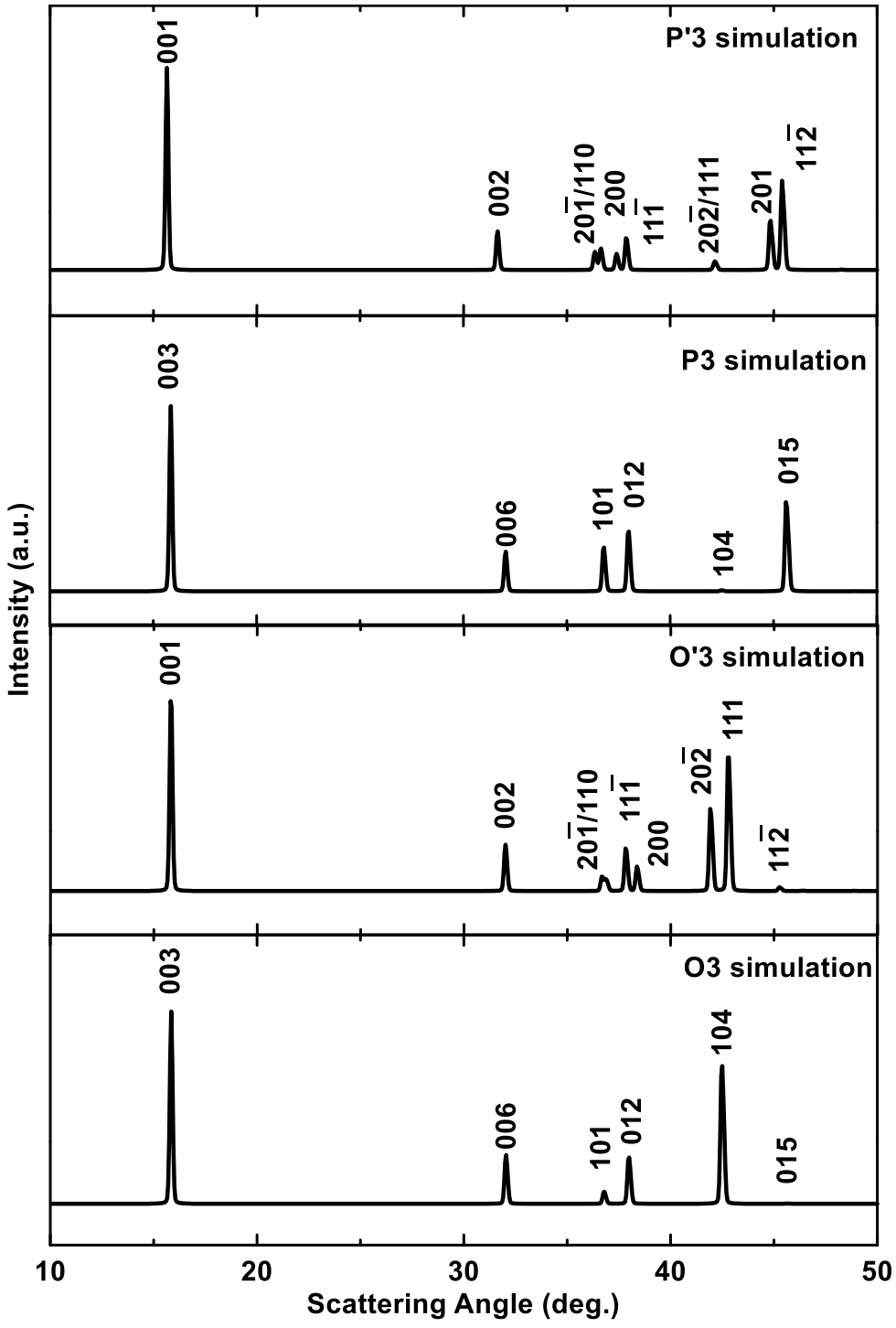


Figure 7.5 Simulated XRD patterns of O3, O'3, P3 and P'3 phases.

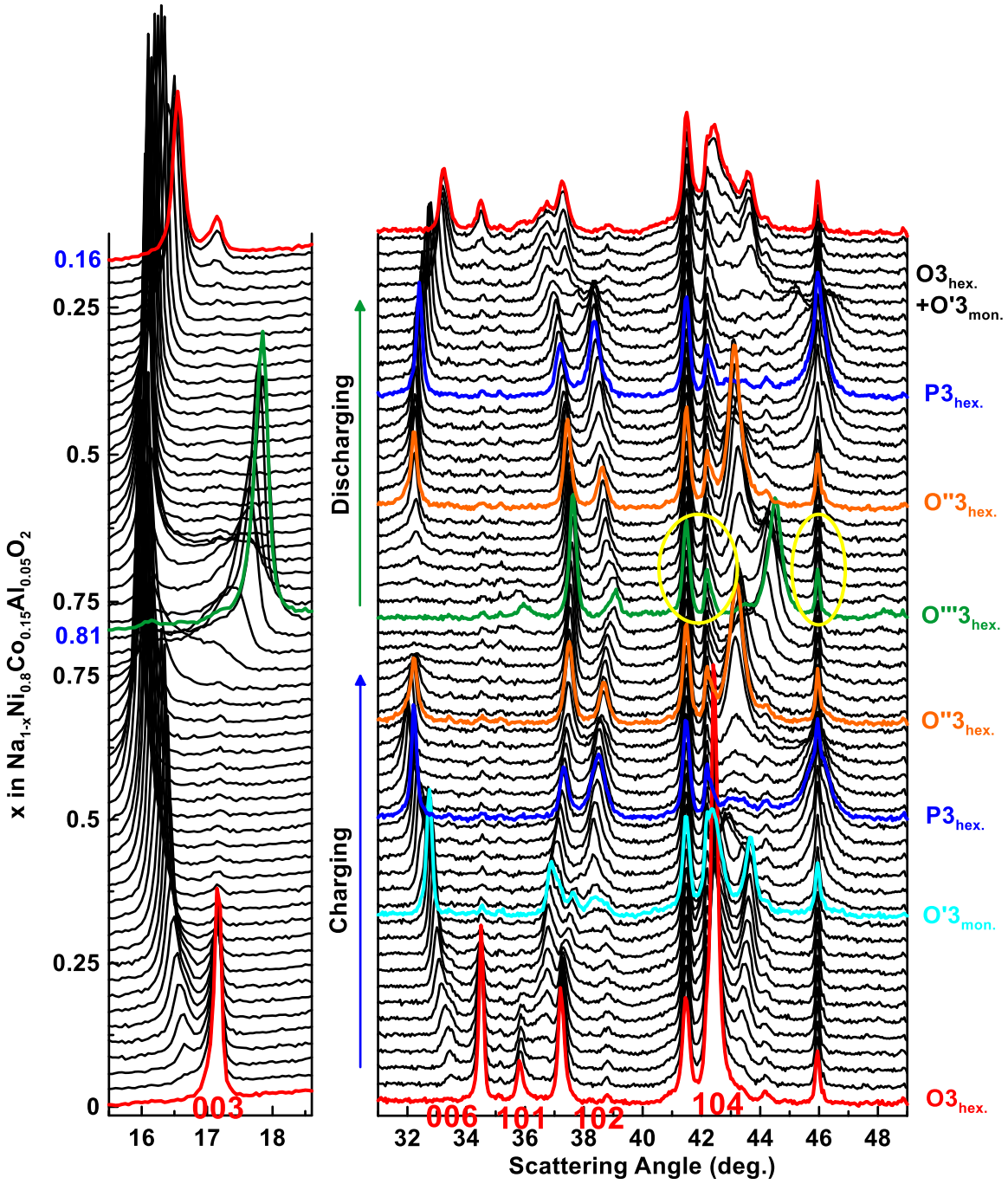


Figure 7.6 Raw XRD patterns measured during the first cycle of the quenched O3 Na-NCA *in situ* cell.

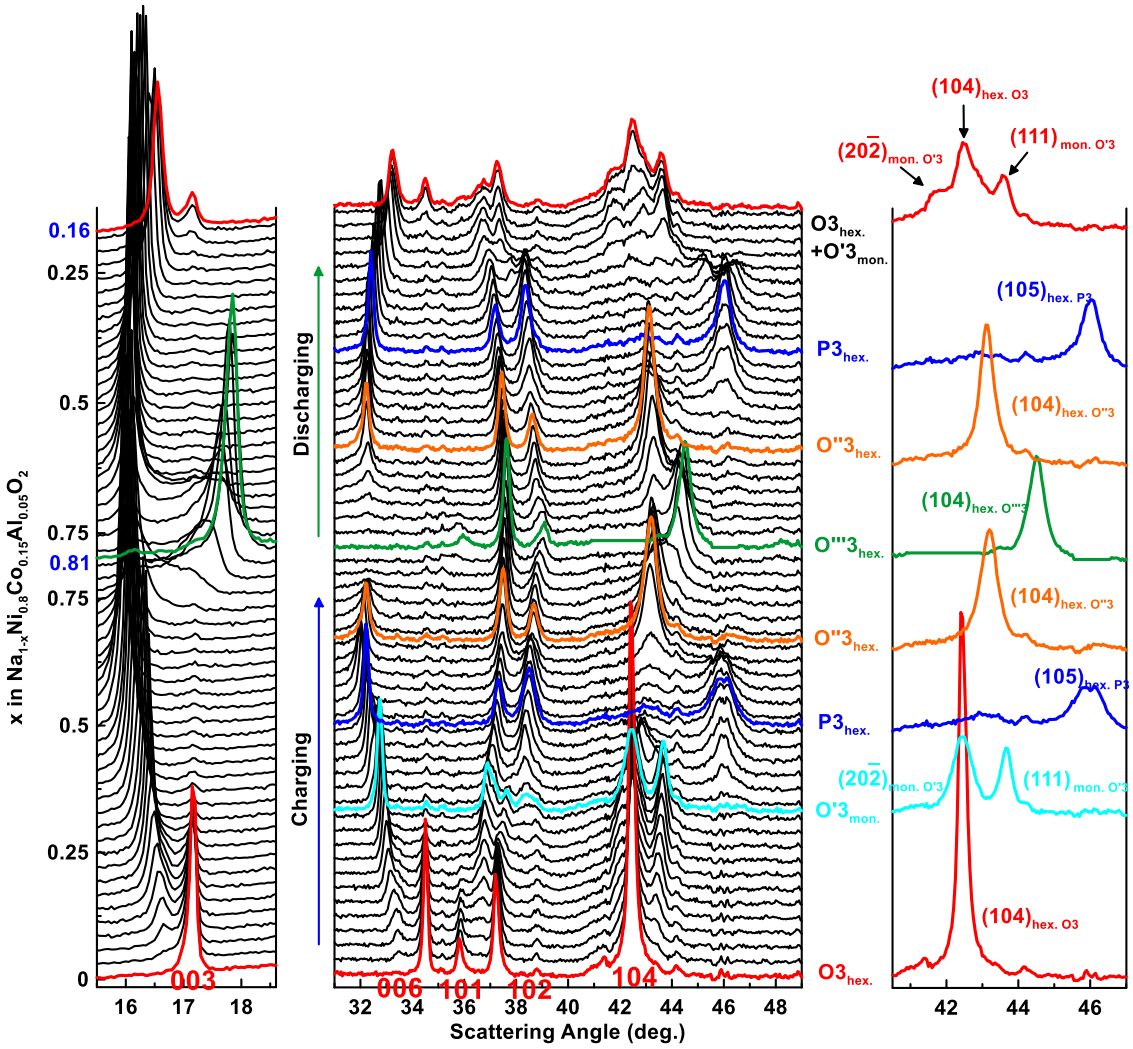


Figure 7.7 Corrected *in situ* XRD patterns measured during the first cycle of O3 Na-NCA.

Figure 7.6 shows the raw data obtained from *in situ* XRD experiments for O3 Na-NCA. Only every second diffraction pattern is shown to prevent confusion. Peaks from the inactive cell components can be observed at ~42° and ~46°. These peaks overlapped with peaks from active phases at some point. For example, the peak at ~46° coincides with the (015) peak, which is essential to differentiate O3 and P3 phases, as discussed above. Therefore the fixed cell peaks were subtracted from all the *in situ* XRD results. Figure 7.7 shows the resulting corrected *in situ* XRD patterns of the O3 Na-NCA *in situ* cell. *In situ*

XRD data for O'3 Na-NCA, shown in Figure 7.8, were similarly corrected to remove cell part peaks from the measured XRD patterns, shown in Figure 7.9.

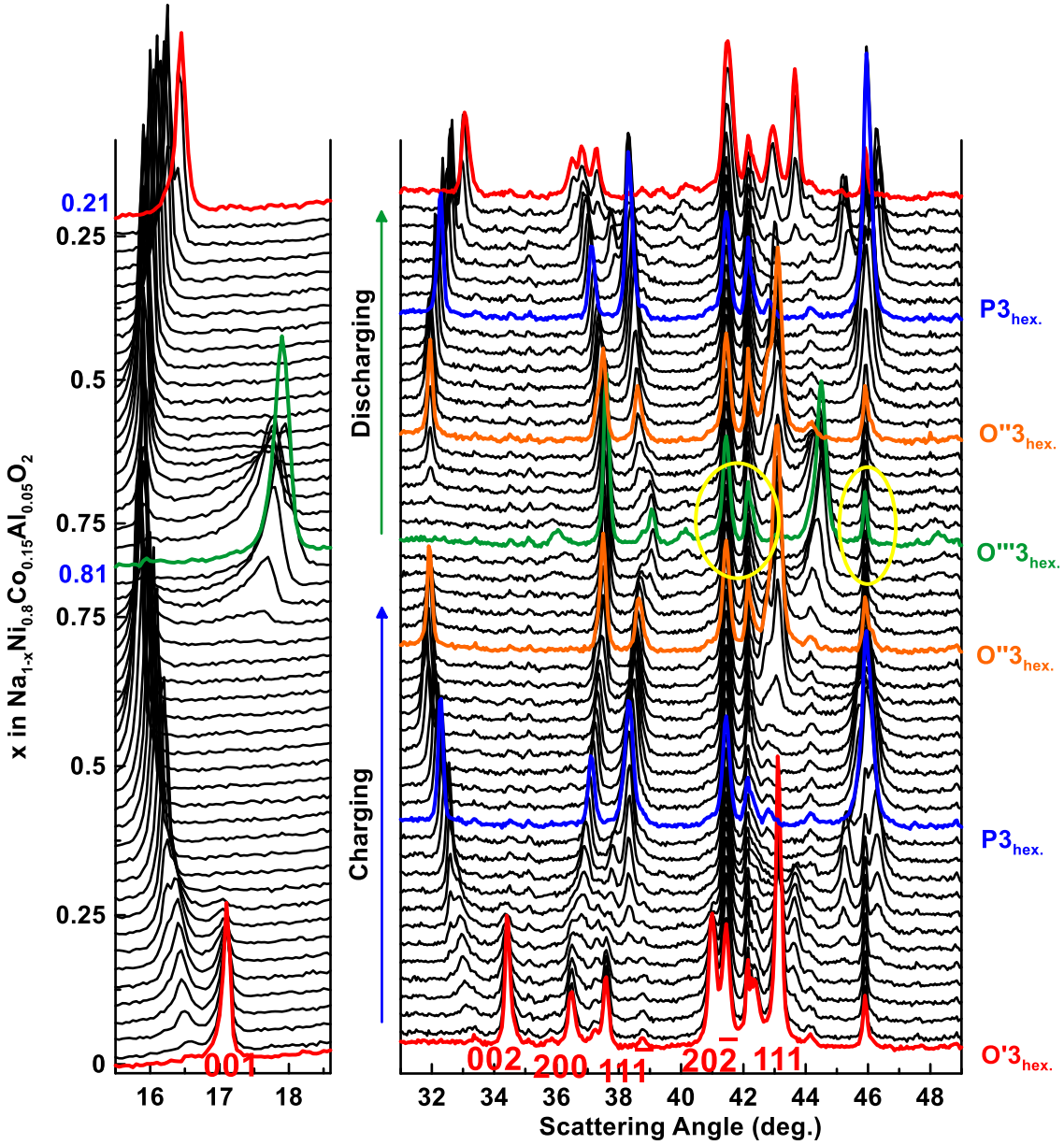


Figure 7.8 Raw XRD patterns measured during the first cycle of the slow-cooled O'3 Na-NCA *in situ* cell.

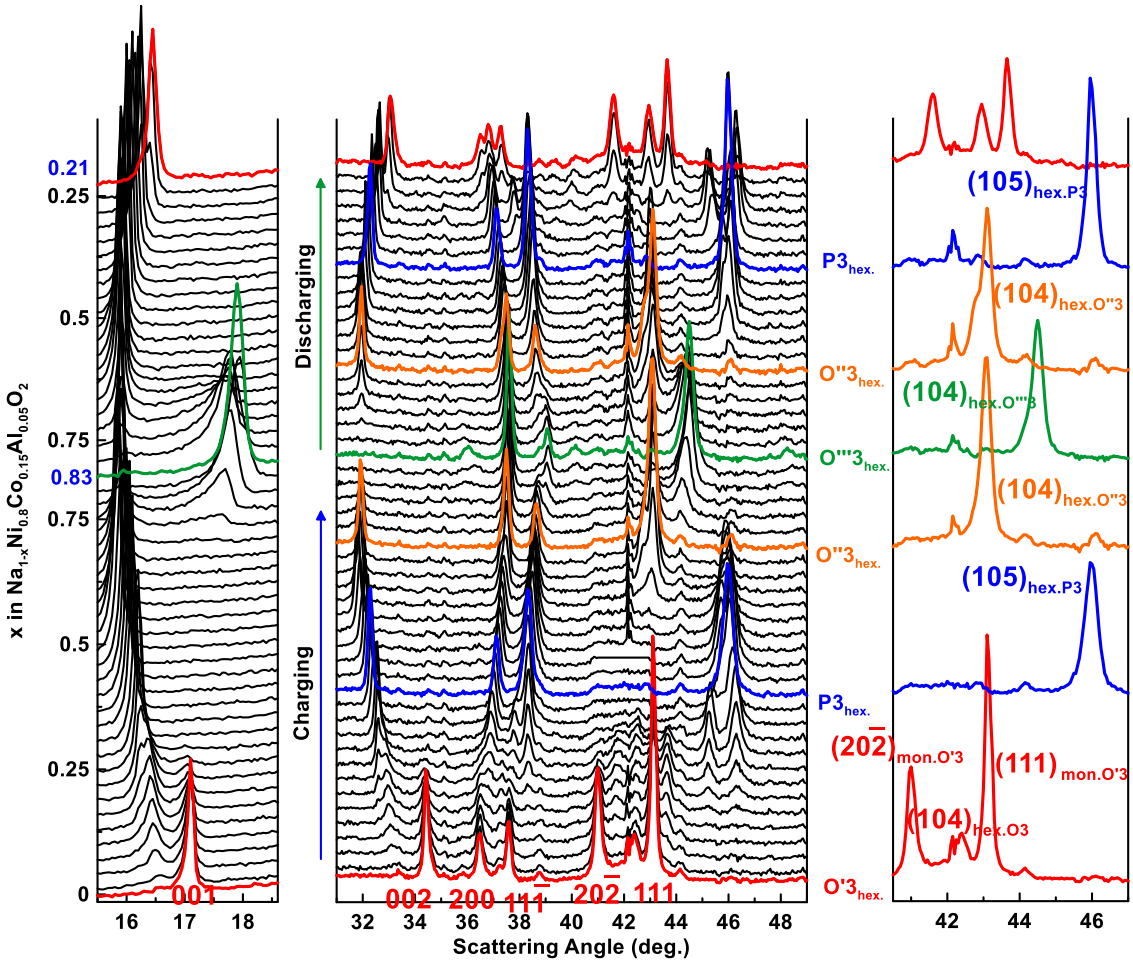


Figure 7.9 Corrected *in situ* XRD patterns measured during the first cycle of O'3 Na-NCA.

It has been reported that when $NaNiO_2$ is made into an electrode coating, a sodium-deficient phase immediately forms even before any electrochemical cycling, which is probably due to the acute hygroscopicity of $NaNiO_2$ [109,149]. Nevertheless for both Na-NCAs, the initial XRD patterns at the bottom of Figure 7.7 and Figure 7.9 are indistinguishable from the synthesized materials. No sodium-deficient phases could be observed in these coatings. This implies that Na-NCA materials are more stable towards humidity exposure than $NaNiO_2$. During the first charge of both Na-NCAs, it can be seen that the (00l) peaks shift to a lower angle, while the (l0l) peaks shift to a higher angle. This

indicates that the *c* axis is expanding and the *a* axis is contracting while Na is being removed. Multiple phases are observed in the cycling process. For O3 Na-NCA, upon charging, the pristine phase disappears and a monoclinic O'3 phase forms. Further charging transforms the O'3 phase to a P3 phase. The P3 phase then gradually transitions back to a hexagonal O3 phase. At the end of charging to 4.5 V, *in situ* XRD shows another hexagonal O3 phase with a very small interlayer distance, as can be seen by the (003) peak shifting to higher angle. The contraction of the lattice at the end of charge also agrees with previous papers [144,158]. During the first discharge, the above process is mostly reversible, except that the material does not completely transition back to pure O3 phase, but a mixture of hexagonal O3 and monoclinic O'3 phase. This O3(O'3) – P3– O3 phase transition process also occurs for O'3 Na-NCA, as shown in the *in situ* XRD patterns. However, a monoclinic P'3 phase is observed during the charge/discharge of O'3 Na-NCA, which is absent during the charge/discharge of O3 Na-NCA.

Overall, the phase transitions are consistent with many other O3-$NaMO_2$ (M = one or more transition metal) systems reported [144,158]. In recent publications, both galvanostatic charge/discharge and XRD results show that the pristine $NaNiO_2$ phase cannot be obtained by discharging a charged $Na_{1-x}NiO_2$ cell. Instead, a sodium-deficient phase, identified as $Na_{0.91}NiO_2$, was obtained [109,149]. This phenomenon has been ascribed to the increased kinetic barrier as the sodium concentration approaches its pristine state [109,149]. O'3 Na-NCA exhibits similar properties: it has a high irreversible capacity and exhibits an irreversible structure transition, as shown in Figure 7.9, in which the discharged product is a completely different phase than the original phase. In contrast, some pristine phase can be restored at the end of discharge of O3 Na-NCA, suggesting a

more reversible reaction, as also evidenced by its smaller irreversible capacity. The evolution of the interslab distances and metal-metal distances during *in situ* XRD cycling for both materials is summarized in Figure 7.10. The same general trend is observed for both materials. Initially the interslab distances increase due to the increased oxygen-oxygen repulsion as sodium is deintercalated. When ~80% of sodium is removed, a drastic contraction in the interlayer space occurs. Cycling at voltages above which this contraction occurs results in capacity fade, as mentioned above. The metal-metal distances also decrease as sodium content decreases. The reverse process occurs when discharging.

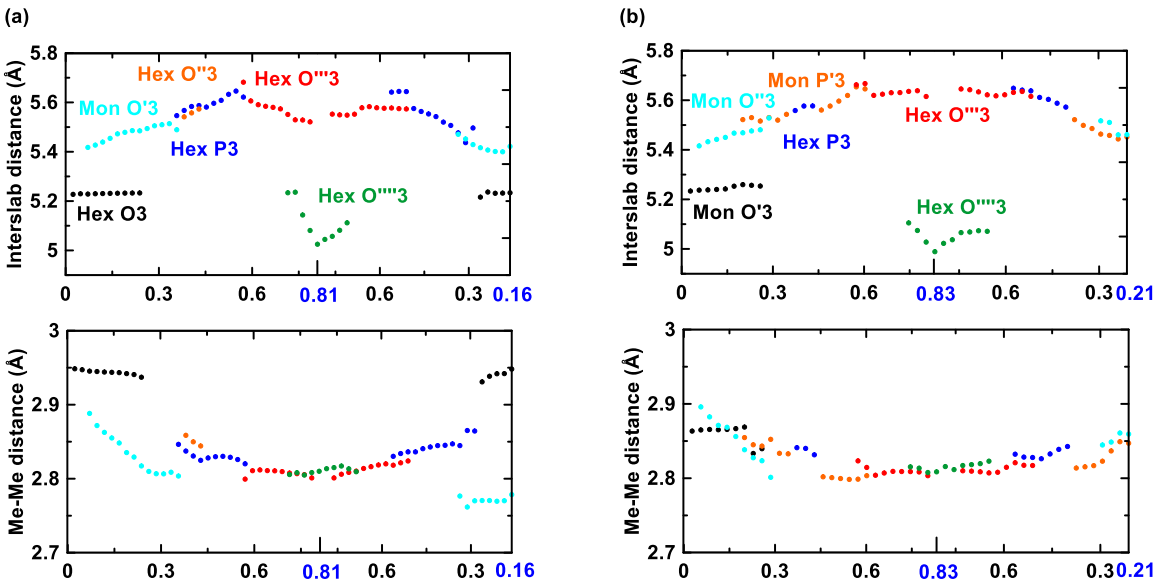


Figure 7.10 The evolution of the interslab distances and metal-metal distances during *in situ* XRD cycling of (a) O3 Na-NCA and (b) O'3 Na-NCA.

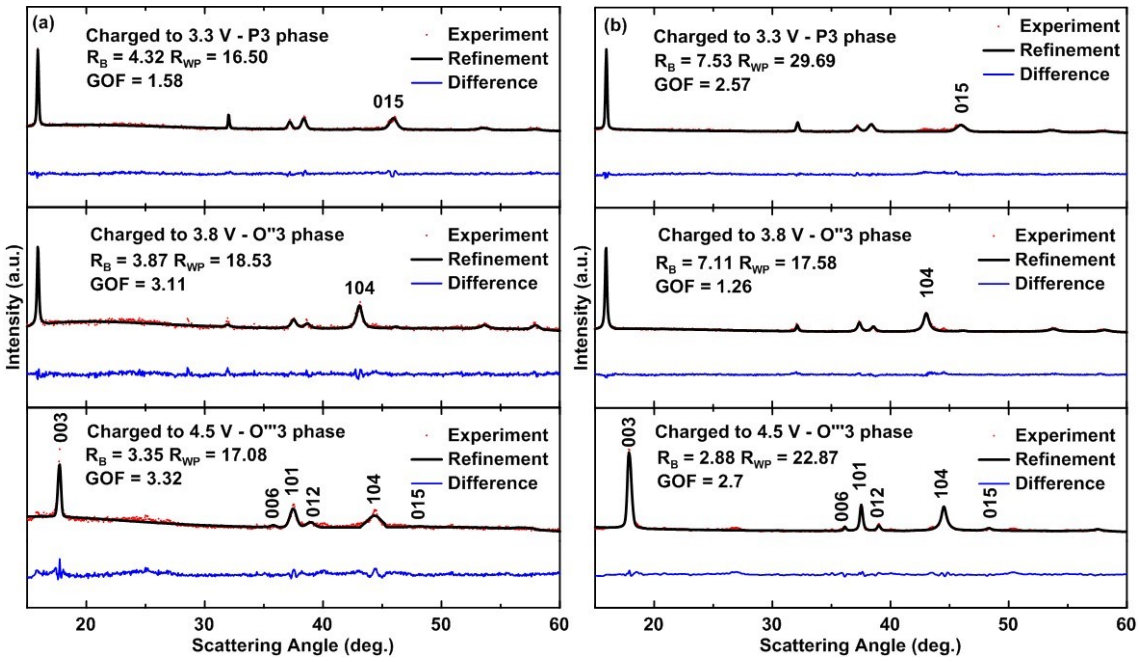


Figure 7.11 *Ex situ* XRD patterns and Rietveld refinements of electrodes cycled to different cutoff voltages for (a) O3 Na-NCA and (b) O'3 Na-NCA.

Since the *in situ* XRD measurements were performed during cycling under non-equilibrium conditions, coin cells were charged to indicated voltages and held at the voltage for 10 hours to obtain higher quality *ex situ* XRD patterns under equilibrium conditions. Figure 7.11 shows the *ex situ* XRD patterns of the two Na-NCA materials at different voltages. Here, only single phase was present in the *ex situ* XRD results. The *ex situ* XRD patterns were well-fitted with O3 or P3 structures for all the materials, which confirms the trend of O3(O'3)-P3(P'3)-O3 phase change and the drastic contraction at the end of charge observed in *in situ* XRD patterns. Crystal data for refinements are shown in Table 7.2 and Table 7.3. The sodium content is variable during the refinement and the refined sodium occupancy agrees very well with the sodium content measured by electrochemical desodiation. Lattice parameters obtained also confirm the results shown in Figure 7.10.

Table 7.3 Crystal data of the slow-cooled $NaNi_{0.8}Co_{0.15}Al_{0.05}O_{\delta}$ at different state-of-charge obtained by Rietveld refinements. Data with * are allowed to vary freely during refinements.

| Slow-cooled $NaNi_{0.8}Co_{0.15}Al_{0.05}O_{\delta}$ charged to 3.5 V - space group $R\bar{3}m$ (No. 166) | | | | |
|---|---|---|---|---|
| Atom | x | y | z | Occupancy |
| Na | 0 | 0 | 0.170±0.002* | 0.73±0.02* |
| Ni | 0 | 0 | 0 | 0.8 |
| Co | 0 | 0 | 0 | 0.15 |
| Al | 0 | 0 | 0 | 0.05 |
| O | 0.333 | 0.666 | 0.060±0.001* | 2 |
| $a$ = 2.829±0.003* Å, $c$ = 16.81±0.02* Å | | | | |

| Slow-cooled $NaNi_{0.8}Co_{0.15}Al_{0.05}O_{\delta}$ charged to 3.8 V - space group $R\bar{3}m$ (No. 166) | | | | |
|---|---|---|---|---|
| Atom | x | y | z | Occupancy |
| Na | 0 | 0 | 0.5 | 0.43±0.02* |
| Ni | 0 | 0 | 0 | 0.8 |
| Co | 0 | 0 | 0 | 0.15 |
| Al | 0 | 0 | 0 | 0.05 |
| O | 0 | 0 | 0.234±0.001* | 2 |
| $a$ = 2.807±0.001* Å, $c$ = 16.90±0.02* Å | | | | |

| Slow-cooled $NaNi_{0.8}Co_{0.15}Al_{0.05}O_{\delta}$ charged to 4.5 V - space group $R\bar{3}m$ (No. 166) | | | | |
|---|---|---|---|---|
| Atom | x | y | z | Occupancy |
| Na | 0 | 0 | 0.5 | 0.26±0.02* |
| Ni | 0 | 0 | 0 | 0.8 |
| Co | 0 | 0 | 0 | 0.15 |
| Al | 0 | 0 | 0 | 0.05 |
| O | 0 | 0 | 0.272±0.002* | 2 |

$a$ = 2.823±0.003* Å, $c$ = 15.17±0.03* Å

Table 7.4 Crystal data of the quenched $NaNi_{0.8}Co_{0.15}Al_{0.05}O_{\delta}$ at different state-of-charge obtained by Rietveld refinements. Data with * are allowed to vary freely during refinements.

| Quenched $NaNi_{0.8}Co_{0.15}Al_{0.05}O_{\delta}$ charged to 3.3 V - space group $R\bar{3}m$ (No. 166) | | | | |
|---|---|---|---|---|
| Atom | x | y | z | Occupancy |
| Na | 0 | 0 | 0.155±0.001* | 0.83±0.03* |
| Ni | 0 | 0 | 0 | 0.8 |
| Co | 0 | 0 | 0 | 0.15 |
| Al | 0 | 0 | 0 | 0.05 |
| O | 0.333 | 0.666 | 0.060±0.001* | 2 |

$a$ = 2.831±0.002* Å, $c$ = 16.763±0.001* Å,

| Quenched $NaNi_{0.8}Co_{0.15}Al_{0.05}O_{\delta}$ charged to 3.8 V - space group $R\bar{3}m$ (No. 166) | | | | |
|---|---|---|---|---|
| Atom | x | y | z | Occupancy |
| Na | 0 | 0 | 0.5 | 0.42±0.01* |
| Ni | 0 | 0 | 0 | 0.8 |
| Co | 0 | 0 | 0 | 0.15 |
| Al | 0 | 0 | 0 | 0.05 |
| O | 0 | 0 | 0.2272±0.0009* | 2 |

$a$ = 2.8083±0.0007* Å, $c$ = 16.727±0.008* Å,

| Quenched $NaNi_{0.8}Co_{0.15}Al_{0.05}O_{\delta}$ charged to 4.5 V - space group $R\bar{3}m$ (No. 166) | | | | |
|---|---|---|---|---|
| Atom | x | y | z | Occupancy |
| Na | 0 | 0 | 0.5 | 0.16±0.02* |
| Ni | 0 | 0 | 0 | 0.8 |
| Co | 0 | 0 | 0 | 0.15 |
| Al | 0 | 0 | 0 | 0.05 |
| O | 0 | 0 | 0.264±0.001* | 2 |

$a$ = 2.8027±0.0010* Å, $c$ = 14.903±0.010* Å,

Figure 7.12 compares the *ex situ* XRD patterns of the two materials after one cycle and after ten cycles. After one cycle, O3 Na-NCA consists of a mixture of pristine O3 and an intermediate O'3 phases, in agreement with the *in situ* XRD results. The ratio of the two phases is determined to be 33:67 by Rietveld refinement. This ratio decreased to 18:82 after ten cycles, as can be clearly seen from the XRD patterns from a reduction in O3 phase peak intensity. This suggests that the original O3 structure gradually transitions to O'3 phase during cycling, possibly because O'3 phase is more stable at room temperature. For O'3 Na-NCA, there is little change in the *ex situ* XRD patterns after one cycle and after 10 cycles. A single O'3 phase is present in the XRD patterns. This structural stability might also explain the better cycling performance of O'3 Na-NCA compared to O3 Na-NCA.

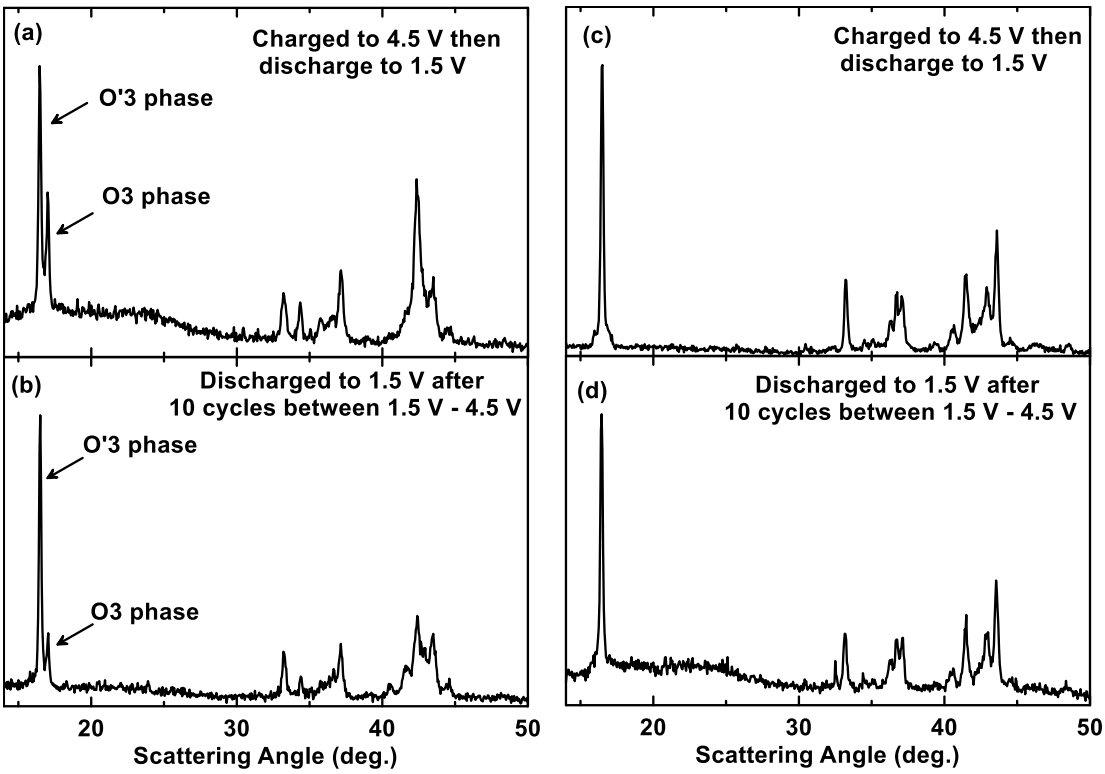


Figure 7.12 *Ex situ* XRD patterns of (a) an O3 Na-NCA electrode after one cycle, (b) an O3 Na-NCA electrode after ten cycles, (c) an O'3 Na-NCA electrode after one cycle, and (d) an O'3 Na-NCA electrode after ten cycles.

## 7.4 Conclusion

$NaNi_{0.8}Co_{0.15}Al_{0.05}O_2$ (Na-NCA) materials with hexagonal O3 or monoclinic O'3 structure were synthesized for the first time by either quenching or slow cooling heated precursors. Quenched Na-NCA preserves more oxygen vacancies, leading to the presence of $Ni^{2+}$, less Jahn-Teller $Ni^{3+}$ ions and an O3 structure. The structural evolution of O3 and O'3 Na-NCA during cycling were studied using *in situ* and *ex situ* XRD. It was found that O'3 Na-NCA has better cycling performance as a result of a more stable structure at room temperature. Compared to undoped $NaNiO_2$, both types of Na-NCA have improved cycling performance and are more stable when exposed to ambient air. These results may provide a new approach to develop novel sodium ion battery cathode materials.

# CHAPTER 8 STABILIZING $NaCrO_2$ BY SODIUM SITE DOPING WITH CALCIUM

## 8.1 Introduction

O3-type $NaCrO_2$ has relatively high average voltage and good energy density among all sodium transition metal oxides [159,160]. Moreover, Xia et al. showed that $NaCrO_2$ has great thermal stability and there is virtually no reactivity between desodiated $Na_{0.5}CrO_2$ and non-aqueous electrolyte up to 350°C [78]. They attributed the lack of exothermic behavior to the minimal oxygen release of $Na_{0.5}CrO_2$ [78]. Hatchard et al. demonstrated a high coulombic efficiency of 99.97% for $NaCrO_2$/$NaCrO_2$ symmetric cells, the highest coulombic efficiency reported so far for sodium ion batteries materials [77]. Interestingly, the lithium counterpart, $LiCrO_2$, is inactive in lithium cells, despite the same transition metal and similar morphology possessed by $NaCrO_2$ and $LiCrO_2$ [75]. This phenomenon is attributed to the different size of interstitial spaces in $NaCrO_2$ and $LiCrO_2$ structures. The irreversible migration of chromium ions into the tetrahedral sites in lithium layer of $LiCrO_2$ causes the material to be inactive after the first charge [75]. Such migration is less favorable for $Na_{1-x}CrO_2$ when $x \leq 0.5$ due to the larger tetrahedral sites in $NaCrO_2$ [82,161]. Further removal of sodium ($x > 0.5$) also makes the material to gradually become inactive [82,161]. Therefore, previous work limited the desodiation process to $Na_{1-x}CrO_2$ ($x = \sim 0.5$) in order for $NaCrO_2$ to cycle well [159,160]. A capacity fade of ~20% in 50 cycles is usually observed for $NaCrO_2$ in organic solvents [160,162,163]. Some research regarding improving the capacity retention of $NaCrO_2$ have been published. Ding et al. and Yu et al. reported carbon coated $NaCrO_2$ with enhanced cycling performance [160,162]. Tsuchiya et al. used ball-milling and reheating to introduce more grain boundaries in

$NaCrO_2$. They demonstrated that the enriched grain boundaries could suppress the O3-P3 phase transition, resulting in better cyclability [163].

While substantial work on sodium layered oxides so far has been conducted on transition metal layer doping, there has been few reports on sodium layer doping. Cation mixing in the alkaline metal layer is well known to be detrimental to the battery performance, with the classic example of Li/Ni mixing in cathode materials for lithium ion batteries [121]. Due to the blocked alkaline ion diffusion pathway, cation mixing results in decreased capacity and increased hysteresis, and is usually avoided [75,164]. Recently, Matsui et al. and Han et al. reported the structure and electrochemistry of calcium substituted P2-$Na_xCoO_2$ [165,166]. The ionic radius of calcium (~1 Å) is similar to that of sodium (~1.03 Å) and is significantly larger than most first row transition metals (0.5 – 0.7 Å). Therefore, it is energetically more favorable for calcium to occupy sites in the sodium layers, instead of the transition metal layers. P2-$Na_xCoO_2$ is known for its step-like profiles in voltage versus capacities plots, due to sodium/vacancy ordering during the (de)intercalation of sodium. Calcium substitution was reported to hinder such ordering, leading to smoothed voltage curves and improved cyclability, at the expense of a slight loss of capacity [165,166]. Such a strategy of using sodium site substitution is attractive and might presents opportunities for the development of new sodium cathode materials. In this study, calcium-substituted $Na_{1-2x}Ca_xCrO_2$ was synthesized and characterized for the first time. It is shown that calcium doping not only improves cycling performance, but also surprisingly enhances air-stability.

## 8.2 Experimental

$Na_{1-2x}Ca_xCrO_2$ were prepared by mixing stoichiometric quantities of $Na_2CO_3$ (99.0%, Sigma Aldrich), CaO (99.9%, Sigma Aldrich), and $Cr_2O_3$ (98.0%, Sigma Aldrich) using a SPEX 8000 mill. Generally, four 7/16 inch stainless steel balls and ~6g of powders were milled for one hour in air. The resulting powders were then pressed into pellets and heated under flowing Ar (with an upstream Ti sponge) at 900 °C for 3 hours. Samples were then quenched to room temperature and transferred to Ar-filled glovebox without air exposure.

Electrode preparation was carried out in an Ar-filled glove box. Slurries were made by mixing active material, PVDF binder (HSV 900, KYNAR), and carbon black (Imerys Graphite and Carbon) in an 8:1:1 weight ratio with an appropriate amount of N-methyl-2-pyrrolidone (Sigma Aldrich, anhydrous 99.5%). These components were mixed with two 0.5 inch tungsten carbide balls in a Retsch PM200 rotary mill (100 rpm, 1 hour) to create a uniform slurry. Typically, ~0.4 g of active material was loaded in the milling jar for making slurry. The slurry was then coated onto aluminum foil with a coating bar having a ~0.015 cm gap and dried under vacuum at 80°C overnight. Circular electrodes were punched from the coating and incorporated into 2325-type coin cells in an Ar-filled glove box. Na disks punched from thin foil (~0.3 mm) rolled from sodium ingot (Sigma Aldrich, ACS reagent grade) were used as counter/reference electrodes. Two Celgard 2300 and one blown microfiber separator (3M Company) were used as separators. 1 M $NaClO_4$ (Aldrich, 98%) in propylene carbonate (PC, BASF) with 2% monofluoroethylene carbonate (FEC, BASF) was used as electrolyte. Cells were cycled with a Maccor Series 4000 Automated

Test System (Maccor Inc., Tulsa OK). The ambient cycling temperature was 30.0°C (±0.1°C).

X-ray diffraction (XRD) measurements were made using a Rigaku Ultima IV Diffractometer equipped with a Cu anode x-ray tube, a scintillation detector, and a diffracted beam monochromator. All samples were loaded into a gas-tight sample holder (DPM Solutions) in argon atmosphere for XRD measurements. For *ex-situ* measurements, coin cells cycled to different cutoff voltages were stopped and opened in glovebox. The electrodes were recovered from the cells and rinsed with dimethyl carbonate (DMC, BASF) several times. The recovered materials were then transferred to a zero-background silicon wafer and sealed in the gastight sample holder for the *ex situ* XRD measurements. Scanning electron microscope (SEM) measurements were performed using a field emission scanning electron microscope (TESCAN MIRA 3). Transmission electron microscopy (TEM) images were taken using a Philips CM30 electron microscope. TEM sample powders were sonicated for 5 minutes in hexane and then dropped onto a carbon coated grid for measurements.

**8.3 Results and Discussion**

Figure 8.1 shows the XRD patterns of the synthesized $Na_{1-2x}Ca_xCrO_2$ samples. Phase-pure samples with an O3 structure were obtained for $x \leq 0.05$. For samples with $x \geq 0.07$, $CaCr_2O_4$ and $Cr_2O_3$ impurities become visible in the XRD profiles, as shown in Figure 8.1 (b). This indicates a limited solid solution range under the synthesis conditions used here. Rietveld refinements were performed on phase-pure samples with $x \leq 0.05$. The O3-type α-$NaFeO_2$ structure was used for the refinements. In initial refinements Na and Cr

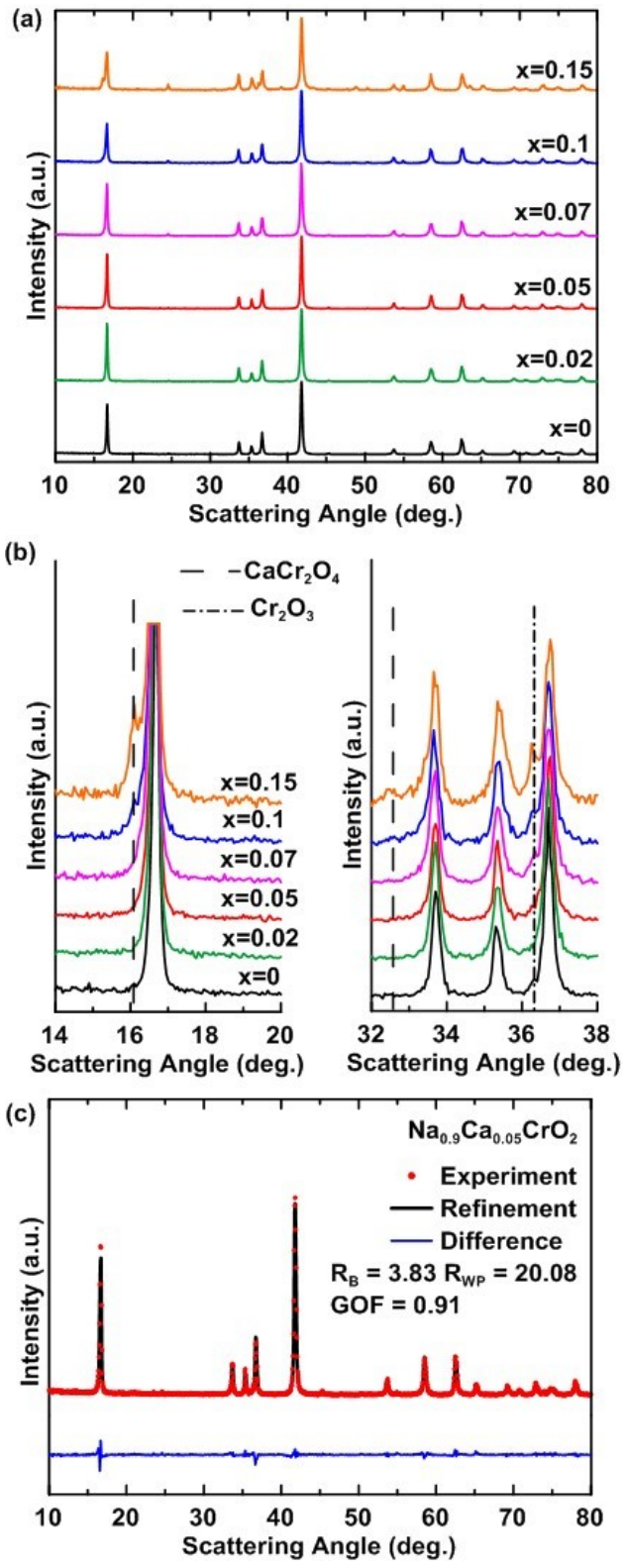


Figure 8.1 (a) XRD patterns of synthesized $Na_{1-2x}Ca_xCrO_2$ series. (b) Enlarged XRD patterns. (c) Rietveld refinement of $Na_{0.9}Ca_{0.05}CrO_2$.

were allowed to mix, however this resulted in a negative occupancy of Na/Cr in Cr/Na sites. The same phenomenon was observed when Ca and Cr were allowed to mix. This indicates the large size difference between Na/Ca and Cr tends to make cation mixing unfavorable. This suggests that calcium ions are only located in sodium sites, consistent with previous studies of calcium doped $Na_xCoO_2$. Therefore cation mixing was not considered in the final refinements. Reasonably good fits with Bragg R values less than 5 were obtained for calcium-substituted samples. An example of a refined pattern is shown in Figure 8.1(c) for the composition with x = 0.05. Previous studies have shown that dopant may cause a reduction in the grain size of the O3 phase when transition metal is doped into $NaCrO_2$ [167]. It is also believed that the improved cyclability of transition metal doped $NaCrO_2$ may be a consequence of reduced grain size [167]. Such phenomenon is not observed in this study as the compounds synthesized in the $Na_{1-2x}Ca_xCrO_2$ ($x \leq 0.05$) series have identical grain sizes (~30 nm) as calculated from XRD patterns.

Figure 8.2(a-b) shows the SEM images of $NaCrO_2$ and $Na_{0.9}Ca_{0.05}CrO_2$. Both materials consist of ~300 nm plates with hexagonal morphology. There are no observable impurity phases in the SEM images. Figure 8.2(c-d) shows the TEM images and corresponding selected area electron diffraction (SAED) patterns of $NaCrO_2$ and $Na_{0.9}Ca_{0.05}CrO_2$. The electron diffraction patterns indicate the crystal structure is similar for both samples. The SAED patterns can be indexed as [001] zone axis for both samples. Hexagonally arranged diffraction spots were indexed to O3 structure (*R-3m*). EDS analysis were also conducted on individual plates. For $Na_{0.9}Ca_{0.05}CrO_2$, 10 randomly selected particles had the same Ca/Cr ratio (~0.05). It is therefore reasonable to conclude that the composition of the plates is fairly homogeneous.

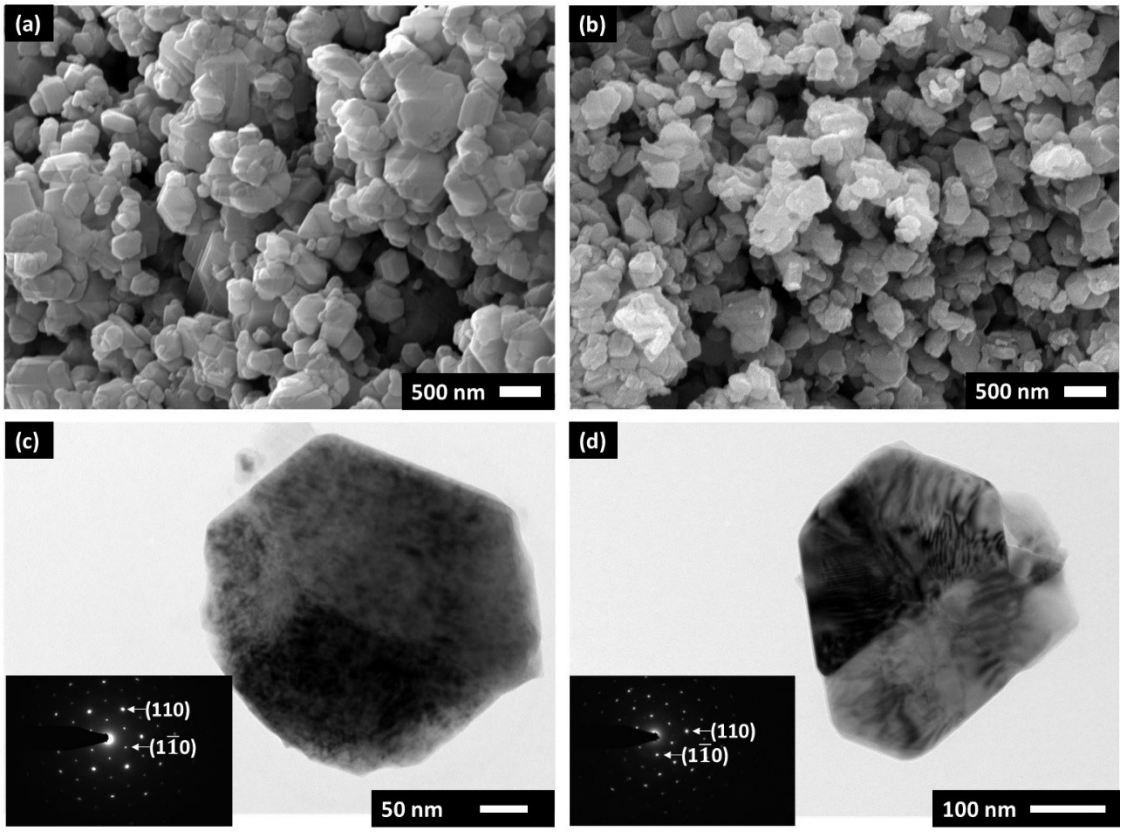


Figure 8.2 (a) SEM image of $NaCrO_2$. (b) SEM image of $Na_{0.9}Ca_{0.05}CrO_2$. (c) TEM image of $NaCrO_2$. (d) TEM image of $Na_{0.9}Ca_{0.05}CrO_2$.

It has been reported that $NaCrO_2$ can be cycled with good reversibility with an upper cutoff voltage of 3.6 V [75]. Cycling beyond this point causes significant irreversible capacity and poor cyclability [82,161]. This is also demonstrated in Figure 8.3, where the voltage-capacity curve of $NaCrO_2$ and $Na_{0.9}Ca_{0.05}CrO_2$ cycled in different voltage ranges are shown. When cycled between 2 V – 3.6 V, $NaCrO_2$ has a reversible capacity of 120 mAh/g and an irreversible capacity less than 10 mAh/g. When the cell was charged to 3.7 V, both reversible and irreversible capacities slightly increase. As the upper cutoff voltage increases to 3.8 V, an irreversible capacity of 100 mAh/g is obtained with large hysteresis. Further charging to 4 V, where almost all the sodium has been removed from the structure,

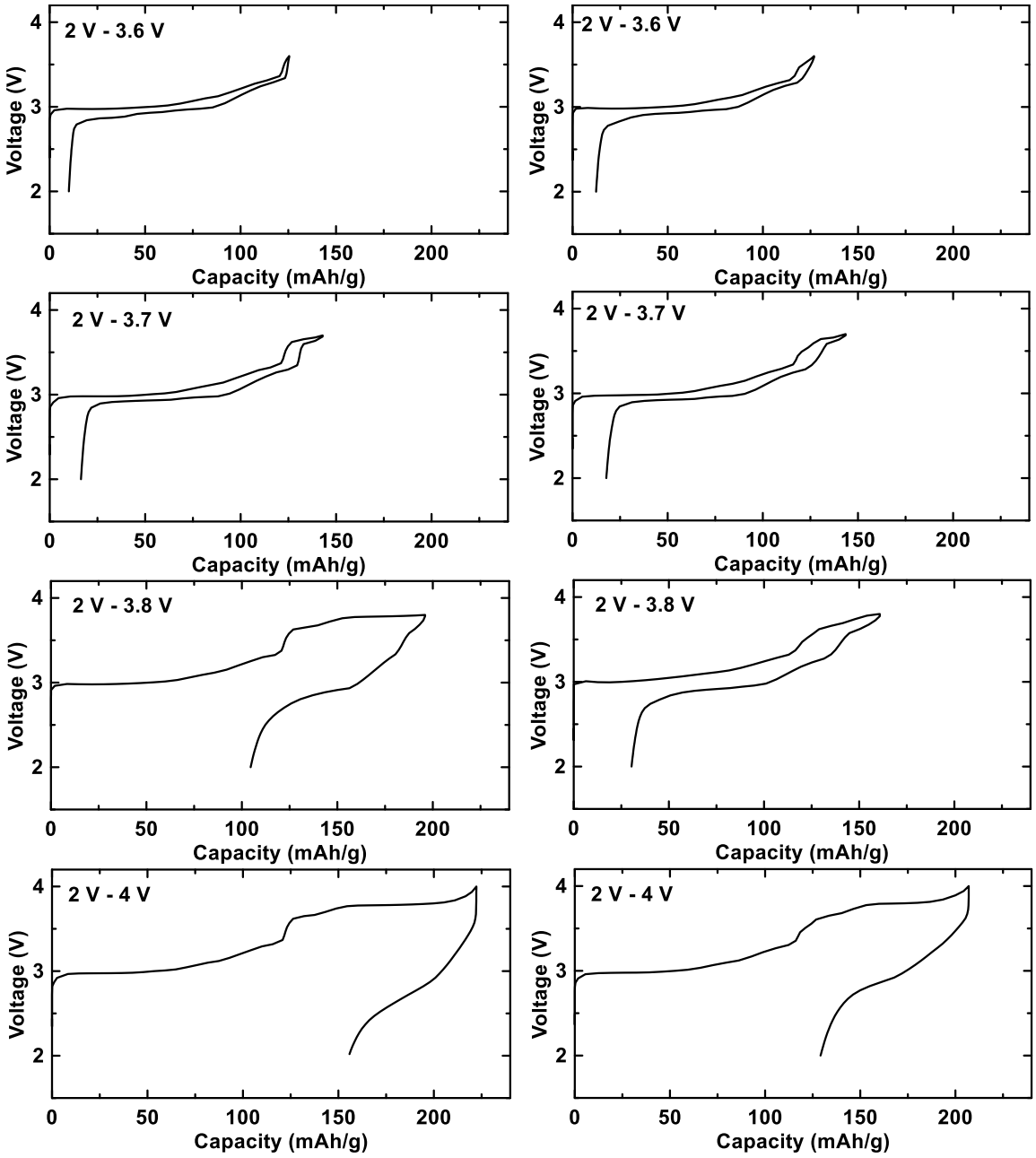


Figure 8.3 Voltage-capacity curve of NaCrO2 (left) and $Na_{0.9}Ca_{0.05}CrO_2$ (right) in different voltage ranges.

results in significantly increased hysteresis and decreased capacity. For $Na_{0.9}Ca_{0.05}CrO_2$, similar behavior can be observed when it is cycled between 2 V – 3.6 V and 2 V – 3.7 V. However, when cycled between 2 V – 3.8 V and 2 V – 4 V, $Na_{0.9}Ca_{0.05}CrO_2$ has higher reversible capacity and smaller hysteresis, compared to $NaCrO_2$ cycled in the same voltage

range. The reason for this improvement is unclear. It is speculated that calcium-substitution results in a more stable structure during sodium (de)intercalation, as will be shown below. It might also be possible that the $Ca^{2+}$ prevents the migration of chromium ions into the sodium layer due to the stronger electrostatic repulsion resulting from the 2+ charge of the $Ca^{2+}$ ion. The voltage curves of $Na_{0.9}Ca_{0.05}CrO_2$ also have less distinct plateaus compared to $NaCrO_2$. This can be easily seen in the differential capacity curves shown in Figure 8.4, where less intense and broader peaks are observed for $Na_{0.9}Ca_{0.05}CrO_2$.

Figure 8.5(a-b) shows the cycling performance of $NaCrO_2$ and $Na_{0.9}Ca_{0.05}CrO_2$. After 50 cycles in the voltage range of 2 V – 3.6 V, 83.0% of initial capacity is retained for $NaCrO_2$. This number is consonant with other research. When the cycling voltage range is increased to 2 V – 3.7 V, the initial capacity slightly increased but capacity retention became worse, with only ~77.8% of initial capacity left after 50 cycles. $Na_{0.9}Ca_{0.05}CrO_2$ displays enhanced capacity retention of 90.8% and 89.7% when cycled between 2 V – 3.6 V and 2 V – 3.7 V, respectively. Figure 8.5(c-d) compares the long-term cyclability and coulombic efficiency of the two materials. Significant improvement can be observed for the calcium substituted sample. $Na_{0.9}Ca_{0.05}CrO_2$ retains 76.1% and 67.9% of capacity after 500 cycles in the voltage range of 2 V – 3.6 V and 2 V – 3.7 V, while less than half of the initial capacity is retained for $NaCrO_2$ in both voltage ranges. The fade rate per cycle of $Na_{0.9}Ca_{0.05}CrO_2$ in the last 100 cycles is only 0.029%, compared to 0.082% for $NaCrO_2$. The coulombic efficiency of $Na_{0.9}Ca_{0.05}CrO_2$ (~99.8%) is also constantly higher than that of $NaCrO_2$ (~99.6%).

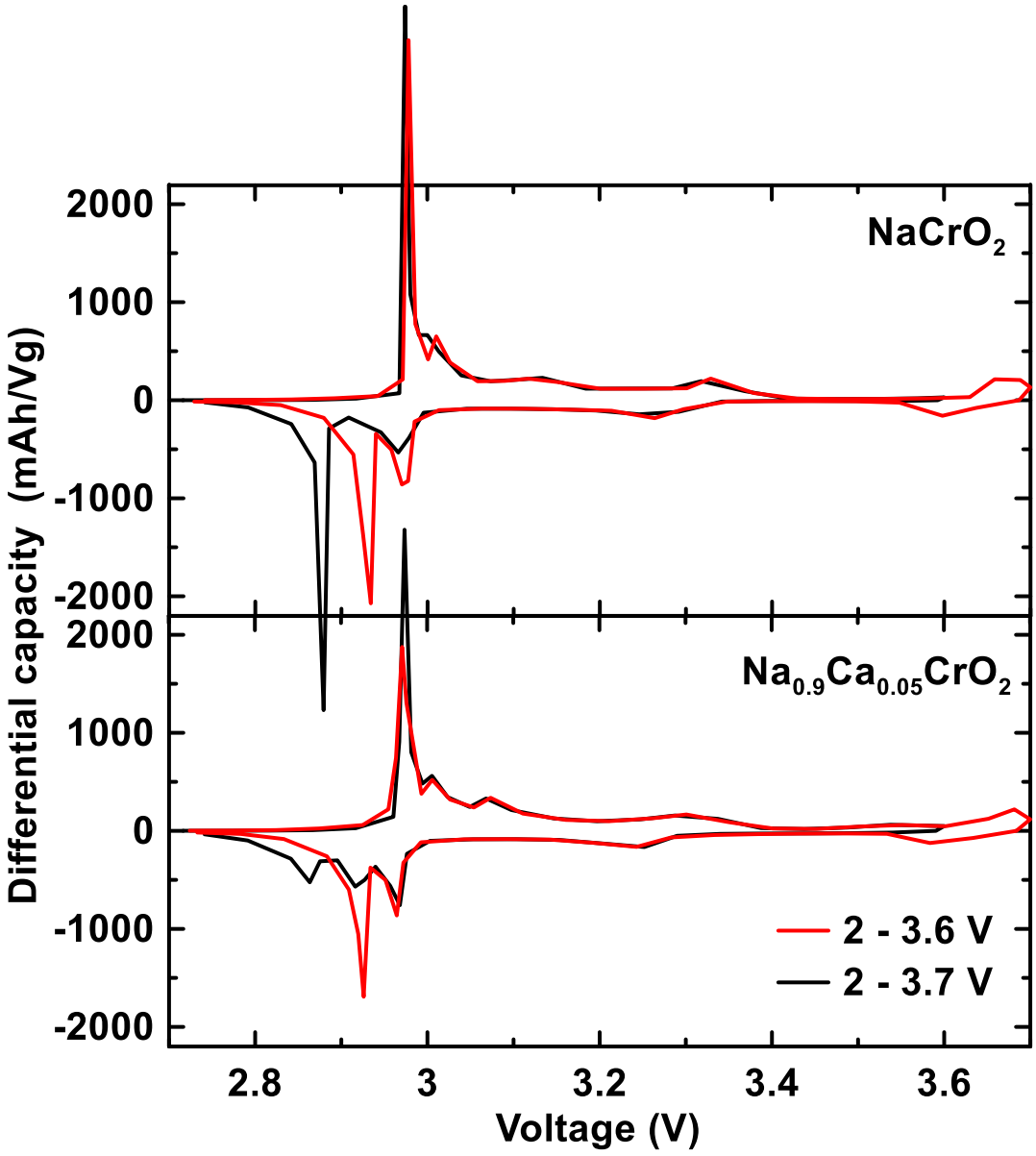


Figure 8.4 Differential capacity curve of $NaCrO_2$ and $Na_{0.9}Ca_{0.05}CrO_2$.

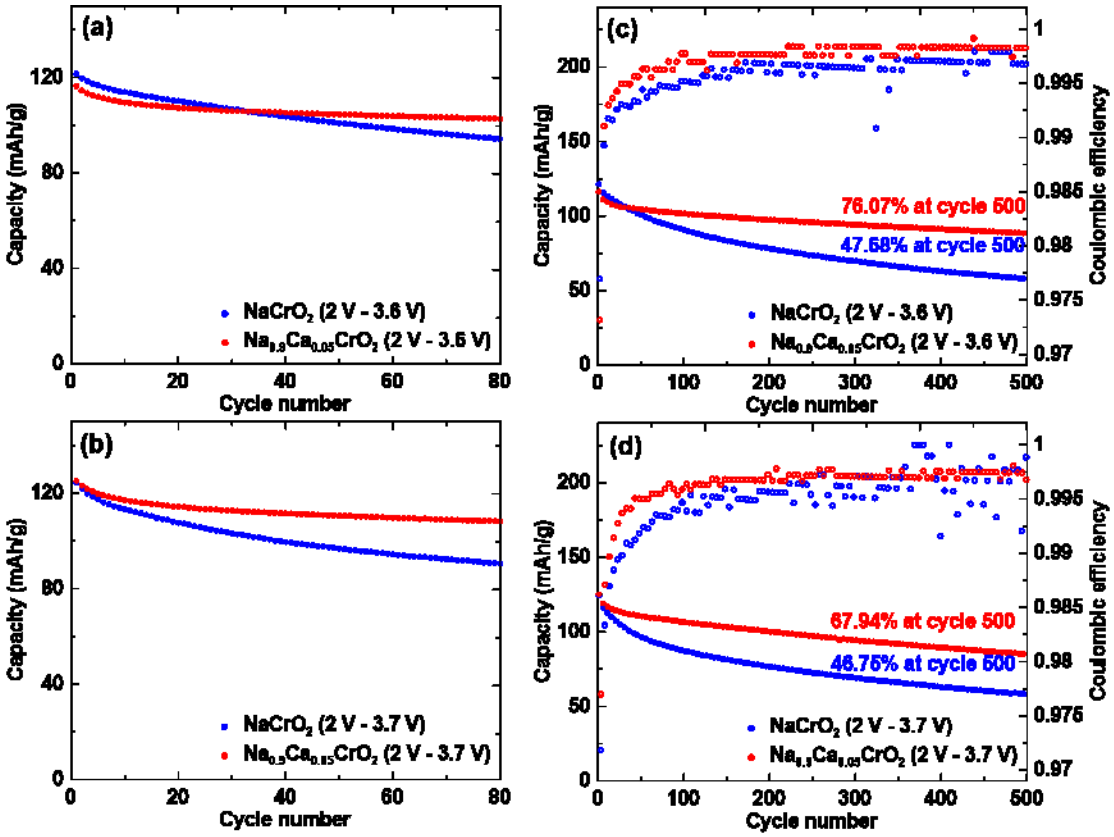


Figure 8.5 Discharge capacity and coulombic efficiency versus cycle number of $NaCrO_2$ and $Na_{0.9}Ca_{0.05}CrO_2$.

As immobile calcium in the sodium sites might hinder sodium diffusion, it is possible that the rate capability might be compromised by calcium doping. However, reports by Matsui et al. and Han et al. show that calcium substituted samples have rate capabilities at least as good as undoped samples [165,166]. Han et al. even showed that $Na_{0.6}Ca_{0.07}CoO_2$ displayed much better rate performance than $Na_{0.73}CoO_2$ [166]. They attributed the improved rate performance to the more stable structure of $Na_{0.6}Ca_{0.07}CoO_2$, which facilitates sodium diffusion over the entire potential range. Figure 8.6 shows a comparison of the rate performance of $NaCrO_2$ and $Na_{0.9}Ca_{0.05}CrO_2$. Both $NaCrO_2$ and $Na_{0.9}Ca_{0.05}CrO_2$ display impressive rate performance. At a high current of 8C (1000 mA/g), both materials retain a capacity of more than 80 mAh/g. This indicates that a small amount

of calcium doping does not deteriorate the rate capability. This result is in agreement with studies by Matsui et al. and Han et al. regarding calcium doped $Na_xCoO_2$.

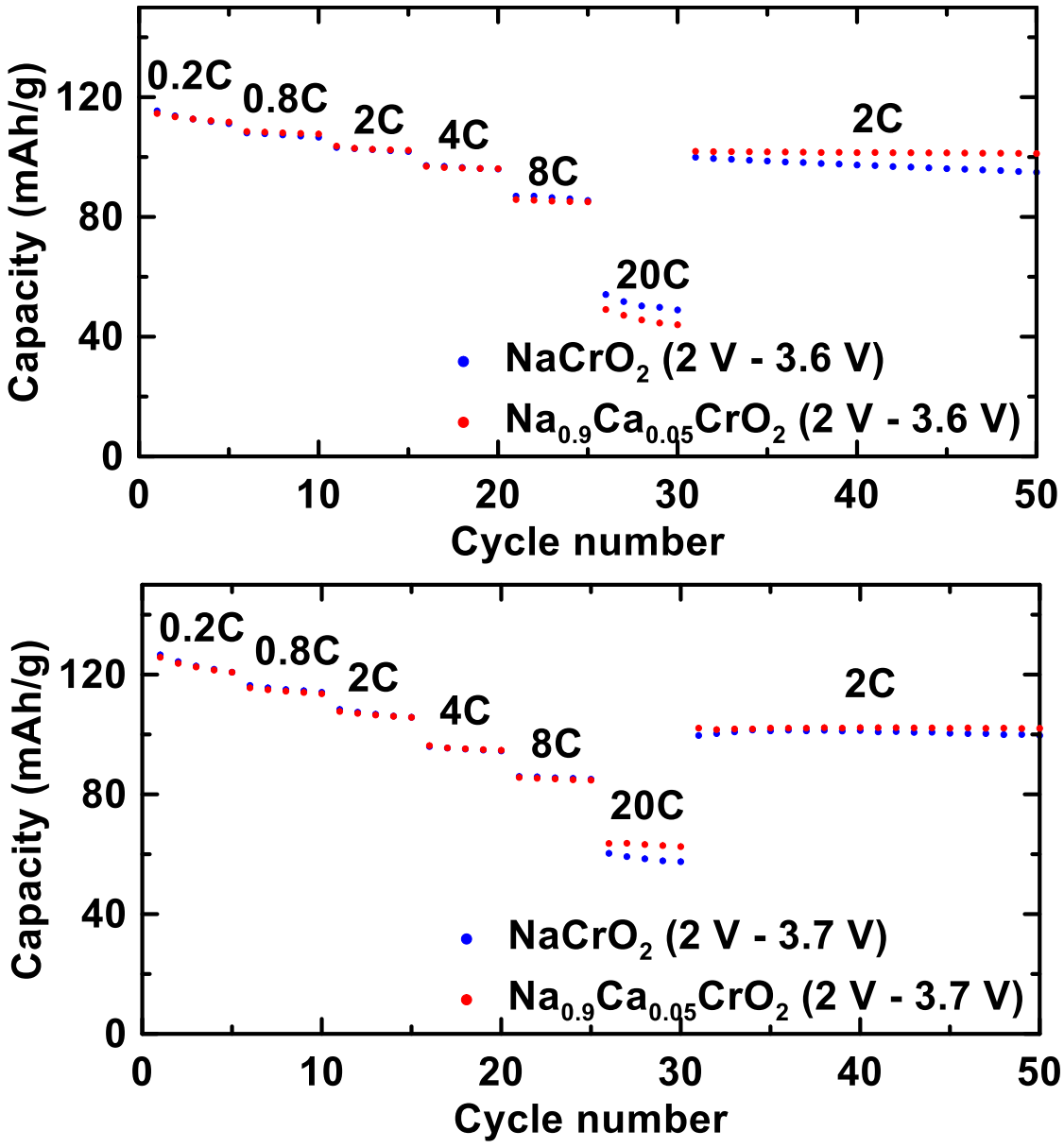


Figure 8.6 Discharge capacity of $NaCrO_2$ and $Na_{0.9}Ca_{0.05}CrO_2$ cycled at different C-rates.

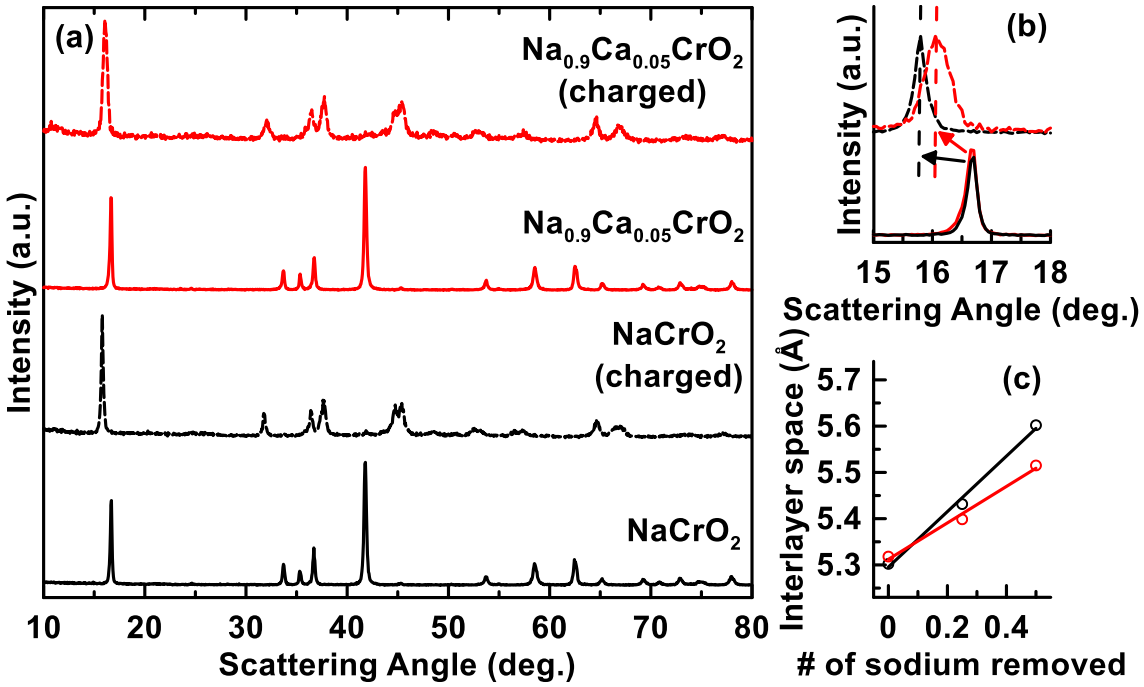


Figure 8.7 (a) *Ex situ* XRD patterns of $NaCrO_2$ and $Na_{0.9}Ca_{0.05}CrO_2$ after being charged to 3.6 V, compared to uncharged XRD patterns. (b) Enlarged XRD patterns showing the position change of (003) peak between 15° to 18°. (c) Calculated interlayer distance of $NaCrO_2$ and $Na_{0.9}Ca_{0.05}CrO_2$ during charging.

In order to understand the superior cycling performance of calcium-substituted $Na_{0.9}Ca_{0.05}CrO_2$, *ex-situ* XRD measurements were performed on both $NaCrO_2$ and $Na_{0.9}Ca_{0.05}CrO_2$. The results are compared in Figure 8.7. Figure 8.7(a) shows that both materials transition from an O3 to a P'3 phase when charged to 3.6 V. The shift of the (003) peaks of both materials to lower angle indicates an increase in interlayer distance during desodiation. This is due to the reduced screening effect of sodium between oxygen layers and a resulting stronger repulsion between alternating oxygen layers. Such anisotropic expansion/contraction along the *c* axis during cycling gradually causes irreversible structural change and capacity fade [168]. A closer examination in Figure 8.7(b) shows that although both charged materials have the same phase behavior, the (003) peak shift during charging is less pronounced for $Na_{0.9}Ca_{0.05}CrO_2$ than $NaCrO_2$. This indicates a

greater expansion of the interlayer distance in $NaCrO_2$ during charging, as shown in Figure 8.7c. It should be noted that the interlayer space of desodiated $Na_{0.5}CrO_2$ measured in this study (~5.6 Å) is consistent with previous studies [82,159]. It is believed the strong interaction between $Ca^{2+}$ and $O^{2-}$ leads to mitigated volume expansion, resulting in a more stable structure and improved cyclability. The peak broadening of desodiated $Na_{0.9}Ca_{0.05}CrO_2$ shown in Figure 8.7 (b) might be caused by stacking faults due to the presence of calcium in partially desodiated layers.

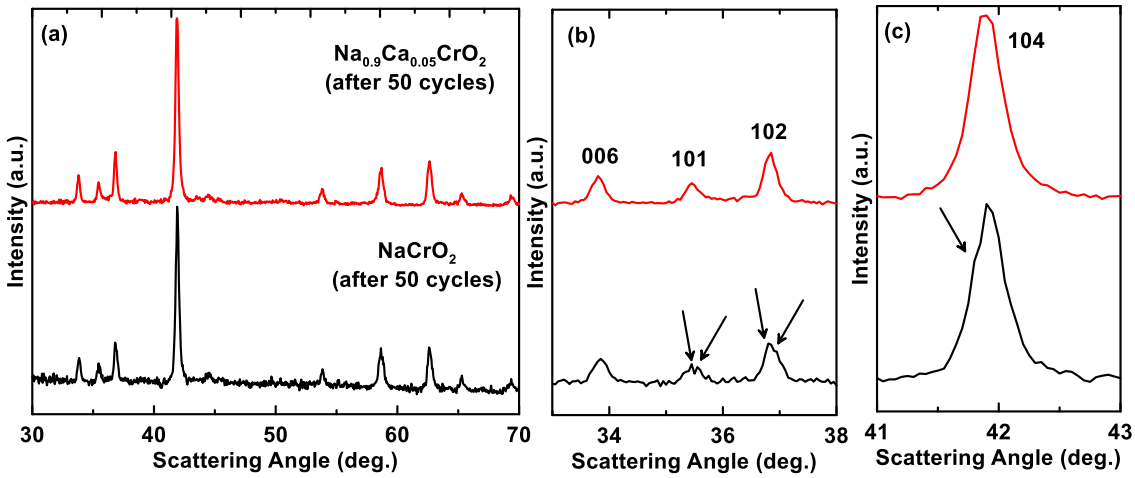


Figure 8.8 (a) *Ex situ* XRD patterns of $NaCrO_2$ and $Na_{0.9}Ca_{0.05}CrO_2$ electrodes after 50 cycles. (b) Enlarged XRD patterns between 33° to 38°. (b) Enlarged XRD patterns between 41° to 43°. Arrows indicate shoulders in the XRD peaks from peak fitting due to the formation of the O'3 phase.

Figure 8.8(a) shows *ex-situ* XRD profiles of $NaCrO_2$ and $Na_{0.9}Ca_{0.05}CrO_2$ electrodes in their fully discharged state after 50 cycles. Even though both cycled materials have similar O3-type XRD patterns, a careful examination shows that peak splitting can be observed for cycled $NaCrO_2$ but not for cycled $Na_{0.9}Ca_{0.05}CrO_2$. Some examples are shown in the enlarged XRD patterns in Figure 8.8(b-c) for the (101), (102), and (104) diffraction lines. The peak splitting of $NaCrO_2$ after extensive cycling can be ascribed to the formation

of the O'3 phase. According to other research, O3 phase $NaCrO_2$ starts to transition to O'3 phase once the desodiation starts [75,82]. This result shows that the O3 structure of $Na_{0.9}Ca_{0.05}CrO_2$ is retained after 50 cycles, while the O3 structure of cycled $NaCrO_2$ is not completely recovered. The gradual phase transition of $NaCrO_2$ from the O3 to O'3 phase during cycling indicates a less stable structure, compared to $Na_{0.9}Ca_{0.05}CrO_2$.

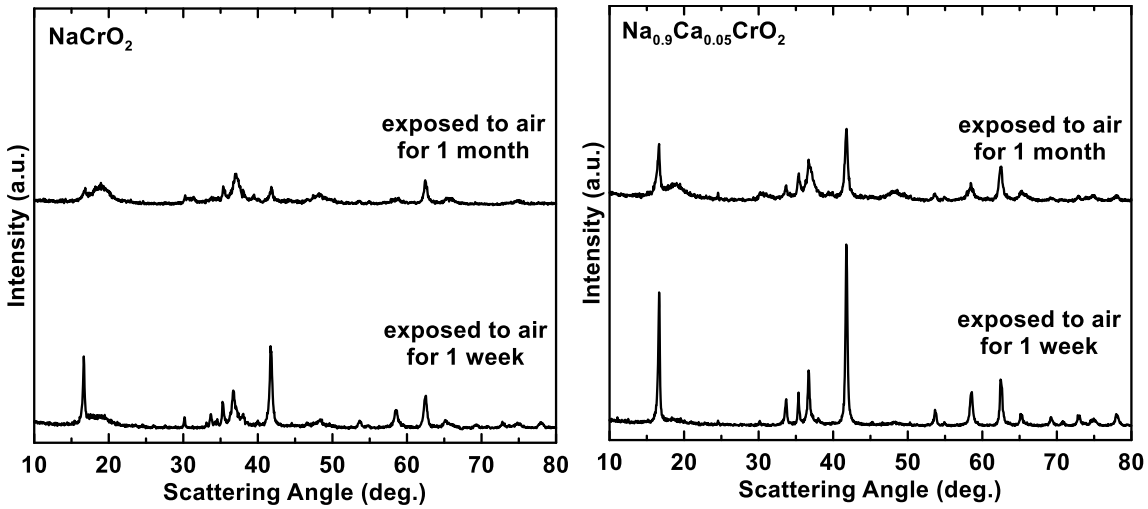


Figure 8.9 XRD patterns of $NaCrO_2$ and $Na_{0.9}Ca_{0.05}CrO_2$ after air exposure for different durations.

It is well-known that most O3-type sodium cathode materials readily react with air when exposed to atmosphere [13]. Such behavior is typically accompanied by desodiation and/or the intercalation of water [13]. Air-sensitivity of cathode materials is one of the main obstacles that hinder the commercialization of sodium ion batteries. Improving the air-stability and development of air-stable materials therefore is of high importance. Figure 8.9 shows the XRD patterns of $NaCrO_2$ and $Na_{0.9}Ca_{0.05}CrO_2$ after being exposed to room air for 1 week and 1 month. After 1 week, broadened and weakened peaks indicative of structural change are observed for $NaCrO_2$. Some unidentified impurity peaks are also present. Meanwhile, only slight changes can be observed in the $Na_{0.9}Ca_{0.05}CrO_2$ XRD

pattern. After 1 month exposure, $NaCrO_2$ becomes almost amorphous and the pristine structure is barely retained, while the XRD profile of $Na_{0.9}Ca_{0.05}CrO_2$ only shows broadened and weakened peaks, resembling $NaCrO_2$ after 1 week air exposure. These results suggest that even though calcium substitution cannot eliminate air-sensitivity, the reaction between $Na_{0.9}Ca_{0.05}CrO_2$ and air is mitigated and slowed compared to $NaCrO_2$.

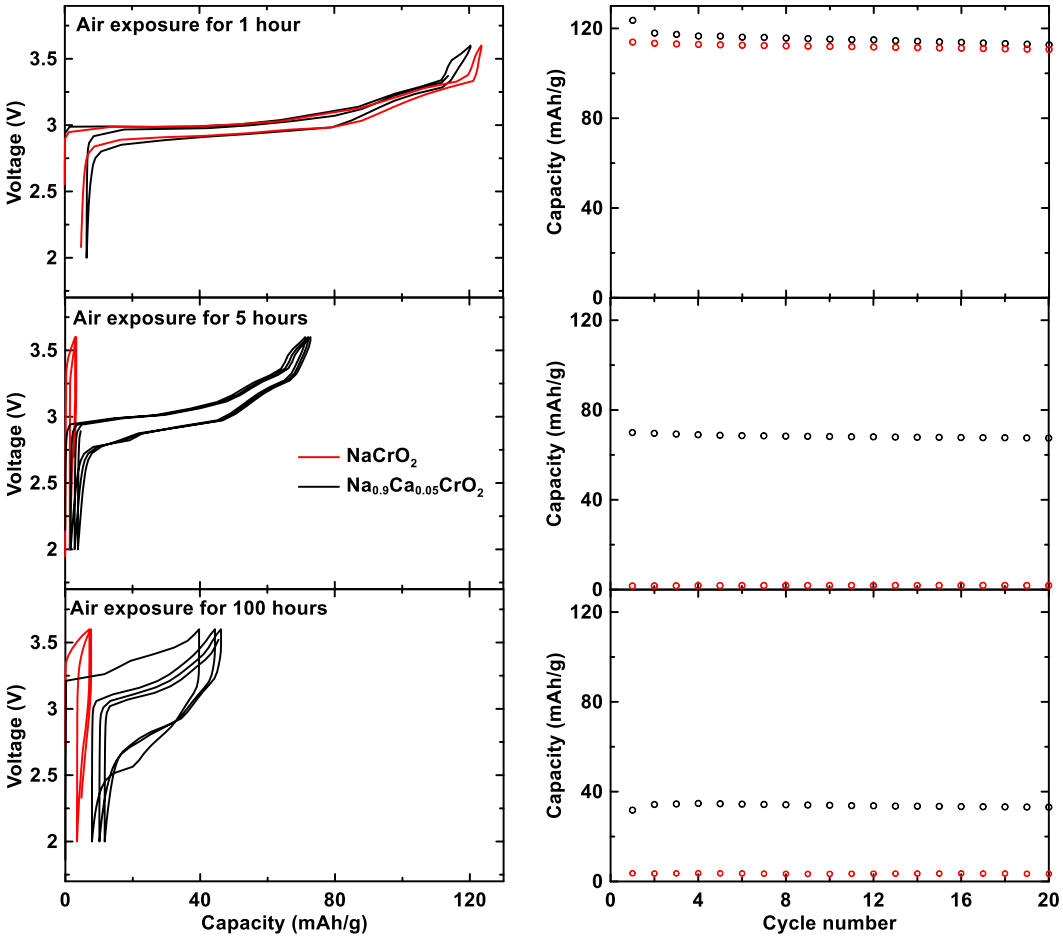


Figure 8.10 Voltage curves and cycling performance of $NaCrO_2$ and $Na_{0.9}Ca_{0.05}CrO_2$ after air exposure for different durations.

To confirm the improved air stability of calcium substituted $NaCrO_2$, electrochemical tests were conducted. Electrodes were intentionally exposed to air for 1 hour, 5 hours, and 100 hours, then incorporated into coin cells without any further

treatment. It was noticeable to the naked eye that the color of the $NaCrO_2$ electrode quickly changes from black to grey after only several hours of air exposure, while a same color change in the $Na_{0.9}Ca_{0.05}CrO_2$ electrode can only be observable after a few days of air exposure. The grey color might arise from the formation of $NaOH/Na_2CO_3$ during air exposure. Figure 8.10 shows the voltage curve and cyclability of the exposed materials. After an hour air exposure, both materials have identical performance to unexposed materials. However, after 5 hours air exposure, $NaCrO_2$ become inactive. On the other hand, a reversible capacity of 70 mAh/g was achieved for $Na_{0.9}Ca_{0.05}CrO_2$. After 100 hours of air exposure, $Na_{0.9}Ca_{0.05}CrO_2$ still retains a capacity of 40 mAh/g. This result confirms the suppressed air-sensitivity of $Na_{0.9}Ca_{0.05}CrO_2$, but also reveals that the slow reaction between the doped sample and air still occurs. More studies are required to further improve the air-stability.

## 8.4 Conclusions

In summary, calcium doped $Na_{0.9}Ca_{0.05}CrO_2$ was synthesized and its electrochemical and phase behavior investigated. Compared to undoped $NaCrO_2$, $Na_{0.9}Ca_{0.05}CrO_2$ has significantly improved cycling performance and higher coulombic efficiency. The capacity fade rate per cycle of $Na_{0.9}Ca_{0.05}CrO_2$ is only 0.029%, rendering the material an attractive cathode for sodium ion batteries. *Ex-situ* XRD patterns show that this superior performance can be ascribed to greater structural stability during cycling, possibly due to a stronger calcium-oxygen interaction. Furthermore, both XRD and electrochemical studies show that $Na_{0.9}Ca_{0.05}CrO_2$ also has better air-stability than undoped $NaCrO_2$. It is anticipated that such doping strategies could benefit the development of practical sodium ion batteries cathode materials.

# CHAPTER 9 MECHANOFUSION COATING FOR ENHANCING LITHIUM ION BATTERY CATHODE MATERIAL PERFORMANCE[6]

## 9.1 Introduction

Applications of lithium ion batteries in electric vehicles or grid energy storage applications require long battery lifetimes [5]. Various approaches have been shown to improve the cycle life of lithium ion batteries, such as the use of electrolyte additives or modification of cathode material composition [27,40]. Electrolyte deterioration is one of the reasons that causes capacity fade [169]. The ageing of electrolyte mainly occurs on electrode surfaces [170]. Therefore, surface chemistry plays a crucial role in cycling performance. As reported by many researchers, surface coating of cathode material particles is an effective way to improve long-term cycling performance [39].

Metal oxides are the most commonly used materials to coat positive electrode material particles [39]. There are multiple possible mechanisms that lead to the improvement observed when cathode particles are coated with metal oxides. Kim et al. compared the effect of different metal oxide coatings ($ZrO_2$, $Al_2O_3$, $TiO_2$, ect.) on $LiCoO_2$ and concluded that oxide coatings can suppress cobalt dissolution, resulting in improved cycling behavior [172]. Xiong et al. showed that an $Al_2O_3$ coating suppresses impedance growth of layered $Li[Ni_xMn_yCo_z]O_2$ cathodes and improves coulombic efficiency and capacity retention [171]. Interestingly, Chen et al. compared the behavior of heated $LiCoO_2$

[6] This chapter was adapted with permission from Zheng, L.; Hatchard, T. D.; Obrovac, M. N. A High-Quality Mechanofusion Coating for Enhancing Lithium-Ion Battery Cathode Material Performance. *MRS Communications*, Published online: 05 October 2018 [182]. Copyright 2018, Materials Research Society. The author's contribution includes performing the experimental work and writing the manuscript.

and oxide-coated $LiCoO_2$, and observed a similar cycling performance. They proposed that it is the heat treatment, not the presence of the metal oxide, that is most important [173,174]. Therefore, the processing steps may cause cycling improvement rather than the coating itself. For this reason, it is always important to compare coated materials with uncoated materials that have undergone the same processing steps.

So far few studies of coated Na-ion cathode materials exist. One reason for this is that most of the coating methods reported so far are wet methods, which are incompatible with most Na-ion cathode materials, which are typically moisture sensitive [13]. Even for Li-ion battery materials wet methods are not optimal, since they produce waste liquid and require filtering and additional drying/heating processes [175]. The environmental friendliness of these procedures is doubtful. Other common coating methods use deposition techniques, such as atomic layer deposition (ALD), which are expensive and difficult to scale up [176].

Mechanofusion is a dry processing method that has been shown to coat small particles onto larger host particles [177]. In this method the particles are forced through a narrow gap, resulting in high shear and compression forces. As a result, the larger host particles can be coated with a dense layer composed of the fine coating particles [177]. In this study, $LiNi_{0.6}Mn_{0.2}Co_{0.2}O_2$ (NMC622) was dry-processed with nano-alumina powder using the mechanofusion process. NMC622 was also coated with nano-alumina using hand grinding for comparison. These materials were then characterized in Li cells. The mechanofusion method was shown to produce a robust, non-porous coating on the NMC622 surface, which significantly enhances its cycling performance. This method not only enables low-cost solvent-free particle coating, which can significantly reduce the cost

and environmental impact of Li-ion cathode materials, but is also not limited by aqueous chemistry. In principle any coating can be applied by this method. This work gives an example of the synthesis and characterization of a mechanofusion coated cathode. We believe these results will open up a new research area in cathode material development for both Li-ion and Na-ion cells.

## 9.2 Experimental

Commercial $LiNi_{0.6}Mn_{0.2}Co_{0.2}O_2$ (NMC622) powders (obtained from Umicore) and nano-$Al_2O_3$ (99.8%, 13 nm by TEM, from Sigma-Aldrich) were used in this study. Mechanofusion-coated NMC622 was made using a Hosokawa AM-15F mechanofusion system. NMC622 and nano-$Al_2O_3$ powders were added to the processing vessel in a weight ratio of 97:3 with a total tapped powder volume of ~ 50 mL. Mechanofusion was conducted for 30 min. with a press-head gap of 1 mm, a scraper gap of ~0.4 mm and a rotation speed of ~1400 rpm. NMC622 was also coated with $Al_2O_3$ by hand-grinding NMC622 and 3% $Al_2O_3$ powders in a 97:3 weight ratio using mortar and pestle until a homogeneous mixture was obtained (~ 30 minutes).

The morphology and elemental distribution of samples were measured using a field emission scanning electron microscope (FESEM, TESCAN MIRA 3). Cross sections of samples were prepared using a cross section polisher (JEOL, IB-19530CP). Single point BET measurements were conducted using a Micromeritics FlowSorb II 2300 with a nitrogen/helium flow (28.6% $N_2$). Samples were degassed at 150 °C for 30 minutes to remove moisture before each measurement. Densities were measured using a Micromeritics AccuPyc II 1340 Pycnometer. X-ray diffraction (XRD) patterns were

measured with a Rigaku Ultima IV X-ray diffractometer equipped with a Cu anode X-ray tube, a scintillation detector, and a diffracted beam monochromator.

Electrodes were made from slurries containing active materials, PVDF binder (polyvinylidene fluoride, Kynar HSV 900), carbon black (Super C65, Imerys Graphite and Carbon) at a ratio of 86:7:7 and an appropriate amount of N-methyl-2-pyrrolidone (Sigma Aldrich, anhydrous 99.5%). Slurries were mixed using a Mazerustar planetary mixer. The mixed slurries were coated onto aluminum foil using a coating bar with a ~0.015 cm gap and dried at 120 °C in air. Circular electrode disks were punched from the coating and dried under vacuum at 120 °C overnight before cell assembling. Coin cells (2325-size) were assembled with 1M $LiPF_6$ in a solution of ethylene carbonate and diethyl-carbonate (volume ratio 1:2, from BASF) as electrolyte, with two Celgard 2300 and one polypropylene blown microfiber separator (3M Company) as separators, and lithium foil as the counter/reference electrode. Cells were cycled at 30.0 ± 0.1°C with a Maccor Series 4000 Automated Test System.

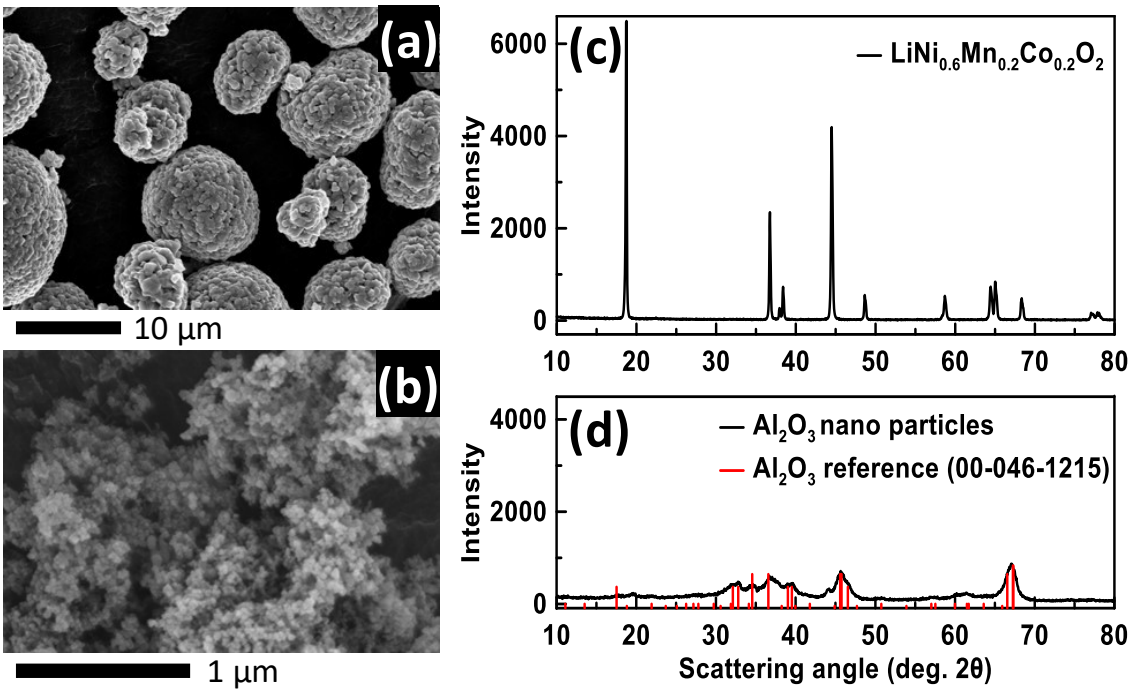


Figure 9.1 (a) SEM image of $LiNi_{0.6}Mn_{0.2}Co_{0.2}O_2$; (b) SEM image of $Al_2O_3$; (c) XRD pattern of $LiNi_{0.6}Mn_{0.2}Co_{0.2}O_2$; (d) XRD pattern of nano-$Al_2O_3$.

**9.3 Results and Discussion**

Figure 9.1(a) shows a scanning electron microscopy (SEM) image of the NMC622 powder used in this study. This material is in the form of ~10 µm spherical secondary particles composed of ~1 µm irregular polyhedral primary particles. Figure 1(b) shows an SEM image of the nano-$Al_2O_3$ powder used in this study. The $Al_2O_3$ particles (~13 nm) are much smaller than NMC622 and are even smaller than the resolution of the SEM itself. We have found that a small coating particle size is critical in ensuring a close-packed dense and uniform coating on the surface of the host particles by dry processing. The X-ray diffraction (XRD) patterns of NMC622 and nano-$Al_2O_3$ are shown in Figure 1(c-d). Both materials are phase-pure. Compared to NMC622, which is highly crystalline, the XRD

pattern of nano-$Al_2O_3$ powder has broad peaks, corresponding to a grain size that is on the scale of 10 nm.

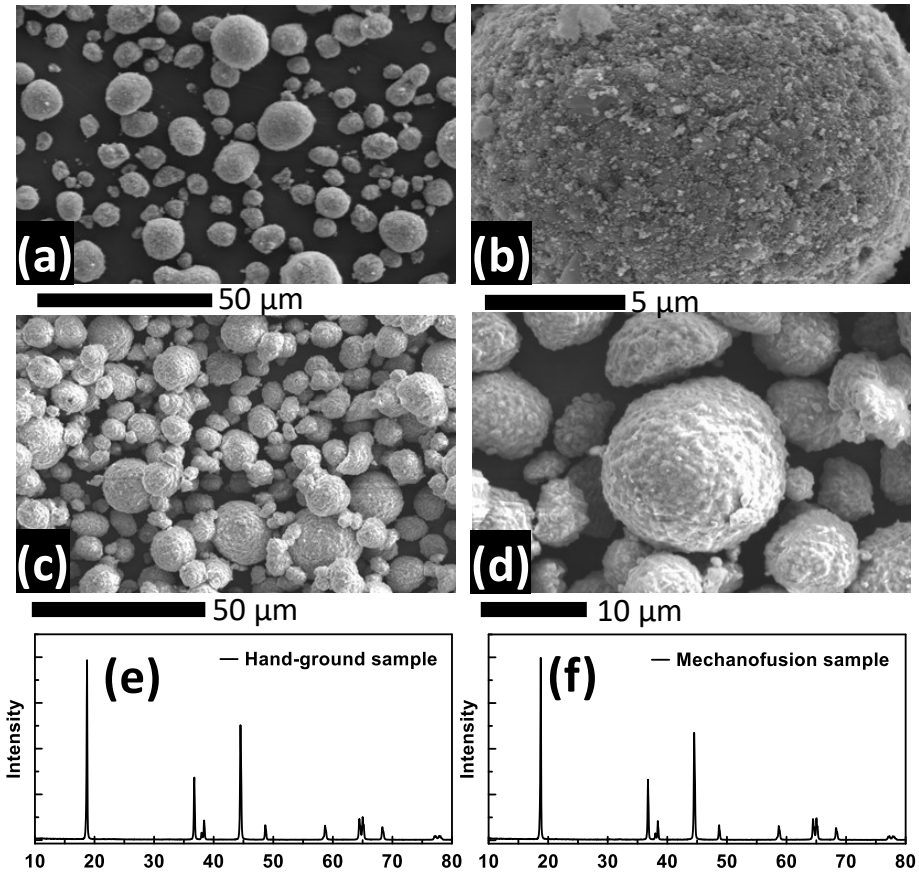


Figure 9.2 SEM images of NMC622 coated with $Al_2O_3$ by (a,b) hand grinding and (c,d) mechanofusion. XRD patterns of these samples are shown in (e) and (f), respectively.

Figure 9.2 shows SEM images and XRD patterns of NMC622 particles coated with 3 wt.% $Al_2O_3$ by hand-grinding or by mechanofusion, respectively. The primary particles of NMC622 can no longer be seen in these samples, suggesting both methods can produce a coating layer. However, while the mechanofusion method produces a homogeneous and dense coating, hand-grinding resulted in a much more diffuse and porous coating layer. The hand-ground sample also has some free $Al_2O_3$ particles present that are not closely attached to the NMC622, while very little free $Al_2O_3$ particles were observed in the sample

coated by mechanofusion. The XRD patterns of both samples Figure 2(e,f) are identical to pristine NMC622, showing that both methods do not affect the bulk NMC crystal structure.

Table 9.1 BET specific surface area (SSA) measured for all samples.

| Sample | NMC622 | nano-$Al_2O_3$ | hand-grinding | mechanofusion |
|---|---|---|---|---|
| SSA ($m^2/g$) | 0.30 | 128.67 | 1.61 | 0.23 |

Table 9.1 shows the BET specific surface area of all the samples. NMC622 has a specific surface area of ~0.3 $m^2/g$, similar to previous reports [178]. Despite the $Al_2O_3$ having a very large surface area, the sample coated by mechanofusion has a smaller surface area (~0.23 $m^2/g$), compared to pristine NMC622. This indicates that the $Al_2O_3$ coating formed must be very dense, so as to be impermeable to the $N_2$ gas used in the BET measurement. Furthermore, as the secondary particle size did not change after the coating process, the reduced surface area is due to alumina filling the holes on the surface of secondary particles, as shown in the SEM images in Figure 9.2(b,c). On the other hand, the specific surface area of the sample coated by hand-grinding (1.61 $m^2/g$) is higher than pristine NMC622, reflecting a less dense coating layer and the presence of loose $Al_2O_3$ powder, as observed in the SEM images discussed above. The coating formed by mechanofusion is not porous on the scale which can be observed by SEM. Density measurements were also conducted and the density is 4.78 $g/cm^3$ for pristine NMC622 and 4.34 $g/cm^3$ for mechanofusion coated NMC622. It is believed that after the mechanofusion coating process, the internal porosity of the NMC622 particles became inaccessible to the helium of the pycnometer. Therefore the measured volume is smaller than the real volume,

leading to a decreased density of coated sample. This result also confirms the non-porous nature of the mechanofusion coating.

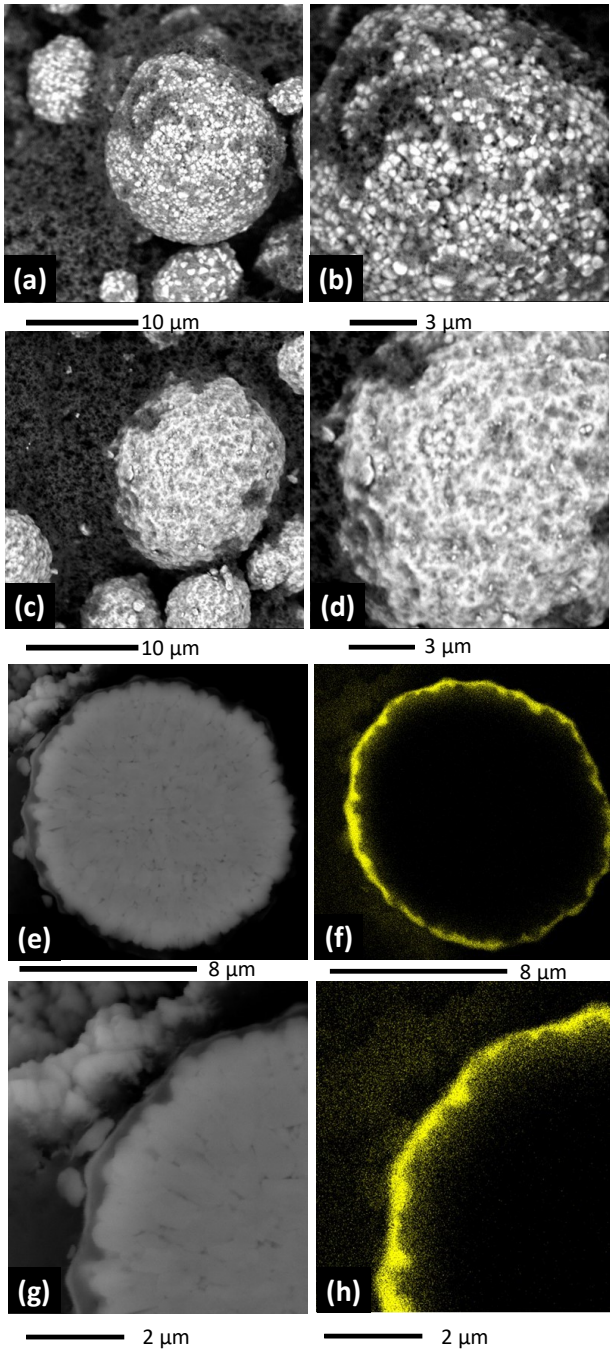


Figure 9.3 SEM images of composite electrodes of NMC622 coated with $Al_2O_3$ by (a,b) hand grinding and (c,d) mechanofusion. SEM (e,g) and corresponding EDS aluminum maps (f,h) of a cross section of an electrode of mechanofusion coated NMC622.

Figure 9.3(a,b) and (c,d) show SEM images of electrodes made from the hand-ground and mechanofusion $Al_2O_3$-coated NMC622, respectively. The $Al_2O_3$ coating is no longer present on the sample coated using hand-grinding. This indicates that the hand-ground coating was not robust enough to adhere onto the particle surface during the slurry making process. In contrast, the $Al_2O_3$ coating made by the mechanofusion process clearly remains intact and adhered to the coated electrode particles Figure 9.3(c,d). To further confirm that the $Al_2O_3$ coating is preserved on the surface of mechanofusion coated NMC622, EDS mapping of a cross section of this electrode was conducted. The results are shown in Figure 9.3(f), where the presence of Al is shown as yellow. By comparing the shape of the enlarged SEM/EDS images of the mechanofusion coated sample, shown in Figure 9.3(g) and (h), the surface coating can be identified as the alumina coating. This coating is highly dense and completely coats the NMC622 surface, as shown in Figure 9.3(g). This example also shows that for surface coating studies, it is important to characterize the composite electrode, instead of just the coated powders, to confirm that the particle coating can survive the slurry mixing process.

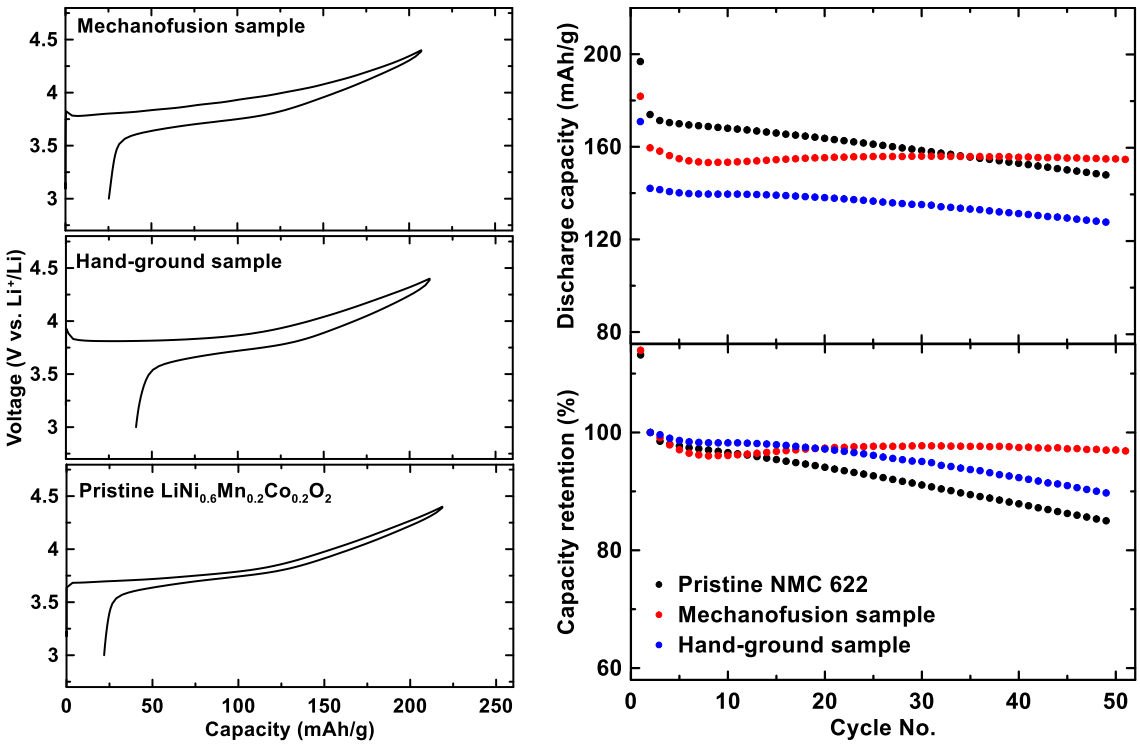


Figure 9.4 Voltage curve and cycling performance of pristine NMC 622, and NMC 622 coated with $Al_2O_3$ by mechanofusion and hand-grinding.

Figure 9.4 shows voltage curves of pristine NMC622, and of NMC622 coated with $Al_2O_3$ by mechanofusion and hand-grinding. Compared to the pristine sample, the coated samples have lower capacities and larger hysteresis, due to the presence of non-conductive and inactive $Al_2O_3$. The hysteresis of the mechanofusion coated sample is slightly larger than the one coated by hand-grinding. This is expected, since the dense $Al_2O_3$ coating produced by mechanofusion would tend to impede ion conduction. The cycling performance for all the materials cycled between 3 V – 4.4 V is shown in Figure 4. The uncoated NMC622 sample has significant capacity fade (~18% fade/50 cycles) when cycled in this voltage range, as has been previously observed by others. The NMC622 sample that was hand-ground has only slightly better capacity retention (~15% fade/50 cycles). This is understandable, since, as shown above, the $Al_2O_3$ coating made by hand

grinding came off the particles during the slurry making process. The slightly improved cycling of this sample can be attributed to the HF scavenging effect of the residual $Al_2O_3$ in the electrode [39,179]. $LiPF_6$ reacts with water to form HF, which corrodes the active material and leads to poor cycling. The HF concentration in electrolyte can be reduced with the presence of $Al_2O_3$, resulting in improved cycling [39,179]. The NMC622 sample coated by mechanofusion has significantly improved cycling performance, with little capacity fade in 50 cycles. It can therefore be concluded that the good cycling performance of the mechanofusion coated sample results from a combination of the $Al_2O_3$ HF scavenger effect, and the protective layer formed by the dense $Al_2O_3$ coating that isolates the NMC surface from the electrolyte.

### 9.4 Conclusions

Li-ion battery cathode materials are typically coated to improve cycling performance, using aqueous-based coating techniques that require filtering, drying and even sintering of the final product. Here, spherical $LiNi_{0.6}Mn_{0.2}Co_{0.2}O_2$ particles were coated with nano-$Al_2O_3$ using the dry mechanofusion method. This method produced a durable, non-porous $Al_2O_3$ coating that is retained during slurry making. Mechanofusion coatings significantly improved Li-ion battery cathode cycling at high voltages, enabling high energy densities, while offering inexpensive, scalable and environmentally friendly solvent-free synthesis. This opens up new possibilities, since, not being limited by synthesis chemistry, mechanofusion can in principle be used to apply any coating material. Now that the method has been established here with a standard Li-ion battery cathode, it can be used in the future for coating Na-ion battery materials.

# CHAPTER 10 CONCLUSIONS AND FUTURE WORK

## 10.1 Conclusions

Sodium ion battery cathode materials have several drawbacks such as poor cycling performance and air-sensitivity, which prevent their commercialization. Much effort has been devoted to understanding and solving these problems. In this thesis, the structural and electrochemical properties of Na-ion cathode materials are studied. Several strategies to optimize Na-ion battery cathode materials are discussed.

Chapter 3 describes a design strategy for new cathode materials using a high valence state element, such as bismuth, to enrich the nickel content. A composition of $Na_3Ni_2BiO_6$ ($NaNi_{2/3}Bi_{1/3}O_2$) resulted in a honeycomb structure due to the in-plane ordering between $Ni^{2+}$ and $Bi^{5+}$ ions. Structural changes during cycling were confirmed using *in situ* and *ex situ* XRD. This material has better cycling performance than its lithium counterpart, due to a lower tendency of Na/Ni cation mixing than Li/Ni cation mixing.

Chapter 4 and 5 describes the role of certain transition metals (copper and titanium) in improving the electrochemical performance of sodium cathode materials. Both these two dopants can smooth voltage curves and improve cycling. At the same time, it has been shown that transition metal substitution causes complex capacity and voltage behavior. The capacity and operating voltage of doped compounds are highly dependent upon the voltage range used for testing. For example, although copper doping decreases the overall capacity, in certain voltage ranges the capacity is increased. Similarly, titanium doping increases the operating voltage but in certain voltage ranges the average voltage is decreased.

Chapter 6 describes a study of the air-sensitivity of $NaNi_{0.5}Mn_{0.5}O_2$. It was determined that the exposure of untreated $NaNi_{0.5}Mn_{0.5}O_2$ powders to moisture results in desodiation and material degradation. The air-sensitivity of $NaNi_{0.5}Mn_{0.5}O_2$ is complex and involves synergistic interactions between $NaNi_{0.5}Mn_{0.5}O_2$, water, oxygen, and carbon dioxide. Washing $NaNi_{0.5}Mn_{0.5}O_2$ with water completely destroys its crystal structure, while washing $NaNi_{0.5}Mn_{0.5}O_2$ with ethanol removes most of the sodium residues on $NaNi_{0.5}Mn_{0.5}O_2$ surfaces without damaging the crystal structure, resulting in improved air stability, smaller hysteresis and higher capacity.

Chapter 7 describes a study on $NaNi_{0.8}Co_{0.15}Al_{0.05}O_2$ (Na-NCA), inspired by commercial $LiNi_{0.8}Co_{0.15}Al_{0.05}O_2$ (Li-NCA). It was demonstrated that cooling conditions after high temperature synthesis can significantly affect the crystal structure and corresponding electrochemistry of the products. Compared to $NaNiO_2$, Na-NCA has better reversibility and cycling performance. *In situ* and *ex situ* XRD were used to study the structural transitions of materials during cycling. The structure change during cycling was found to be more reversible for quenched O3-type NCA than slow-cooled O'3-type NCA.

Chapter 8 describes a study of calcium doping in the sodium site of $NaCrO_2$. O3-type $NaCrO_2$ is a promising cathode material as it offers decent energy density and is easy to synthesize. In this chapter, it is shown that $Na_{0.9}Ca_{0.05}CrO_2$ has improved cycling performance, higher coulombic efficiency, and better air-stability than $NaCrO_2$ without sacrificing the capacity. *Ex-situ* XRD patterns show that the superior performance can be ascribed to the more stable structure of $Na_{0.9}Ca_{0.05}CrO_2$ during cycling.

Chapter 9 describes a mechanofusion method to apply $Al_2O_3$ coating on commercial NMC 622 spherical particles. This method produced a durable, non-porous $Al_2O_3$ coating that is retained during slurry making. Mechanofusion coatings significantly improved Li-ion battery cathode cycling at high voltages, enabling high energy densities, while offering inexpensive, scalable, and environmentally friendly solvent-free synthesis. The developed method is applicable to coating Na-ion cathode materials, which are not compatible with the commonly used wet methods used to coat Li-ion cathode materials.

## 10.2 Future work

The effect of using different elements, M, In $NaMO_2$ cathode materials has been extensively studied by researchers[168]. Limitless combinations of transition metals and other substitution elements are possible. It is therefore important to understand the role of each element and perhaps the synergistic effect of multiple elements on structure and electrochemistry. Besides the more commonly studied first row transition metals, other metals and metalloids can be substituted into the transition metal layer. Some elements with high oxidation states, such as $V^{5+}$, $Nb^{5+}$, $Ta^{5+}$, $W^{6+}$, $Mo^{6+}$, might be useful for enriching the nickel content of the transition metal layer and thus increasing capacity.

Metal substitution into the sodium layer can also be useful to improve the structural and electrochemical performance of sodium cathode materials. The study of calcium substitution in some of the common sodium cathode materials, such as $Na_{2/3}Mn_{1/2}Fe_{1/2}O_2$, $NaNi_{1/2}Mn_{1/2}O_2$, $NaFe_{1/2}Co_{1/2}O_2$, $Na_{2/3}Ni_{1/3}Mn_{2/3}O_2$ can help understand the mechanism of sodium layer substitution. Other cations that have similar radius with sodium, such as $Bi^{3+}$ (ionic radius 1.03 Å), might also be used for sodium layer cation substitution. Besides the

conventional high-temperature solid state synthesis, other methods, such as ion exchange, could be used to prepare calcium (or other cation) substituted layered oxides.

For O3 type $NaMO_x$ materials with a sodium stoichiometry of 1, the total charge in the transition metal layer is fixed to be 3+ in order for the charge to be balanced. The charge balance condition becomes modified if a multivalent cation is substituted in the sodium layer. For example, enriching the $Ni^{2+}$ ion content might also be achieved by adding calcium ion the sodium layer. The relationship between x,y, and z in $Na_{1-x}Ca_xNi^{2+}{}_yM^{z+}{}_{1-y}O_2$ is:

$$y = \frac{z + x - 3}{z - 2}$$

When z equals 4, such as in the case of $Mn^{4+}$ in $Na_{1-x}Ca_xNi^{2+}{}_yMn^{4+}{}_{1-y}O_2$, the relationship between x and y is:

$$y = \frac{1 + x}{2}$$

This equation shows that O3 materials can tolerate more $Ni^{2+}$ ions as calcium substitution increases. The same applies to P2-type materials. This effect would increase the redox capacity limit. Therefore, sodium site substitution might offer a new strategy for designing high capacity positive electrode materials for sodium ion batteries.

Air-sensitivity of most sodium cathode materials remains one of the biggest challenges in commercialization of sodium ion batteries. Methods improving the air-stability have to be developed in order for sodium cathode materials to gain practical application. Surface modification is promising as it can change the surface properties of

cathode materials. Chapter 6 shows the beneficial effect of washing $NaNi_{0.5}Mn_{0.5}O_2$ with ethanol in terms of air-stability and electrochemistry. The effect of ethanol washing on different air-sensitive sodium cathode materials should be studied. It is also valuable to investigate washing with other solvents besides ethanol.

Mechanofusion was shown to be a convenient method to apply surface coatings on Li-ion battery materials. The advantage of the mechanofusion method lies in the fact that it is not limited by the various chemistries of the different coating materials. Theoretically any material can be used as the surface coating. Different oxides, nitrides, carbons, organic compounds need to be evaluated as the coating material. A comparison between coated cathodes synthesized usingdifferent methods, such as wet chemistry or atomic layer deposition, would be of interest for future studies. Mechanofusion should also be applied to Na-ion battery materials. Being a dry processing method it is ideal for Na-ion cathodes, which tend to be moisture sensitive. Since mechanofusion produces a very dense surface coating that is gas-tight, as shown in Chapter 9, such coatings might mitigate the undesired reaction between sodium cathode surfaces and air, leading to improved air-stability.

All the cells in this thesis were tested as half-cells using alkali metal foils. Sodium metal is very reactive and causes rapid electrolyte deterioration. Further investigation using full cells or symmetric cells can provide greater insights into the practical relevance of sodium cathode materials. Electrolyte additives have rarely been studied in sodium ion batteries. For full cells or symmetric cells, the effect of electrolyte additives should be evaluated.

## BIBLIOGRAPHY


[1] N. Yabuuchi, K. Kubota, M. Dahbi, S. Komaba, Research Development on Sodium-Ion Batteries, Chem. Rev. 114 (2014) 11636–11682.

[2] M. Höök, X. Tang, Depletion of Fossil Fuels and aAnthropogenic Climate Change-A Review, Energy Policy. 52 (2013) 797–809.

[3] Canada's Plan to Reduce Emissions From the Electricity Sector. https://www.canada.ca/en/environment-climate-change/news/2018/12/canadas-plan-to-reduce-emissions-from-the-electricity-sector.html (acessed Jan 29, 2019).

[4] S. Rehman, L.M. Al-Hadhrami, M.M. Alam, Pumped Hydro Energy Storage System: A Technological Review, Renew. Sustain. Energy Rev. 44 (2015) 586–598.

[5] B. Dunn, H. Kamath, J.-M. Tarascon, Electrical Energy Storage for the Grid: A Battery of Choices, Science. 334 (2011) 928–935.

[6] G. Zubi, R. Dufo-López, M. Carvalho, G. Pasaoglu, The Lithium-Ion Battery: State of the Art and Future Perspectives, Renew. Sustain. Energy Rev. 89 (2018) 292–308.

[7] N. Nitta, F. Wu, J.T. Lee, G. Yushin, Li-Ion Battery Materials: Present and Future, Mater. Today. 18 (2015) 252–264.

[8] USGS, Lithium Ressources, Miner. Commod. Summ. 2017. (2017) 100–101.

[9] USGS, Lithium Ressources, Miner. Commod. Summ. 2018. (2018) 98–99.

[10] M.D. Slater, D. Kim, E. Lee, C.S. Johnson, Sodium-Ion Batteries, Adv. Funct. Mater. 23 (2013) 947–958.

[11] N. Yabuuchi, M. Kajiyama, J. Iwatate, H. Nishikawa, S. Hitomi, R. Okuyama, R. Usui, Y. Yamada, S. Komaba, P2-Type $Na_x[Fe_{1/2}Mn_{1/2}]O_2$ Made from Earth-Abundant Elements for Rechargeable Na Batteries, Nat. Mater. 11 (2012) 512–517.

[12] M.H. Han, E. Gonzalo, G. Singh, T. Rojo, A Comprehensive Review of Sodium Layered Oxides: Powerful Cathodes for Na-Ion Batteries, Energy Environ. Sci. 8 (2015) 81–102.

[13] K. Kubota, S. Komaba, Review—Practical Issues and Future Perspective for Na-Ion Batteries, J. Electrochem. Soc. 162 (2015) A2538–A2550.

[14] B.L. Ellis, K.T. Lee, L.F. Nazar, Positive Electrode Materials for Li-Ion and Li-Batteries, Chem. Mater. 22 (2010) 691–714.

[15] C. Delmas, C. Fouassier, P. Hagenmuller, Structural Classification and Properties of the Layered Oxides, Phys. B+C. 99 (1980) 81–85.

[16] N. Yabuuchi, Y. Kawamoto, R. Hara, T. Ishigaki, A. Hoshikawa, M. Yonemura, T. Kamiyama, S. Komaba, A Comparative Study of $LiCoO_2$ Polymorphs: Structural and Electrochemical Characterization of O2-, O3-, and O4-type Phases, Inorg. Chem. 52 (2013) 9131–9142.

[17] S.A. Needham, G.X. Wang, H.K. Liu, V.A. Drozd, R.S. Liu, Synthesis and Electrochemical Performance of Doped $LiCoO_2$ Materials, J. Power Sources. 174 (2007) 828–831.

[18] G.G. Amatucci, J.M. Tarascon, L.C. Klein, $CoO_2$, The End Member of the $LiCoO_2$ Solid Solution, Electrochem. Soc. 143 (1996) 1114–1123.

[19] J. Xu, F. Lin, M.M. Doeff, W. Tong, A Review of Ni-based Layered Oxides for Rechargeable Li-Ion Batteries, J. Mater. Chem. A. 5 (2017) 874–901.

[20] H. Chen, J.A. Dawson, J.H. Harding, Effects of Cationic Substitution on Structural Defects in Layered Cathode Materials $LiNiO_2$, J. Mater. Chem. A. 2 (2014) 7988–7996.

[21] J. Molenda, P. Wilk, J. Marzec, Structural, Electrical and Electrochemical Properties of $LiNiO_2$, Solid State Ionics. 146 (2002) 73–79.

[22] H. Liu, Y. Yang, J. Zhang, Reaction Mechanism and Kinetics of Lithium Ion Battery Cathode Material $LiNiO_2$ with $CO_2$, J. Power Sources. 173 (2007) 556–561.

[23] J.R. Dahn, E.W. Fuller, M.N. Obrovac, U. von Sacken, Thermal-Stability of $Li_xCoO_2$, $Li_xNiO_2$ and $\lambda$-$MnO_2$ and Consequences for the Safety of Li-Ion Cells, Solid State Ionics. 69 (1994) 265–270.

[24] J.K. Ngala, N.A. Chernova, M. Ma, M. Mamak, P.Y. Zavalij, M.S. Whittingham, The Synthesis, Characterization and Electrochemical Behavior of the Layered $LiNi_{0.4}Mn_{0.4}Co_{0.2}O_2$ Compound, J. Mater. Chem. 14 (2004) 214–220.

[25] T. Ohzuku, A. Ueda, M. Kouguchi, Synthesis and Characterization of $LiAl_{1/4}Ni_{3/4}O_2$ (R3m) for Lithium-Ion (Shuttlecock) Batteries, 142 (1995) 4033–4039.

[26] H.J. Bang, H. Joachin, H. Yang, K. Amine, J. Prakash, Contribution of the Structural Changes of $LiNi_{0.8}Co_{0.15}Al_{0.05}O_2$ Cathodes on the Exothermic Reactions in Li-Ion Cells, J. Electrochem. Soc. 153 (2006) A731–A737.

[27] Z. Lu, D.D. MacNeil, J.R. Dahn, Layered $Li[Ni_xCo_{1-2x}Mn_x]O_2$ Cathode Materials for Lithium-Ion Batteries, Electrochem. Solid-State Lett. 4 (2001) A200–A203.

[28] T. Ohzuku, Y. Makimura, Layered Lithium Insertion Material of $LiCo_{1/3}Ni_{1/3}Mn_{1/3}O_2$ for Lithium-Ion Batteries, Chem. Lett. 30 (2001) 642–643.

[29] H.J. Noh, S. Youn, C.S. Yoon, Y.K. Sun, Comparison of the Structural and Electrochemical Properties of Layered $Li[Ni_xCo_yMn_z]O_2$ (x = 1/3, 0.5, 0.6, 0.7, 0.8 and 0.85) Cathode Material for Lithium-Ion Batteries, J. Power Sources. 233 (2013) 121–130.

[30] A. Manthiram, B. Song, W. Li, A Perspective on Nickel-rich Layered Oxide Cathodes for Lithium-Ion Batteries, Energy Storage Mater. 6 (2017) 125–139.

[31] H.J. Bang, B.-C. Park, J. Prakash, Y.-K. Sun, Synthesis and Electrochemical Properties of $Li[Ni_{0.45}Co_{0.1}Mn_{0.45-x}Zr_x]O_2$ (x = 0, 0.02) via Co-precipitation Method, J. Power Sources. 174 (2007) 565–568.

[32] P.Y. Liao, J.G. Duh, H.S. Sheu, Structural and Thermal Properties of $LiNi_{0.6-x}Mg_xCo_{0.25}Mn_{0.15}O_2$ Cathode Materials, J. Power Sources. 183 (2008) 766–770.

[33] K.C. Kam, A. Mehta, J.T. Heron, M.M. Doeff, Electrochemical and Physical Properties of Ti-Substituted Layered Nickel Manganese Cobalt Oxide (NMC) Cathode Materials, J. Electrochem. Soc. 159 (2012) A1383–A1392.

[34] N. Yabuuchi, K. Yoshii, S.T. Myung, I. Nakai, S. Komaba, Detailed Studies of a High-Capacity Electrode Material for Rechargeable Batteries, $Li_2MnO_3$-$LiCo_{1/3}Ni_{1/3}Mn_{1/3}O_2$, J. Am. Chem. Soc. 133 (2011) 4404–4419.

[35] S.-H. Kang, C.S. Johnson, J.T. Vaughey, K. Amine, M.M. Thackeray, The Effects of Acid Treatment on the Electrochemical Properties of $0.5\ Li_2MnO_3 \cdot 0.5\ LiNi_{0.44}Co_{0.25}Mn_{0.31}O_2$ Electrodes in Lithium Cells, J. Electrochem. Soc. 153 (2006) A1186–A1192.

[36] C.S. Johnson, N. Li, C. Lefief, M.M. Thackeray, Anomalous Capacity and Cycling Stability of $xLi_2MnO_3 \cdot (1 - x)LiMO_2$ Electrodes (M = Mn, Ni, Co) in Lithium Batteries at 50 °C, Electrochem. Commun. 9 (2007) 787–795.

[37] A.D. Robertson, P.G. Bruce, Mechanism of Electrochemical Activity in $Li_2MnO_3$, Chem. Mater. 15 (2003) 1984–1992.

[38] J. Zheng, S. Myeong, W. Cho, P. Yan, J. Xiao, C. Wang, J. Cho, J.G. Zhang, Li- and Mn-Rich Cathode Materials: Challenges to Commercialization, Adv. Energy Mater. 7 (2017) 1601284.

[39] Z. Chen, Y. Qin, K. Amine, Y.-K. Sun, Role of Surface Coating on Cathode Materials for Lithium-Ion Batteries, J. Mater. Chem. 20 (2010) 7606–7612.

[40] S.S. Zhang, A Review on Electrolyte Additives for Lithium-Ion Batteries, J. Power Sources. 162 (2006) 1379–1394.

[41] Y.K. Sun, S.T. Myung, M.H. Kim, J. Prakash, K. Amine, Synthesis and Characterization of $Li[(Ni_{0.8}Co_{0.1}Mn_{0.1})_{0.8}(Ni_{0.5}Mn_{0.5})_{0.2}]O_2$ with the Microscale Core-Shell Structure as the Positive Electrode Material for Lithium Ba, J. Am. Chem. Soc. 127 (2005) 13411–13418.

[42] G. Xu, Z. Liu, C. Zhang, G. Cui, L. Chen, Strategies for Improving the Cyclability and Thermo-Stability of $LiMn_2O_4$-based Batteries at Elevated Temperatures, J. Mater. Chem. A. 3 (2015) 4092–4123.

[43] W.J. Zhang, Structure and Performance of $LiFePO_4$ Cathode Materials: A Review, J. Power Sources. 196 (2011) 2962–2970.

[44] J. Jiang, J.R. Dahn, ARC Studies of the Thermal Stability of Three Different Cathode Materials: $LiCoO_2$; $Li[Ni_{0.1}Co_{0.8}Mn_{0.1}]O_2$; and $LiFePO_4$, in $LiPF_6$ and LiBoB EC/DEC Electrolytes, Electrochem. Commun. 6 (2004) 39–43.

[45] W. Xu, J. Wang, F. Ding, X. Chen, E. Nasybulin, Y. Zhang, J.G. Zhang, Lithium Metal Anodes for Rechargeable Batteries, Energy Environ. Sci. 7 (2014) 513–537.

[46] D. Aurbach, E. Zinigrad, H. Teller, P. Dan, Factors Which Limit the Cycle Life of Rechargeable Lithium (Metal) Batteries, J. Electrochem. Soc. 147 (2000) 1274–1279.

[47] J.R. Dahn, T. Zheng, Y. Liu, J.S. Xue, Mechanisms for Lithium Insertion in Carbonaceous Materials, Science. 270 (1995) 590–593.

[48] H. Shi, J. Barker, M.Y. Saidi, R. Koksbang, Structure and Lithium Intercalation Properties of Synthetic and Natural Graphite, J. Electrochem. Soc. 143 (1996) 3466–3472.

[49] C. Birkenmaier, B. Bitzer, M. Harzheim, A. Hintennach, T. Schleid, Lithium Plating on Graphite Negative Electrodes: Innovative Qualitative and Quantitative Investigation Methods, J. Electrochem. Soc. 162 (2015) A2646–A2650.

[50] E. Björklund, D. Brandell, M. Hahlin, K. Edström, R. Younesi, How the Negative Electrode Influences Interfacial and Electrochemical Properties of $LiNi_{1/3}Co_{1/3}Mn_{1/3}O_{1/3}$ Cathodes in Li-Ion Batteries, J. Electrochem. Soc. 164 (2017) A3054–A3059.

[51] T.F. Yi, S.Y. Yang, Y. Xie, Recent Advances of $Li_4Ti_5O_{12}$ as a Promising Next Generation Anode Material for High Power Lithium-Ion Batteries, J. Mater. Chem. A. 3 (2015) 5750–5777.

[52] K. Zaghib, M. Simoneau, M. Armand, M. Gauthier, Electrochemical Study of $Li_4Ti_5O_{12}$ as Negative Electrode for Li-Ion Polymer Rechargeable Batteries, J. Power Sources. 81–82 (1999) 300–305.

[53] J.B. Goodenough, Y. Kim, Challenges for Rechargeable Li Batteries, Chem. Mater. 22 (2010) 587–603.

[54] M.N. Obrovac, V.L. Chevrier, Alloy Negative Electrodes for Li-Ion Batteries, Chem. Rev. 114 (2014) 11444–11502.

[55] M.N. Obrovac, L.J. Krause, Reversible Cycling of Crystalline Silicon Powder, J. Electrochem. Soc. 154 (2007) A103.

[56] J. Park, Principles and Applications of Lithium Secondary Batteries, 2012.

[57] S. Tan, Y.J. Ji, Z.R. Zhang, Y. Yang, Recent Progress in Research on High-Voltage Electrolytes for Lithium-Ion Batteries, ChemPhysChem. 15 (2014) 1956–1969.

[58] S.F. Lux, I.T. Lucas, E. Pollak, S. Passerini, M. Winter, R. Kostecki, The Mechanism of HF Formation in $LiPF_6$ Based Organic Carbonate Electrolytes, Electrochem. Commun. 14 (2012) 47–50.

[59] P. Verma, P. Maire, P. Novák, A Review of the Features and Analyses of the Solid Electrolyte Interphase in Li-Ion Batteries, Electrochim. Acta. 55 (2010) 6332–6341.

[60] S.K. Jeong, M. Inaba, Y. Iriyama, T. Abe, Z. Ogumi, Interfacial Reactions Between Graphite Electrodes and Propylene Carbonate-Based Solutions: Electrolyte-Concentration Dependence of Electrochemical Lithium Intercalation Reaction, J. Power Sources. 175 (2008) 540–546.

[61] L. Liu, J. Park, X. Lin, A.M. Sastry, W. Lu, A Thermal-Electrochemical Model that Gives Spatial-Dependent Growth of Solid Electrolyte Interphase in a Li-Ion Battery, J. Power Sources. 268 (2014) 482–490.

[62] Z. Chen, W.Q. Lu, J. Liu, K. Amine, $LiPF_6$/LiBOB Blend Salt Electrolyte for High-Power Lithium-Ion Batteries, Electrochim. Acta. 51 (2006) 3322–3326.

[63] S. Kikkawa, S. Miyazaki, M. Koizumi, Deintercalated $NaCoO_2$ and $LiCoO_2$, J. Solid State Chem. 62 (1986) 35–39.

[64] C. Delmas, J.J. Braconnier, C. Fouassier, P. Hagenmuller, Electrochemical Intercalation of Sodium in $Na_xCoO_2$ Bronzes, Solid State Ionics. 3–4 (1981) 165–169.

[65] S.W. Kim, D.H. Seo, X. Ma, G. Ceder, K. Kang, Electrode Materials for Rechargeable Sodium-Ion Batteries: Potential Alternatives to Current Lithium-Ion Batteries, Adv. Energy Mater. 2 (2012) 710–721.

[66] J.M. Paulsen, R.A. Donaberger, J.R. Dahn, Layered T2-, O6-, O2-, and P2-Type $A_{2/3}[M'^{2+}_{1/3}M^{4+}_{2/3}]O_2$ Bronzes, A = Li, Na; M' = Ni, Mg; M = Mn, Ti, Chem. Mater. 12 (2000) 2257–2267.

[67] Y. Lei, X. Li, L. Liu, G. Ceder, Synthesis and Stoichiometry of Different Layered Sodium Cobalt Oxides, Chem. Mater. 26 (2014) 5288–5296.

[68] J.M. Paulsen, Layered Li-Mn-Oxide with the O2 Structure: A Cathode Material for Li-Ion Cells Which Does Not Convert to Spinel, J. Electrochem. Soc. 146 (1999) 3560.

[69] R.J. Balsys, R.L. Davis, The structure of $Li_{0.43}Na_{0.36}CoO_{1.96}$ using neutron powder diffraction, 69 (1994) 69–74.

[70] R. Berthelot, M. Pollet, D. Carlier, C. Delmas, Reinvestigation of the OP4-(Li/Na)$CoO_2$-Layered System and First Evidence of the (Li/Na/Na)$CoO_2$ Phase with OPP9 Oxygen Stacking, Inorg. Chem. 50 (2011) 2420–2430.

[71] S. Kim, X. Ma, S.P. Ong, G. Ceder, A Comparison of Destabilization Mechanisms of the Layered $Na_xMO_2$ and $Li_xMO_2$ Compounds upon Alkali De-Intercalation, Phys. Chem. Chem. Phys. 14 (2012) 15571–15578.

[72] D.H. Lee, J. Xu, Y.S. Meng, An Advanced Cathode for Na-Ion Batteries with High Rate and Excellent Structural Stability, Phys. Chem. Chem. Phys. 15 (2013) 3304–12.

[73] K. Ado, M. Tabuchi, H. Kobayashi, H. Kageyama, O. Nakamura, Y. Inaba, R. Kanno, M. Takagi, Y. Takeda, Preparation of $LiFeO_2$ with Alpha-$NaFeO_2$-Type Structure Using a Mixed-Alkaline Hydrothermal Method, J. Electrochem. Soc. 144 (1997) L177–L180.

[74] N. Yabuuchi, H. Yoshida, S. Komaba, Crystal Structures and Electrode Performance of Alpha-$NaFeO_2$ for Rechargeable Sodium Batteries, Electrochemistry. 80 (2012) 716–719.

[75] S. Komaba, C. Takei, T. Nakayama, A. Ogata, N. Yabuuchi, Electrochemical Intercalation Activity of Layered $NaCrO_2$ vs. $LiCrO_2$, Electrochem. Commun. 12 (2010) 355–358.

[76] J.S. Throne, R.A. Dunlap, M.N. Obrovac, Structure and Electrochemistry of $Na_xFe_xMn_{1-x2}$ ($1.0 \leq x \leq 0.5$) for Na-Ion Battery Positive Electrodes, J. Electrochem. Soc. 147 (2013) A461–A473.

[77] T.D. Hatchard, M.N. Obrovac, Evaluation of Electrolyte Salts and Solvents for Na-Ion Batteries in Symmetric Cells, J. Electrochem. Soc. 161 (2014) A1748–A1752.

[78] X. Xia, J.R. Dahn, $NaCrO_2$ is a Fundamentally Safe Positive Electrode Material for Sodium-Ion Batteries with Liquid Electrolytes, Electrochem. Solid-State Lett. 15 (2012) A1–A4.

[79] L. Zheng, J. Li, M.N. Obrovac, Crystal Structures and Electrochemical Performance of Air-Stable $Na_{2/3}Ni_{1/3-x}Cu_xMn_{2/3}O_2$ in Sodium Cells, Chem. Mater. 29 (2017) 1623–1631.

[80] X. Wang, G. Liu, T. Iwao, M. Okubo, A. Yamada, Role of Ligand-to-Metal Charge Transfer in O3-Type $NaFeO_2$-$NaNiO_2$ Solid Solution for Enhanced Electrochemical Properties, J. Phys. Chem. C. 118 (2014) 2970–2976.

[81] N. Yabuuchi, M. Yano, H. Yoshida, S. Kuze, S. Komaba, Synthesis and Electrode Performance of O3-Type $NaFeO_2$-$NaNi_{1/2}Mn_{1/2}O_2$ Solid Solution for Rechargeable Sodium Batteries, J. Electrochem. Soc. 160 (2013) A3131–A3137.

[82] K. Kubota, I. Ikeuchi, T. Nakayama, C. Takei, N. Yabuuchi, H. Shiiba, M. Nakayama, S. Komaba, New Insight into Structural Evolution in Layered $NaCrO_2$ during Electrochemical Sodium Extraction, J. Phys. Chem. C. 119 (2015) 166–175.

[83] A. Maazaz, C. Delmas, P. Hagenmuller, A Study of the $Na_xTiO_2$ System by Electrochemical Deintercalation, J. Incl. Phenom. 1 (1983) 45–51.

[84] H. Yoshida, N. Yabuuchi, S. Komaba, $NaFe_{0.5}Co_{0.5}O_2$ as High Energy and Power Positive Electrode for Na-ion Batteries, Electrochem. Commun. 34 (2013) 60–63.

[85] V. Duffort, E. Talaie, R. Black, L.F. Nazar, Uptake of $CO_2$ in Layered P2-$Na_{0.67}Mn_{0.5}Fe_{0.5}O_2$: Insertion of Carbonate Anions, Chem. Mater. 27 (2015) 2515–2524.

[86] L. Zheng, L. Li, R. Shunmugasundaram, M.N. Obrovac, Effect of Controlled-Atmosphere Storage and Ethanol Rinsing on $NaNi_{0.5}Mn_{0.5}O_2$ for Sodium-Ion Batteries, ACS Appl. Mater. Interfaces. 10 (2018) 38246–38254.

[87] Z. Lu, J.R. Dahn, Intercalation of Water in P2, T2 and O2 Structure $A_z[CO_xNi_{1/3-x}Mn_{2/3}]O_2$, Chem. Mater. 13 (2001) 1252–1257.

[88] L. Mu, S. Xu, Y. Li, Y.-S. Hu, H. Li, L. Chen, X. Huang, Prototype Sodium-Ion Batteries Using an Air-Stable and Co/Ni-Free O3-Layered Metal Oxide Cathode, Adv. Mater. (2015) 6928–6933.

[89] Y. Li, Z. Yang, S. Xu, L. Mu, L. Gu, Y.-S. Hu, H. Li, L. Chen, Air-Stable Copper-Based P2-$Na_{7/9}Cu_{2/9}Fe_{1/9}Mn_{2/3}O_2$ as a New Positive Electrode Material for Sodium-Ion Batteries, Adv. Sci. (2015) 1500031.

[90] B. Jache, P. Adelhelm, Use of Graphite as a Highly Reversible Electrode with Superior Cycle Life for Sodium-Ion Batteries by Making use of Co-Intercalation Phenomena, Angew. Chemie Int. Ed. 53 (2014) 10169–10173.

[91] B. Jache, J.O. Binder, T. Abe, P. Adelhelm, A Comparative Study on the Impact of Different Glymes and Their Derivatives as Electrolyte Solvents for Graphite Co-Intercalation Electrodes in Lithium-Ion and Sodium-Ion Batteries, Phys. Chem. Chem. Phys. 18 (2016) 14299–14316.

[92] D.A. Stevens, J.R. Dahn, High Capacity Anode Materials for Rechargeable Sodium-Ion Batteries, J. Electrochem. Soc. 147 (2000) 1271–1273.

[93] D.A. Stevens, J.R. Dahn, The Mechanisms of Lithium and Sodium Insertion in Carbon Materials, J. Electrochem. Soc. 148 (2001) A803–A811.

[94] R. Fielden, M.N. Obrovac, Low Voltage Sodium Intercalation in $Na_xNi_{x/2}Ti_{1-x/2}O_2$ ($0.5 \leq x \leq 1.0$), J. Electrochem. Soc. 161 (2014) A1158–A1163.

[95] C. Bommier, W. Luo, W.Y. Gao, A. Greaney, S. Ma, X. Ji, Predicting Capacity of Hard Carbon Anodes in Sodium-Ion Batteries Using Porosity Measurements, Carbon. 76 (2014) 165–174.

[96] S. Komaba, T. Ishikawa, N. Yabuuchi, W. Murata, A. Ito, Y. Ohsawa, Fluorinated Ethylene Carbonate as Electrolyte Additive For Rechargeable Na Batteries, ACS Appl. Mater. Interfaces. 3 (2011) 4165–4168.

[97] W. Luo, J. Schardt, C. Bommier, B. Wang, J. Razink, J. Simonsen, X. Ji, Carbon Nanofibers Derived from Cellulose Nanofibers as a Long-Life Anode Material for Rechargeable Sodium-Ion Batteries, J. Mater. Chem. A. 1 (2013) 10662–10666.

[98] T.T. Tran, M.N. Obrovac, Alloy Negative Electrodes for High Energy Density Metal-Ion Cells, J. Electrochem. Soc. 158 (2011) A1411–A1416.

[99] L. Zheng, R.A. Dunlap, M.N. Obrovac, The Electrochemical Reaction Mechanism of Tin Phosphide with Sodium, J. Electrochem. Soc. 163 (2016) A1188–A1191.

[100] V.L. Chevrier, G. Ceder, Challenges for Na-ion Negative Electrodes, J. Electrochem. Soc. 158 (2011) A1011–A1014.

[101] L.D. Ellis, B.N. Wilkes, T.D. Hatchard, M.N. Obrovac, In Situ XRD Study of Silicon, Lead and Bismuth Negative Electrodes in Nonaqueous Sodium Cells, J. Electrochem. Soc. 161 (2014) A416–A421.

[102] L.D. Ellis, T.D. Hatchard, M.N. Obrovac, Reversible Insertion of Sodium in Tin, J. Electrochem. Soc. 159 (2012) A1801–A1805.

[103] L. Wu, D. Buchholz, D. Bresser, L. Gomes Chagas, S. Passerini, Anatase $TiO_2$ Nanoparticles for High Power Sodium-ion Anodes, J. Power Sources. 251 (2014) 379–385.

[104] P. Senguttuvan, G. Rousse, V. Seznec, J.M. Tarascon, M.R. Palacín, $Na_2Ti_3O_7$: Lowest Voltage Ever Reported Oxide Insertion Electrode for Sodium Ion Batteries, Chem. Mater. 23 (2011) 4109–4111.

[105] A. Rudola, K. Saravanan, S. Devaraj, H. Gong, P. Balaya, $Na_2Ti_6O_{13}$: A Potential Anode for Grid-Storage Sodium-Ion Batteries, Chem. Commun. 49 (2013) 7451–7453.

[106] H. Yu, Y. Ren, D. Xiao, S. Guo, Y. Zhu, Y. Qian, L. Gu, H. Zhou, An Ultrastable Anode for Long-Life Room-Temperature Sodium-Ion Batteries, Angew. Chemie Int. Ed. 53 (2014) 8963–8969.

[107] Y. Wang, R. Xiao, Y.S. Hu, M. Avdeev, L. Chen, P2-$Na_{0.6}[Cr_{0.6}Ti_{0.4}]O_2$ Cation-Disordered Electrode for High-Rate Symmetric Rechargeable Sodium-Ion Batteries, Nat. Commun. 6 (2015) 1–9.

[108] R. Shanmugam, W. Lai, $Na_{2/3}Ni_{1/3}Ti_{2/3}O_2$: "Bi-Functional" Electrode Materials for Na-Ion Batteries, ECS Electrochem. Lett. 3 (2014) A23–A25.

[109] P. Vassilaras, X. Ma, H. Chen, G. Ceder, Electrochemical Properties of Monoclinic $NaNiO_2$, J. Electrochem. Soc. 160 (2013) A207–A211.

[110] H. Yoshida, N. Yabuuchi, K. Kubota, I. Ikeuchi, A. Garsuch, M. Schulz-Dobrick, S. Komaba, P2-type $Na_{2/3}Ni_{1/3}Mn_{2/3-x}Ti_xO_2$ as a New Positive Electrode for Higher Energy Na-Ion Batteries, Chem. Commun. 50 (2014) 3677–3680.

[111] D. Yuan, X. Liang, L. Wu, Y. Cao, X. Ai, J. Feng, H. Yang, A Honeycomb-Layered $Na_3Ni_2SbO_6$: A High-Rate and Cycle-Stable Cathode for Sodium-Ion Batteries, Adv. Mater. 26 (2014) 6301–6306.

[112] A. Gupta, C. Buddie Mullins, J.B. Goodenough, $Na_2Ni_2TeO_6$: Evaluation as a Cathode for Sodium Battery, J. Power Sources. 243 (2013) 817–821.

[113] S. Komaba, N. Yabuuchi, T. Nakayama, A. Ogata, T. Ishikawa, I. Nakai, Study on the Reversible Electrode Reaction of $Na_{1-x}Ni_{0.5}Mn_{0.5}O_2$ for a Rechargeable Sodium-Ion battery, Inorg. Chem. 51 (2012) 6211–6220.

[114] Z. Lu, J.R. Dahn, In Situ X-Ray Diffraction Study of P2-$Na_{2/3}[Ni_{2/3}Mn_{2/3}]O_2$, J. Electrochem. Soc. 148 (2001) A1225–A1229.

[115] P. Manikandan, D. Ramasubramonian, M.M. Shaijumon, Layered P2-Type $Na_{0.5}Ni_{0.25}Mn_{0.75}O_2$ as a High Performance Cathode Material for Sodium-Ion Batteries, Electrochim. Acta. 206 (2016) 199–206.

[116] B. Mortemard de Boisse, G. Liu, J. Ma, S. Nishimura, S.-C. Chung, H. Kiuchi, Y. Harada, J. Kikkawa, Y. Kobayashi, M. Okubo, A. Yamada, Intermediate Honeycomb Ordering to Trigger Oxygen Redox Chemistry in Layered Battery Electrode, Nat. Commun. 7 (2016) 11397.

[117] E.M. Seibel, J.H. Roudebush, H. Wu, Q. Huang, M.N. Ali, H. Ji, R.J. Cava, Structure and Magnetic Properties of the α-$NaFeO_2$-Type Honeycomb Compound $Na_3Ni_2BiO_6$, Inorg. Chem. 52 (2013) 13605–13611.

[118] G. Singh, N. Tapia-Ruiz, J.M. Lopez del Amo, U. Maitra, J.W. Somerville, A.R. Armstrong, J. Martinez de Ilarduya, T. Rojo, P.G. Bruce, High Voltage Mg-Doped $Na_{0.67}Ni_{0.3-x}Mg_xMn_{0.7}O_2$ ( x = 0.05, 0.1) Na-Ion Cathodes with Enhanced Stability and Rate Capability, Chem. Mater. 28 (2016) 5087–5094.

[119] J. Xu, D.H. Lee, R.J. Clément, X. Yu, M. Leskes, A.J. Pell, G. Pintacuda, X.-Q. Yang, C.P. Grey, Y.S. Meng, Identifying the Critical Role of Li Substitution in P2–$Na_x[Li_yNi_zMn_{1-y-z}]O_2$ ($0 < x, y, z < 1$) Intercalation Cathode Materials for High-Energy Na-Ion Batteries, Chem. Mater. 26 (2014) 1260–1269.

[120] L. Nim, B.M. Mg, A. Ni, R. Berthelot, W. Schmidt, S. Muir, J. Eilertsen, L. Etienne, a W. Sleight, M. a Subramanian, New Layered Compounds with Honeycomb Ordering: $Li_3Ni_2BiO_6$, $Li_3NiM'BiO_6$ (M' = Mg, Cu, Zn), and the Delafossite $Ag_3Ni_2BiO_6$, Inorg. Chem. 6 (2012) 5377–5385.

[121] X. Ma, K. Kang, G. Ceder, Y.S. Meng, Synthesis and Electrochemical Properties of Layered $LiNi_{2/3}Sb_{1/3}O_2$, J. Power Sources. 173 (2007) 550–555.

[122] X. Wu, J. Guo, D. Wang, G. Zhong, M.J. McDonald, Y. Yang, P2-type $Na_{0.66}Ni_{0.33-x}Zn_xMn_{0.67}O_2$ as New High-Voltage Cathode Materials for Sodium-Ion Batteries, J. Power Sources. 281 (2015) 18–26.

[123] C.W. Mason, F. Lange, K. Saravanan, F. Lin, D. Nordlund, Beyond Divalent Copper: A Redox Couple for Sodium Ion Battery Cathode Materials, ECS Electrochem. Lett. 4 (2015) A41–A44.

[124] W. Kang, Z. Zhang, P.K. Lee, T.W. Ng, W. Li, Y. Tang, W. Zhang, C.S. Lee, D.Y. Wai Yu, Copper Substituted P2-type $Na_{0.67}Cu_xMn_{1-x}O_2$ : a Stable High-Power Sodium-Ion Battery Cathode, J. Mater. Chem. A. 3 (2015) 22846–22852.

[125] S.-Y. Xu, X.-Y. Wu, Y.-M. Li, Y.-S. Hu, L.-Q. Chen, Novel Copper Redox-Based Cathode Materials for Room-Temperature Sodium-Ion Batteries, Chinese Phys. B. 23 (2014) 118202.

[126] N. Yabuuchi, R. Hara, M. Kajiyama, K. Kubota, T. Ishigaki, A. Hoshikawa, S. Komaba, New O2/P2-Type Li-Excess Layered Manganese Oxides as Promising Multi-Functional Electrode Materials for Rechargeable Li/Na Batteries, Adv. Energy Mater. 4 (2014) 1301453.

[127] J. Billaud, G. Singh, A.R. Armstrong, E. Gonzalo, V. Roddatis, M. Armand, T. Rojo, P.G. Bruce, $Na_{0.67}Mn_{1-x}Mg_xO_2$ ($0 \leq x \leq 0.2$): a High Capacity Cathode for Sodium-Ion Batteries, Energy Environ. Sci. 7 (2014) 1387–1391.

[128] H. Yu, S. Guo, Y. Zhu, M. Ishida, H. Zhou, Novel Titanium-Based O3-type $NaTi_{0.5}Ni_{0.5}O_2$ as a Cathode Material for Sodium Ion Batteries, Chem. Commun. 50 (2014) 457–459.

[129] H. Wang, Y. Xiao, C. Sun, C. Lai, X. Ai, A Type of Sodium-Ion Full-Cell with a Layered $NaNi_{0.5}Ti_{0.5}O_2$ Cathode and a Pre-Sodiated Hard Carbon Anode, RSC Adv. 5 (2015) 106519–106522.

[130] K. Kang, D. Carlier, J. Reed, E. Arroyo, G. Ceder, L. Croguennec, C. Delmas, Synthesis and Electrochemical Properties of Layered $Li_{0.9}Ni_{0.45}Ti_{0.55}O_2$, Chem. Mater. 15 (2003) 4503–4507.

[131] N. Yabuuchi, R. Hara, K. Kubota, J. Paulsen, S. Kumakura, S. Komaba, A New Electrode Material for Rechargeable Sodium Batteries: P2-Type $Na_{2/3}[Mg_{0.28}Mn_{0.72}]O_2$ with Anomalously High Reversible Capacity, J. Mater. Chem. A. 2 (2014) 16851–16855.

[132] R. Shanmugam, W. Lai, Study of Transport Properties and Interfacial Kinetics of $Na_{2/3}[Ni_{1/3}Mn_xTi_{2/3-x}]O_2$ (x = 0,1/3) as Electrodes for Na-Ion Batteries, J. Electrochem. Soc. 162 (2014) A8–A14.

[133] H. Guo, Y. Wang, W. Han, Z. Yu, X. Qi, K. Sun, Y.-S. Hu, Y. Liu, D. Chen, L. Chen, Na-Deficient O3-Type Cathode Material $Na_{0.8}[Ni_{0.3}Co_{0.2}Ti_{0.5}]O_2$ for Room-Temperature Sodium-Ion Batteries, Electrochim. Acta. 158 (2015) 258–263.

[134] J. Ma, S.H. Bo, L. Wu, Y. Zhu, C.P. Grey, P.G. Khalifah, Ordered and Disordered Polymorphs of $Na(Ni_{2/3}Sb_{1/3})O_2$: Honeycomb-Ordered Cathodes for Na-Ion Batteries, Chem. Mater. 27 (2015) 2387–2399.

[135] Z. Chen, J.R. Dahn, Effect of a $ZrO_2$ Coating on the Structure and Electrochemistry of $Li_xCoO_2$ When Cycled to 4.5 V, Electrochem. Solid-State Lett. 5 (2002) A213–A216.

[136] Y. Liu, X. Fang, A. Zhang, C. Shen, Q. Liu, H.A. Enaya, C. Zhou, Layered P2-$Na_{2/3}[Ni_{1/3}Mn_{2/3}]O_2$ as High-Voltage Cathode for Sodium-Ion Batteries: The Capacity Decay Mechanism and $Al_2O_3$ Surface Modification, Nano Energy. 27 (2016) 27–34.

[137] R. Moshtev, P. Zlatilova, S. Vasilev, I. Bakalova, A. Kozawa, Synthesis, XRD Characterization and Electrochemical Performance of Overlithiated $LiNiO_2$, J. Power Sources. 81–82 (1999) 434–441.

[138] X. Zheng, X. Li, Z. Wang, H. Guo, Z. Huang, G. Yan, D. Wang, Investigation and Improvement on the Electrochemical Performance and Storage Characteristics of $LiNiO_2$-Based Materials for Lithium Ion Battery, Electrochim. Acta. 191 (2016) 832–840.

[139] M. Sathiya, K. Hemalatha, K. Ramesha, J.M. Tarascon, A.S. Prakash, Synthesis, Structure, and Electrochemical Properties of the Layered Sodium Insertion Cathode Material: $NaNi_{1/3}Mn_{1/3}Co_{1/3}O_2$, Chem. Mater. 24 (2012) 1846–1853.

[140] R. Fielden, L. Cole, M.N. Obrovac, Low Voltage Sodium Intercalation in $Na_xV_xTi_{1-x}O_2$ ($2/3 \leq x \leq 1.0$), J. Electrochem. Soc. 164 (2017) A490–A497.

[141] N. Yabuuchi, Y. Koyama, N. Nakayama, T. Ohzuku, Solid-State Chemistry and Electrochemistry of $LiCo_{1/3}Ni_{1/3}Mn_{1/3}O_2$ for Advanced Lithium-Ion Batteries, J. Electrochem. Soc. 152 (2005) A1434–A1440.

[142] L. Li, Z. Chen, Q. Zhang, M. Xu, X. Zhou, H. Zhu, K. Zhang, A Hydrolysis-Hydrothermal Route for the Synthesis of Ultrathin $LiAlO_2$-Inlaid $LiNi_{0.5}Co_{0.2}Mn_{0.3}O_2$ as a High-Performance Cathode Material for Lithium Ion Batteries, J. Mater. Chem. A. 3 (2015) 894–904.

[143] J.S. Thorne, R.A. Dunlap, M.N. Obrovac, Investigation of P2-$Na_{2/3}Mn_{1/3}Fe_{1/3}Co_{1/3}O_2$ for Na-Ion Battery Positive Electrodes, J. Electrochem. Soc. 161 (2014) A2232–A2236.

[144] X. Li, D. Wu, Y.-N. Zhou, L. Liu, X.-Q. Yang, G. Ceder, O3-Type $Na(Mn_{0.25}Fe_{0.25}Co_{0.25}Ni_{0.25})O_2$: A Quaternary Layered Cathode Compound for Rechargeable Na Ion Batteries, Electrochem. Commun. 49 (2014) 51–54.

[145] J.-Y. Hwang, C.S. Yoon, I. Belharouak, Y.-K. Sun, A Comprehensive Study of the Role of Transition Metals in O3-Type Layered $Na[Ni_xCo_yMn_z]O_2$ ($x = 1/3$, 0.5, 0.6, and 0.8) Cathodes for Sodium-Ion Batteries, J. Mater. Chem. A. 4 (2016) 17952–17959.

[146] L.D. Dyer, B.S. Borie, G.P. Smith, Alkali Metal-Nickel Oxides of the Type $MNiO_2$, J. Am. Chem. Soc. 76 (1954) 1499–1503.

[147] E. Garc, Study of the ferrodistorsive orbital ordering in $NaNiO_2$ by neutron diffraction and submillimeter wave ESR, Eur. Phys. J. B. 17 (2000) 615–622.

[148] J.J. Braconnier, C. Delmas, P. Hagenmuller, Etude par Desintercalation Electrochimique des Systemes $Na_xCrO_2$ et $Na_xNiO_2$, Mater. Res. Bull. 17 (1982) 993–1000.

[149] M.H. Han, E. Gonzalo, M. Casas-Cabanas, T. Rojo, Structural Evolution and Electrochemistry of Monoclinic $NaNiO_2$ upon the First Cycling Process, J. Power Sources. 258 (2014) 266–271.

[150] E. Zhecheva, R. Stoyanova, Stabilization of the Layered Crystal Structure of $LiNiO_2$ by Co-Substitution, Solid State Ionics. 66 (1993) 143–149.

[151] H. Arai, S. Okada, Y. Sakurai, J. Yamaki, Electrochemical and Thermal Behavior of $LiNi_{1-z}M_zO_2$ ( M = Co , Mn , Ti ), J. Electrochem. Soc. 144 (1997) 3117–3125.

[152] G.X. Wang, S. Zhong, D.H. Bradhurst, S.X. Dou, H.K. Liu, $LiAl_\delta Ni_{1-\delta}O_2$ Solid Solutions as Cathodic Mmaterials for Rechargeable Lithium Batteries, Solid State Ionics. 116 (1999) 271–277.

[153] D.J. Lee, B. Scrosati, Y.K. Sun, $Ni_3(PO_4)_2$-Coated $Li[Ni_{0.8}Co_{0.15}Al_{0.05}]O_2$ Lithium Battery Electrode with Improved Cycling Performance at 55°C, J. Power Sources. 196 (2011) 7742–7746.

[154] J.D. Jorgensen, H. Shaked, D.G. Hinks, B. Dabrowski, B.W. Veal, A.P. Paulikas, L.J. Nowicki, G.W. Crabtree, W.K. Kwok, L.H. Nunez, H. Claus, Oxygen Vacancy Ordering and Superconductivity in $YBa_2Cu_3O_{7-x}$, Phys. C Supercond. Its Appl. 153–155 (1988) 578–581.

[155] J.D. Jorgensen, B.W. Veal, W.K. Kwok, G.W. Crabtree, A. Umezawa, L.J. Nowicki, A.P. Paulikas, Structural and Superconducting Properties of Orthorhombic and Tetragonal $YBa_2Cu_3O_{7-x}$: The Effect of Oxygen Stoichiometry and Ordering on Superconductivity, Phys. Rev. B. 36 (1987) 5731–5734.

[156] A. Yamada, K. Miura, K. Hinokuma, M. Tanaka, Synthesis and Structural Aspects of $LiMn_2O_{4\pm\delta}$ as a Cathode for Rechargeable Lithium Batteries, J. Electrochem. Soc. 142 (1995) 2149–2156.

[157] X.Q. Yang, X. Sun, M. Balasubramanian, J. McBreen, Y. Xia, T. Sakai, M. Yoshio, The Population of Oxygen Vacancies in $Li_{1+y}Mn_{2-y}O_{4-\delta}$ Type Cathode Materials: The Primary Factor of Temperature Dependent Structural Changes, Electrochem. Solid-State Lett. 4 (2001) A117–A120.

[158] X. Li, Y. Wang, D. Wu, L. Liu, S.H. Bo, G. Ceder, Jahn−Teller Assisted Na Diffusion for High Performance Na Ion Batteries, Chem. Mater. 28 (2016) 6575–6583.

[159] S. Komaba, T. Nakayama, A. Ogata, T. Shimizu, C. Takei, S. Takada, A. Hokura, I. Nakai, Electrochemically Reversible Sodium Intercalation of Layered $NaNi_{0.5}Mn_{0.5}O_2$ and $NaCrO_2$, ECS Trans. 16 (2009) 43–55.

[160] C.Y. Yu, J.S. Park, H.G. Jung, K.Y. Chung, D. Aurbach, Y.K. Sun, S.T. Myung, $NaCrO_2$ Cathode for High-Rate Sodium-Ion Batteries, Energy Environ. Sci. 8 (2015) 2019–2026.

[161] S.H. Bo, X. Li, A.J. Toumar, G. Ceder, Layered-to-Rock-Salt Transformation in Desodiated $Na_xCrO_2$ (x 0.4), Chem. Mater. 28 (2016) 1419–1429.

[162] J.J. Ding, Y.N. Zhou, Q. Sun, Z.W. Fu, Cycle Performance Improvement of $NaCrO_2$ Cathode by Carbon Coating for Sodium Ion Batteries, Electrochem. Commun. 22 (2012) 85–88.

[163] Y. Tsuchiya, A.M. Glushenkov, N. Yabuuchi, Effect of Nanosizing on Reversible Sodium Storage in a $NaCrO_2$ Electrode, ACS Appl. Nano Mater. 1 (2018) 364–370.

[164] X. Zhang, W.J. Jiang, A. Mauger, Qilu, F. Gendron, C.M. Julien, Minimization of the Cation Mixing in $Li_{1+x}(NMC)_{1-x}O_2$ as Cathode Material, J. Power Sources. 195 (2010) 1292–1301.

[165] M. Matsui, F. Mizukoshi, N. Imanishi, Improved Cycling Performance of P2-Type Layered Sodium Cobalt Oxide by Calcium Substitution, J. Power Sources. 280 (2015) 205–209.

[166] S.C. Han, H. Lim, J. Jeong, D. Ahn, W.B. Park, K.S. Sohn, M. Pyo, Ca-doped $Na_xCoO_2$ for Improved Cyclability in Sodium Ion Batteries, J. Power Sources. 277 (2015) 9–16.

[167] M.N. Obrovac, T.D. Hatchard, D.S. Iaboni, U. S. PATENT US 2016/0049653, (2016).

[168] R.J. Clément, P.G. Bruce, C.P. Grey, Review—Manganese-Based P2-Type Transition Metal Oxides as Sodium-Ion Battery Cathode Materials, J. Electrochem. Soc. 162 (2015) A2589–A2604.

[169] I. Buchberger, S. Seidlmayer, A. Pokharel, M. Piana, J. Hattendorff, P. Kudejova, R. Gilles, H.A. Gasteiger, Aging Analysis of Graphite/$LiNi_{1/3}Mn_{1/3}Co_{1/3}O_2$ Cells Using XRD, PGAA, and AC Impedance, J. Electrochem. Soc. 162 (2015) A2737–A2746.

[170] J. Vetter, P. Novák, M.R. Wagner, C. Veit, K.C. Möller, J.O. Besenhard, M. Winter, M. Wohlfahrt-Mehrens, C. Vogler, A. Hammouche, Ageing Mechanisms in Lithium-Ion Batteries, J. Power Sources. 147 (2005) 269–281.

[171] D.J. Xiong, T. Hynes, L.D. Ellis, J.R. Dahn, Effects of Surface Coating on Gas Evolution and Impedance Growth at $Li[Ni_xMn_yCo_{1-x-y}]O_2$ Positive Electrodes in Li-Ion Cells, J. Electrochem. Soc. 164 (2017) A3174–A3181.

[172] Y.J. Kim, J. Cho, T.-J. Kim, B. Park, Suppression of Cobalt Dissolution from the $LiCoO_2$ Cathodes with Various Metal-Oxide Coatings, J. Electrochem. Soc. 150 (2003) A1723–A1725.

[173] Z. Chen, J.R. Dahn, Methods to Obtain Excellent Capacity Retention in $LiCoO_2$ Cycled to 4.5 V, Electrochim. Acta. 49 (2004) 1079–1090.

[174] Z. Chen, J.R. Dahn, Improving the Capacity Retention of $LiCoO_2$ Cycled to 4.5 V by Heat-Treatment, Electrochem. Solid-State Lett. 7 (2004) A11–A14.

[175] W. Liu, X. Li, D. Xiong, Y. Hao, J. Li, H. Kou, B. Yan, D. Li, S. Lu, A. Koo, K. Adair, X. Sun, Significantly Improving Cycling Performance of Cathodes in Lithium Ion Batteries: The Effect of $Al_2O_3$ and $LiAlO_2$ Coatings on $LiNi_{0.6}Co_{0.2}Mn_{0.2}O_2$, Nano Energy. 44 (2018) 111–120.

[176] A.M. Wise, C. Ban, J.N. Weker, S. Misra, A.S. Cavanagh, Z. Wu, Z. Li, M.S. Whittingham, K. Xu, S.M. George, M.F. Toney, Effect of $Al_2O_3$ Coating on Stabilizing $LiNi_{0.4}Mn_{0.4}Co_{0.2}O_2$ Cathodes, Chem. Mater. 27 (2015) 6146–6154.

[177] R. Pfeffer, R.N. Dave, D. Wei, M. Ramlakhan, Synthesis of Engineered Particulates with Tailored Properties Using Dry Particle Coating, Powder Technol. 117 (2001) 40–67.

[178] R. Jung, M. Metzger, F. Maglia, C. Stinner, H.A. Gasteiger, Chemical versus Electrochemical Electrolyte Oxidation on NMC111, NMC622, NMC811, LNMO, and Conductive Carbon, J. Phys. Chem. Lett. 8 (2017) 4820–4825.

[179] J. Liu, N. Liu, D. Liu, Y. Bai, L. Shi, Z. Wang, L. Chen, V. Hennige, A. Schuch, Improving the Performances of $LiCoO_2$ Cathode Materials by Soaking Nano-Alumina in Commercial Electrolyte, J. Electrochem. Soc. 154 (2007) A55.

[180] L. Zheng, M.N. Obrovac, Honeycomb Compound $Na_3Ni_2BiO_6$ as Positive Electrode Material in Na Cells, J. Electrochem. Soc. 163 (2016) A2362–A2367.

[181] L. Zheng, M.N. Obrovac, Investigation of O3-Type $Na_{0.9}Ni_{0.45}Mn_xTi_{0.55-x}O_2(0 \leq x \leq 0.55)$ as Positive Electrode Materials for Sodium-Ion Batteries, Electrochim. Acta. 233 (2017) 284–291.

[182] L. Zheng, T.D. Hatchard, M.N. Obrovac, A High-Quality Mechanofusion Coating for Enhancing Lithium-Ion Battery Cathode Material Performance, MRS Commun. (2018) 1–6.

# APPENDIX: COPYRIGHT PERMISSIONS

**Order Details**

Journal of the Electrochemical Society

Billing Status: **N/A**

| | |
|---|---|
| **Order detail ID:** | 71747955 |
| **ISSN:** | 1945-7111 |
| **Publication Type:** | e-Journal |
| **Volume:** | |
| **Issue:** | |
| **Start page:** | |
| **Publisher:** | Electrochemical Society |
| **Author/Editor:** | Electrochemical Society |

**Permission Status:** ✓ **Granted**

**Permission type:** Republish or display content
**Type of use:** Republish in a thesis/dissertation
**Order License Id:** 4501490548827

| | |
|---|---|
| **Requestor type** | Academic institution |
| **Format** | Print, Electronic |
| **Portion** | chapter/article |
| **The requesting person/organization** | Lituo Zheng |
| **Title or numeric reference of the portion(s)** | Chapter of PhD thesis |
| **Title of the article or chapter the portion is from** | full article |
| **Editor of portion(s)** | N/A |
| **Author of portion(s)** | Lituo Zheng |
| **Volume of serial or monograph** | N/A |
| **Page range of portion** | |
| **Publication date of portion** | May 2019 |
| **Rights for** | Main product |
| **Duration of use** | Life of current edition |
| **Creation of copies for the disabled** | no |
| **With minor editing privileges** | yes |
| **For distribution to** | Worldwide |
| **In the following language(s)** | Original language of publication |
| **With incidental promotional use** | no |
| **Lifetime unit quantity of new product** | Up to 499 |
| **Title** | Chapter of PhD thesis |
| **Institution name** | Dalhousie University |
| **Expected presentation date** | May 2019 |

Title: Crystal Structures and Electrochemical Performance of Air-Stable Na2/3Ni1/3−xCuxMn2/3O2 in Sodium Cells

Author: Lituo Zheng, Jierui Li, M. N. Obrovac

Publication: Chemistry of Materials

Publisher: American Chemical Society

Date: Feb 1, 2017



**PERMISSION/LICENSE IS GRANTED FOR YOUR ORDER AT NO CHARGE**

This type of permission/license, instead of the standard Terms & Conditions, is sent to you because no fee is being charged for your order. Please note the following:

- Permission is granted for your request in both print and electronic formats, and translations.
- If figures and/or tables were requested, they may be adapted or used in part.
- Please print this page for your records and send a copy of it to your publisher/graduate school.
- Appropriate credit for the requested material should be given as follows: "Reprinted (adapted) with permission from (COMPLETE REFERENCE CITATION). Copyright (YEAR) American Chemical Society." Insert appropriate information in place of the capitalized words.
- One-time permission is granted only for the use specified in your request. No additional uses are granted (such as derivative works or other editions). For any other uses, please submit a new request.

BACK CLOSE WINDOW

**Title:** Investigation of O3-type Na0.9Ni0.45MnxTi0.55-xO2 (0 ≤ x ≤ 0.55) as positive electrode materials for sodium-ion batteries

**Author:** Lituo Zheng,M.N. Obrovac

**Publication:** Electrochimica Acta

**Publisher:** Elsevier

**Date:** 10 April 2017